

UNIVERSIDADE DE SÃO PAULO
INSTITUTO DE FÍSICA

**Reações Induzidas por Prótons em ^8Li a Baixas Energias
e Espectroscopia do ^9Be Altamente Excitado**

Erich Leistenschneider

Orientadora: Prof^a. Dr^a. Alinka Lépine-Szily

Dissertação de mestrado apresentada ao Instituto de Física da Universidade de São Paulo para a obtenção do título de Mestre em Ciências.

Banca Examinadora:

Prof^a. Dr^a. Alinka Lépine-Szily (Orientadora, IF-USP)
Prof. Dr. Marcos Aurelio Gonzalez Alvarez (IF-USP)
Prof. Dr. Paulo Roberto Silveira Gomes (IF-UFF)

São Paulo
2014

-
-
-

FICHA CATALOGRÁFICA
Preparada pelo Serviço de Biblioteca e Informação
do Instituto de Física da Universidade de São Paulo

Leistenschneider, Erich

Proton-induced reactions on ^8Li at low energies
– Reações induzidas por prótons em ^8Li a baixas
energias. São Paulo, 2014.

Dissertação (Mestrado) – Universidade de São Paulo.
Instituto de Física. Depto. de Física Nuclear

Orientador: Profa. Dra. Alinka Lépine-Szily

Área de Concentração: Física Nuclear

Unitermos: 1. Física nuclear; 2. Estrutura nuclear;
3. Reações nucleares.

USP/IF/SBI-026/2014

UNIVERSITY OF SÃO PAULO
INSTITUTE OF PHYSICS

**Proton-Induced Reactions on ^8Li at Low Energies
and Spectroscopy of ^9Be at High Excitation Energies**

Erich Leistenschneider

Advisor: Prof^a. Dr^a. Alinka Lépine-Szily

Dissertation submitted to the Institute of Physics of
the University of São Paulo for the Master of Science
degree.

Examining committee:

Prof^a. Dr^a. Alinka Lépine-Szily (Orientadora, IF-USP)

Prof. Dr. Marcos Aurelio Gonzalez Alvarez (IF-USP)

Prof. Dr. Paulo Roberto Silveira Gomes (IF-UFF)

São Paulo
2014

Erich Leistenschneider: *Proton-Induced Reactions on ^8Li at Low Energies, and Spectroscopy of ^9Be at High Excitation Energies* , April 2014

This work was financially supported by Fundação de Amparo à Pesquisa do Estado de São Paulo.

Este trabalho foi apoiado financeiramente pela Fundação de Amparo à Pesquisa do Estado de São Paulo.



*The man who voyages strange seas must
of necessity be a little unsure of himself.*

— Fred Hoyle

Dedicado a Emili, Mario e Taís.

RESUMO

Reações induzidas por prótons são importantes no estudo do consumo de ${}^8\text{Li}$ em alguns cenários astrofísicos. Neste trabalho, as seções de choque para as reações ${}^8\text{Li}(p,p)$, ${}^8\text{Li}(p,\alpha)$ e ${}^8\text{Li}(p,d)$ foram medidas em cinemática inversa entre $E_{\text{cm}} = 0.7$ e 2.2 MeV. Foi usado um feixe de ${}^8\text{Li}$ de alta pureza selecionado pelo Sistema RIBRAS no Laboratório Pelletron (IF-USP), São Paulo, que colidia com um alvo grosso de polietileno ($(\text{CH}_2)_n$, $7.7(8)$ mg/cm²), um plástico rico em prótons. Os produtos de reação foram medidos por um telescópio formado por detectores de barreira de superfície de silício posicionados em um ângulo dianteiro. As funções de excitação medidas foram analisadas através da metodologia de matriz-R e puderam fornecer informações sobre ressonâncias pouco conhecidas do núcleo composto ${}^9\text{Be}$ a altas energias de excitação. A importância de outros canais de decaimento e consequências das reações estudadas na nucleossíntese também são discutidas.

ABSTRACT

Proton-induced reactions are important in the study of the destruction of ${}^8\text{Li}$ in some astrophysical scenarios. In this work, the cross sections for the reactions ${}^8\text{Li}(p,p)$, ${}^8\text{Li}(p,\alpha)$ and ${}^8\text{Li}(p,d)$ were measured in inverse kinematics between $E_{\text{cm}} = 0.7$ and 2.2 MeV. A highly pure ${}^8\text{Li}$ beam selected by RIBRAS System in the Pelletron Laboratory (IF-USP), São Paulo, was used impinging on a thick polyethylene target ($(\text{CH}_2)_n$, $7.7(8)$ mg/cm²), a proton-rich plastic. The reaction products were detected by a telescope formed by silicon surface barrier detectors placed at a forward angle. The measured excitation functions were analysed through the R-matrix methodology and could provide information about poorly known high-lying resonances of the ${}^9\text{Be}$ compound nucleus. The importance of other decay channels and the consequences of the studied reactions on nucleosynthesis are also discussed.

Scientists are not dependent on the ideas of a single man, but on the combined wisdom of thousands of men, all thinking of the same problem and each doing his little bit to add to the great structure of knowledge which is gradually being erected.

— Ernest Rutherford (1936)

AGRADECIMENTOS

Faz quase sete anos que ingressei no grupo de Reações Diretas e Núcleos Exóticos do DFN-IF-USP, orientado pela professora Alinka. Devo dizer que dificilmente teria um início de carreira tão enriquecedor e empolgante. Esta seção é minha homenagem àqueles que tornaram isso possível, e a quem sou muito grato:

Aos professores que me acompanharam, Rubens Lichtenthäler, Valdir Guimarães e Pierre Descouvemont.

Aos demais professores do departamento, Medina, Nemi, Suaide, Leandro e Marcos.

Aos meus amigos e companheiros de laboratório, Vitor, Valdir, Jeremias, Pedro, Djalma, Kelly, Carmem, Juan, Adriana, Rubén, Vivi, Vinicius, Tati, Renato, Caio, Elienos, Ernesto e Hellen.

Aos técnicos e funcionários, Eduardo, Wanda, Otávio, Rone, Abreu, Tromba, Silvinho, Jorge, Tiago, Messias, Vitório, Edmilson, Celso, Espanhol, Márcio, Luis, Sérgio e Fábio.

Ao velhos amigos da graduação, Bruno, Juliana, Tim, Dobay, Cláudio, Wilson, Renato, Kaonan, Rebeca, Thiago, Rafael e a todos da salinha.

Por fim, à Alinka, aos meus pais, Mario e Emili, e à Taís. A estes, especialmente, estaria sendo imensamente injusto se ousasse escrever uma lista finita de razões pelas quais sou grato.

CONTENTS

1	INTRODUCTION	1
1.1	The role of ^8Li in Nucleosynthesis	3
1.1.1	Non-standard Big Bang Nucleosynthesis	4
1.1.2	R-process Nucleosynthesis	5
1.2	Structure of ^9Be and the $^8\text{Li}(p,\alpha)$ Experiment	7
1.3	Goals	10
2	THEORETICAL ASPECTS	11
2.1	Compound Nuclear Reactions	11
2.1.1	Resonances	12
2.2	Astrophysical Implications	14
2.2.1	Coulomb Barrier and Penetrabilities	15
2.2.2	Reaction Rates	17
2.3	R-Matrix Theory	18
3	EXPERIMENTAL PROCEDURE	23
3.1	Laboratory Overview	23
3.2	Ion Source	27
3.3	Pelletron Accelerator	28
3.4	RIBRAS System	31
3.4.1	Production Target Setup	31
3.4.2	Superconducting Solenoids	33
3.4.3	Scattering and Auxiliary Chambers	36
3.5	Detection Systems	37
3.5.1	Surface Barrier Detectors	37
3.5.2	Microchannel Plate Detector (MCP)	43
3.5.3	Faraday Cup	47
3.5.4	Electronics	47
3.6	^8Li Beam Handling and Characterization	51
3.6.1	Purity and Contaminants	52
3.6.2	Resolution and Intensity	55
3.6.3	Focusing	58
3.7	Target Characterization	60
3.7.1	^9Be , ^{197}Au and C targets	60
3.7.2	Polyethylene targets	61
3.8	Thick Target Method	63
3.9	Experiment Planning	65
3.9.1	Feasibility and Priorities	65
3.9.2	Beam Requirements	66
3.9.3	Reaction Products	67
3.9.4	Detector Dimensioning	70
3.9.5	Energy Resolution	71
3.9.6	Influence of Contaminant Carbon	72
3.10	Resume of the Experimental Procedure	73

4	DATA REDUCTION AND ANALYSIS	77
4.1	Excitation Functions from the TTIK Method	79
4.2	Alpha Spectra	83
4.2.1	Background	84
4.2.2	Final Spectra and Previous Results	86
4.3	Proton Spectra	88
4.3.1	Background	89
4.3.2	Final Spectra	91
4.4	Deuteron Spectra	92
4.4.1	Final Spectra and Previous Results	92
4.5	Other Decay Channels	94
4.5.1	Tritons	94
4.5.2	Neutrons and Gammas	96
4.6	R-Matrix Analysis	97
4.6.1	Resonance at $E_{\text{cm}} = 1.1$ MeV	101
4.6.2	Overlapping resonances at $E_{\text{cm}} \simeq 1.7$ MeV	102
4.6.3	Widths, ambiguities and other considerations	107
4.7	Astrophysical Reaction Rate	112
5	CONCLUSIONS AND OUTLOOK	115
	APPENDIX	119
A	REACTION KINEMATICS	121
A.1	Center-of-Mass Frame	123
A.2	Inverse Kinematics	125
B	SIM-RIBRAS SIMULATION TOOL	127
B.1	CineRIBRAS	127
B.2	SolFocus	129
C	SELECTION RULES	131
	BIBLIOGRAPHY	133
	List of Figures	146
	List of Tables	155

CONVENTIONS

For clarity and simplicity, some conventions are used along this work:

1. The reactions ${}^1\text{H}({}^8\text{Li}, {}^1\text{H})$, ${}^1\text{H}({}^8\text{Li}, {}^2\text{H})$ and ${}^1\text{H}({}^8\text{Li}, {}^4\text{He})$ will be denoted by ${}^8\text{Li}(p,p)$, ${}^8\text{Li}(p,d)$ and ${}^8\text{Li}(p,\alpha)$, respectively. Similar notation may be used for other reactions when convenient;
2. A decay channel of a compound nucleus may be designated as the name of the lightest particle of the pair. For example, an excited ${}^9\text{Be}$ decays in the *deuteron channel* if the resulting pair is ${}^7\text{Li} + d$;
3. The uncertainties are represented in the parenthesis notation.

ACRONYMS

RIBRAS Radioactive Ion Beams in Brazil

BBN Big Bang Nucleosynthesis

NEC National Electrostatics Corporation

MC-SNICS Multicathode Source of Negative Ions by Cesium Sputtering

GVM Generating Volt Meter

MCP Microchannel Plate Detector

PSD Position Sensitive Detector

ToF Time of Flight

DAQ Data Acquisition System

CFD Constant Fraction Discriminator

ADC Analog-to-Digital Converter

TAC Time-to-Amplitude Converter

CAMAC Computer Automated Measurement and Control
(acquisition system)

$(\text{CH}_2)_n$ Polyethylene (plastic)

TTIK Thick Target Inverse Kinematics Method

INTRODUCTION

One of the most prolific sources of information about the history of the Universe is the measurement of elemental abundances in the cosmos [1]. In figure 1 is shown a *local galactic* abundance distribution based on chondrite meteorites composition analysis and on spectroscopic data from nearby stars and nebulae [2].

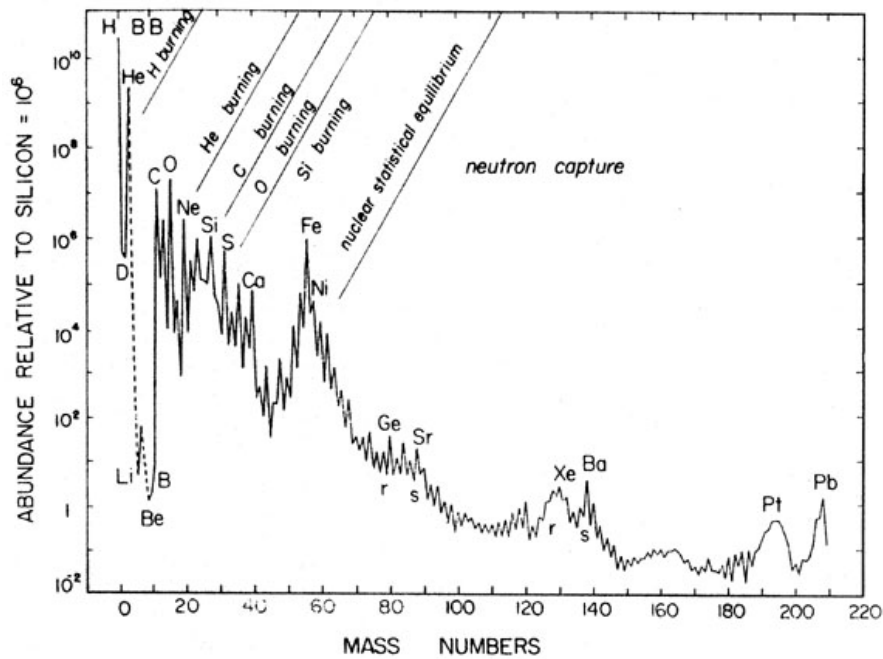


Figure 1: Local galactic abundances of isobars, adapted from [3].

To extract information from these abundance curves, astrophysical models on several steps of Universe evolution are employed [4]. Better the agreement between measured and calculated abundances, better the models used to describe the nucleosynthesis processes that occur in nature. Some of these processes are indicated at several points in figure 1, from the light elements produced right after the Big Bang to the heavy elements produced in processes based on neutron capture.

It is remarkable how some nuclear properties can be associated with structures present in abundance curves [4, 2]. The first is a prominent peak around mass number 60, associated with the region of maximum binding energy per nucleon (the Iron group, see figure 2), which are the most stable nuclei. Smaller peaks are also present around the neutron magic nuclei ^{88}Sr and ^{138}Ba and around the double-magic ^{208}Pb .

Magic numbers are number of nucleons (p or n) that form a closed shell in the nucleus [5]. They have higher binding energy per nucleon than nuclei in their vicinity. Magic numbers are N or Z = 2, 8, 20, 28, 50, 82 and 126.

The persistent oscillation between adjacent points is also due to the fact that odd nuclei are less bound than even nuclei and, thus, more fragile. The low abundance of the *fragile* isotopes of Li, Be and B is partially a consequence of the much higher binding energy per nucleon of their neighboring nuclei ${}^4\text{He}$ and ${}^{12}\text{C}$ [6]. Upon a detailed analysis, many other characteristics could be pointed out [2].

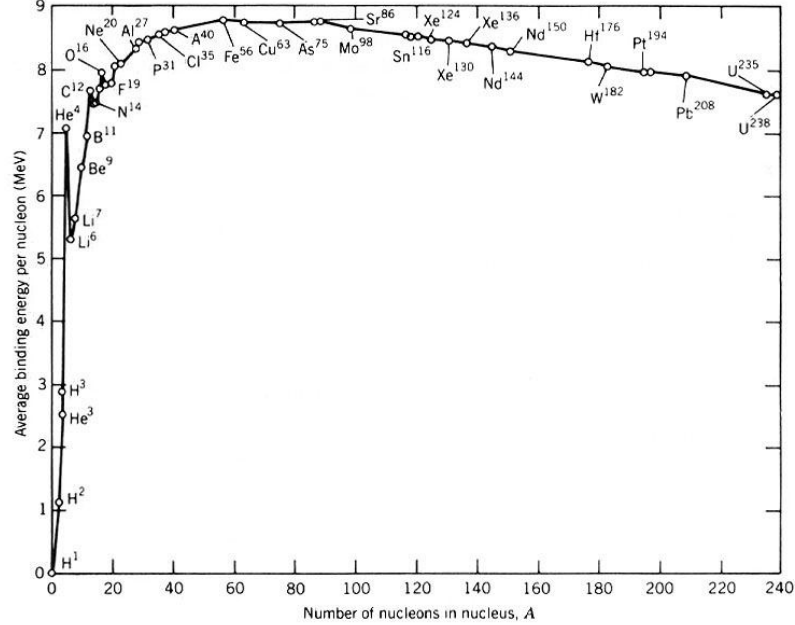


Figure 2: Average binding energy per nucleon as a function of the atomic mass number A . Adapted from [7].

These characteristics indicate how important the knowledge of nuclear structure is to understand the nucleosynthesis and the evolution of the Universe.

However, many of the theoretical approaches in astrophysics rely on data extrapolations and on model-dependant estimates and not on actually measured data [1, 8, 9]. The description of some astrophysical scenarios can depend on reactions involving unstable or exotic nuclei, which are much more difficult to be produced and studied than stable nuclei [10].

In the last few decades, new facilities able to produce beams of unstable species opened a wide field of study in nuclear science [11, 10]. Not only the study of nuclear matter at extreme conditions of isospin, excitation energy, density and many other characteristics became possible, but also new tests on astrophysically relevant situations could be carried out [9].

In this work are presented the measurements on reactions between the unstable ${}^8\text{Li}$ and protons performed at RIBRAS System (Radioactive Ion Beams in Brazil [12, 13]) at low energies. These results may have some useful consequences for astrophysical models.

1.1 THE ROLE OF ${}^8\text{Li}$ IN NUCLEOSYNTHESIS

${}^8\text{Li}$ has a half-life of 839(1)ms and decays by β^- to the unbound ${}^8\text{Be}$ [14], which decays into two alpha particles. ${}^8\text{Li}$ could be produced in a neutron abundant environment by the capture reaction ${}^7\text{Li}(n,\gamma){}^8\text{Li}$ [15]. Other authors indicate that with sufficient neutron abundance the ${}^8\text{Li}$ production is also possible through the reaction chain ${}^4\text{He}(2n,\gamma){}^6\text{He}(2n,\gamma){}^8\text{He}(\beta^-){}^8\text{Li}$ [16, 17].

The reaction ${}^7\text{Li}(d,p){}^8\text{Li}$ [18] could also produce ${}^8\text{Li}$ in a neutron poor environment, but it is not pointed as an important reaction or part of any relevant reaction chain in these scenarios.

The available ${}^8\text{Li}$ may be consumed in the synthesis of heavier elements [19] and help on the surpassing of the $A = 8$ mass gap through the following reactions:

${}^8\text{Li}(\alpha, n){}^{11}\text{B}$: this is referenced by some authors as the most important reaction that employs ${}^8\text{Li}$ to synthesize heavier elements [20, 21]. However, there are several discrepancies between the measurements done by different groups [22], as can be seen at figure 3.

${}^8\text{Li}(n,\gamma){}^9\text{Li}$: the ${}^9\text{Li}$ decays into ${}^9\text{Be}$ through β^- emission. The branching ratio for the decay into the ground state of ${}^9\text{Be}$ is 50(5)% [14]. The decay into excited states may lead to the break of ${}^9\text{Be}$ into $2\alpha + n$, competing with the synthesis of heavier elements. This reaction was measured through the inverse mechanism ${}^9\text{Li}(\gamma, n){}^8\text{Li}$ in experiments of Coulomb dissociation of ${}^9\text{Li}$ [23, 24].

${}^8\text{Li}(p,\gamma){}^9\text{Be}$: this reaction forms ${}^9\text{Be}$ at a high excitation energies in which several decay channels are open. The decay into other channels compete against the synthesis of elements heavier than ${}^8\text{Li}$. Available experimental informations about this reaction were obtained only through indirect methods [25, 26].

${}^8\text{Li}(d, n){}^9\text{Be}$: considered important to create ${}^9\text{Be}$ from ${}^8\text{Li}$, but it is not a relevant ${}^8\text{Li}$ consuming reaction [26, 27].

The synthesis of heavier elements through ${}^8\text{Li}$ must compete with several other processes that destroy the ${}^8\text{Li}$ and feed back lower masses. The first is its own decay by β^- emission, whose final products are two alpha particles, but other reactions must be also considered.

Given the high abundance of hydrogen in the Universe, it is reasonable to assume that protons are present in large quantities in almost any astrophysical environment. Thus, it is important to study destruction reactions induced by protons.

At figure 4 are depicted possible reaction chains with low mass nuclides at astrophysical scenarios, including the role of ${}^8\text{Li}$.

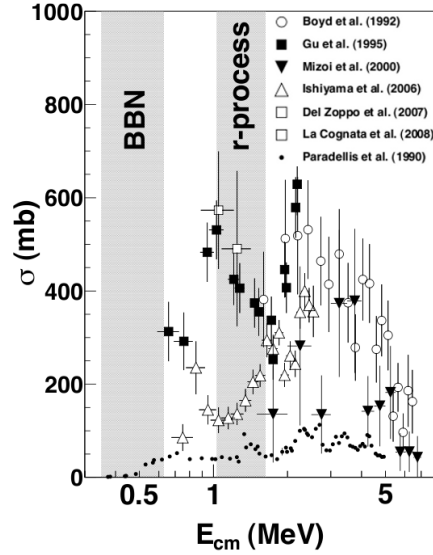


Figure 3: Cross section measurements of the ${}^8\text{Li}(\alpha, n){}^{11}\text{B}$ reaction at astrophysical energies [22].

In the next sections a brief description is given about the two possible scenarios in which the ${}^8\text{Li}$ could have a relevant astrophysical role: the inhomogeneous Big Bang nucleosynthesis and the r-process.

1.1.1 Non-standard Big Bang Nucleosynthesis

According to the homogeneous (or standard) Big Bang Nucleosynthesis (BBN) model [28, 29], in the very first minutes after the Big Bang, stable elements like ${}^2\text{H}$, ${}^3\text{He}$, ${}^4\text{He}$ and ${}^7\text{Li}$ would be produced from protons and neutrons created in the hadronization of primordial quark-gluon plasma [30]. This primordial nucleosynthesis would not be able to produce heavier elements beyond $A = 8$ mass gap.

This model implies on final abundances for ${}^1\text{H}$, ${}^2\text{H}$, ${}^3\text{He}$ and ${}^4\text{He}$ with fair agreement with the observational values. However, it fails to describe the observed abundance of ${}^7\text{Li}$, which is about one fourth of the calculated value. This disagreement is called the *lithium problem* [31].

Recently, an observation of elemental abundance of a low-metallicity galaxy suggests that the lithium depletion is due to post-BBN processes [33].

Although, some models also consider different conditions for BBN and are called *non-standard* BBN scenarios. Particularly, the inhomogeneous scenario considers a spatial inhomogeneity on the distribution of protons and neutrons after hadronization [34, 35]. Some regions could have peaks of high and low neutron-to-proton ratio, and may have the participation of unstable nuclei in the reaction chain.

In these scenarios, the BBN could produce elements up to $A = 12$, and the formation of ${}^8\text{Li}$ would consume part of the available ${}^7\text{Li}$

Metallicity of an astronomical object is the proportion of its matter made from elements different from hydrogen and helium. A low metallicity indicates that the object passed through little post-BB nucleosynthesis and may be considered an old object [32].

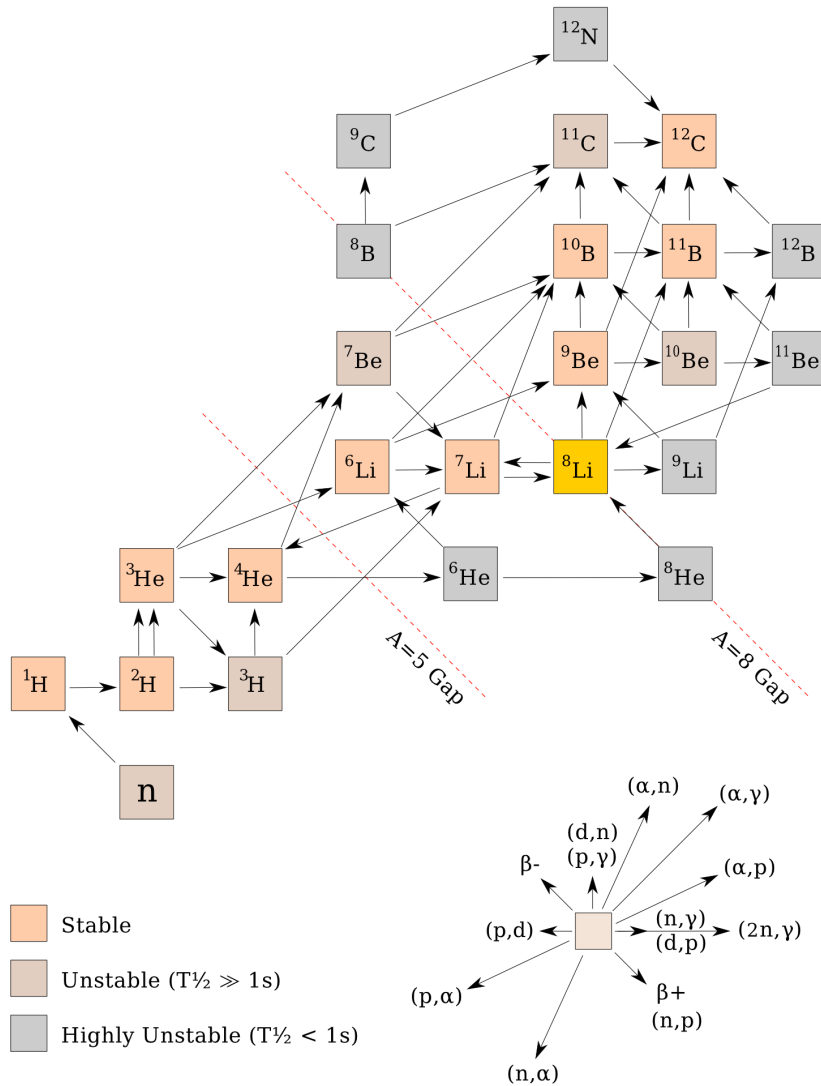


Figure 4: Possible astrophysical reaction chains with low mass nuclides, emphasizing the role of ^8Li . Sequential decays are not depicted.

and could also act as a catalyst to the formation of heavier elements [21, 36, 37]. Some authors predict that the formation of ^{12}C during the BBN is highly dependant on the abundance of ^8Li [38].

1.1.2 *R*-process Nucleosynthesis

The production of heavy elements beyond the iron group is described by processes based on neutron capture. One of these processes, the *s*-process (*s* for *slow*), can occur along the stability line in a not very neutron-rich stellar environment [39]. However, the *s*-process cannot explain all the heavy element abundances.

The other major neutron capture process is the *r*-process (*r* for *rapid*). Responsible for almost half of the production of such heavy ele-

ments, it is expected to occur in explosive environments that generate an extremely high neutron flux [39]. The most probable sites for r-process are core-collapse supernovae [40].

In these environments, neutrons are rapidly captured through successive (n, γ) reactions. The neutron flux is so high and the process so quick that (n, γ) reactions occur faster than the decay by β^- emission, getting further away from the stability line.

The neutron capture continues as the neutrons become less and less bound, and at some point, β^- decay half-lives become comparable to capture times or greater than it. This happens near the neutron drip-line or at closed neutron-shells (neutron-magic nuclei) and are called *waiting-points*. After β^- decay, the nuclei may continue capturing neutrons until the next waiting-point.

When the neutron flux ceases, the remaining neutron-rich nuclei will β^- decay towards the valley of stability. This process employs unstable neutron-rich nuclei as progenitors of heavy and stable nuclei of similar mass. At figure 5 are depicted the predicted paths of r-process, note that many of the waiting-points are nuclei that have never been observed.

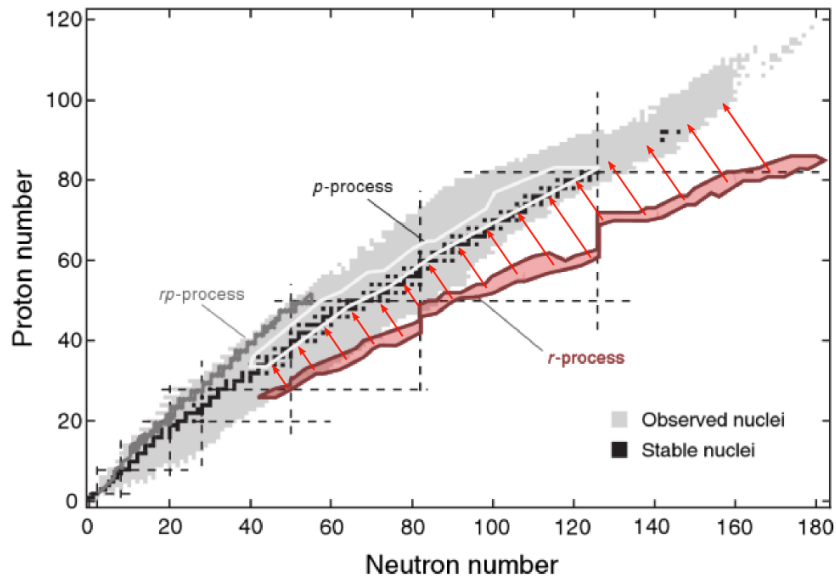


Figure 5: Predicted paths of r-process, showing the waiting-points (red region) and their paths upon β^- decay (red arrows). Magic numbers are represented by dashed lines. Paths of other processes are also depicted (adapted from [39]).

Very important parameters of any r-process model are the seed nuclei: stable or near stable nuclei from which the whole process will start. The seeds, their abundances and their immediate reactions heavily affect the dynamics of the entire process.

The first r-process models considered those nuclei around the iron group ($A \geq 40$) as the main seeds. However, recent studies suggest

that the r-process could initiate from very low masses, making the ${}^8\text{Li}$ an important waypoint [40, 19, 21]. Thus, the competition between different ${}^8\text{Li}$ consuming reactions could lead the r-process to completely different paths.

1.2 STRUCTURE OF ${}^9\text{Be}$ AND THE ${}^8\text{Li}(p,\alpha)$ EXPERIMENT

As mentioned, the study of proton induced reactions with ${}^8\text{Li}$ is of astrophysical interest. Reactions in the ${}^8\text{Li} + p$ system pass through resonances of the compound nucleus ${}^9\text{Be}$, whose proton threshold is high: 16.8882 MeV [14].

Therefore, even low incident energies can form the ${}^9\text{Be}$ nucleus at high excitation energies, where it is unbound and presents poorly known resonances. At figure 6 is depicted a level scheme of the ${}^9\text{Be}$ nucleus.

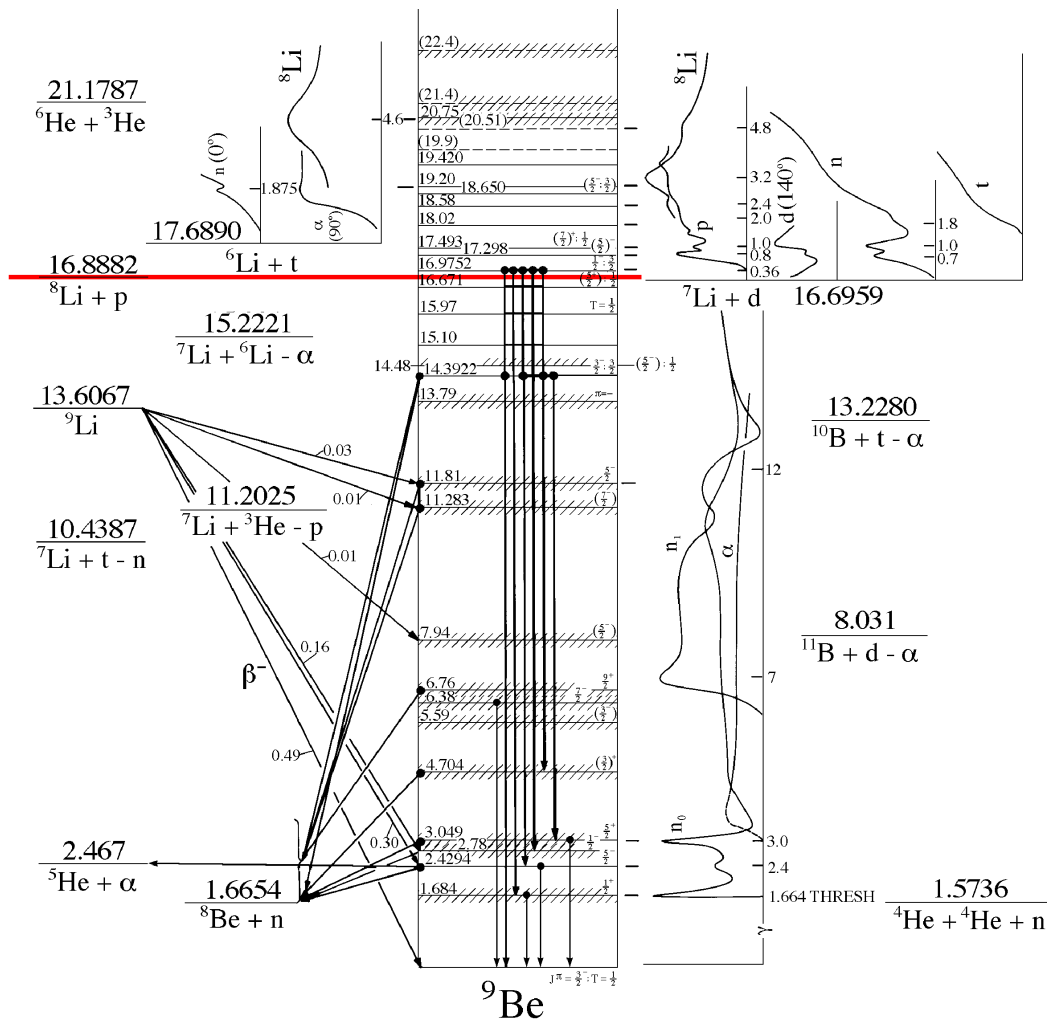


Figure 6: Energy levels for ${}^9\text{Be}$, the ${}^8\text{Li} + p$ threshold is emphasized [14].

Recently, a direct measurement of the ${}^8\text{Li}(p,\alpha)$ reaction between $E_{\text{cm}} = 0.2$ and 2.1 MeV [41] allowed the determination of a detailed excitation function and a reliable reaction rate.

The measurement was performed at the RIBRAS facility [12, 13] at the Pelletron Laboratory of IF-USP in São Paulo, Brazil. A hydrogen-rich polyethylene $(\text{CH}_2)_n$ target and a radioactive ${}^8\text{Li}$ beam were employed under the concept of the thick target method in inverse kinematics. The alpha particles from the reaction were measured at frontal laboratory angles by silicon surface barrier detectors forming a $E - \Delta E$ telescope and an excitation function could be determined.

The obtained data were analyzed through the R-matrix formalism [42] to determine the spectroscopic parameters of the observed resonances in the excitation function. Both the measured data and the R-matrix calculations are shown at figure 7.

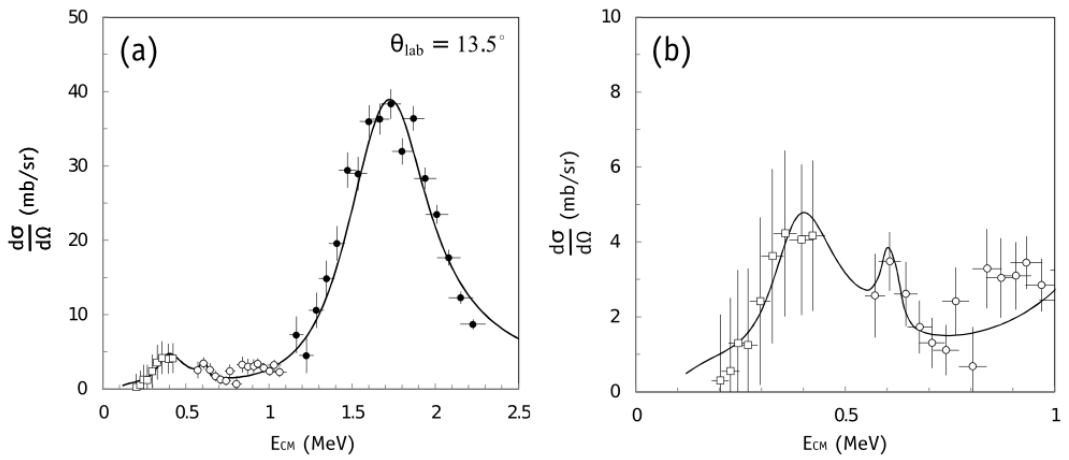


Figure 7: ${}^8\text{Li}(p,\alpha)$ differential cross sections at $\theta_{\text{lab}} = 13.5^\circ$, with the R-matrix fit (solid line): (a) full measured spectrum and (b) zoom at lower energies. Taken from [41].

The data revealed two resonances at the lower energy part of the excitation function, already known from previous works [14]. At the higher energy part, a broad peak could be described as two overlapping resonances.

The obtained data are compatible with the previously known spectroscopic parameters of ${}^9\text{Be}$ and improved the characterization of the nuclide at these high excitation energies.

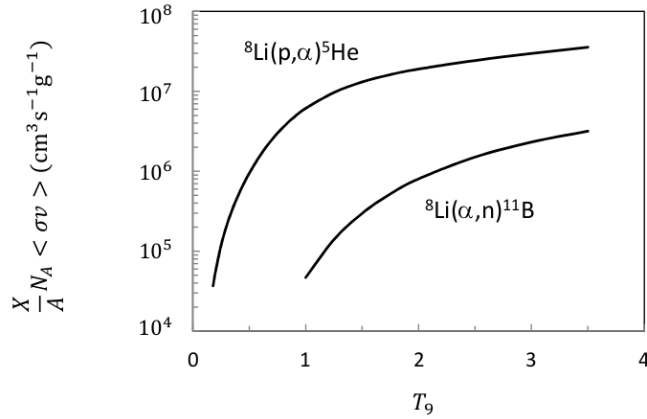
The presently available experimental data on ${}^9\text{Be}$ resonances near the ${}^8\text{Li} + p$ threshold are shown at table 1. It includes both the data from ${}^8\text{Li}(p,\alpha)$ experiment [41] and those previously known in the literature, compiled by [14].

Table 1: Available experimental data on ${}^9\text{Be}$ resonances near the ${}^8\text{Li} + p$ threshold (16.8882 MeV), including the compilation from [14] and the work of [41] on ${}^8\text{Li}(p,\alpha)$.

${}^9\text{Be}$ Res. E_x	Literature [14]				Previous Work - D. Mendes et al. [41]						
	E_r	$J^\pi; T$	Γ	Decay	E_r	J^π	($l; l$)	Γ_p	Γ_α	Θ_p^2	Θ_α^2
15.97	-0.92(3)	$T = \frac{1}{2}$	~ 300	γ							
16.671	-0.217(8)	$(\frac{5}{2}^+); \frac{1}{2}$	41(4)	γ	-0.22	$\frac{5}{2}^+$	$(\frac{5}{2}; 0)$	550(100)	41(4)	19.7	0.3
16.9752	0.087(1)	$\frac{1}{2}^-; \frac{3}{2}^-$	0.389(10)	γ, n, p, d							
17.298	0.410(7)	$(\frac{5}{2}^-)$	200	γ, n, p, d, α	0.38(8)	$\frac{5}{2}^-$	$(\frac{5}{2}; 1)$	5(1)	180(50)	2.7	1.4
17.493	0.605(7)	$(\frac{7}{2}^+); \frac{1}{2}$	47	γ, n, p, d, α	0.61(3)	$\frac{7}{2}^+$	$(\frac{5}{2}; 2)$	1.4(4)	39(15)	3.5	0.3
18.02	1.13(5)			γ							
18.58	1.69(4)			γ, n, p, d, α	1.69(3)	$\frac{5}{2}^+$	$(\frac{5}{2}; 0)$	250(50)	430(80)	4.3	3.1
18.65	1.76(5)	$(\frac{5}{2}^-; \frac{3}{2}^-)$	300(100)	p	1.76(4)	$\frac{7}{2}^+$	$(\frac{3}{2}; 2)$	70(13)	420(80)	8.4	3.5
19.20	2.31(5)		310(80)	n, p, d, t							

Energies E in MeV, widths Γ in keV, dimensionless reduced widths Θ^2 in %. The relative uncertainties on the reduced widths are identical to those of the partial widths.

The astrophysical implications of the reaction could also be studied. From the measured data, it was possible to calculate the astrophysical reaction rate for the ${}^8\text{Li}(p,\alpha)$, which was compared to the reaction rate obtained from one of the measurements [36] of the reaction ${}^8\text{Li}(\alpha, n){}^{11}\text{B}$. It is depicted on figure 8.


 Figure 8: ${}^8\text{Li}(p,\alpha){}^5\text{He}$ and ${}^8\text{Li}(\alpha, n){}^{11}\text{B}$ reaction rates multiplied by proton and alpha mass fractions for adequate comparison [41].

1.3 GOALS

After the realisation of the ${}^8\text{Li}(p,\alpha)$ experiment [41], RIBRAS System has received several improvements. From a new scattering chamber after the second solenoid that allows the production of very pure radioactive beams, to the acquisition of new set of detectors and the adoption of new techniques, like time-of-flight measurements. This creates a good opportunity to revisit, upgrade and extend the work on high lying resonances of ${}^9\text{Be}$ around the ${}^8\text{Li} + \text{proton}$ threshold performed through the measurement of the alpha decay channel in the previous experiment.

Besides the astrophysical interest in the measurement of the largest possible number of proton induced reactions with ${}^8\text{Li}$, the measurement of other decay channels can provide more information about the highly excited states of ${}^9\text{Be}$ by the population of resonances that cannot be accessed by the ${}^8\text{Li}(p,\alpha)$ reaction due to selection rules (see [41] and appendix C).

This work aims the measurement of the same excitation function for the alpha decay channel, but also exploring other reactions like ${}^8\text{Li}(p,p)$ and ${}^8\text{Li}(p,d)$, with an improved experimental setup at the RIBRAS System.

The experiment again was performed in inverse kinematics through a highly pure ${}^8\text{Li}$ beam provided by RIBRAS impinging on a thick $(\text{CH}_2)_n$ target. The reaction products were measured at a forward laboratory angle by silicon surface barrier detectors forming a $E - \Delta E$ telescope and the excitation functions obtained were analyzed by the R-matrix formalism.

The theoretical aspects related to this work are briefly described in chapter 2. The description of the experimental facility, devices, methods and techniques associated with this experiment are presented in chapter 3. The experimental results and the performed analysis are reported in chapter 4. In chapter 5 are addressed the main conclusions and final considerations.

THEORETICAL ASPECTS

In the collision of two nuclear systems, two extreme categories of nuclear reactions were identified: the formation of compound nucleus and direct reactions [43].

In direct reactions, the two colliding nuclei make a brief contact and then separate. In this quick interaction, the nuclear matter may be rearranged: nucleons may be exchanged or the nuclei may be excited. In compound nuclear reactions, the two nuclei fuse together and form a compound system, possibly excited, which eventually decays.

At lower relative energies, as those found in astrophysical scenarios, the formation of compound nucleus is usually prevalent over direct reactions [43]. As mentioned, the ${}^8\text{Li} + \text{p}$ system forms the ${}^9\text{Be}$ compound nucleus [41], so this kind of reaction should be studied in more detail.

2.1 COMPOUND NUCLEAR REACTIONS

After the fusion of the two initial nuclei, the compound nucleus may stay for a relatively long time in the excited state it was formed before decaying. This time may range from 10^{-20} to 10^{-15} seconds, much longer than the time scale of direct reactions (10^{-22} s) and enough to dissipate most of the information about the formation of the compound system among all of its constituents [43, 39, 5].

Eventually, the excited compound nucleus decays by the emission of a particle, that can be a β^- particle, a nucleon, or a small nuclear system like deuteron or alpha, or even by γ decay. Usually, the time scales for β and γ decays are higher than the lifetime of highly excited compound systems, making these decay modes less likely to occur.

Compound nuclear reactions can be described as a two-step process, which are relatively independent from each other. The first is the formation of the nucleus, which depends on the initially interacting particle pair, called *entrance channel* or *formation channel*. Some possible entrance channels for the formation of a ${}^9\text{Be}$ are ${}^8\text{Li} + \text{p}$, ${}^7\text{Li} + \text{d}$ or ${}^6\text{Li} + \text{t}$.

The second is the decay of the nucleus, that depends on the final ejected particles, called *decay channel* or *exit channel*. The final cross section σ is given by the product of probabilities of the two processes, this is called the *independence hypothesis* [43]:

$$\sigma(E) = \sigma(E)_{\text{form}} \cdot P(E)_{\text{decay}} \quad (1)$$

At a given energy E, $\sigma(E)_{\text{form}}$ is the cross section for the formation of the compound nucleus while $P(E)_{\text{decay}}$ is the probability of decay in the considered channel.

This hypothesis means that if a compound nucleus is formed in the same intermediate state (spin, parity, isospin, etc.) with the same total energy by different entrance channels, the probability P_{decay} for the decay in a specific channel is the same. This is a consequence of the loss of information about the formation of the compound system. See [44] for a classic experimental verification of this hypothesis.

Another remarkable property of compound nuclear reactions is their characteristic angular distribution. The products are emitted almost isotropically in the center-of-mass system. Accordingly to the independence hypothesis, the relative internal motions of the nucleons inside the compound system should disperse the motion of the nucleons of the incident beam after some time, thus the decay should be totally isotropic.

However, this is not completely true. Specifically, the angular momentum of the system cannot be dispersed and lost in anyway. If the angular momentum is large, the particles will preferentially be emitted from the equator of the rotating system. This will cause the angular distribution to be proportional to $1/\sin\theta$ [43].

Differently from direct reactions, compound nuclear reactions are often characterized by the sudden variations of the cross section with energy. This is due to the population of excited states in the compound nucleus, which originate resonances in the excitation functions [45].

2.1.1 Resonances

It is known that nuclei exhibit discrete quantum states, each with its characteristic energy, spin and parity. A quantum system described by a wave function which is an eigenfunction of the system's hamiltonian will remain in a well defined energy level unless it suffers an external disturbance.

However, from a specific threshold energy, there is enough energy in the system to detach a particle from it. The system is still bound, but it will eventually decay by the emission of this particle.

Obviously, as the system is bound, quantum states keep existing even very above this threshold. Yet, as the system is not able to be kept in a quasi-stationary state forever, it will have a characteristic lifetime τ associated.

According to the uncertainty principle [46], this lifetime consequently is associated to an imprecision in the decay energy. The energy of the emitted particle will follow a probability distribution of width Γ :

\hbar is the reduced
Planck constant.

$$\Gamma = \frac{\hbar}{\tau} \quad . \quad (2)$$

At a sufficiently high excitation energy, many decay channels may be open, which means that the system is above the threshold for the emission of many kinds of particles. In this situation, the lifetime

of the excited nucleus is related to the lifetime of all of the decay channels, and a total width Γ for the state can be defined.

It is intuitive that the most probable decay channel is the one which has the smallest lifetime τ_j , and consequently the higher Γ_j . The total width may be defined as

$$\Gamma = \sum_j \Gamma_j \quad . \quad (3)$$

Therefore, the probability of decay in a specific channel is given by

$$P_j(E)_{\text{decay}} = \frac{\Gamma_j(E)}{\Gamma(E)} \quad . \quad (4)$$

These highly excited states may be populated in the formation of a compound nucleus. If the initial system has a bombarding energy of E in the center-of-mass system, it will produce the compound nucleus at an excitation energy of E plus the threshold energy (separation energy of the compound system into the initial system).

If this energy matches the energy of one of the quasi-stationary states of the compound nucleus, the cross section for its formation will increase. And, according to equation 1, the shape of the excitation function for the detected reaction products will also reveal a peak at this energy. This is represented in the scheme in figure 9.

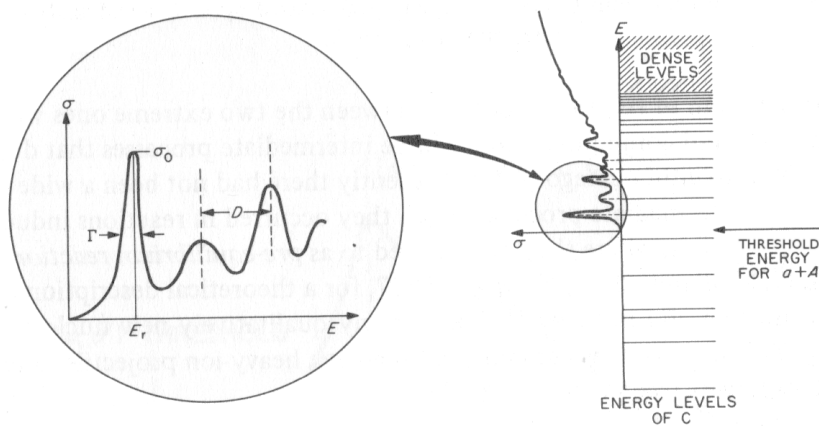


Figure 9: Scheme of an excitation function for a reaction obtained through the entrance system $\alpha + A$. The peaks are related to states of the compound nucleus C . Picture taken from [43].

This phenomenon is called *resonance* because it is caused by a matching between the incident and internal wave functions, causing the amplitude of the induced internal wave function to reach its maximum, and raising the probability of formation of the compound nucleus [43, 5].

From this point, the index i defines a specific formation channel, while the index j defines a specific decay channel. The absence of index denotes the total value of that quantity.

An isolated resonance in an excitation function usually has the shape of a lorentzian curve (or a Breit-Wigner curve) around the energy of the state E_R :

$$\sigma(E) \propto g \frac{\Gamma_i \Gamma_j}{(E - E_R)^2 + \left(\frac{\Gamma}{2}\right)^2} \quad (5)$$

in which g is a statistical spin term:

$$g = \frac{2J + 1}{(2I_1 + 1)(2I_2 + 1)} \quad (6)$$

However, in several conditions the Breit-Wigner shape cannot describe the shape of resonances. For example, when there are interferences between direct and compound contributions or when there are overlaps between states too close to each other. Examples of shapes a resonance can assume are given at figure 10.

I_1 and I_2 are the spins of the particles in the formation channel, J is the total spin of the compound nucleus in the state:
 $J = I_1 + I_2 + \ell$, being ℓ the angular momentum of the system.

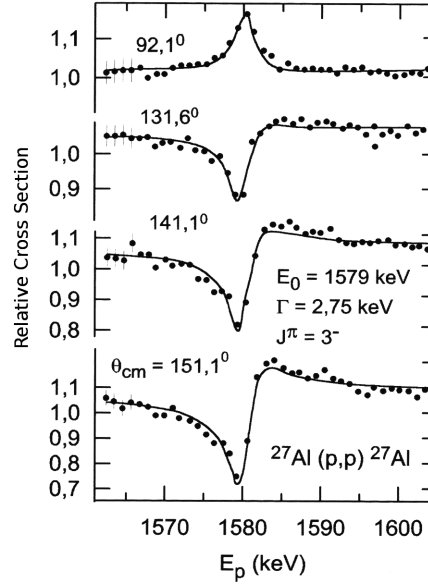


Figure 10: Measurements of differential cross section for the $^{27}\text{Al}(p,p)$ reaction at several angles around 1579 keV resonance [47], showing the several shapes a resonance can assume. A typical Breit-Wigner shape can be seen at the measurements at $\theta_{\text{cm}} = 92.1^\circ$.

At section 2.3 is presented a very powerful tool to determine the cross sections through measurable characteristics of internal states of a compound nucleus. The astrophysical implications of resonances are discussed in the next section.

2.2 ASTROPHYSICAL IMPLICATIONS

Nucleosynthesis sites are at temperatures in which the energy is very low for nuclear reactions, typically from some keV to very few MeV. So it is important to know what to expect from reactions at this conditions.

2.2.1 Coulomb Barrier and Penetrabilities

For a nuclear reaction to occur, the two participating nuclei should overcome the energy barrier due to electrostatic repulsion, called Coulomb barrier¹. A scheme of the Coulomb barrier is depicted at figure 11. A simple model for the Coulomb barrier between two nuclei (indexes 1 and 2) is given by:

$$E_{CB} = \frac{Z_1 Z_2 e^2}{r_0 (A_1^{1/3} + A_2^{1/3})} \quad (7)$$

Z and A are the atomic and mass numbers of the nuclei. For calculation purposes, $e^2 = 1.44 \text{ MeV} \cdot \text{fm}$ and $r_0 = 1.2 \text{ fm}$.

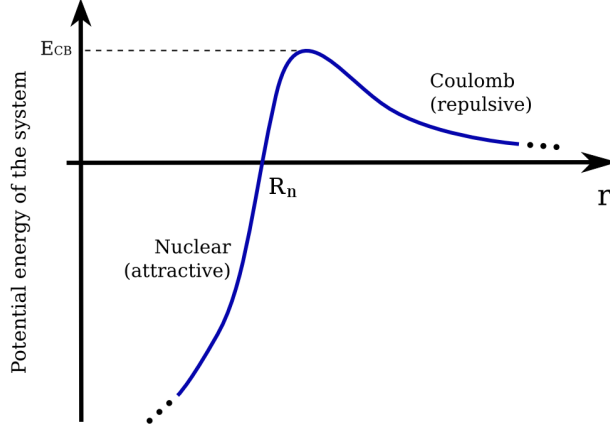


Figure 11: Scheme of the Coulomb barrier for two interacting nuclei in function of their distance.

If the energy of the system is very much below the Coulomb barrier, the interaction will be given only by the Coulomb force, and the Rutherford scattering will be dominant:

$$\left(\frac{d\sigma}{d\Omega} \right)_{\text{Ruth}} = \left(\frac{e^2}{4\pi\epsilon_0} \cdot \frac{Z_1 Z_2}{4E_{cm}} \right)^2 \frac{1}{\sin^4(\theta_{cm}/2)} \quad (8)$$

Classically, in this condition, no nuclear reaction should happen but only elastic Rutherford scattering. Yet, quantum tunneling may occur and the compound system can still be formed.

It is important to know how much of the incident wave function will be able to tunnel through the barrier and reach the internal region or, in other words, how much is the barrier penetrability.

By looking to the scheme at figure 11, it is intuitive that the penetrability should be dependent on the energy of the system E (center-of-mass frame) and on the nuclear radius R_n , that gives the boundary between regions of nuclear and Coulomb dominance, besides the electrostatic properties of the system. The penetrability for the ℓ^{th} partial wave is given by [48]:

$$P_\ell = \frac{1}{F_\ell^2(E, R_n) + G_\ell^2(E, R_n)} \quad (9)$$

ϵ_0 is the permittivity of free space, E_{cm} and θ_{cm} are energy and scattering angle at center-of-mass frame (see appendix A). For calculation purposes, with E_{cm} in MeV, the constant $(e^2/4\pi\epsilon_0) = 4.548$ and the differential cross section will be given in mb/sr.

¹ Unless one of the particles is a neutron, for which there is no electrostatic interaction.

The Coulomb wave equation describes the behavior of charged particles under the influence of a Coulomb potential:

$$\left(\frac{d^2}{d\rho^2} + \frac{\ell(\ell+1)}{\rho^2} - 1\right)\psi = 0$$

μ is the reduced mass of the system:

$$\mu = \frac{M_1 M_2}{M_1 + M_2}$$

in which F_ℓ and G_ℓ are the regular and irregular solutions of the Coulomb wave equation for a relative angular momentum ℓ [49, 50].

At very low energies ($E \ll E_{CB}$), P_ℓ can be written as (Wentzel-Kramers-Brillouin approximation [51]):

$$P_\ell \simeq e^{-2\pi\eta} \quad , \quad (10)$$

in which η is the Sommerfeld parameter:

$$\eta = \frac{Z_1 Z_2 e^2}{\hbar} \sqrt{\frac{\mu}{2E}} \quad . \quad (11)$$

As the reaction cross section is dependent on the penetrability, it also drops exponentially with decreasing energy. This is a very limiting factor for experiments of astrophysical interest and many parameters used in astrophysical models are extrapolations from data measured at higher energies.

Usually, a simple factorization of the cross section is employed to eliminate this energy dependence. It is called the astrophysical S-factor [39]:

$$S(E) = \frac{E \sigma(E)}{e^{-2\pi\eta}} \quad . \quad (12)$$

Typical dependences of the cross section and the S-factor with astrophysical energies, without the presence of resonances, can be seen at figure 12.

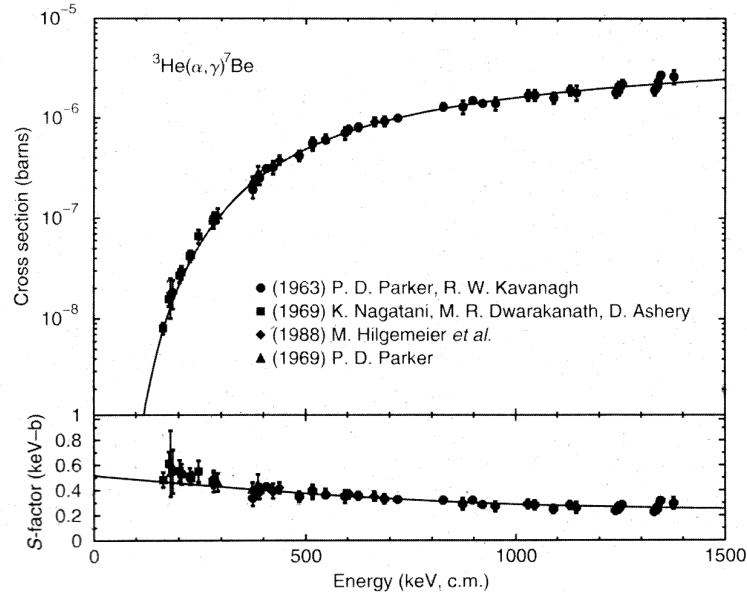


Figure 12: Typical dependence of the cross section and S-factor with energy observed in the ${}^3\text{He}(\alpha,\gamma){}^7\text{Be}$ data. Picture taken from [39].

2.2.2 Reaction Rates

The yield of a specific nuclear reaction that occurs in a nucleosynthesis environment is not only dependent on the reaction cross section, but also on the densities of each initial component and on the temperature of the medium [39].

Since this reaction rate should depend linearly on the densities of the particles, it is common to define a quantity that treats the reaction probability for one pair of interacting particles: $\langle \sigma v \rangle$.

The energy E of particles inside a thermal bath of temperature T follows the Maxwell-Boltzmann probability distribution [52], given by:

$$\phi_{\text{MB}}(E, T) = 2 \sqrt{\frac{E}{\pi}} \left(\frac{1}{k_B T} \right)^{3/2} \exp \left(-\frac{E}{k_B T} \right) . \quad (13)$$

k_B is the Boltzmann constant:
 $8.617 \cdot 10^{-5} \text{ eV/K}$.

As mentioned, for temperatures of nucleosynthesis environments the energies of a Maxwell-Boltzmann distribution are very low even at the most energetic part of the distribution. The product of the two probabilities, of finding a particle at some energy ($\phi_{\text{MB}}(E, T)$) and of reaction likelihood ($\sigma(E)$), is called the *Gamow distribution* and has a maximum in a region called *Gamow window* that is the relevant intersection between the two distributions' tails. This is depicted at figure 13.

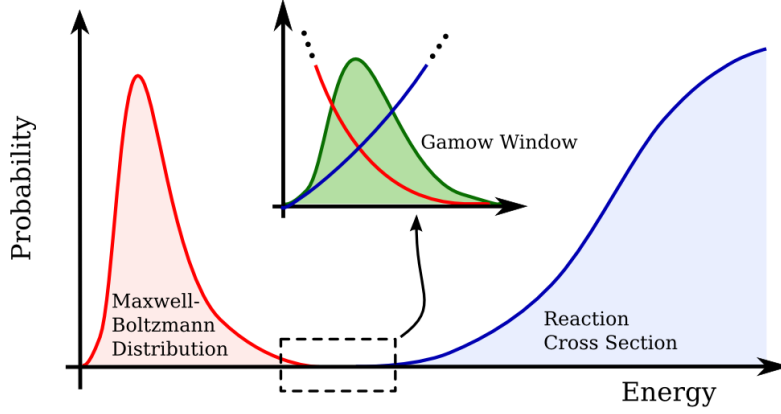


Figure 13: Schematic example of a Gamow window at some nucleosynthesis environments.

The quantity $\langle \sigma v \rangle$ should be given by [48]:

$$\langle \sigma v \rangle = \int_0^{\infty} \phi_{\text{MB}}(E, T) E \sigma(E) dE \quad (14)$$

$$= \sqrt{\frac{8}{\pi \mu (k_B T)^3}} \int_0^{\infty} \sigma(E) E e^{-E/k_B T} dE \quad , \quad (15)$$

or, in terms of the astrophysical S-factor,

$$\langle \sigma v \rangle = \sqrt{\frac{8}{\pi \mu (k_B T)^3}} \int_0^\infty S(E) e^{-\left(\frac{E}{k_B T} + \frac{b}{\sqrt{E}}\right)} dE \quad , \quad (16)$$

in which b is given by

$$b = \sqrt{2\mu} Z_1 Z_2 \frac{\pi e^2}{\hbar} \quad . \quad (17)$$

The Gamow energy E_G in which the Gamow distribution has its maximum and the width Δ_G of the distribution are [48]:

$$E_G = \left(\frac{b k_B T}{2}\right)^{\frac{2}{3}} \quad , \quad (18)$$

$$\Delta_G = 4 \sqrt{\frac{E_G k_B T}{3}} \quad . \quad (19)$$

The reaction rate will strongly depend on the S-factor inside the Gamow window ($E_G \pm \Delta_G$) for the environmental temperature. If the cross section exhibits a resonance inside or around the window, the reaction rate may be greatly enhanced and may affect significantly the nucleosynthesis reaction network if compared to a smooth and non-resonant S-factor.

A classic example on this phenomenon is the triple alpha reaction that forms ^{12}C at stars. The direct and non-resonant reaction chain $\alpha(\alpha, \gamma)^8\text{Be}(\alpha, \gamma)^{12}\text{C}$ cannot explain the observed ^{12}C abundances. The explanation comes from the existence of a resonance at 287 keV above the 3α threshold in ^{12}C spectra, which is called the *Hoyle resonance* [53].

The contribution of a typical Breit-Wigner resonance at E_R (eq.5) for the Gamow distribution is [39]:

$$\langle \sigma v \rangle = \left(\frac{2\pi}{\mu k_B T}\right)^{3/2} \hbar^2 (\omega\gamma)_R e^{-E_R/k_B T} \quad , \quad (20)$$

in which $(\omega\gamma)_R$ is called the *strength* of a resonance:

$$(\omega\gamma)_R = g \frac{\Gamma_i \Gamma_j}{\Gamma} \quad . \quad (21)$$

2.3 R-MATRIX THEORY

The interactions in the interior of a nucleus are extremely complex and its full description is an open problem. Details of the nuclear potential, mainly at extreme conditions, are still object of study, so the characteristics of internal levels of a nucleus cannot be well determined by purely theoretical approaches [39].

As previously mentioned, the simple Breit-Wigner shape cannot describe the cross section at many situations, mainly for broad resonances, interfering resonances and due to the contribution of direct reactions. An elaborate mathematical methodology is needed to properly connect measurements to nuclear structure and the dynamics of nuclear scattering. A powerful tool to realize this is the R-matrix theory [42].

The general idea of the R-matrix methodology is to take advantage of the short range property of nuclear interaction and define a spherical surface of radius a around the nucleus beyond which the nuclear force is negligible.

The external region ($r > a$) is dominated only by the Coulomb interaction and the wave functions of the formation and decay channels. For this situation, the solutions of the Schrödinger equation are the well known Coulomb functions. In the internal region ($r < a$), where the Coulomb and nuclear forces are both present, the wave function is not well known but the internal dynamics can be expressed in terms of a set of properties of the states of the compound nucleus. At the boundary ($r = a$), the wave functions of internal and external region must match and be smoothly connected.

This formulation does not provide information on any new nuclear phenomenon, but provides an easy way to extract internal properties from measured data and to predict cross sections for well known resonances. It is largely employed in the study of compound nuclear reactions, being a reliable tool for nuclear spectroscopy and nuclear astrophysics [43].

General lines and basic concepts of the R-matrix are explained below. For a more detailed explanation, see references [42, 54, 48, 55].

The problem consists of finding the solutions for the Schrödinger equation for the system's hamiltonian:

$$\begin{aligned} H_{\text{int}} &= T + V_C + V_N & r \leq a, \\ H_{\text{ext}} &= T + V_C & r > a. \end{aligned}$$

T is the total kinetic energy, V_C and V_N are the Coulomb and the nuclear potentials.

It was already mentioned that the regular $F_\ell(E, r)$ and irregular $G_\ell(E, r)$ Coulomb functions are radial solutions for the external non-nuclear part for the ℓ^{th} partial wave, but it is useful to rewrite them in a form of incoming (I_ℓ) and outgoing (O_ℓ) partial waves [54]:

$$\begin{aligned} I_\ell &= G_\ell - iF_\ell \quad , \\ O_\ell &= G_\ell + iF_\ell \quad . \end{aligned}$$

The general solution for the external part should be, upon a normalization, the combination of both incoming and outgoing waves:

$$\psi_{\ell, \text{ext}} = I_\ell(E, r) - U_\ell \cdot O_\ell(E, r) \quad . \quad (22)$$

U_ℓ is called the *collision function*. By looking to equation 22, it is quite intuitive that the measured cross section should be somehow connected to the collision function.

The equation 22 can be generalized to a multi-channel case [54]. Calling the entrance channel i and exit channel j , both with their own total spins J and parities π , the behavior of the wave function is given by

k is the wave number:

$$k = \frac{\sqrt{2\mu E}}{\hbar}$$

C_i is a normalization coefficient.

$$\psi_{j(i), \text{ext}} = C_i \sqrt{\frac{\mu_j}{\hbar k_j}} [\delta_{i,j} \cdot I_j(E, r) - U_{i,j} \cdot O_j(E, r)] \quad . \quad (23)$$

The term $\delta_{i,j}$ at equation 23 imposes that incoming flux only appears at elastic scattering ($i = j$). The collision matrix \mathbf{U} is formed from the elements $U_{i,j}$ from all open channels at a given energy. The conservation of flux imposes that \mathbf{U} is unitary.

On the other hand, the internal solution is not known but can be written as a set of base functions [54, 55]:

$$\psi_{\ell, \text{int}} = \sum_{\lambda} c_{\lambda, \ell} u_{\lambda, \ell}(r) \quad . \quad (24)$$

The functions $u_{\lambda}(r)$ can be associated with the quasi-stationary states λ of the compound nucleus, they should be orthonormal and their derivative should be zero at the boundary $r = a$.

The problem is to connect the internal and external wavefunctions at the boundary to find the coefficients $c_{\lambda, \ell}$ and the collision matrix \mathbf{U} (for simplicity, some coefficients were omitted):

$$\sum_{\lambda} c_{\lambda} u_{\lambda}(a) = \delta_{i,j} \cdot I_j(a) - U_{i,j} \cdot O_j(a) \quad . \quad (25)$$

Another important equation can be obtained by imposing the smoothness of the wavefunction at the boundary, which gives through some manipulations:

$$c_{\lambda} (E_{\lambda} - E) = \frac{\hbar^2 a}{2\mu} u_{\lambda}(a) [\delta_{i,j} \cdot I_j'(a) - U_{i,j} \cdot O_j'(a)] \quad . \quad (26)$$

By solving the system of equations 25 and 26, the collision matrix is obtained:

$$\mathbf{U} = (\mathbf{Z}^*)^{-1} \cdot \mathbf{Z} \quad , \quad (27)$$

in which the elements of the matrix \mathbf{Z} are:

$$Z_{i,j}(E) = \delta_{i,j} \cdot I_j(E, a) - a \sqrt{k_i k_j} I_j'(E, a) \cdot R_{i,j}(E) \quad . \quad (28)$$

The term $R_{i,j}(E)$ is the R-matrix element for a given partial wave:

$$R_{i,j}(E) = \sum_{\lambda} \frac{\gamma_{\lambda, i} \gamma_{\lambda, j}}{E_{\lambda} - E} \quad . \quad (29)$$

As can be seen, the R-matrix has poles that can be associated with the position of resonances. The quantities γ_λ are the reduced widths of the resonances in both entrance and decay channels. The quantities that appear in equation 29 are called *formal* quantities, but they are related to the observed ones by well known transformations [56]. The reduced widths are closely related to the measured partial widths $\Gamma_{\lambda,i}$ by:

$$\Gamma_{\lambda,i} = 2\gamma_{\lambda,i}^2 P_\ell(E_\lambda) \quad . \quad (30)$$

It is also common to represent the reduced width in terms of a dimensionless reduced width:

$$\Theta_{\lambda,i}^2 = \frac{\gamma_{\lambda,i}^2}{\gamma_w^2} \quad , \quad (31)$$

in which γ_w^2 is the Wigner limit:

$$\gamma_w^2 = \frac{3\hbar^2}{2\mu_i a^2} \quad . \quad (32)$$

The dimensionless reduced width is useful to determine the nature of the cluster structure of the resonance. Small values ($\Theta^2 \leq 0.01$) are usually related to spherical or compact states, while large values ($\Theta^2 \geq 0.1$) correspond to deformed states [41]. Θ^2 should never be greater than 1, and rarely is close to it. It is also common to represent the dimensionless reduced width in the form of a percentage.

Many formal parameters like the reduced widths are dependent on the channel radius a . However, this dependence is compensated by the Coulomb functions and the collision matrix is independent of a .

The differential cross section is then obtained by:

$$\frac{d\sigma_{i,j}}{d\Omega}(E, \theta) = \frac{1}{10k_i^2} \sum_{\ell} B_\ell(E) P_\ell(\cos \theta) \quad . \quad (33)$$

The quantity $B_\ell(E)$ is called the *anisotropy coefficient* and is directly deduced from the collision matrix. For a detailed description of this transformation, see section VIII in reference [42].

The R-matrix formalism is complete in the description of scattering cross section at many situations, mainly for compound nuclear reactions. The concept was successfully applied to several other reaction mechanisms like radioactive capture and methods like the continuum discretized coupled channel method (CDCC)[54].

The data analysis of this work was performed with the R-matrix methodology. A description on the selection rules for formation and decay of compound nucleus can be found at appendix C.

$P_\ell(E_\lambda)$ is the penetrability, as shown at equation 9 with $R_n = a$.

$P_\ell(\cos \theta)$ are the Legendre polynomials, the detection angle θ and energy E are in the center-of-mass frame.

EXPERIMENTAL PROCEDURE

A typical experiment in nuclear physics consists of a beam of accelerated charged particles hitting a target, where nuclear reactions may occur and their products can be studied by a set of detectors placed around it [43].

In the case of this experiment, performed at the Pelletron Accelerator Facility in São Paulo [57], an ^8Li radioactive beam impinged a hydrogen-rich plastic target made of polyethylene (chemical formula: $(\text{CH}_2)_n$). The reaction products, mainly protons, deuterons and alphas, were detected in a telescope formed by silicon surface barrier detectors, placed at frontal angles. The ^8Li beam was produced by a reaction with a stable ^7Li beam provided and accelerated by the 8-UD Pelletron Tandem and selected by the RIBRAS System [12, 13].

In this chapter are presented the details of this experiment and of the associated equipments and procedures.

3.1 LABORATORY OVERVIEW

In 1972, the Institute of Physics of University of São Paulo installed the Pelletron 8-UD, a tandem electrostatic accelerator manufactured by National Electrostatics Corporation (NEC) [58]. The accelerator facility was set up in the Oscar Sala building, whose scheme can be seen in figure 14.

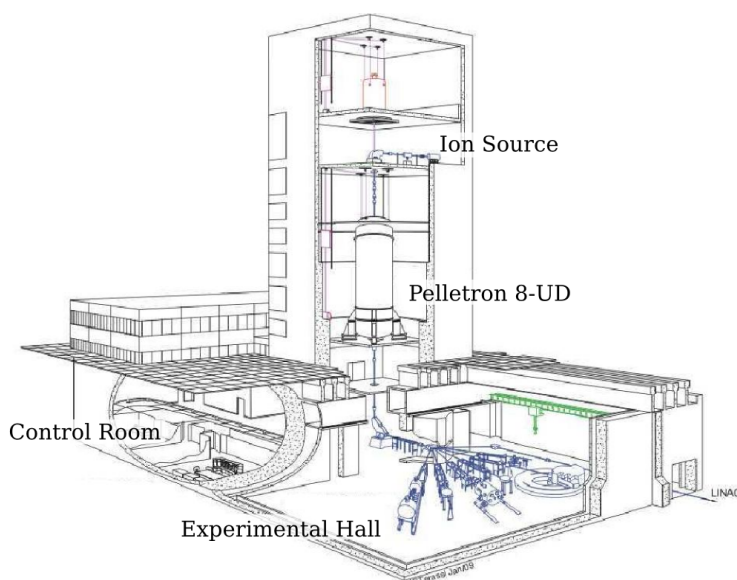


Figure 14: Scheme of the Oscar Sala building, showing the main parts of the accelerator facility (Author: J.C. Terassi).

In the Pelletron Laboratory, negatively charged ion beams are produced by a MC-SNICS Ion Source (Multicathode Source of Negative Ions by Cesium Sputtering [59]) of NEC. A detailed description can be found in section 3.2. The beam is produced from a sample made of a material which contains the atoms that are going to be accelerated. In the case of this experiment, a sample made of Lithium Oxide (Li_2O) was used to produce a ${}^7\text{Li}^{-1}$ beam in the ion source.

V_i is the
pre-acceleration
voltage.

The beam extracted from the source is pre-accelerated through an electric potential of $V_i = -90\text{kV}$. In this phase, the beam can be a mixture of several components of the sample, from isolated ions to molecules. The desired ion beam is selected from the other fragments by the analysing magnet ME20. This magnet deflects the beam in 90° and directs it towards the Pelletron accelerator.

$+V_T$ is the
accelerator's
terminal voltage
and e is the
elementary charge:
 $+1.60218 \cdot 10^{-19}\text{C}$.

In a Tandem accelerator, the high voltage terminal is located in the center of the acceleration tube and its ends are grounded [60]. Therefore, in the first half the negative ion gains an energy equivalent to $E = e V_T$. In the center of the terminal, the beam crosses a thin stripper foil made of carbon (thickness of about $5 \mu\text{g}/\text{cm}^2$) where it loses electrons and becomes positively charged. The amount of electrons lost in the stripper foil may vary according to the beam and its energy [61]. Between $V_T = 2.1\text{MV}$ and 8.0MV (accelerator's maximum), the most probable charge state of ${}^7\text{Li}$ is $+3$ (see figure 15).

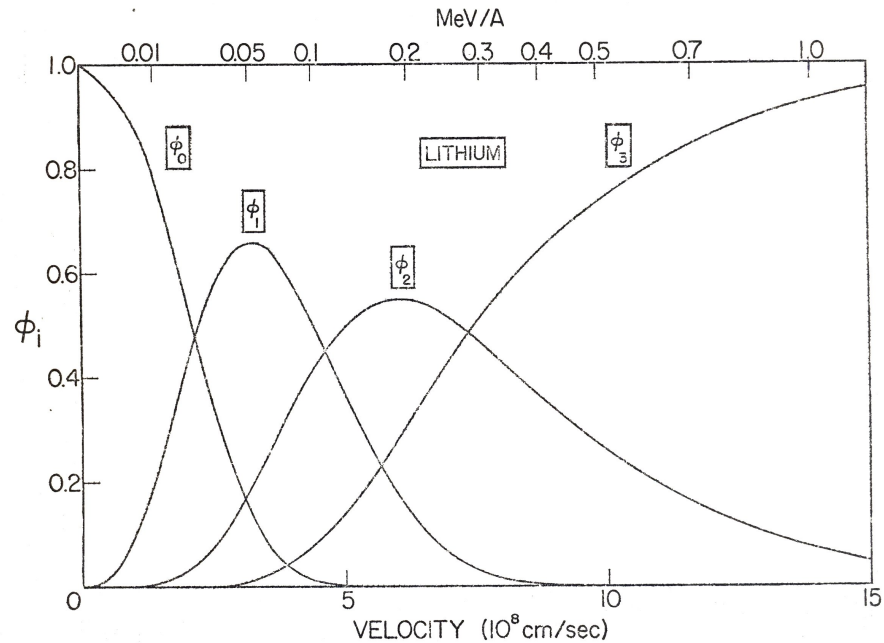


Figure 15: Probability ϕ_i of emerging from the carbon stripper foil for each charge state i of a ${}^7\text{Li}$ beam as a function of particle's energy [61].

q is the charge state
of the particle after
the stripper foil.

In the second half of the accelerator, the beam gains an energy proportional to its new charge state: $E = q e V_T$. Finally, the particle

leaves the accelerator with an energy given by:

$$E = e(q + 1) V_T + e|V_i| \quad . \quad (34)$$

As particles of the beam can leave the terminal with different charge states, a new selection in energy is needed. It is done by the analysing magnet ME200, which also bends the beam trajectory in 90° . Also, in this stage the beam energy is measured, with high precision, by Nuclear Magnetic Resonance [62] of a water sample placed inside the magnet, very close to the beam's trajectory. If the magnetic field is so that the NMR frequency of the sample is f , an ion beam whose mass is M and charge state is q will be selected by ME200 if its energy E is given by [63]:

$$E = M c^2 \left(\sqrt{1 + \frac{2q^2 f^2 K}{M}} - 1 \right) \quad , \quad (35)$$

c is the speed of light
in vacuum:
 $2.9979 \cdot 10^8$ m/s.

in which K is a geometric parameter of the ME200 magnet. The fine control of beam energy is also made in this stage (see sec.3.3).

After the energy selection, the ion beam is available to the seven beamlines in the experimental hall (fig.16). A switching magnet directs the beam to the chosen beamline. This experiment was realized at the RIBRAS System, placed in the 45B beamline.

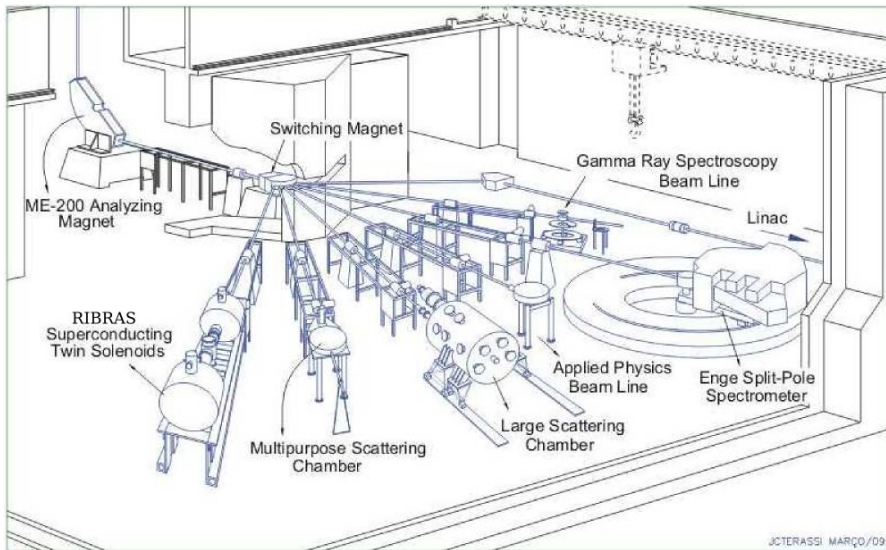


Figure 16: Scheme of the Pelletron Laboratory's Experimental Hall, showing the experimental beamlines available (Author: J.C. Terassi).

Elements for beam optics controlling and monitoring, such as slits, Faraday Cups, trimmers and magnetic quadrupoles, are placed all along the beamline. A vacuum of the order of 10^{-8} Torr is maintained along the beamline by several vacuum pumps. A detailed scheme of the Pelletron Laboratory's Beamline is displayed in figure 17.

Detailed descriptions on the functioning of the ion source and of the accelerator are available in sections 3.2 and 3.3, respectively.

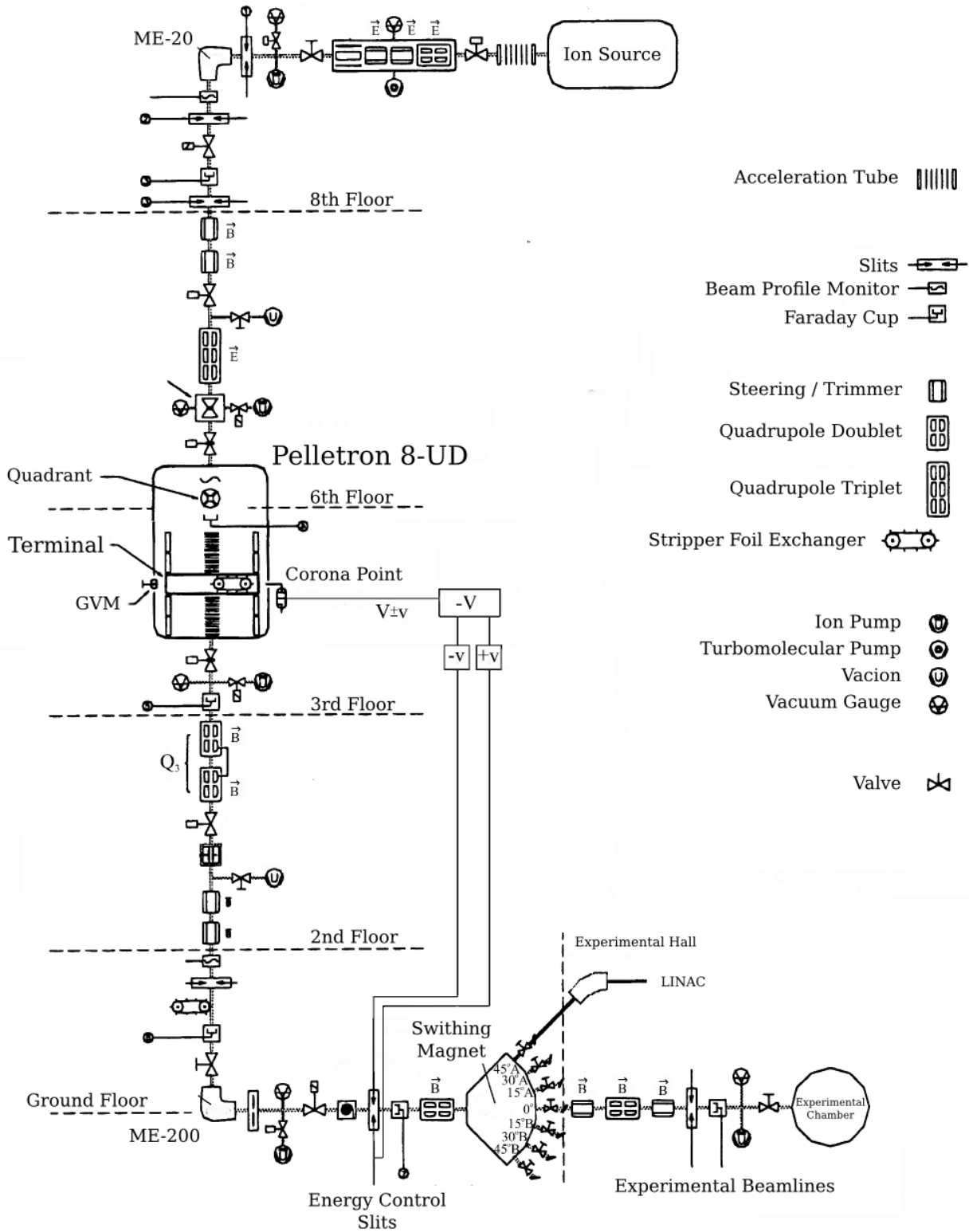


Figure 17: Detailed scheme of the Pelletron Laboratory beamline (Author: J.C. Terassi).

3.2 ION SOURCE

The Multicathode Source of Negative Ions by Cesium Sputtering (MC-SNICS), assembled by NEC, is a negative ion source able to produce beams of almost any element or molecule [59]. In this source, a reservoir containing cesium is heated to about 120° C, creating a neutral vapor of Cs inside the source, which is in vacuum.

Part of the cesium vapor condenses on the cooled cathode, which is a sample of the material used to produce the beam. In this multicathode version, many samples can be placed in the source and one can easily change from one sample to another without interrupting the source operation.

Part of the vapor also reaches the surface of a ionizer, heated to ~ 1200° C. Due to this high temperature, the cesium may be ionized to Cs⁺. The equilibrium between Cs⁰ that reaches the ionizer and Cs⁺ that leaves it is given by Saha-Langmuir's Law [64, 65]:

$$\frac{N(\text{Cs}^{+1})}{N(\text{Cs}^0)} = \exp\left(\frac{W - \phi_{\text{Cs}}}{k_B T}\right) \quad (36)$$

in which $\phi_{\text{Cs}} = 3.9\text{eV}$ is the ionization energy of Cs [66] and W is the thermionic work function of the metal on the surface of the ionizer. In order to obtain a high level of ionization, the ionizer's surface is made of tantalum, whose W is 4.25eV [67].

The ionized cesium is accelerated towards the cathode, producing sputtering on the sample. The sputtered atoms cross the neutral cesium layer before emerging from the sample. Due to cesium's very low electronegativity, the atoms may gain electrons from this layer and become negatively charged.

The negative ions are extracted from the sample by an electric field and carried out to the pre-accelerator tube, forming a negative ion beam. A scheme of the operation of this ion source can be seen on figure 18.

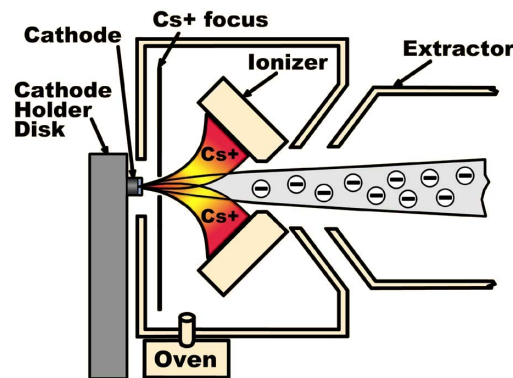


Figure 18: Scheme of the operation of the MC-SNICS ion source [68].

k_B is the Boltzmann constant and T is the absolute temperature.

3.3 PELLETRON ACCELERATOR

More information about the Pelletron accelerators can be found at references [57, 58, 60, 69].

The 8-UD Pelletron is an electrostatic tandem accelerator whose maximum terminal voltage is 8 MV. Its name comes from its charging system, which uses a chain made of metallic pellets connected by insulating nylon links. As mentioned in section 3.1, the high voltage terminal is located in the middle of the acceleration tube, with a device for changing the charge state of the ion in the terminal from negative to positive, thus using the positive terminal voltage twice.

The terminal is charged by electrostatic induction. The charging chain moves between two pulleys, one inside the terminal, which is electrically connected to it, and another grounded near the bottom of the accelerator. A pellet link in contact with the terminal pulley passes near a positively polarized inductor, which induces negative charge in the pellet. When the pellet loses contact with the pulley, while still under influence of the inductor's electric field, it charges the pulley positively by taking electrons out of it. By the rotation of the chain, the pellet is carried to the grounded pulley (or drive pulley), where its negative charge is suppressed, also by induction.

This process essentially takes away negative charge from the terminal, charging it positively. The inverse process occurs when the pellets are traveling from the drive pulley to the terminal pulley, when they carry positive charge to the terminal. The suppressor and inductor in the drive pulley are polarized by high-voltage sources, while the same devices in the terminal pulley are charged by the pickoff pulleys, which take some amount of charge from the pellets. A scheme of the charging system can be seen in figure 19.

The charge accumulated in the terminal is distributed along the acceleration tube by several metallic disks connected to each other by high-precision resistors, creating an uniform electric field inside the acceleration tube.

Except to the interior of the acceleration tube, which is in vacuum, the whole setup is immersed in a sulfur hexafluoride (SF_6) environment at high pressure (~ 70 psi). This gas is a very good electrical insulator and thermal conductor, which favors the stability of the accelerator. The setup is located inside a large metallic tank of ~ 3 m of diameter and ~ 10 m of height.

The beam energy control is done by the control of the voltage in the terminal, as expressed in equation 34. This control is done by a corona needle placed near the terminal that generates a corona discharge between the needle's point and the terminal. Changes in the corona current can tune the voltage in the terminal. The corona current can be controlled by two devices: by the Generating Volt Meter (GVM) or by the slits.

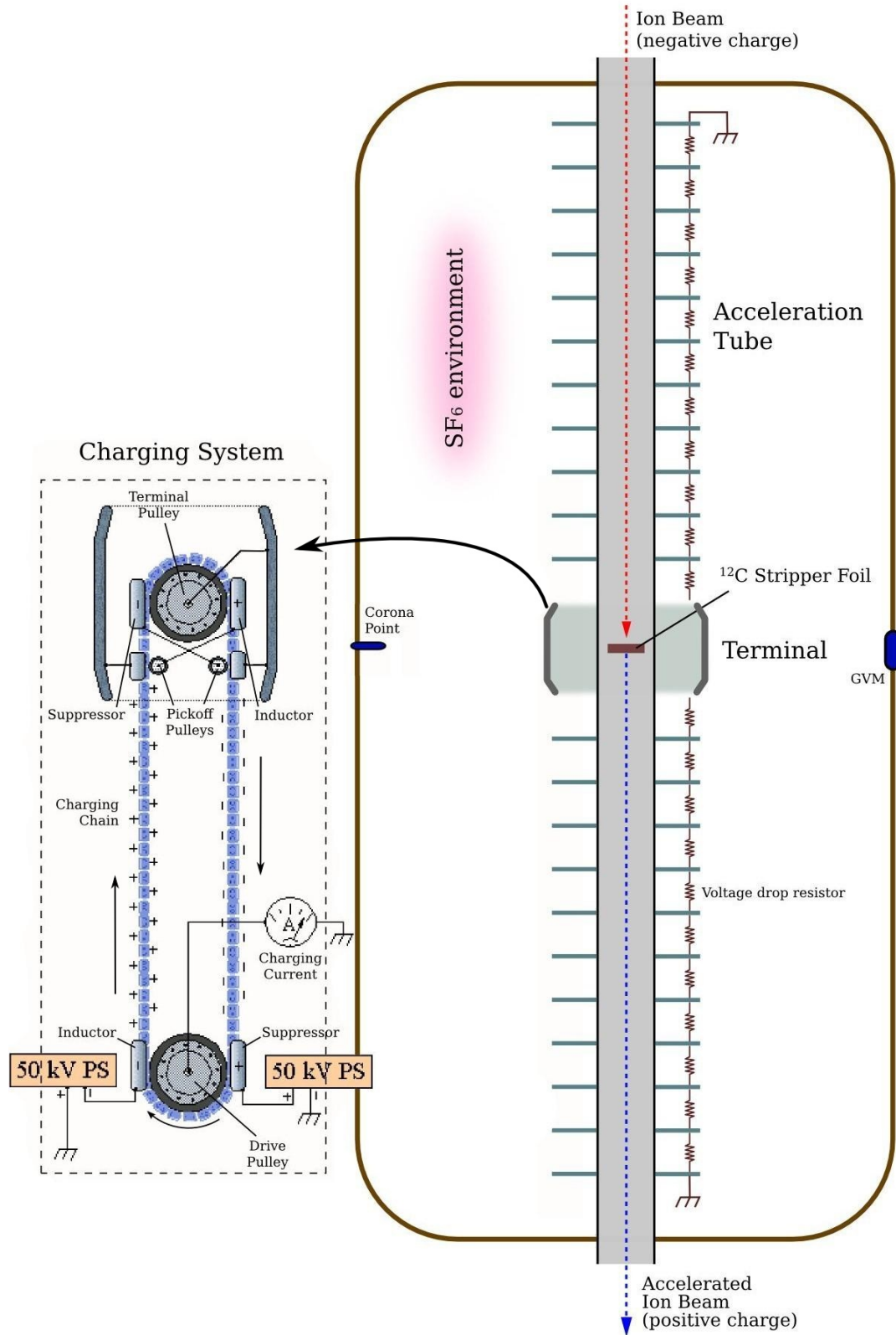


Figure 19: Scheme of the Pelletron accelerator, including its charging system and the acceleration tube. Picture adapted from [70].

The GVM is an instrument that measures the electric field produced by the terminal. It consists of a rotating helix placed near the terminal and another one fixed and concentric to the first, placed right behind it. The rotating helix is grounded and, by its rotation, it alternates in covering and exposing the fixed one. The fixed helix, on the other hand, experiences a charge induction when it is exposed to the terminal voltage. When it is fully covered by the rotating one, the helix can no longer feel the terminal's electric field. It generates an alternated current in the fixed helix that can be measured. The amplitude of this alternated current is proportional to V_T . At São Paulo's Pelletron facility, this method is used for coarse energy adjustment and for controlling the terminal voltage while the beam is not on.

The fine energy control is done by the selection capabilities of the analysing magnet ME200. A pair of vertical slits is placed right after the ME200. If the terminal voltage suffers a slight instability, the beam energy and its trajectory inside the magnet are changed. This would cause the beam to hit one of the slits and, by the current generated in the slit, a correction can be sent to the corona point. This system allows the Pelletron Accelerator to provide a high precision in the beam's energy. A scheme of the energy control system is shown at fig. 20.

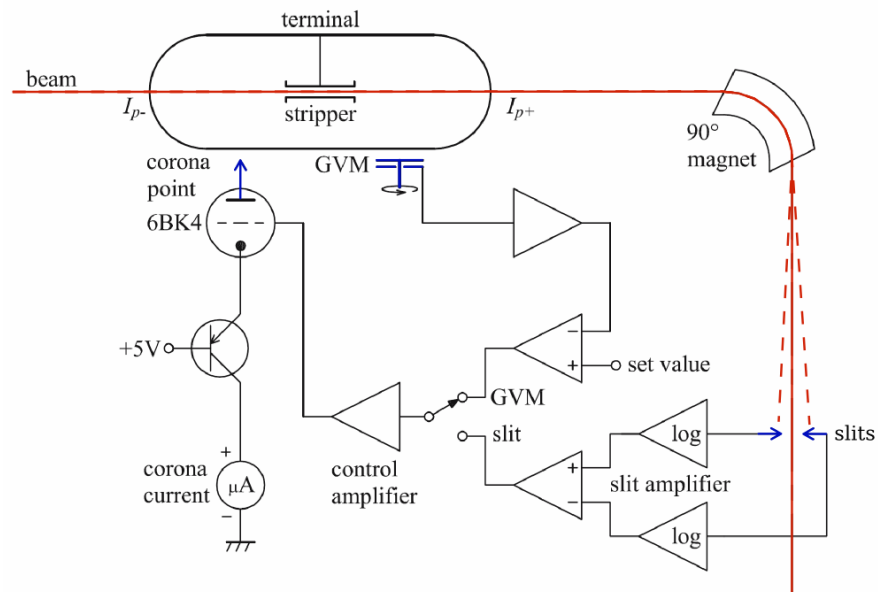


Figure 20: Scheme of the Pelletron accelerator's energy control system (adapted from [60]).

3.4 RIBRAS SYSTEM

The RIBRAS System (Radioactive Ion Beams in Brazil) was set up in 2004 at the 45B beamline of the Pelletron Laboratory [12, 13]. It uses the *in-flight* production and selection of radioactive ion beams [10] to perform experimental nuclear physics studies. The system provides light secondary beams of exotic species like ${}^8\text{Li}$, ${}^6\text{He}$ and ${}^8\text{B}$ at intensities ranging from 10^4 to 10^6 ions/s and at low energies, typically from 2 to 5 MeV/nucleon.

In the *in-flight* method of production of radioactive beams, unstable nuclei are produced in nuclear reactions between a stable primary beam and a production target. These unstable reaction products emerge from the target and are selected by an electromagnetic *in-flight* separator, forming a secondary beam available for experiments.

This method has some advantages over other methods [10]: the no need of a post-acceleration and the capability to produce beams of short-lived exotic nuclei, since the typical time of flights between production and experiment are very short (in the order of hundreds of nanoseconds). On the other hand, in the *in-flight* method the secondary beam's emittance is high ($\sim 0.15 \text{ mm} \cdot \text{rad}$) and the energy resolution is poorer due to straggling in the production target.

The RIBRAS System consists of a production target setup, two superconducting solenoids, two scattering chambers (one smaller between the two solenoids and a large after the second solenoid) and other auxiliary chambers placed along the beamline. RIBRAS System's beamline and its schematic drawing are depicted in figure 21. Each component and its role in RIBRAS System are described below.

3.4.1 Production Target Setup

The production target, or primary target, is a film¹ where the unstable beam of interest is produced by a nuclear reaction, usually a transfer reaction, with the beam provided by the Pelletron Accelerator. Using a proper choice of primary beam and target, many unstable ion beams can be produced. Some examples of beams that can be produced at RIBRAS are shown in table 2.

The primary target cell allows the use of gaseous or solid targets. It consists of a cubic metallic box of 2cm in its sides; in the sides that are facing the beam's direction there are circular windows. If a solid target is going to be used, it may be simply mounted in one of these windows. If a gaseous target is going to be used, a gas circulation device is connected to the cell and thin films can be placed in the windows to prevent the gas to escape. If the primary beam's intensity

¹ The thickness of the primary target may vary from some hundreds of $\mu\text{g}/\text{cm}^2$ to a few mg/cm^2 , depending on the material. For more details, see sec. 3.7.

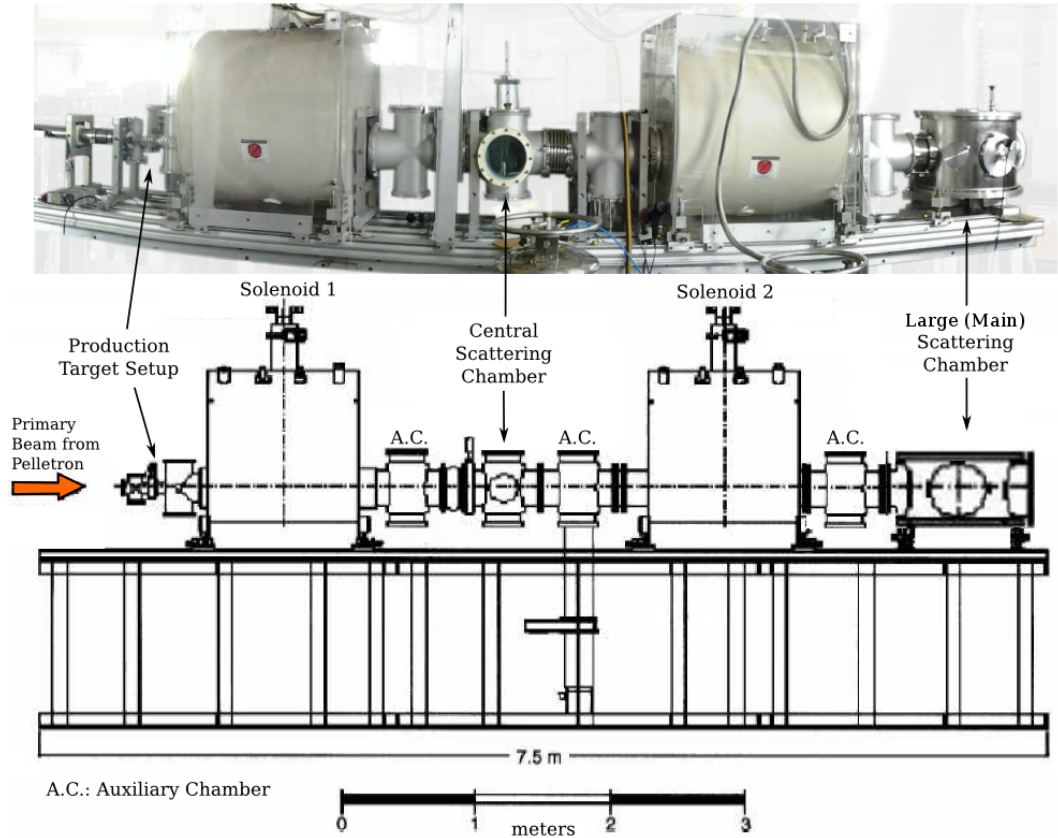


Figure 21: RIBRAS System at Pelletron Laboratory's 45-B Beamline. Panoramic picture (above) and schematic drawing (below), showing its main components (adapted from [71]).

Table 2: Examples of radioactive beams that can be produced at RIBRAS [13].

RADIOACTIVE BEAM	PRODUCTION REACTION
${}^8\text{Li}$	${}^9\text{Be}({}^7\text{Li}, {}^8\text{Li}){}^8\text{B}$
${}^6\text{He}$	${}^9\text{Be}({}^7\text{Li}, {}^6\text{He}){}^{10}\text{B}$
${}^{12}\text{B}$	${}^9\text{Be}({}^7\text{Li}, {}^{12}\text{B}){}^4\text{He}$
${}^7\text{Be}$	${}^3\text{He}({}^7\text{Li}, {}^7\text{Be}){}^3\text{H}$
${}^7\text{Be}$	${}^3\text{He}({}^7\text{Li}, {}^7\text{Be}){}^2\text{H}$
${}^8\text{B}$	${}^3\text{He}({}^6\text{Li}, {}^8\text{B})\text{n}$

is to high ($> 0,7\mu\text{A}$ of a ${}^7\text{Li}$ beam, for exemple), a solid target may need refrigeration. In this case, helium gas or simply air can circulate through the cell to cool the primary target.

Most of the primary beam crosses the production target without interacting. Moreover, it has an intensity of about 10^6 times larger than the intensity of a typical secondary beam. Thus, it must be blocked in

order to not interfere in the experiments with radioactive secondary beams. This blocking is done by a Faraday Cup placed right after the target, at zero degrees. It is also used to integrate the accumulated charge of the primary beam (details in sec. 3.5.3). This is necessary for data normalization.

The Faraday Cup blocks the incoming beam between zero and two degrees. A collimator placed after the production target also limits the scattering angle to a maximum of 6° . Thus, the intensity of the secondary beam will firstly depend on the cross section of the production reaction between 2° and 6° in the laboratory frame, as well as on the intensity of the primary beam and on the thickness of the target, which must be very well dimensioned as an increase on the thickness also increases the beam straggling and worses the beam's energy resolution.

In figure 22 is shown a scheme of the production target setup.

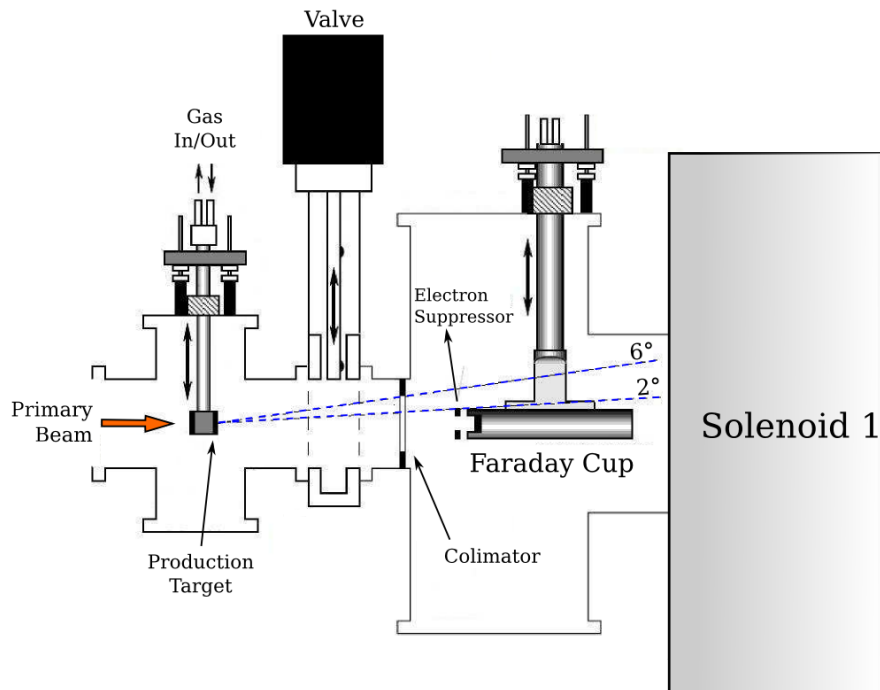


Figure 22: Scheme of the Production Target Setup at RIBRAS System (adapted from [71]).

3.4.2 Superconducting Solenoids

The secondary beam travels away from the production target, divergently. RIBRAS employs superconducting solenoids around the beam-line to bend the ion trajectories and make the beam convergent in a small region, where a nuclear target can be placed.

RIBRAS' beamline has a diameter of 25 cm to account for the large angular acceptance needed to produce an intense secondary beam.

To cover this large angular acceptance, a solenoid is more efficient than a conventional dipole [71]. Solenoids would act as biconvex magnetic lenses; ions produced at one point along the radial axis of the solenoid will be focused at another point along this axis after the solenoid through the action of Lorentz force:

q is the charge state of the ion, \vec{v} is its velocity and \vec{B} is the magnetic field acting on the particle.

$$\vec{F} = q\vec{v} \times \vec{B} \quad . \quad (37)$$

RIBRAS' solenoids were manufactured by Cryomagnetics Inc. Their coils are made of Niobium-Titanium (NbTi) alloy, superconductive at temperatures below 9.2K [72]. Superconductive materials are of great advantage as they can hold high electrical currents without losses through Joule Effect and power sources are just needed while the current inside the coils is being changed. The solenoids can produce a highly uniform magnetic field up to 6.5T in their interior

The coils are cooled with liquid helium at 4K. The thermal shielding is done by vacuum and a layer of liquid nitrogen (77K). Details of the solenoids can be found at figure 23.

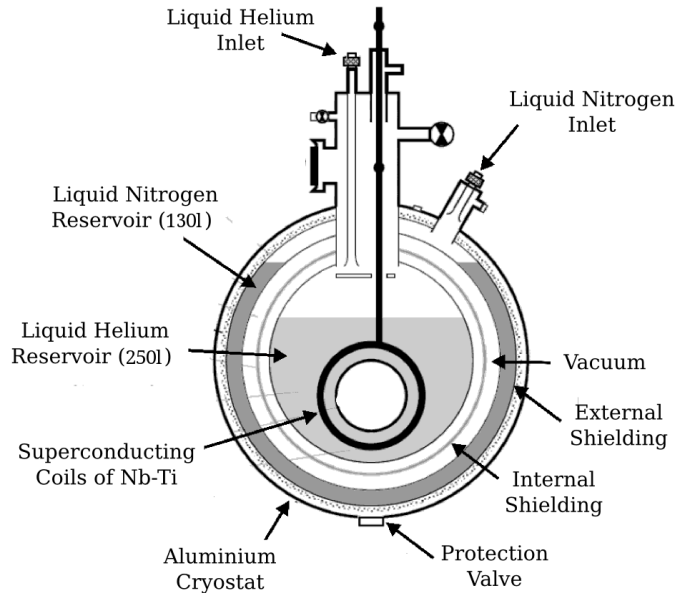


Figure 23: Schematic cross section of the solenoids employed at RIBRAS (adapted from [55]).

Each solenoid has its focal point in the center of a scattering chamber. In the case of the first solenoid, its focal point is the central chamber between both solenoids, while the focal point of the second solenoid is the center of the large (or *main*) chamber, having as origin point the center of the central one. An example of ion trajectory bending by RIBRAS is shown at figure 24. A focalization curve for ${}^8\text{Li}$, relating beam energy to the current in the solenoids needed to converge ${}^8\text{Li}$ beam at the focal points, is shown at figure 25.

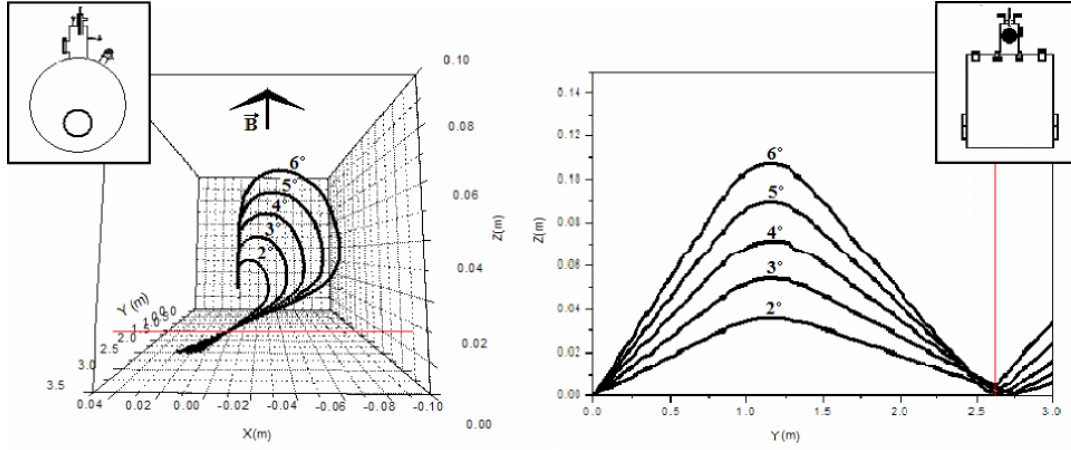


Figure 24: Example of simulated ion trajectories inside RIBRAS, leaving the production target and being focused in the center of the central scattering chamber (red line) by the first solenoid [71].

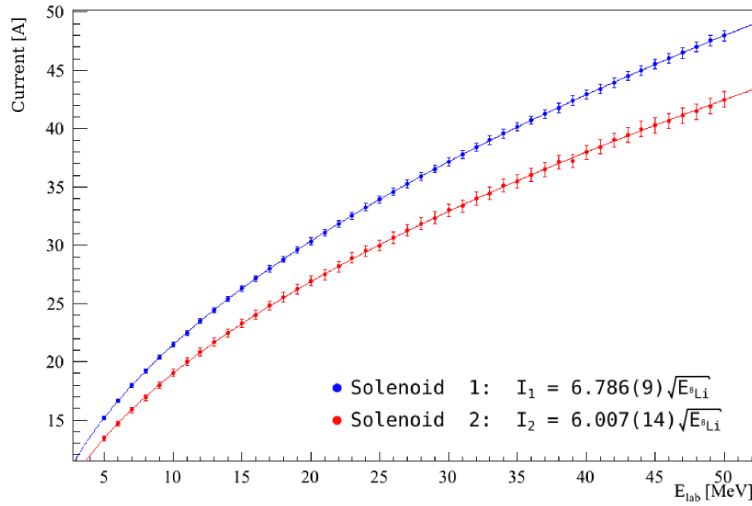


Figure 25: Simulated focalization curves for ${}^8\text{Li}$, showing the electrical current that must be applied in the solenoids in order to focus ${}^8\text{Li}$ at various energies in the scattering chambers. These curves were generated by the code `sol-focus` (appendix B).

The selection by the solenoids is done by magnetic rigidity $B\rho$ of the ions:

$$B\rho = \frac{\sqrt{2mE}}{q} \quad (38)$$

It means that any particle that emerges from the production target with the same magnetic rigidity as the particle of interest, but with different mass, energy or charge state, will also be focused together. These particles are called *contaminants*. The determination of the energy of a contaminant is very important; following equation 38,

m and *E* are the mass and the kinetic energy of the ion, respectively.

the energy E_{cont} of a contaminant beam $(^AX^{+q})_{\text{cont}}$ is, in relation to the energy E_{int} of the beam of interest $(^AY^{+q})_{\text{int}}$, given by:

$$E_{\text{cont}} = \left(\frac{q_{\text{cont}}}{q_{\text{int}}} \right)^2 \frac{A_{\text{int}}}{A_{\text{cont}}} E_{\text{int}} \quad . \quad (39)$$

The focalization itself could be easily done with just one solenoid. Many experiments at RIBRAS were done in the central scattering chamber before the main chamber was completed [41, 73, 74, 75, 76, 77]. But the use of a double solenoid system has many advantages, mainly when used for beam purification.

The *crossover* mode of operation is the one described until now, in which the secondary beam is focused at the focal point of the central chamber, also called *crossover point*, and then refocused in the main scattering chamber by the second solenoid. The most efficient technique for beam purification is to place an energy degrader foil in the crossover point. As the beam (contaminant or of interest) passes through the degrader, it loses energy through ionization and changes its magnetic rigidity. As the energy loss by ionization is proportional to $m\alpha^2/E$ (see sec. 3.5.1) and not to $B\rho$, each beam species loses energy in different amounts, changing their $B\rho$ in a manner that they may not be focused together by the second solenoid. With a correct dimensioning of the energy degrader according to the beam of interest and its predicted contaminants, high purities can be reached in the main scattering chamber.

Other use for the crossover point in the central chamber is the possibility of placing a timing detector at it for time-of-flight measurements of the secondary beam between the two chambers (see section 3.5.2).

Another use for the double solenoid system is to operate in *parallel* mode instead of the crossover mode. In the parallel mode the secondary beam would not be focused in the center of the central chamber. Instead, its trajectory would be partially bent by the first solenoid, and then totally focused in the center of the main scattering chamber by the second solenoid. This would be the preferred mode of operation for beams whose magnetic rigidity is too high (high energy or high mass). The double solenoid system is very versatile and several other applications are being proposed for more advanced experiments in the future.

More detailed description on beam handling at RIBRAS can be found at section 3.6.

3.4.3 Scattering and Auxiliary Chambers

The experimental setup is assembled in the scattering chambers according to the needs of the experiment. A typical experiment would use the main and largest chamber to hold the main experimental

setup like nuclear targets and detectors, while the central chamber would hold auxiliary equipment like monitoring or complementary detectors and energy degraders. However, simpler experiments may use solely the central chamber to hold the full experiment.

In both scattering chambers the detectors are mounted on rotating plates that make the change of their angular positions very easy. The main chamber counts with two independent and concentric plates while the central chamber has just one. The chambers also have vertically moving rods in their centers where targets and detectors can be mounted, depending on the experimental setup.

Along RIBRAS' beamline there are three auxiliary chambers that are not prepared to hold experiments but can receive other equipments like collimators, blockers and vacuum pumps.

3.5 DETECTION SYSTEMS

Experiments in nuclear physics may employ several techniques and devices to measure events and detect particles. In this experiment, two main kinds of detectors were used: silicon surface barrier detectors to characterize an absorbed ion by its charge, mass and energy; and a timing detector, to measure time-of-flights. A Faraday Cup was also employed to measure the primary beam intensity.

In this section, the whole electronic setup used in the experiment is also described.

3.5.1 *Surface Barrier Detectors*

A Silicon Surface Barrier Detector is essentially a type of semiconductor detector made from a wafer of n-type silicon with a thin layer of p-type material in one surface [78]. A charged particle passing through the detector will lose energy by Coulomb interaction with electrons of the material, which generates electron-hole pairs by ionization. The detector is inversely polarized by a bias voltage and the electric field generated sweeps the electron-hole pairs. The current signal is collected and integrated, and the charge collected is proportional to the energy left in the detector by the particle² [79]. This analog signal is usually treated by electronic devices (see sec.3.5.4) to generate a digital signal to be recorded by a computer.

² Of course, the particle also interacts with nuclei of the material, but the information about the energy spent in this interaction is lost [79]. On the other hand, the fraction of energy lost in the interaction with nuclei is usually negligible if compared to the interaction with electrons.

The magnitude of the energy ΔE lost by a particle with charge Z and mass M , traveling at speed v and kinetic energy E , when passing through a material of thickness Δx is described, with approximations, by Bethe-Bloch's Formula [80, 81]:

c is the speed of light in vacuum. a and b are constants related to the absorbing material.

$$\Delta E = \frac{dE}{dx} \Delta x = - \left(\frac{a Z^2 c^2}{v^2} \right) \ln \left(\frac{b v^2}{c^2 - v^2} \right) \Delta x \quad . \quad (40)$$

$\frac{dE}{dx}$ is also called *stopping power*. With some approximations and considering the non-relativistic case ($v^2 = 2E/M$), an important property of equation 40 can be emphasized [81]:

$$\frac{dE}{dx} \propto \frac{M Z^2}{E} \quad . \quad (41)$$

This property can be used to characterize the particle also in mass and charge, but this cannot be done by a single detector, as different particles can lose the same amount of energy. It is done by combining two surface barrier detectors in a telescope formed by a thin detector, called ΔE (typically around 50 μm), and a thick one, called E detector (or E_{res} , for *residual energy*).

The particle would pass through the thin ΔE detector, leaving part of its energy, and then stop inside the thick E detector, leaving the remaining of its energy. By plotting ΔE signal versus E signal (or alternatively $E_{tot} = \Delta E + E$, when calibrated), one can see that detected particles with same M and Z will lie on the same hyperbole, disregarding its energy, and there will be a different hiperbole for each (M,Z) pair [81]. A typical $E - \Delta E$ spectrum can be seen on figure 26.

The choice of $E - \Delta E$ telescope detectors must take into account what is going to be measured and at which energy ranges. Light particles tend to have low ionization and should require thicker E and ΔE detectors. If the ΔE detector is not thick enough, the electrical signal generated may be too low and may even be hindered by noise. If the E detector is not thick enough, the particle may not stop inside the detector. On the other hand, heavy or low energy particles generally require thinner ΔE detectors, otherwise they may stop inside it.

It must be also considered that thin surface barrier detectors (like the ΔE s) usually have worst energy resolution than thicker ones. This is due to non-uniformities of the silicon foil originated in the manufacturing process. Also, due to their low thickness, they have high capacitance and are noisier than thicker ones.

Typically, the detection of light particles such as protons and deuterons up to a few tens of MeV employs a set of 50 μm ΔE detector and 1000 μm or 2000 μm E detector, while for heavier particles like lithium are used ΔE detectors of around 20 μm and E detectors of 150 μm are usually enough.

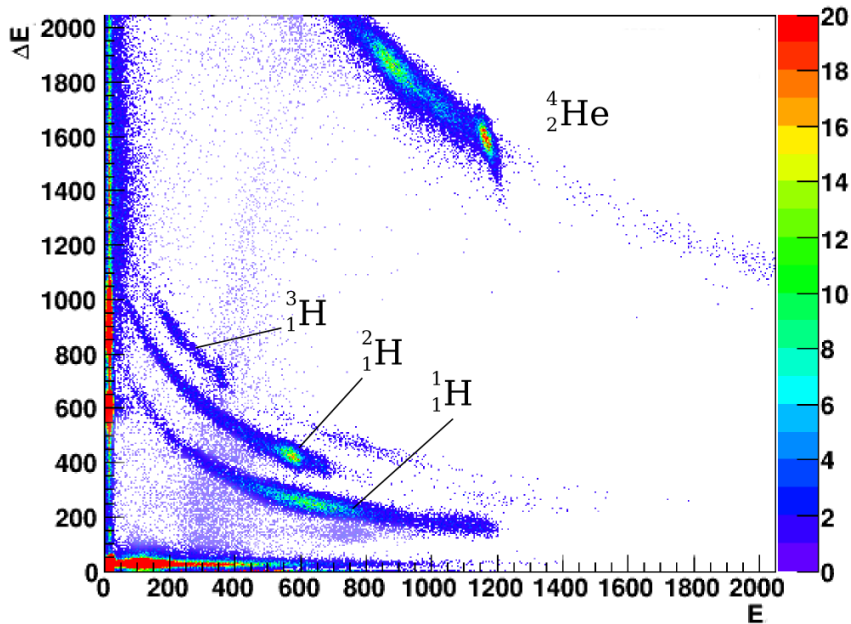


Figure 26: Example of a typical biparametric $E - \Delta E$ spectrum (not calibrated), showing the energy loss in the thin ΔE detector (ordinate axis) as a function of the remaining energy of the detected particle left on the thick E detector. This clearly evidence the identification in mass and charge.

3.5.1.1 Calibration

The energy calibration of these kind of detectors is quite easy for operation in the conditions of this experiment (light masses and low energies [81]). The usual technique is to expose the detector³ to a beam of ions of well known energies, in a way it loses all its energy inside the detector. Measuring the digitized signal from the detector registered by the computer (in channels) and relating it to the energy of the particle, a calibration point can be obtained.

The ions can be provided by an accelerator or by a radioactive source that emits ions, like alpha particles. In the case of this experiment, an ^{241}Am source was used. This source emits alpha particles mainly of 5.486 MeV [82] (see picture 27).

Unless multiple different sources are available, a technique like this can produce only one calibration point. More points are needed for a proper calibration, mainly for linearity testing. A pulser can be used to improve the calibration by verifying the linearity of the associated amplifiers. To do this, the pulser is set to produce pulses with the same amplitude as the detector while registering the event of an alpha particle from the source. Then, the pulser can be set to produce pulses

³ As the calibration is the tuning of not just the detector itself but also of its associated electronic devices, such as amplifiers, it is advisable that the calibration procedure is done with the whole electronic setup (see sec.3.5.4), with the same devices and at identical conditions employed at the experiment.

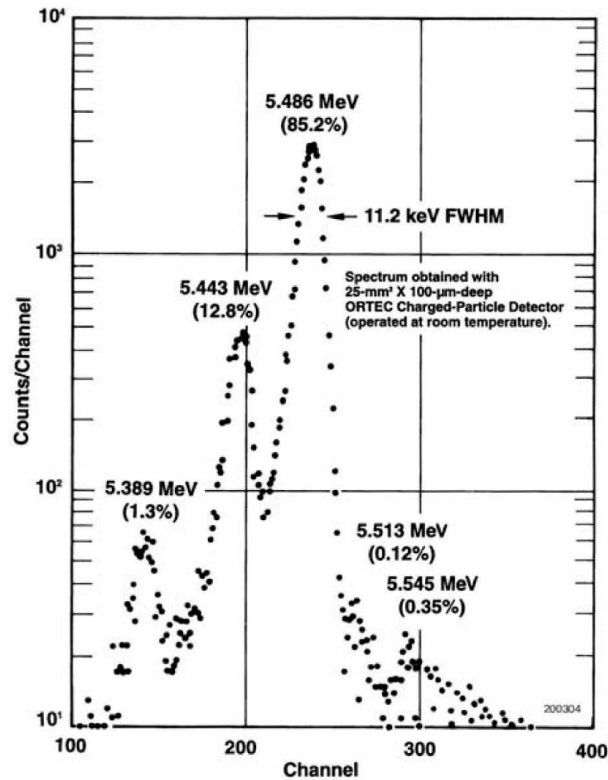


Figure 27: Energy spectrum of a radioactive ^{241}Am alpha source [82]. A spectrum like this can be used to calibrate the detector relating the position (in channels) of the measured peaks to their known energies.

whose amplitude is multiplied by a known factor. Then, a wide region can be calibrated.

When the detector is too thin, usually a ΔE of $\leq 20 \mu\text{m}$, or when the energy of the ions is high enough, the standard particles used in calibration may not stop inside the detector, and the calibration using this technique is usually not very precise. An alternative technique is to calibrate both ΔE and E detectors together as one. For this is necessary a *relative calibration* between them both, which can be done using the *channeling effect*.

The energy loss as presented in equation 40 assumes that the material, and the stopping power consequently, is homogeneous and isotropic. This is not true for crystalline materials such as the silicon of the detectors. If one particle crosses the detector with its trajectory parallel to a crystalline plane, it may suffer less collisions and interactions with atoms of the material, and the stopping power for it will be much lower. This effect is called *channeling* [80, 78].

The thinner the detector, the higher is the probability of a particle suffer channeling in it. This is why ΔE detectors are more likely to present channeling. In practice, some few particles would lose less energy in a ΔE detector but will lose the remaining in the E. So, for

a monochromatic beam, it should be expected a few particles to be registered with less ΔE energy and higher E energy than the majority.

This effect is evident in the $E - \Delta E$ spectrum by a characteristic *tail* that emerges from a large yield peak but does not follow the hiperbole for the corresponding (M,Z) pair (see ${}^8\text{Li}$ in picture 28.a).

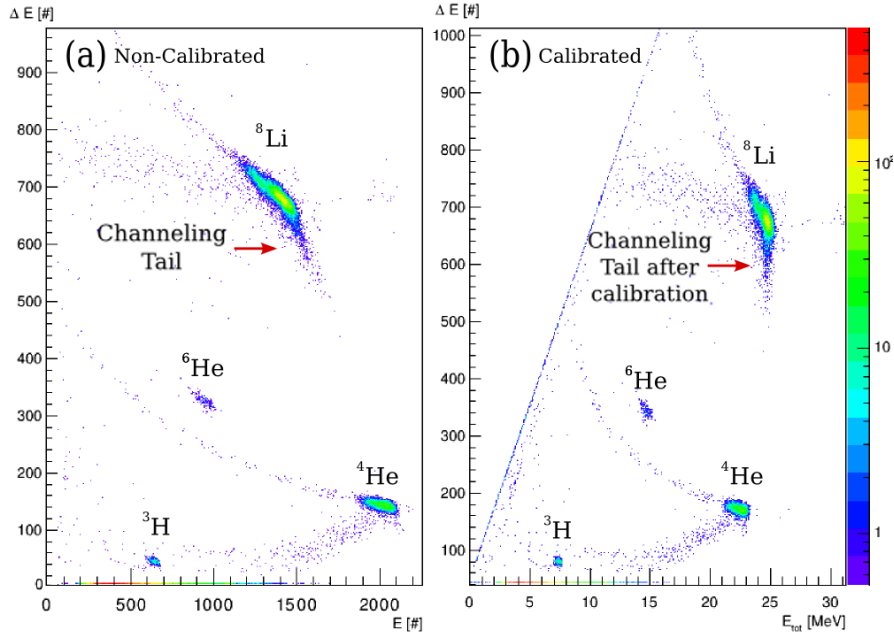


Figure 28: Example of a typical biparametric $E - \Delta E$ spectrum, showing the characteristic channeling tail that follows an intense peak, before (a) and after (b) a proper calibration. The calibrated spectrum is in function of the particle's total energy E_{tot} .

The difference between the peak and the *tail* is just how the total energy of the particle was distributed among E or ΔE detectors, but there should be no difference in the total energy itself. So, after a proper calibration, both the peak and the tail should have the same total energy E_{tot} . In other words, the tail should be as *vertical* as possible in a $\Delta E - E_{\text{tot}}$ spectrum, as can be seen in picture 28.b.

The calibration procedure in this case consists into finding the optimized α factor⁴ in $E_{\text{tot}} = E + \alpha \cdot \Delta E$ (in channels) that *verticalizes* the tail, making its centroid coincident to the centroid of the peak in a $\Delta E - E_{\text{tot}}$ spectrum.

This is a *relative calibration* that corrects the amplification gain difference between the E and ΔE signals. The second step is to properly calibrate E_{tot} in energy, using the reference energy of the ion beam.

The verticalization of the *channeling tail* from high intensity peaks can also be used to verify the quality of a calibration made with other methods.

⁴ Depending on the characteristics of the electronics used, a constant factor B summed to the formula may also be necessary: $E_{\text{tot}} = B + E + \alpha \cdot \Delta E$.

3.5.1.2 Solid Angle and Effective Angle

A solid angle is a two-dimensional angle in a three-dimensional space. It is a 3D analog of the angle between two intersecting lines in a 2D space.

Another important property of an $E - \Delta E$ detector when employed at an experiment is its solid angle from the reaction point. It measures the angular region covered by the detector from the target. If the effective area of the detector is a and its distance from the center of the target is d , the solid angle will be given by:

$$\Delta\Omega = \frac{a}{d^2} \quad [\text{Sr}]. \quad (42)$$

This equation is an approximation valid with error less than 1% for solid angles smaller than 40 msr, which is much bigger than those commonly used. The effective area is determined by geometrical considerations, taking into account the detector's active area and collimators that may be placed before the detector.

A large solid angle enables much more reaction products to be detected, which is convenient as secondary beams are usually poor in intensity. On the other hand, large solid angles may result in a loss of energy resolution due to kinematic broadening, as a large interval of zenithal angles is covered⁵. This compromise must be taken into account, and the design of solid angles involves the distance from the target and, mainly, the collimators placed in front of the detector.

Unless the beam is polarized, it is expected that the scattering should have azimuthal symmetry, but not zenithal symmetry [83]. So collimators are usually rectangular, designed to restrain zenithal angles but to take the maximum of detector's active area at azimuthal angles.

Usually, solid angles in experiments with secondary beams are in the order of msr or a few tens of msr, larger than those with stable primary beams, but rarely will exceed 25 msr.

At section 3.9.4 is shown the procedure and the criteria used in the dimensioning of the detectors and the collimators employed in this experiment.

As the solid angle in this kind of experiment is large, the angular acceptance $\Delta\theta$ of the detector is also large, and can reach up to 5° or greater under some conditions. It means that the detector is effectively integrating the angular distribution along the edges of the detector. If the cross section $\sigma(\theta)$ rapidly varies with angle, as it happens for example in Rutherford scattering (eq. 8), mainly at frontal angles, the angle θ the detector is positioned in relation to the beam may not be the prevailing angle inside the covered angular interval [71].

⁵ In a spherical reference system centered in the target in which the zenith is oriented to the direction of the beam.

In this case, the effective detection angle should be given by:

$$\theta_{eff} = \frac{\int_{\theta^-}^{\theta^+} \sigma(\theta) \theta d\theta}{\int_{\theta^-}^{\theta^+} \sigma(\theta) d\theta}, \quad \theta^\pm = \theta \pm \Delta\theta/2 \quad . \quad (43)$$

The code `ribras.for` [84] uses the Monte-Carlo method to calculate θ_{eff} using the detector geometry, the *shape* of the cross section and other experimental effects like angular straggling and divergence of secondary beam.

3.5.2 Microchannel Plate Detector (MCP)

Time-of-flight (ToF) measurements are very useful in many fields in nuclear physics, such as mass spectrometry, nuclear reactions, etc. [85, 86, 87]. At RIBRAS, as high purity radioactive beams are not always available, ToF measurements help to discriminate overlapping reaction products that come from different beams, whether of interest or contaminant. In other words, ToF helps to determinate the ion beam that originated a specific event.

The ToF technique requires the beam to pass through two timing detectors separated by a distance (usually some meters). The time difference between the registry of the ion's transit by each detector gives the time-of-flight of that ion. Presently, experiments at RIBRAS that use this technique measure the ToF of the beams between the central chamber and the main chamber. One timing signal is provided by a Microchannel Plate Detector (MCP) placed in the central chamber, while the other is provided by the fast signal of the Surface Barrier Detector that registers the event in the main chamber. The distance between the two detectors is about 3 m.

The MCP detector [88] consists of a set of glass sheets with cylindrical microchannels which, when subjected to a high voltage, have the property of electron multiplication and, consequently, of amplification of a low intensity signal produced by the passage of a particle. This type of detector is able to produce very fast pulses and is highly indicated to ToF measurements.

The operating principle of the detector is simple: a beam particle (contaminant or of interest) present in the secondary beam enters the central chamber and passes through a thin foil of aluminized mylar (thickness of 0.18(2) mg/cm²) producing ionization. The foil and the MCP are negatively polarized and the electrons generated in the ionization of the foil are extracted and accelerated by an electric field. Equipotential metallic plates are placed to make the electric field as uniform as possible.

The electrons are deflected 180° from the beam's direction by a magnetic field perpendicular to the direction of motion and guided to the center of an MCP, where a fast timing signal that marks the *start* of the time-of-flight measurement will be produced. The magnetic

field is generated by permanent magnets glued on two plates made of soft iron, mounted on the sides of the detector.

The MCP detector registers the passing of a particle without causing significant interference on its path, as the ionizing foil is very thin and the electric and magnetic fields are weak enough to manipulate just the electrons but not heavy ions. A scheme and a picture of the MCP setup are shown on figures 29 and 30, respectively.

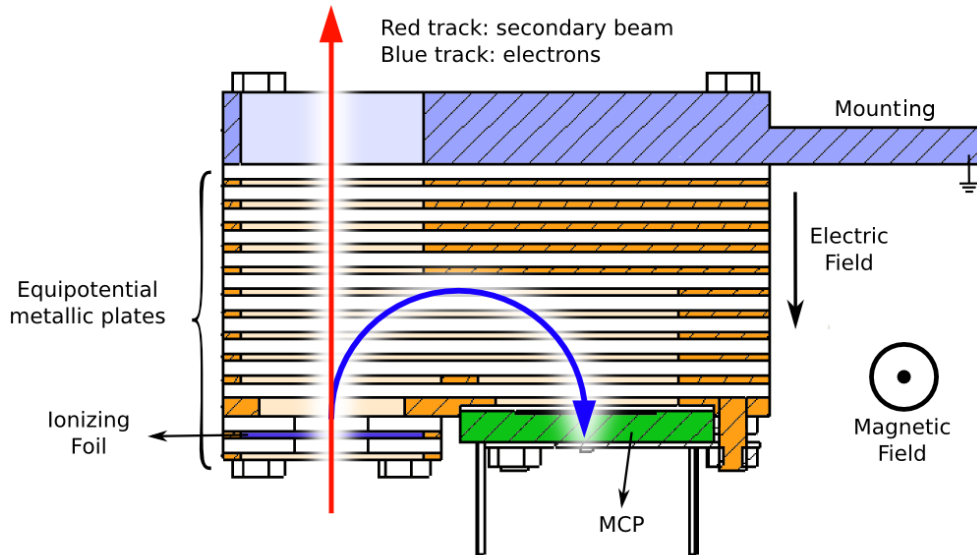


Figure 29: Scheme of the MCP timing detector setup. The permanent magnets are not shown.

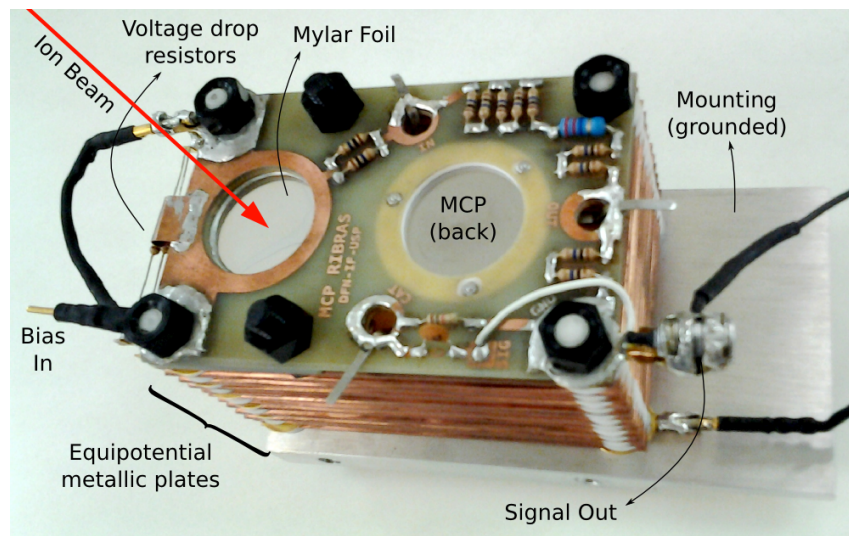
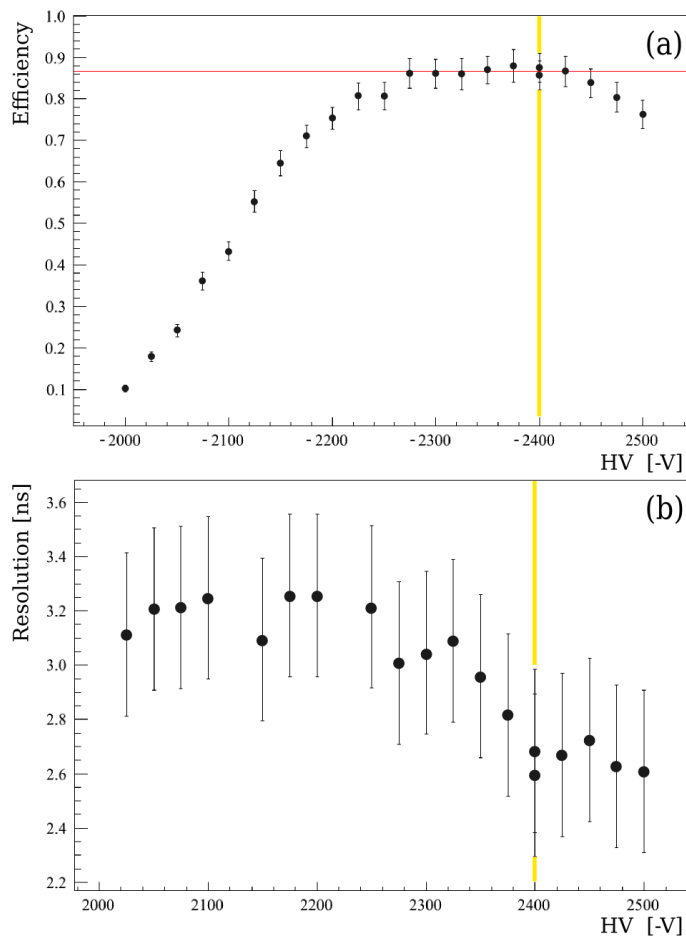


Figure 30: MCP timing detector setup, showing its main parts. The permanent magnets are not shown.

This MCP detector setup was recently developed and assembled for its use at RIBRAS and is still undergoing improvements. The

MCP employed is a *double chevron* [88] configuration manufactured by Tectra (model MCP-25-D-R-A). By the completion of its assembly in the beginning of 2013, the detector and its associated electronics passed through performance tests with a radioactive ^{241}Am alpha source (see fig.27) and a silicon detector. The goal of the measurements was to look for the optimal parameters of operation, such as MCP operating voltage, magnetic field strength and configuration of electronic signal processing, to obtain the best efficiency and the best possible resolution in time.

Efficiency tests were realized by placing the silicon detector right after the exit window of the MCP setup, detecting the same alpha particles that passed through the MCP's ionizing foil. Timing resolution tests consisted of measuring the spread of the distribution of time-of-flights of alpha particles between the MCP and the silicon detector, at a fixed distance between them. An example of results of such inquiries is shown on figure 31.



Efficiency is defined as the ratio between the total number of counts in ToF, which depends on the correlation between a MCP signal and a Si detector signal, and the total number of counts of the silicon detector (efficiency ~ 1).

Figure 31: MCP's performance dependence over polarization bias: detection efficiency (a) and timing resolution (b). Tests performed with alpha particles (details in the text).

Tests revealed an optimal performance around -2400V of polarization bias and 63G of magnetic field magnitude in the center of the detector, with 87% of detection efficiency and ToF resolution of 2.6ns .

This resolution is enough to distinguish masses from almost any secondary beam particle [87, 85]:

$$m = \frac{2E}{D^2} (\text{ToF})^2 \quad . \quad (44)$$

Typical time-of-flights between RIBRAS' central and main chamber should be in the order of hundreds of nanoseconds. D is the distance travelled by the particle.

Together with the selection in magnetic rigidity (eq.38) by RIBRAS' solenoids, it is possible to distinguish the different ions in the incoming secondary beam, but not among ions of same mass with slight differences in energy, for example, ${}^8\text{Li}_{gs}$ and ${}^8\text{Li}_1^*$ ($E_{ex} = 0.9808\text{ MeV}$ [14]).

The resolution obtained is almost the best possible using a Silicon detector, which is considerably *slower* than a MCP. In order to increase the resolution of ToF measurements, another MCP setup is being planned to substitute the *stop* timing at the main chamber made by a surface barrier detector. A ToF measurement made with a pair of MCPs may reach resolutions in the order of hundreds of picoseconds.

In this experiment, the central chamber was not yet shielded against the residual magnetic field from RIBRAS' solenoids, which could reach 26G . This is not negligible compared to the 63G magnetic field from the MCP setup. Therefore, the residual field interfered in the electrons path and many of them could not reach the MCP, reducing considerably the detection efficiency to less than 1% , and not allowing low yield peaks in the spectrum (as reaction products usually are) to be well characterized in time-of-flight.

For this reason, the MCP had a secondary role in this experiment. The discrimination of overlapping reaction products from different origins could not be done due to the low efficiency, but elastically scattered ions from the beam are expected to appear in the detected spectra in large quantities, enough to be characterized in ToF even with the low efficiency of the detector. Thus, the MCP and the ToF measurement helped to monitor the composition of the secondary beam and its purity (see sec.3.6.1), mainly for those components that could not pass the ΔE detector and had their identification hindered.

3.5.3 Faraday Cup

As mentioned in section 3.4.1, the Faraday Cup [89] is placed right after the primary target and has the function of blocking the incoming primary beam at the angular region of 0° and 2° from the target, preventing it to pass to the solenoids and interfere in experiments with secondary beams. But it is not just a blocker, it is also an important measurement device.

The Faraday Cup is a cylindrical tungsten device of 2.4 cm of diameter and 10 cm in length, with a cylindrical hole of 1 cm of diameter and 2 cm in length, where the beam enters (see figure 22). The cup is insulated and grounded, with a picoammeter connected to it. A charged ion beam, when absorbed by the cup, generates an electrical current in it, which can be measured and serves as an indication of beam's intensity. If this current is integrated over time, it serves as a measurement of how many particles reached the cup, and thus passed through the primary target.

To assure a precise current measurement, the cup has a metallic ring right before the entrance hole, polarized at -200 V. It suppresses the electron emission that occurs when the beam hits the tungsten, leading to a wrong current measurement.

The picoammeter can measure beam currents in the Faraday Cup from a minimum of 10^{-10} A, which is in the order of 10^8 particles/s. Typical primary beam currents at RIBRAS are in the order of 10^{-7} A, or 10^{11} particles/s.

How the measurements taken with the Faraday Cup are employed is explained in section 3.6.

3.5.4 Electronics

Typically, the electronic line employed for a silicon surface barrier detector is almost always the same. The signal generated by the detectors passes through a pre-amplifier, which decomposes the signal in two components: one fast signal for timing purposes, and an amplitude signal, which carries the information about the energy deposited in the detector.

The timing signal may be used as a *gate*. The gate is a logical trigger that opens the data acquisition system (DAQ) to receive new events. To shape the pre-amplifier timing signal to be used as a gate, it passes through a fast amplifier and is treated by a constant fraction discriminator (CFD), which produces logical signals from the amplified analog signals. Then, the logical signal passes through a gate generator, that stretches the length of the logical signal to the amount of time the DAQ should be open to new events.

If multiple detectors are used to open the gate, all the signals from the CFDs have to pass through a coincidence unit (operating at *OR*

For more information about electronic signal processing see references [78, 80].

mode), and just one signal should be sent to the gate generator. The CFDs are also used to cut off random noises by not allowing voltage signals to open the gate if a certain threshold is not satisfied.

The pre-amplifier enhances the amplitude of a signal at a certain fixed gain, but it is not enough to be registered by the DAQ. The amplitude signal must be properly amplified by a linear amplifier, which allows the choice of the gain used and can be adjusted to the configurations of the acquisition. The amplified signal is processed by an Analog-to-digital converter (ADC), and the digitized signal is registered by the DAQ if the gate is open.

However, as protons and deuterons are lightweight particles, any attempt to measure them simultaneously with other heavier particles such as alphas and lithium would entail a significant loss in energy resolution in the proton and deuteron spectra. This is due to the low gain of the amplifiers that would be needed to include the heavier particles in the spectrum. To solve this issue, every amplitude signal coming out of the pre-amplifiers was divided and passed through two amplifiers with different gains, one with high gain for proton and deuteron signals and one with low gain for the other particles. Thus, it was possible to acquire spectra with good resolution for both light and heavy particles simultaneously, as can be seen at figure 32.

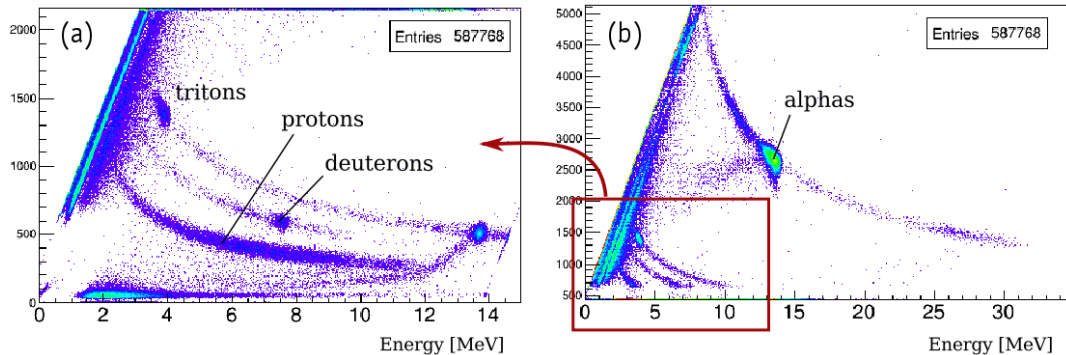


Figure 32: $E - \Delta E$ spectra acquired simultaneously from the same detectors, but passed through different amplification lines: (a) high gain to favor light particles and (b) low gain to favor heavier particles.

The MCP produces only a timing signal, which is treated almost in the same way as the timing signal of a silicon detector by passing through a fast amplification and a CFD. The ToF measurement is done through a time-to-amplitude converter (TAC), that receives the signals from the CFDs of the MCP and of the silicon detectors and generates a pulse whose amplitude is proportional to the time spent between the two signals (start and stop).

Regardless the MCP signal should come first, as the particle passes through it before it is absorbed by the silicon detector, the MCP signal is delayed in about 250 ns and used as a *stop* signal to the TAC, while the silicon detector is used as *start*. It is done this way because the

MCP receives much more particles than the silicon detector. While through the MCP passes the entire secondary beam focused in the central chamber, the silicon detector will absorb just those particles scattered at a narrow solid angle in the main chamber. The MCP is usually full of events that would overload the TAC and many useful events may be lost. By using the silicon detector as the *start*, just the useful MCP events are selected.

The primary beam hitting the Faraday cup generates an electrical current which is integrated by a digital current integrator. This module generates a logical pulse everytime the integrated current reaches a charge threshold (e.g one pulse each 10^{-10} C). This signal is treated by a single channel analyzer or by a gate generator (for pulse shaping), and then a scaler counts the number of pulses in that acquisition run.

The data acquisition system used was a CAMAC-USB module [90], which is a crate controller with built-in ADC modules that interfaces to a computer through the USB port. It uses the CAMAC standard (Computer Automated Measurement and Control) for data acquisition and control [80]. The acquisition software used was the SPM-Root [91], responsible for the communication with the CAMAC-USB module and to record the data in the computer, event by event.

In figure 33 is presented a scheme of the electronics employed in this experiment.

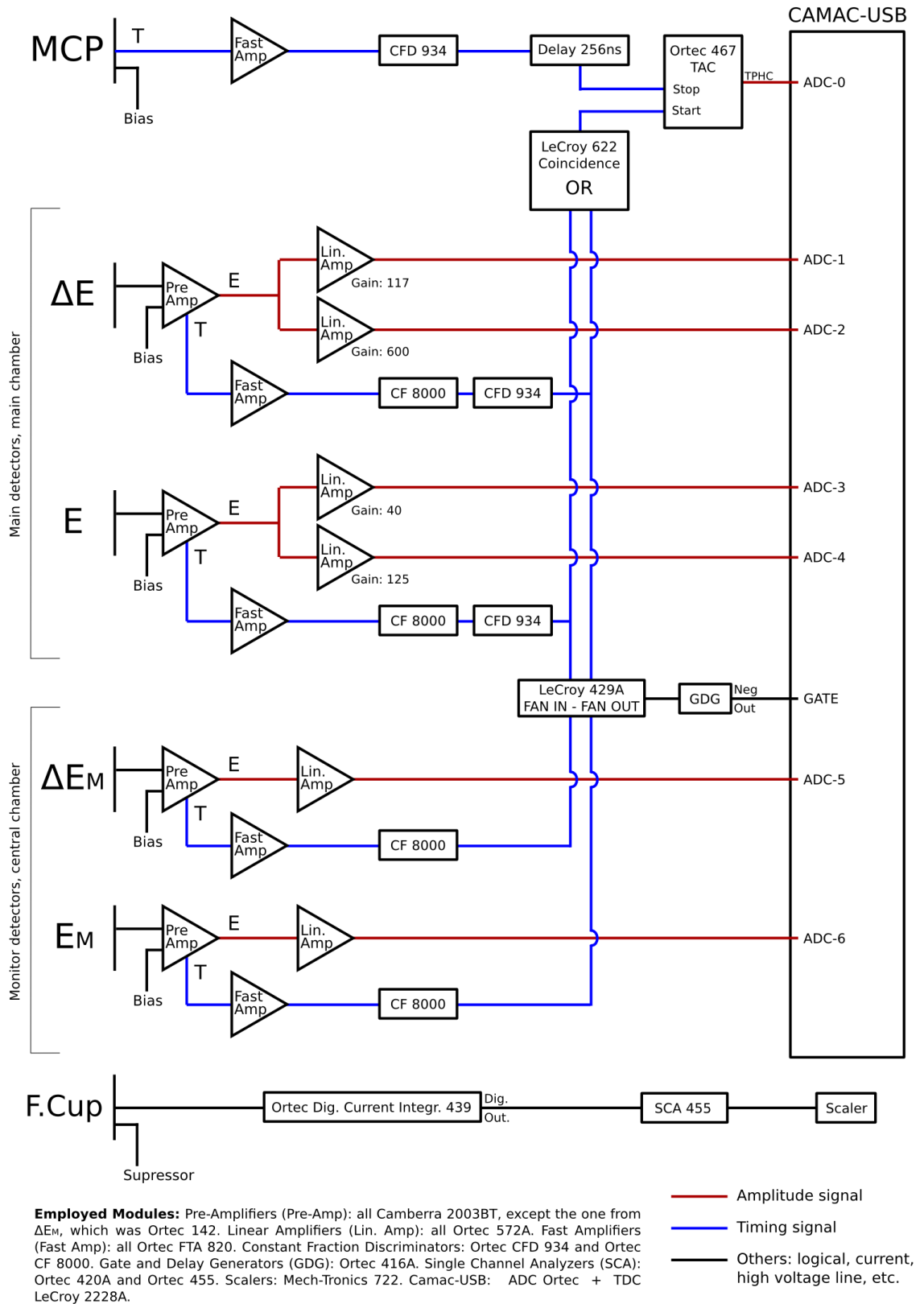


Figure 33: Scheme of the electronics employed in the experiment.

3.6 ^8Li BEAM HANDLING AND CHARACTERIZATION

As mentioned in section 3.4, the ^8Li beam is produced at RIBRAS through the transfer reaction $^9\text{Be}(^7\text{Li},^8\text{Li})^8\text{Be}$ ($Q = 0.367$ MeV) by a ^7Li beam provided by Pelletron accelerator hitting a primary ^9Be target (thickness of $17.4(3)$ μm). The beam is then focused in the central and main chambers following the focalization curves (figure 25).

Quality parameters of the secondary beam, such as beam energy, resolution, intensity, purity and presence of certain contaminants, must be measured and optimized in both central and main chambers to evaluate if it fits to the specific requirements of the experiment. It is usually done with a single $E - \Delta E$ detector (called *monitor*) in two variations:

1. Placement of the monitor detector at frontal angles to measure scattered particles from the beam in a high Z target, usually made of gold, placed in the center of the chamber. The measurement in this case is indirect, as the monitor detects the Rutherford scattered particles from the beam that arrives into the target. However, it can measure any of the quality parameters quite well upon a transformation considering the scattering, the energy loss and the straggling in the target. It is the preferred way to measure beam intensity during experiments (see below). When made at the same chamber where the experiment will take place, the most frontal $E - \Delta E$ detector prepared for the experience is used as monitor.
2. Placement of the monitor detector right in the center of the chamber, commonly on the target holder, facing the incoming beam. It measures the beam directly, being preferred to measure aspects like energy, resolution and purity; but not intensity at full experimental operation, as in this case the primary beam intensity must be reduced to the minimum (1 to 5 nA of primary ^7Li) to avoid damage in the detectors while absorbing direct secondary beam. It is the only way to make this measurement in the central chamber if the MCP is in use, as it occupies almost all the space available for placing detectors in this chamber. If the beam spot is large, or the detector is not exactly in the crossover point, the intensity is underestimated.

The optimization, mainly of beam intensity, is done through the fine adjustment of the electrical current in the solenoids or through slight variations in the primary beam energy. Changing beam's energy is way faster and more practical than changing solenoid's currents, so it is usually the preferred method. Commonly, but not necessarily, the beam is optimized in the central chamber through

slight variations in the beam's energy, then passed to the main chamber and optimized through the variation of the second solenoid's current.

The following qualities must be optimized according to the experience. Generally, high beam intensities are always desired when dealing with radioactive beams. In the case of this experiment, purity is more important than energy resolution of the incident beam. Some contaminants, like ${}^7\text{Li}$, may produce reactions in the secondary target whose products are the same as those produced by the reactions of interest. Meanwhile, the thick target method (see section 3.8) is not sensitive to a poor energy resolution of the incident secondary beam.

Each beam quality trait in this experiment is discussed in detail below.

3.6.1 Purity and Contaminants

The most common contaminants present when dealing with ${}^8\text{Li}$ beam at RIBRAS are: ${}^7\text{Li}$, ${}^8\text{Li}^*$, ${}^4\text{He}$, ${}^6\text{He}$, triton, deuteron and proton. Almost all of them are byproducts of reactions at the primary target and lose energy by scattering on the Faraday Cup and on slits and collimators, presenting a continuous energy distribution. They are focused with the ${}^8\text{Li}$ beam due to a match on their magnetic rigidity (see eq. 39). Typical contaminants of ${}^8\text{Li}$ secondary beam and their expected energies are summarized in table 3.

Table 3: Common contaminants present with ${}^8\text{Li}$ beam and their expected energies relative to ${}^8\text{Li}$'s energy (in MeV).

CONTAMINANT BEAM	ENERGY
${}^8\text{Li}^*$	$E_{s_{\text{Li}}} - 0.98$
${}^7\text{Li}^{+3}$ (prim.)	$\sim 1.055 \cdot E_{s_{\text{Li}}}$ †
${}^7\text{Li}^{+2}$	$0.508 \cdot E_{s_{\text{Li}}}$
${}^4\text{He}$	$0.889 \cdot E_{s_{\text{Li}}}$
${}^6\text{He}$	$0.593 \cdot E_{s_{\text{Li}}}$
${}^3\text{H}$	$0.296 \cdot E_{s_{\text{Li}}}$
${}^2\text{H}$	$0.444 \cdot E_{s_{\text{Li}}}$
${}^1\text{H}$	$0.889 \cdot E_{s_{\text{Li}}}$

† - Based on energy loss calculations for the primary beam and not on B ρ matching. Valid only for this experiment.

Specialy, ${}^8\text{Li}^*$ is produced together with ${}^8\text{Li}$ in the primary target but in its first excited state ($E_{ex} = 0.9808$ MeV), after its decay it has about 1 MeV less kinetic energy than the main ${}^8\text{Li}$ beam, produced at ground state. As their energies are very close, and so are their magnetic rigidities, they are usually focused together. A careful op-

timization may eliminate the $^8\text{Li}^*$ with little loss in intensity of the main ^8Li beam, if desired.

^7Li is particularly a problem in this experiment because of the reactions $^{12}\text{C}(^7\text{Li},\alpha)^{15}\text{N}$ and $p(^7\text{Li},p)^7\text{Li}$ that may occur in the secondary target and result in undesirable alpha particles and protons in the spectrum [41]. The expected ^7Li beam comes from two different sources. One, with charge state of +3, is the scattered primary beam in the primary target. Even if it does not have the same magnetic rigidity as the ^8Li to be focused together, the intensity of the primary beam is so high that a considerable amount of ^7Li particles manages to reach the scattering chambers. The other source of ^7Li contamination is the degraded primary beam that suffers multiple scattering on slits, blockers and collimators present inside the beamline. They may present a broad energy spectrum and charge states. Those with +2 charge state and inside a certain energy window may match the ^8Li 's magnetic rigidity.

Intensity of the primary beam is about 10^6 times the intensity of the secondary beam.

Purity can be enhanced through fine adjustments of solenoid current or beam energy, but some pre-experiment procedures may help achieving a much better purity. The placement of beam blockers and collimators in certain places of RIBRAS beamline may help to eliminate some contaminants without losses in the beam of interest, increasing the purity. As discussed in section 3.4, the use of energy degraders may also help the purity. At figure 34 are shown simulated tracks along RIBRAS' beamline for ^8Li and two contaminants, showing how these devices act on purity.

The use of a polyethylene degrader of $5.2(6) \text{ mg/cm}^2$ helped the ^8Li beam to achieve a purity of 99.1% in this experiment, against 65% without the degrader, as can be seen in figure 35. Although this is of great advantage, 100% of purity is not attainable and contaminants will show up, mainly at high exposure spectra.

As mentioned in sec. 3.5.2, in some cases beam purity could not be fully evaluated through the monitor silicon detectors as some species could not pass through the ΔE layer. So the ToF measurement helped in those cases. An example can be seen at figure 36.

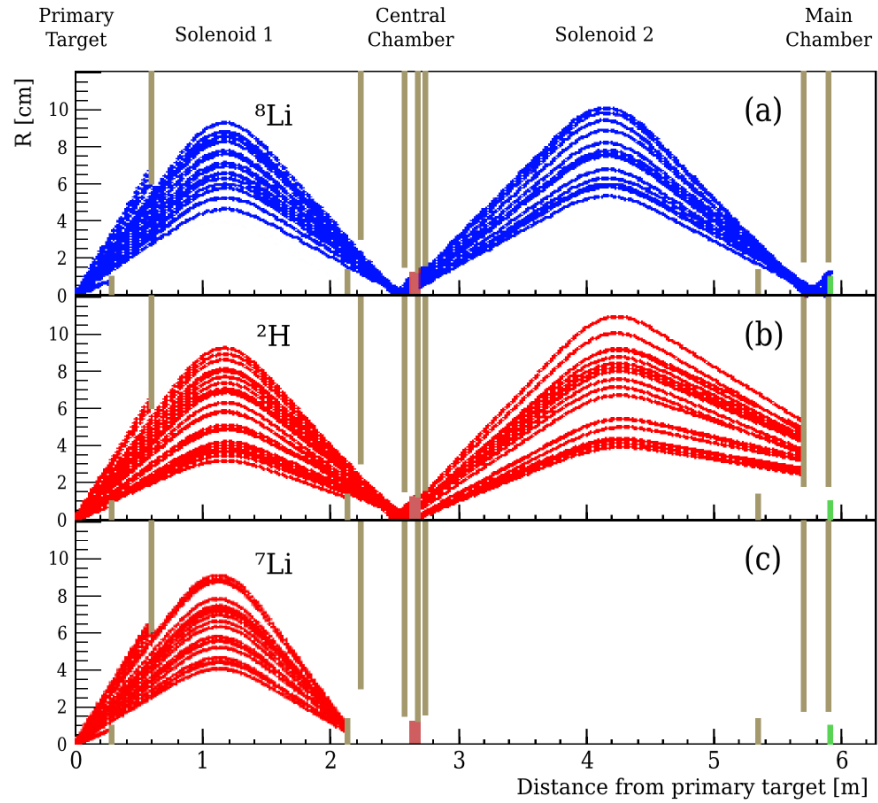


Figure 34: Particle tracks along RIBRAS' beamline simulated by the code sol-focus (appendix B). (a) ^8Li secondary beam, properly focused on secondary target (green block at main chamber). (b) Deuteron contaminant beam, focused with ^8Li in the central chamber but hitting a collimator instead of the secondary target, exemplifying the effect of an energy degrader (red block at central chamber) on changing the contaminant's Bp. (c) ^7Li from primary beam hitting a blocker.

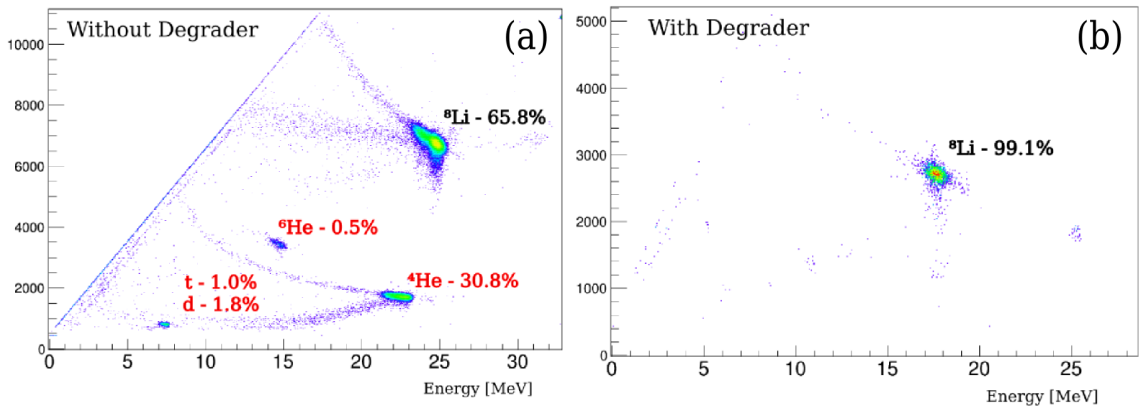


Figure 35: Spectra taken at main chamber with the secondary beam scattered in a gold target, (a) without the use of a degrader in central chamber and (b) with the degrader, pointing to its purifying properties.

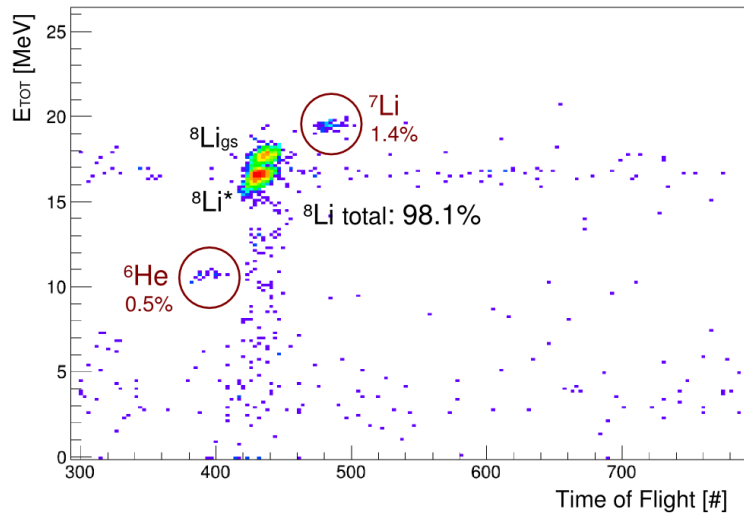


Figure 36: ToF x energy spectrum, showing ^8Li beam purity in a non-optimized situation.

3.6.2 Resolution and Intensity

Energy resolution and intensity of secondary beams are closely related to the production process occurring in the primary target. Obviously, the higher the intensity of the primary beam, higher is the intensity of the secondary beam. Also, a monochromatic primary beam will favor a better energy resolution on the secondary beam. Depending on the case, a more energetic primary beam will also increase the reaction cross section between primary beam and target, thus producing more secondary particles.

But the primary target puts resolution and intensity into a compromise. Thicker the target, more nuclei per unit area, more primary reactions can occur, and so more intense the secondary beam can be, but also greater is the energy straggling, worsening the resolution.

Other processes along the beamline may also interfere in these parameters. Some substantial loss in intensity is verified in the beam transport from one chamber to another. The intensity of ^8Li at the main chamber was measured to be 52% of the intensity at the central chamber, although this number may vary considerably according to the experiment. The use of an energy degrader also affects the resolution and may cause some loss in intensity due to the worse beam emittance caused by the straggling.

As the energy resolution was no concern (see sec. 3.8), the ^8Li beam intensity was taken as priority after purity. A relatively thicker ^9Be primary target was used, $17.4(3) \mu\text{m}$ compared to $\sim 12 \mu\text{m}$ of most experiments with ^8Li at RIBRAS. In this experiment, a mix of ^8Li and $^8\text{Li}^*$ was allowed in order to have the maximum intensity of ^8Li beam reaching the secondary target. This mix would not be allowed in a typical nuclear reaction experiment.

In figure 37 are shown the energy profiles of the employed ^8Li beam during the experiment, at two energies, making clear the mix of ^8Li at ground and excited states. They were measured as the scattered beam in a gold foil positioned as secondary target in the center of the main chamber. The profiles are shown already transformed to what they should look before passing through the secondary target.

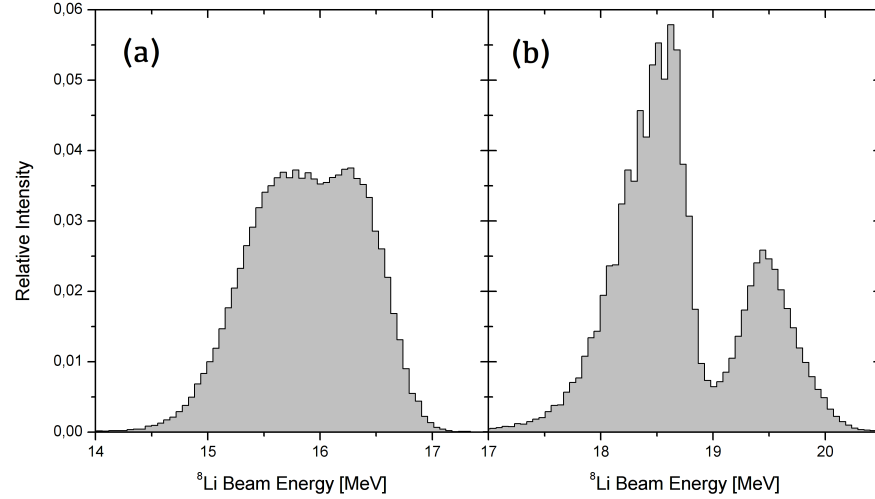


Figure 37: ^8Li beam energy profile at main chamber at two situations during the experiment. Average energies:(a) 15.9 MeV and (b) 18.7 MeV.

At any nuclear physics experiment, the measurement of beam intensity is an important requirement, mainly for normalization of cross section data. Though, the measurement of the intensity of secondary beams is a difficult task. They are not intense enough to be measured through electrical methods, such as Faraday Cups, but are too intense to be measured directly through single event detectors such as surface barrier detectors.

The method currently employed at RIBRAS experiments is an indirect measurement through the intensity of the primary beam. This method is detailed as follows.

The primary beam is stopped by the Faraday Cup after passing through the primary target. The Faraday Cup measures the beam current and integrates it over time (sec. 3.5.3). As almost every particle that reaches the cup is from the primary beam, ^7Li in this case, it is easy to determine from the integrated charge Q_{FC} the number $N_{7\text{Li}}$ of particles that passed through the primary target over that time:

q is the charge state of the ion (+3 for ^7Li) and e is the elementary charge: $+1.60218 \cdot 10^{-19} \text{C}$.

$$N_{7\text{Li}} = \frac{Q_{\text{FC}}}{q \cdot e} = 2.08 \cdot Q_{\text{FC}} [\text{C}] \cdot 10^8 \quad . \quad (45)$$

It is assumed that the amount of particles of secondary beam ($N_{8\text{Li}}$) that reaches the secondary target is directly proportional to the amount of particles of primary beam ($N_{7\text{Li}}$) that reaches the primary target,

at the same period of time, at same conditions. So, it defines the production efficiency of ^8Li as:

$$\epsilon = \frac{N_{^8\text{Li}}}{N_{^7\text{Li}}} \quad (46)$$

If the experimental conditions are the same, it would be enough to measure the production efficiency once or a few times during the experiment and use the integrated charge at the Faraday Cup to obtain the $N_{^8\text{Li}}$ for the whole experiment. This is said because the method employed to measure ϵ requires a brief stop in the experiment.

In this technique, the secondary beam is briefly measured with a gold target in which Rutherford scattering (see sec. 2.2.1) is dominant. As the differential cross section is well known (eq.8), the number of incident particles $N_{^8\text{Li}}$ can be obtained from the experimental differential cross section. The method for obtain the experimental differential cross section is carefully presented in section 4.1, in special at equation 48 and related explanations.

Gold is chemically inert and has high Z . The Coulomb barrier for the system $^8\text{Li} + ^{197}\text{Au}$ is 36.38 MeV (37.86 MeV at laboratory system). The gold foil used had thickness of 5.0(2) mg/cm². Figure 38 shows measurements evidencing the Rutherford behavior of the elastic scattering of ^8Li on ^{197}Au at energies around those used at this experiment.

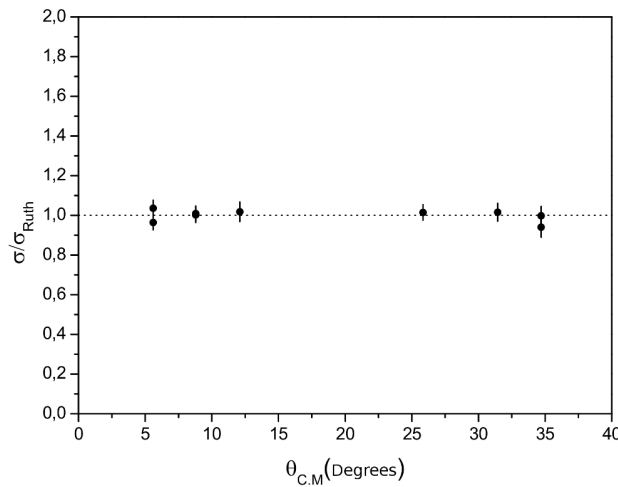


Figure 38: Typical angular distribution of the elastic scattering of ^8Li on ^{197}Au at $E(^8\text{Li})_{\text{lab}} = 19$ MeV [55].

Here is a brief resume of the technique employed to measure the intensity of secondary beams:

After beam optimization and before starting the experiment with the desired secondary target, a gold target is placed to scatter the secondary beam particles for a short period. Using the number of detected scattered ^8Li particles, the number of incident particles ($N_{^8\text{Li}}$) that reached the target during this period can be calculated through

equation 48 and assuming the cross section to be Rutherford (equation 8). It is important to note that the Rutherford cross section should be calculated using the effective detection angle (eq. 43) and in the center-of-mass frame (appendix A).

The production efficiency (eq.46) is then calculated using N_{7Li} obtained through the integrated primary beam's charge (eq.45). The target of interest (in this case, $(CH_2)_n$) is placed in front of the secondary beam and the experiment begins, assuming that the production efficiency will be the same along the experiment and beam intensity can be calculated at any time through the integrated charge Q_{FC} and equations 46 and 45.

Every time the experimental conditions are changed, like beam energy or beam refocalization, this procedure must be repeated. It is also common to repeat it periodically during the experiment, even without the change of conditions, just to monitor if the production efficiency remains constant.

3.6.3 Focusing

In the scattering chambers, the secondary beam must be well focused on degraders or the secondary target, which have a target frame of 2 cm of diameter. If part of the beam reaches the detectors without passing through the target, the spectrum may be severely contaminated. For this it is very important to measure how good is the focusing of the secondary beam in both chambers.

To measure the focusing quality, a Position Sensitive Detector (PSD) [92] was installed on the target holders, centralized so its center coincides with the geometrical center of the chamber. This detector is a surface barrier detector with a resistive layer on its back that enables it to record also the position where the particle has reached in its active area, which is about 3 cm x 0.8 cm. To perform the position calibration, a mask, with slits 2 mm wide spaced by 2 mm, was attached right in front of the detector. The PSD was placed with its position sensitive axis in the horizontal direction.

In each chamber, the 8Li was optimized and had its intensity reduced in order to not damage the PSD. The spectra taken with the PSD for each chamber can be viewed at figures 39.a and 40.a. The spatial distribution of the 8Li beam, extracted from the PSD spectra, can be viewed at figures 39.b (central chamber) and 40.b (main chamber). The spatial distribution spectra are in relative position, so 0.5 means the center of the detector and, consequently, the center of the chamber. The calibration is done through the *shadow* of the mask present in the spectra.

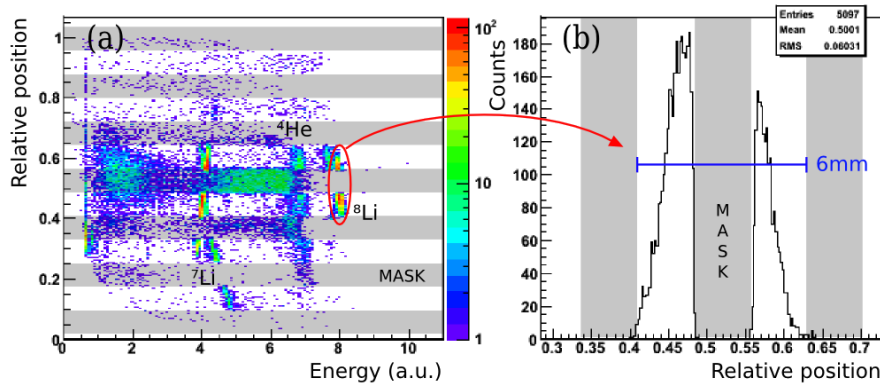


Figure 39: Focusing quality analysis for ^8Li beam at central chamber. (a) PSD spectra, emphasizing the ^8Li . (b) Spatial distribution spectra of ^8Li , extracted from the PSD spectra. The grey strips correspond to the masks put in front of the PSD, each strip is 2 mm wide.

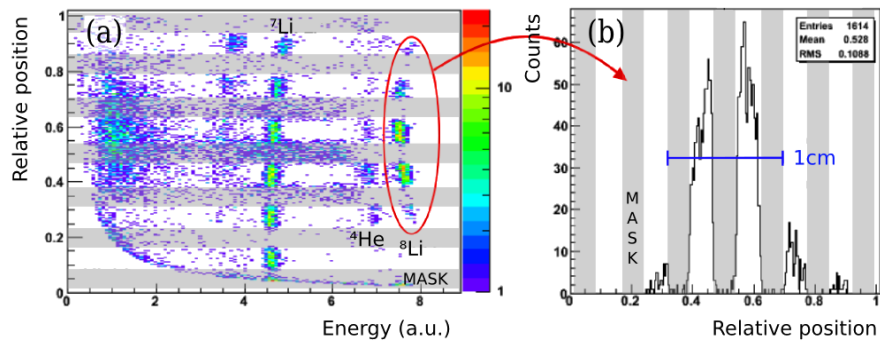


Figure 40: Focusing quality analysis for ^8Li beam at the main chamber. (a) PSD spectra, emphasizing the ^8Li . (b) Spatial distribution spectra of ^8Li , extracted from the PSD spectra. The grey strips correspond to the masks put in front of the PSD, each strip is 2 mm wide.

As can be seen, the ^8Li beam is very well focused in the center of both chambers in the horizontal direction, as in both cases the spatial distribution of the beam is centered at 0.5. The width of these distributions are also good enough to fit the target frames of 2 cm in diameter. At central chamber, this width was 0.45 cm, while at main chamber it was 0.70 cm (both FWHM - full width at half maximum).

As the secondary beam is selected from a angular region of 2° to 6° after the primary target, it is also important to consider that it is going to arrive at the secondary target also with a certain non-zero angle. From simulations on the beam transport (see SolFocus [93] at ap. B), the expected impinging angles range from 1.6° to 4.8° . Thus, detectors at forward angles must be carefully placed to avoid this angular region in their active areas.

3.7 TARGET CHARACTERIZATION

The measurement of target thickness is important because it is related to two processes occurring inside the target: the energy loss of a particle crossing the target, and the number of nuclei present in the target available for nuclear reactions.

There are two common units for target thickness. One is effectively a length measurement, usually in μm or in cm , while the other is an areal density, commonly mg/cm^2 or $\mu\text{g}/\text{cm}^2$. Both can be used according to convenience.

One important parameter that is derived from the thickness is the number of atoms per unit area N_{target} . It is easier if calculated with units in areal density format. For a target made of atoms with atomic mass A and thickness x in mg/cm^2 , N_{target} is given by:

N_{Av} is the
Avogadro's number:
 $6.022 \cdot 10^{23}$.

$$N_{\text{target}} = \frac{x}{A} \cdot N_{\text{Av}} \cdot 10^{-3} \quad [\text{nuclei}/\text{cm}^2]. \quad (47)$$

Another useful unit for N_{target} is nuclei/mb. The conversion from nuclei/ cm^2 to nuclei/mb is done through a multiplication of N_{target} by 10^{-27} .

The targets employed at experiments must be very well characterized, but each target has its own peculiarities that impose restrictions to the characterization.

3.7.1 ${}^9\text{Be}$, ${}^{197}\text{Au}$ and C targets

Among the targets employed at this experiment, a ${}^9\text{Be}$ foil used as primary target and a ${}^{197}\text{Au}$ foil used for data normalization (see sec.3.6.2). The gold target was manufactured locally at the Pelletron Laboratory by the lamination of a pure gold sample [94]. Beryllium is highly toxic and cannot be manufactured locally, the target was purchased already in metallic foils.

The method of thickness measurement of these targets is easy. It consists in the bombarding of target with alpha particles from a source, like ${}^{241}\text{Am}$ (see fig.27), and detecting them with a previously calibrated silicon detector, measuring the energy the particles acquire after passing through the target. The algorithm stopx (see appendix B) is then used to calculate the thickness of the material of the target needed to make an alpha particle of 5.486 MeV lose the measured amount of energy. This method is valid for homogeneous targets.

The thickness of ${}^{197}\text{Au}$ target was measured in 5.0(2) mg/cm^2 and the ${}^9\text{Be}$ target in 17.4(3) μm .

A natural carbon target was also used to measure the contribution of ${}^8\text{Li} + {}^{12,13}\text{C}$ reactions, since the secondary target employed also contains carbon (see sec.3.9.6). This target was purchased already in foils of 15 mg/cm^2 .

3.7.2 Polyethylene targets

This experiment employed two targets made of polyethylene ($(\text{CH}_2)_n$), a hydrogen-rich plastic [95]. One was used as secondary target and the other as energy degrader. Polyethylene was chosen as it is a solid and accessible material with high concentration of hydrogen, and because gaseous secondary target systems are still in implementation at RIBRAS and hydrogen gas is more expensive, more difficult to handle, and dangerous due to its high flammability. Moreover, gaseous targets have much less atoms per cm^2 and require high intensity beams.

Polyethylene is widely used in several industrial applications and the targets were purchased as a commercially available low density polyethylene film.

The thickness of these targets cannot be measured in the same way as described before, as alpha particles from the ^{241}Am radioactive source are expected to stop inside the material. An easy alternative is to weigh the films in a precision scale, and divide the masses by their area, giving thickness in areal density format.

The film employed as secondary target was $7.7(8) \text{ mg/cm}^2$, while the one employed as energy degrader was $5.2(6) \text{ mg/cm}^2$. Even though they are sections of the same plastic foil, the targets do not have the same thickness due to a non-uniformity of the plastic. The roughness is noted in picture 41, where a microscopic photo of the surface of the film is shown.

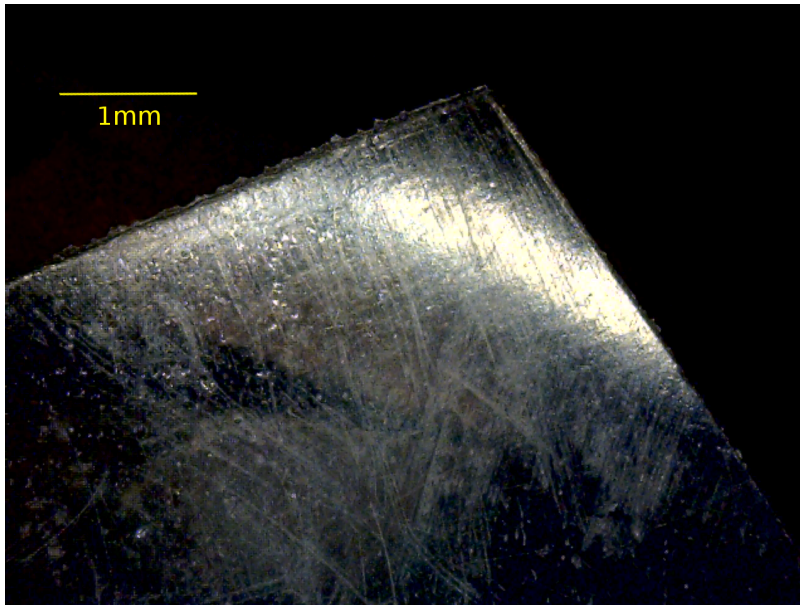


Figure 41: Microscopic photo of the surface of the $(\text{CH}_2)_n$ target employed in the experiment, showing its roughness.

The weighing procedure cannot evaluate quantitatively the roughness in a microscopic scale. To do this, the targets were sliced in several cuts after the experiment and the transversal sections of the targets were analyzed through a microscope (fig. 42.a). The pictures taken were used to define the thickness profile of the cuts (fig. 42.b).

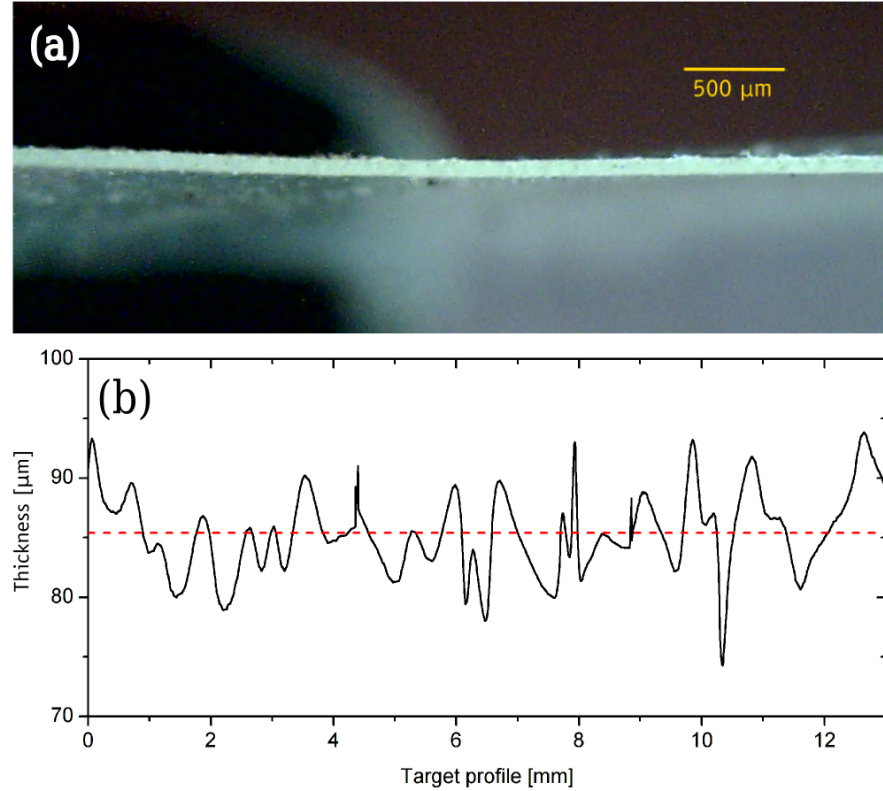


Figure 42: Thickness measurements of the $(\text{CH}_2)_n$ secondary target. (a) Microscopic photo of a transversal cut of the target. (b) Thickness profile extracted from multiple photos of one cut, red dashed line marks the average.

The thickness profiles of the several cuts were summed up, and a thickness histogram could be done, as seen in figure 43. The distributions are perfectly gaussian, and the average thickness of the targets were evaluated in $85.6 \mu\text{m}$ (secondary target) and in $61.2 \mu\text{m}$ (degrader). The width of the distributions, as a standard deviation, were measured as 9.8% of the average thickness.

The density obtained through the average thickness and the weighing is compatible with the density found in the literature for low density polyethylene ($0.91 - 0.94 \text{ g/cm}^3$) [95].

The number of scattering atoms per unit area, N_{targ} , may be calculated in the same way for the $(\text{CH}_2)_n$ targets, but it is not useful in the thick target method. A way to calculate N_{targ} in the context of this method is described in section 4.1.

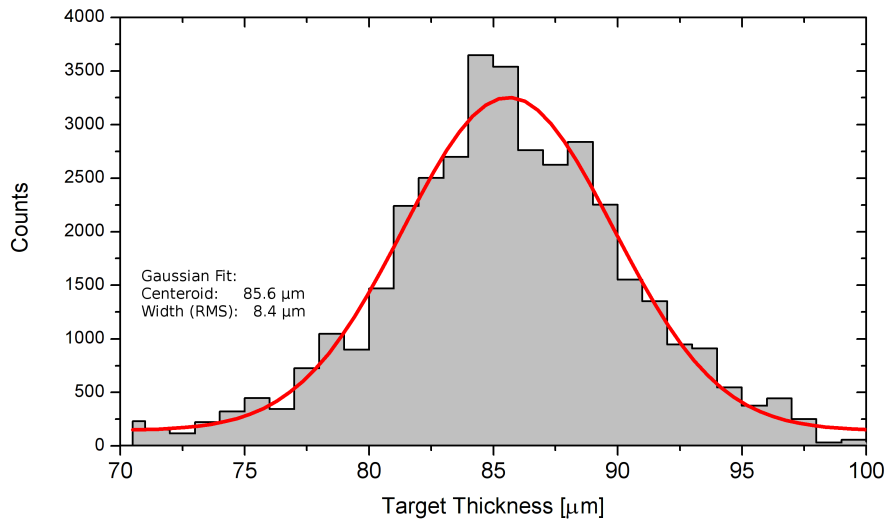


Figure 43: Distribution of thickness measurements of the $(\text{CH}_2)_n$ secondary target, with gaussian fit.

3.8 THICK TARGET METHOD

The usual technique to measure excitation functions is by using a thin target and varying the beam energy in small steps. This process is very time consuming, mainly at experiments using radioactive beams, in which the beam intensity is low. The *inverse kinematics thick target method* (TTIK), or just *thick target method*, is a powerful method to perform resonant scattering reactions, enabling the efficient population of a whole excitation function at a single bombarding energy.

In this method, the target acts also as a beam stopper. As the beam is slowing down inside the target, reactions are induced in a continuous range of energies, from the initial beam energy to zero. If the target material is more transparent to the reaction products than to the beam (see eq. 41), the products can leave the target and reach the detector. Therefore, the excitation function in this energy range, including the resonances that may be present in it, will be directly reproduced in the energy spectrum of the ejectiles. In figure 44 is shown a scheme of the TTIK method applied to the ${}^8\text{Li} + \text{p}$ experiment.

A great advantage of the TTIK method, in the case of light ejectiles (like protons, deuterons and alphas), is the good energy resolution of the excitation function, even if the beam has a large energy spread (like the ones seen at figure 37). Beam particles with slightly different energies will produce the same reaction at the same excitation energy at different points inside the target, but the reaction products will arrive at the detector with practically the same energy. This is also discussed at section 3.9, where are presented the results of simulations regarding this issue.

For more information about this method, see references [96, 97, 98, 99, 83, 100].

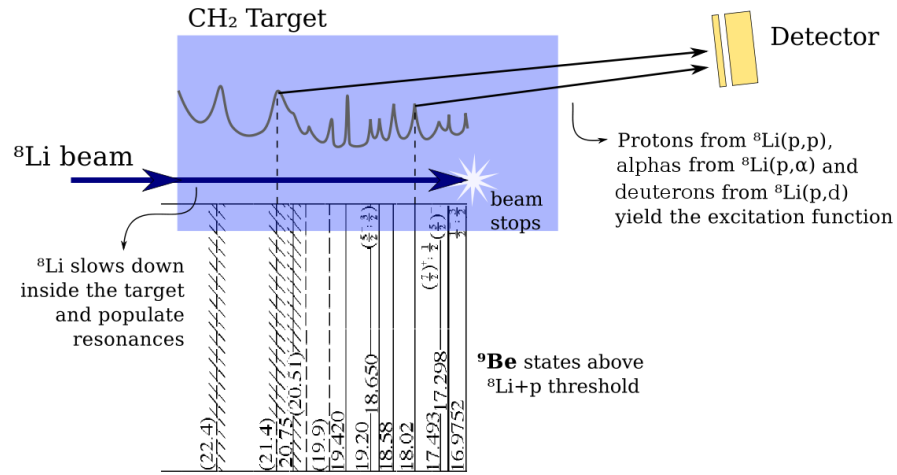


Figure 44: Illustrative scheme of the thick target method applied to the experiment.

This method must fit some requirements:

1. As mentioned, the reaction products must be lighter and lose less energy in the target than the beam in order to leave the target and reach the detector. As the elastic channel is highly important and the most explored through this method, the experiment operated in inverse kinematics (see appendix A). Thus, the reaction products are emitted in forward angles (backward angles at center-of-mass frame).
2. The target thickness and the beam energy are in a compromise. If the beam is so energetic that it passes through the target, the method is still valid but the excitation function will be populated only in the energy range in which the beam is inside the target, it will not exploit the full potential of the method. On the other hand, if the target is so thick that the reaction products lose much energy in the target, the energy resolution of the ejectiles can be spoiled. A good rule of thumb for designing the energy-thickness relation in the TTIK method is to use the bombarding energy which makes the beam to stop close to the rear surface of the target, using almost it whole.
3. The stopping power of the beam and reaction products in the target must be well known. To transform the detected energy spectrum to excitation function at center-of-mass reference, it is needed to take into account not only the reaction kinematics but also that the process involves many steps of energy loss inside the target, both for beam (from the beginning to the reaction point) and products (from the reaction point to target end). A more detailed description of these transformations is shown in section 3.9.

The data analysis in this kind of method is not trivial and many particular considerations must be done, mainly on modifications in the differential cross section formula. These details will be discussed in section 4.1. Also, many aspects regarding the planning and the execution of an experiment using this specific method are presented in section 3.9.

3.9 EXPERIMENT PLANNING

The goal of this work is to revisit, upgrade and extend the work on high lying resonances of ${}^9\text{Be}$ around the ${}^8\text{Li} + \text{proton}$ threshold done through the measurement of the alpha decay channel by [41]. This work aims the measurement of the same excitation function for the alpha and other decay channels, like proton and deuteron, with an improved experimental setup at RIBRAS System.

3.9.1 Feasibility and Priorities

Although the experience acquired in the previous work helps in a new measurement of the alpha channel, it is important to study the feasibility of the measurement of the proton and deuteron channels.

There is a tremendous difference in the experimental complexity between the measurement of these channels. The ${}^8\text{Li}(p,\alpha)$ reaction has a high Q value: +14.42 MeV and the high energy alpha ejectiles are easily detected even in the presence of contaminant beams. On the other hand, as the proton channel is an elastic scattering and thus the reaction has $Q = 0$, the protons may lie in a region flooded with contaminants, this is why a high purity beam is desired. The ${}^8\text{Li}(p,d)$ reaction has also a very low Q value: +0.19 MeV, thus the measurement of the deuteron channel should experience similar problems. The low masses and charge of protons and deuterons also impose some detection restrictions.

The excitation function of the previous work on ${}^8\text{Li}(p,\alpha)$ was measured between $E_{\text{cm}} = 0.2$ and 2.1 MeV. The spectroscopic parameters (resonance energies, widths, spins and parities) obtained with this work were used to perform a R-matrix calculation on how would the excitation function look if measured in the proton channel. The result is exhibited at figure 45. The deuteron channel was not considered in the previous study.

The proton spectra is expected to have a high *background* due to the purely Rutherford elastic component. So, low yield resonances in the compound nucleus, mainly at low energy regions (see eq. 8), may require high statistics to be well described.

As can be noted, the resonance at $E_r = 0.4$ MeV is almost not noticeable in the R-Matrix prediction and the resonance at $E_r = 0.6$ MeV rises only 6% from the baseline. Moreover, these resonances are

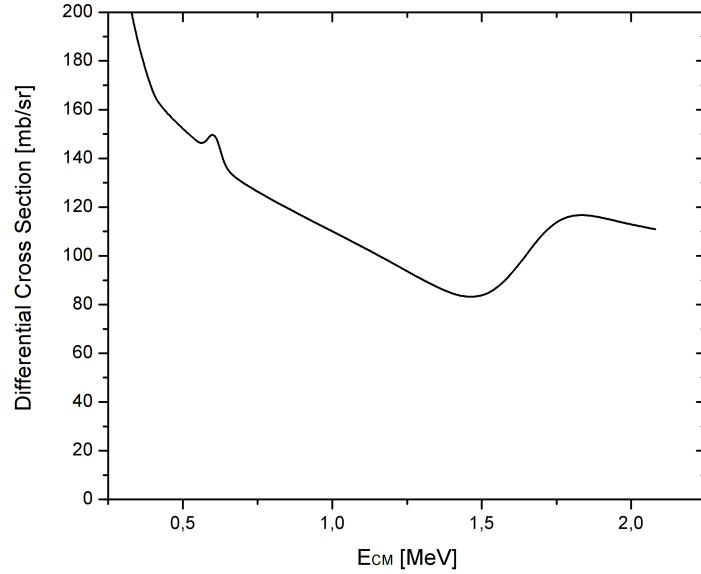


Figure 45: R-matrix prediction of ${}^8\text{Li}(p,p)$ differential cross section at $\theta_{\text{lab}} = 10^\circ$ based on data of the previous work on ${}^8\text{Li}(p,\alpha)$ [41], shown at table 1.

relatively well described in the literature and the results obtained in the previous ${}^8\text{Li}(p,\alpha)$ study are in good agreement with it (see table 1).

The priority should be given to the resonances in the upper part of the excitation function, which are not so well described and are probably easier to be measured.

3.9.2 Beam Requirements

The experiment was performed at two bombarding energies: $E({}^8\text{Li}) = 18.7$ MeV and $E({}^8\text{Li}) = 15.9$ MeV. See the measured beam energy distributions presented at figure 37.

The bombarding energy of $E({}^8\text{Li}) = 18.7$ MeV is enough to measure the excitation function up to $E_{\text{cm}} = 2.1$ MeV, and populate the ${}^9\text{Be}$ resonances between the proton threshold (16.888 MeV) and 19.0 MeV.

If the bombarding energy is decreased by a small factor, the part of the excitation function that remain in the energy range kinematically allowed should experience almost no alteration. But possible contaminants should appear at lower energies in the spectrum due to the change in the magnetic rigidity selection⁶ (eq.38). So, to uncover regions of the spectra hidden by contaminants at the $E({}^8\text{Li}) = 18.7$ MeV bombarding energy, the experiment was also performed at $E({}^8\text{Li}) = 15.9$ MeV ($E_{\text{cm}} = 1.77$ MeV).

These energies are almost perfectly suitable for the employed target to exploit the full potential of the method, as explained at section 3.8.

The relation between the center-of-mass energy and the laboratory energy in this experiment is given by $E_{\text{cm}} = E({}^8\text{Li})/9$ (see eq. 61 at ap. A).

⁶ This phenomenon can be verified at figure 3 of [41].

It is demonstrated on figure 46, where are depicted the results of simulations done for the loss of energy of ^8Li beam inside a $(\text{CH}_2)_n$ thick target. The simulations used the measured energy distributions shown at figure 37.

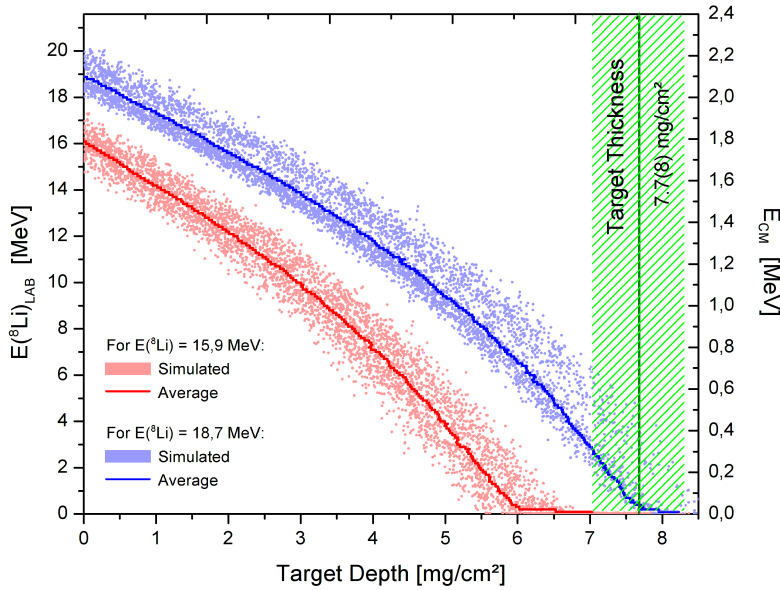


Figure 46: Simulations for ^8Li energy (and equivalent center-of-mass reaction energy for $^8\text{Li} + p$) in function of $(\text{CH}_2)_n$ target depth for both ^8Li bombarding energies employed.

The primary beam energies used were $E(^7\text{Li})_{\text{prim}} = 27.8$ MeV for the highest ^8Li energy and $E(^7\text{Li})_{\text{prim}} = 25.9$ MeV for the lowest. These primary energies are achievable at Pelletron Laboratory through $V_T = 6.93$ and 6.45 MV, respectively (eq.34).

The calculations done to achieve the primary and secondary beam energies were made through the program CineRIBRAS [93], a Monte-Carlo algorithm which takes into account the processes, like energy loss, reactions, straggling, etc. occurring at each element that influences the beam, like primary target, energy degraders, detectors, etc. See appendix B for a detailed description.

3.9.3 Reaction Products

It is also convenient to know what to expect from the possible reaction products. From the calculations done by CineRIBRAS it is easy to extract the resultant energy of the reaction products when they emerge from the target. In figure 47 are shown the energies of detected protons, deuterons and alphas as function of the ^8Li energy (or center-of-mass energy at reaction). These curves are also essential to the conversion of the detected energy spectra into the excitation functions (see sec.4.1). Unlike figure 46, only the average values that resulted from the Monte-Carlo simulation are depicted.

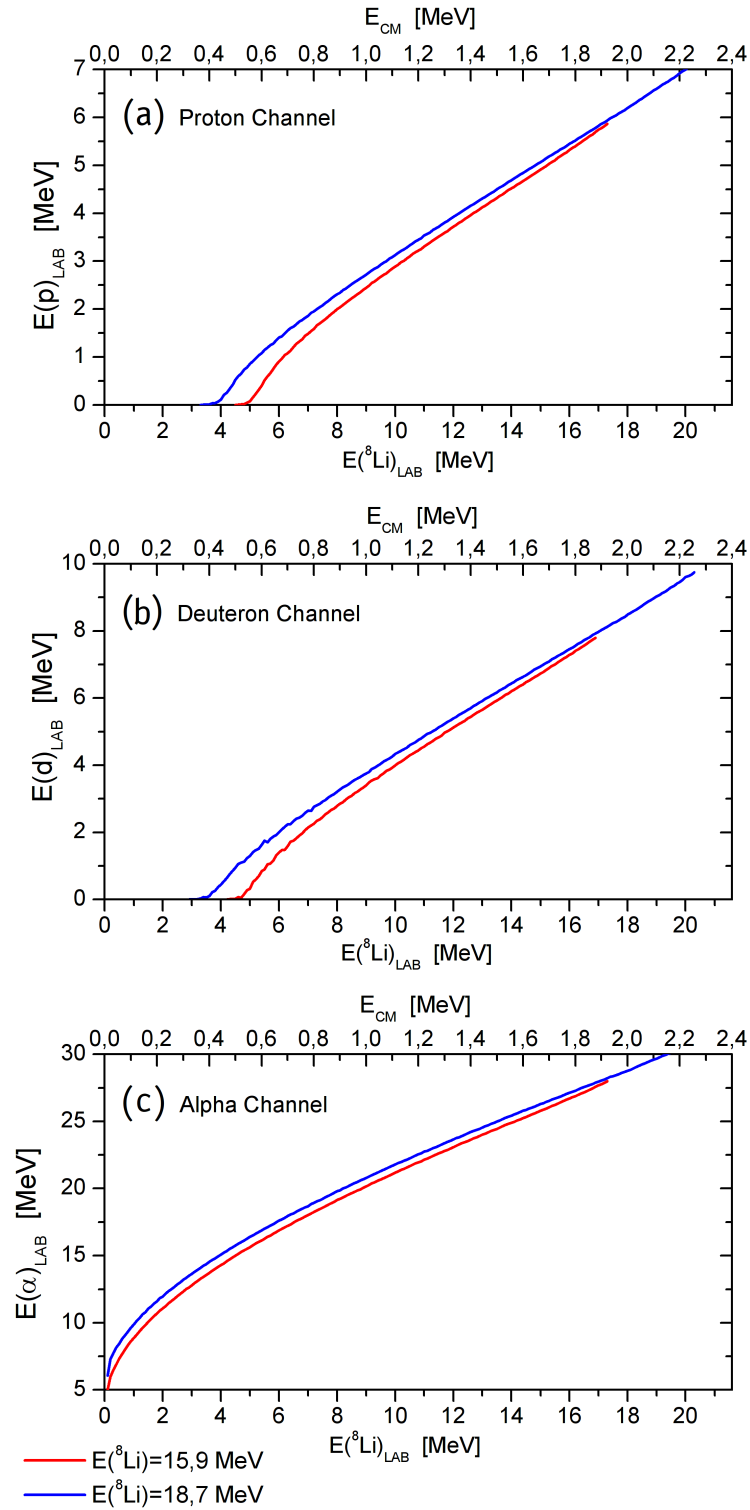


Figure 47: Conversion curves for the energy of reaction products – proton (a), deuteron (b) and alpha (c) – right after emerging from the $(\text{CH}_2)_n$ target in function of the correspondent ${}^8\text{Li}$ energy (and equivalent center-of-mass energy for ${}^8\text{Li} + p$) for both ${}^8\text{Li}$ bombarding energies employed.

As can be seen, due to the high Q value of the ${}^8\text{Li}(p,\alpha)$ reaction, alphas are expected to be highly energetic, ranging from 5 to 32 MeV. However, part of this spectrum is expected to be covered by contaminant alphas. According to table 3, the contaminant alpha beam that went through the second solenoid has energy of $E({}^4\text{He})_{\text{cont}} = 16.6$ MeV for the highest ${}^8\text{Li}$ energy and $E({}^4\text{He})_{\text{cont}} = 14.3$ MeV for the lowest. After losing energy in the target, these contaminants should have energies of 13.1 MeV and 9.9 MeV, respectively. It means that the excitation function should be measured from $E_{\text{cm}} = 0.15$ or 0.3 MeV, depending on the bombarding energy, to 2.15 MeV (see the conversion curves in figure 47). Detection limitations and contaminant reactions could constrain even more the range of the measurable excitation function, but it will be discussed at chapter 4.

On the other hand, protons ejected from the elastic ${}^8\text{Li}(p,p)$ reaction at forward angles have low energies, between 0 to 7 MeV. Part of the excitation function is lost as their protons also stop inside the target. It can be seen in figure 47.a, where the protons able to emerge from the target are those produced at energies higher than $E_{\text{cm}} = 0.4$ or 0.5 MeV, depending on the bombarding energy⁷. This fact already limits the energy range of the measurable excitation function, making the resonance at $E_r = 0.4$ MeV definitely impossible to be measured in this decay channel. The detected deuterons from ${}^8\text{Li}(p,d)$ reaction behave very similarly to the protons, ranging from 0 to 9.7 MeV.

This is not the only limitation on the measurement of proton and deuteron channels. Particles of low energy ($\lesssim 3.0$ MeV) may not be able to cross the Si ΔE detector in a $E - \Delta E$ telescope. As mentioned in section 3.5.1, a Si ΔE detector of 50 μm is indicated for proton measurements, since thinner than this severely impaires the ΔE resolution.

Two sets of silicon ΔE detectors were available: 20 μm and 50 μm . According to calculations using the program stopx (ap.B), protons would be able to cross ΔE detectors of 20 and 50 μm with energies larger than 1.1 and 2.0 MeV, respectively. In other words, using ΔE detectors of 20 and 50 μm , the excitation function could be measured from $E_{\text{cm}} \simeq 0.6$ MeV and 0.8 MeV, respectively.

It means that, with a 20 μm ΔE detector and favorable conditions, it could be possible to measure the resonance around $E_r = 0.6$ MeV in the proton channel.

For deuterons, the detectors are a bit more restrictive. Deuterons would be able to cross a ΔE detector of 50 μm from a minimum of 2.6 MeV ($E_{\text{cm}} = 0.85$ MeV), and a ΔE detector of 20 μm from 1.4 MeV ($E_{\text{cm}} = 0.62$ MeV).

⁷ The curve shown at figure 47.a is an average of several calculations considering the energy spread of the beam and the target thickness. So it is possible that some protons produced at energies lower than those mentioned manage to come out of the target.

Fortunately, contaminant protons with the same magnetic rigidity as the ${}^8\text{Li}$ beam are expected to be highly energetic and would not interfere in the measured proton spectrum from ${}^8\text{Li}(p,p)$ reaction. They are also easily eliminated with the use of a degrader. However, contaminations in the proton spectra may appear due to other sources.

Meanwhile, contaminant deuterons are expected to be much lower energetic than contaminant protons and should cover the regions around $E_{\text{cm}} = 1.5$ MeV and 1.8 MeV of the excitation function, respectively for the lowest and highest incident beam energies. The use of two bombarding energies should be of extreme importance to clean up the spectrum from the contaminant deuteron peak.

3.9.4 Detector Dimensioning

This experiment did not aim to measure angular distributions, thus one $E - \Delta E$ telescope is sufficient to properly measure the excitation function. The E silicon detector chosen was one of 1000 μm , that should be thick enough to stop every expected reaction product. For the ΔE detector, the plan was to measure very well the more energetic part of the excitation function using a ΔE detector of 50 μm . If desired, the detector could also be changed to one of 20 μm in an attempt to measure the resonance around 0.6 MeV.

As this measurement is done in inverse kinematics, the detector should be placed at frontal angles. But it also should avoid the angular region from 0 to 6° in which direct secondary beam may be present⁸ (see sec. 3.6.3). The chosen angle was $\theta_{\text{lab}} = 10^\circ$, a frontal yet safe angle to avoid the direct secondary beam. It is also close to the angle employed at the previous ${}^8\text{Li}(p,\alpha)$ experiment, 13.5° [41].

The entrance of the $E - \Delta E$ set was placed at 85(2) mm from the center of the target. a cylindrical blocker of 6 cm was placed right in front of the detector to ensure that only particles that passed through the target could reach the detector⁹. Rectangular collimators were placed at both ends of the cylindrical one to constrain the angular aperture. The most restrictive one, right in front of the detector's active area, had 15.0 x 6.0 mm.

These geometrical considerations define the solid angle of the detector: $\Delta\Omega = 12.5(3)$ msr (eq.42), and the total angular aperture: 4° . The calculated effective detection angle (eq.43) in the laboratory frame for the given geometry and Rutherford scattering is $\theta_{\text{eff}} = 8.5(5)^\circ$.

⁸ Even if the ${}^8\text{Li}$ beam stops inside the $(\text{CH}_2)_n$ target, light contaminants may cross it and reach the telescope if it is positioned at $\theta_{\text{lab}} \lesssim 6^\circ$. Moreover, measurements with ${}^{197}\text{Au}$ target were also performed, and even the ${}^8\text{Li}$ is able to cross this target at the bombarding energies employed.

⁹ A more clear picture of how this blocker was placed can be found at fig. 49 at sec. 3.10.

3.9.5 Energy Resolution

Note from picture 46 that the only difference between the ejectiles produced at the same reaction energy but by different bombarding ${}^8\text{Li}$ energies is the location of the reaction inside the target and, thus, that they have to cross different amounts of target material before emerging (about 1.8 mg/cm^2 more for those with $E({}^8\text{Li}) = 15.9 \text{ MeV}$ in average). This is why the curves are so close to each other in figure 47.

This gives rise to the fact that even with a secondary beam of poor energy resolution, the TTIK method ends up resulting in a remarkably good energy resolution in the final spectra.

In figure 48 are shown calculations based on simulated data on the resolution of the final excitation function as a function of the detected energy of the reaction products.

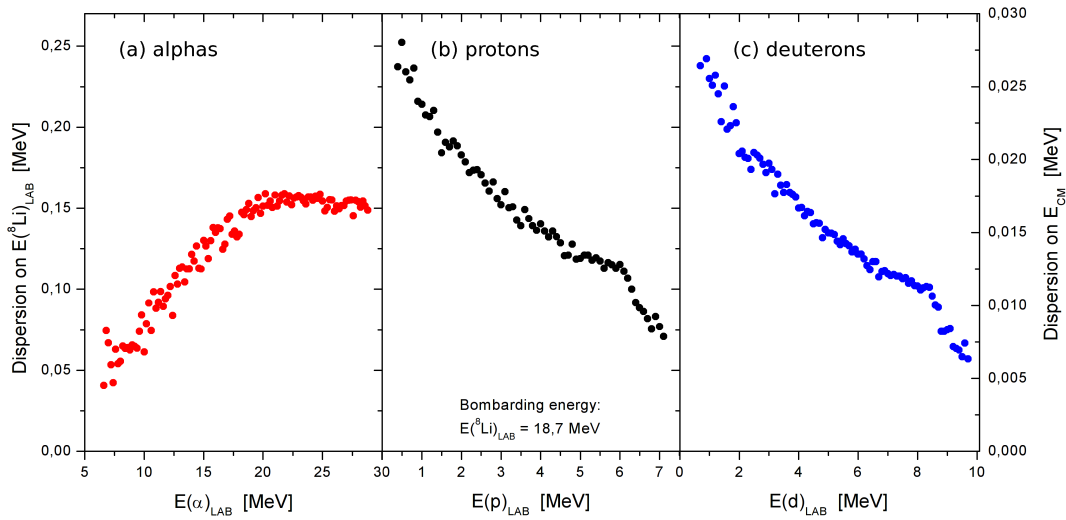


Figure 48: Simulated dispersion (in standard deviation) of the energy of ${}^8\text{Li}$ beam at the reaction point in function of the detectable energy of the products: (a) alphas, (b) protons and (c) deuterons, for bombarding energy of $E({}^8\text{Li}) = 18.7 \text{ MeV}$.

As can be seen, the worst resolution for both protons and deuterons is around $\Delta E_{\text{cm}} = 25 \text{ keV}$, which is enough to unravel any structure present at the R-matrix prediction at figure 45 in the case of protons. In the case of alphas, the worst resolution is around $\Delta E_{\text{cm}} = 17 \text{ keV}$.

3.9.6 Influence of Contaminant Carbon

One important issue regarding the use of a composite target is about the influence of the other components in the final spectra. Could reactions from the interaction ${}^8\text{Li} + {}^{12}\text{C}$ result in protons or alphas at the same expected energy region?

The reaction ${}^{12}\text{C}({}^8\text{Li},\alpha){}^{16}\text{N}$ [41] also has a high Q value: +12.838 MeV. The alphas that reach the detector would range up to 30.5 MeV at $\theta_{\text{lab}} = 10^\circ$, almost the same as the relevant alphas.

However, at the previous ${}^8\text{Li}(p,\alpha)$ experiment, a measurement with a thick natural carbon target (15 mg/cm²) was done to evaluate the contribution of this specific reaction. The results revealed that the average cross section of ${}^8\text{Li}({}^{12}\text{C},\alpha)$ at the energies of this study was not larger than 1 mb/sr (see figure 4 of [41]). Given the yield expected for the ${}^8\text{Li}(p,\alpha)$ measurement, this contribution is negligible.

Meanwhile, the possible reaction ${}^{12}\text{C}({}^8\text{Li},p){}^{19}\text{O}$ also has a high Q value: +10.324 MeV. Because of this, protons generated in this reaction would range very far from the relevant ones: from 11 to 27 MeV. So this reaction should not pose any trouble to this experiments.

The reaction ${}^{12}\text{C}({}^8\text{Li},d){}^{18}\text{O}$ ($Q = +8.593$ MeV) could interfere in the upper part of the deuteron excitation function, from $E_{\text{cm}} = 1.8$ MeV. Deuterons generated in this reaction would range from 7.5 to 26 MeV.

Measurements using a natural carbon target were also done. The target employed had 15 mg/cm², the same used in the previous experiment.

3.10 RESUME OF THE EXPERIMENTAL PROCEDURE

The experiment was carried out between 5th and 12th May, 2013, at Pelletron Laboratory of the Institute of Physics of the University of São Paulo (IF-USP), Brazil, using the RIBRAS System.

A secondary beam of ${}^8\text{Li}$ was produced through the reaction ${}^9\text{Be}({}^7\text{Li}, {}^8\text{Li}){}^8\text{B}$ by a stable ${}^7\text{Li}$ beam impinging on a primary ${}^9\text{Be}$ target. The intensity of the primary beam was measured by a Faraday Cup placed right after the primary target which also acted as a blocker of the primary beam.

The secondary ${}^8\text{Li}$ beam, scattered at laboratory angles between 2° and 6° , was selected by its magnetic rigidity and focalized at RIBRAS' central and main chambers, respectively, by two superconducting solenoids. At the central chamber, a polyethylene degrader was placed to change the magnetic rigidity of contaminant beams in relation to the relevant beam. Thus, beam purity could reach $\sim 99\%$ in the main chamber.

The experiment was performed in the main chamber, where the beam hit a thick $(\text{CH}_2)_n$ target ($7.7(8) \text{ mg/cm}^2$). There, the ${}^8\text{Li}$ beam slowed down and populated resonances of the ${}^8\text{Li} + p$ system, following the concept of the inverse kinematics thick target method. Alpha particles, deuterons and protons were produced inside the target through the reactions ${}^8\text{Li}(p, \alpha)$, ${}^8\text{Li}(p, d)$ and ${}^8\text{Li}(p, p)$ and left the target, reaching a $E - \Delta E$ silicon telescope placed at $\theta_{\text{lab}} = 10^\circ$ with solid angle of $\Delta\Omega = 12.5(3) \text{ msr}$ and total angular aperture of 4° in relation to the center of the secondary target. Measurements with a thick natural carbon target of 15 mg/cm^2 were also carried out to subtract the contribution of the reactions on carbon from the measured spectra.

At figure 49 is shown a photo of the experimental mounting at the main chamber.

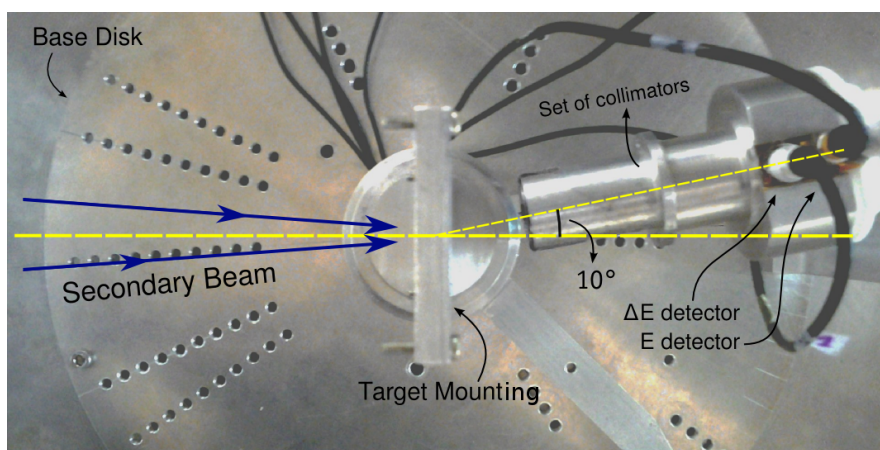


Figure 49: Photo of the experimental mount at main chamber.

The experiment had two main phases of measurement, each one with a different ${}^8\text{Li}$ bombarding energy: $E({}^8\text{Li}) = 18.7$ MeV and 15.9 MeV. At each phase, the ${}^8\text{Li}$ beam was optimized to arrive at the secondary target at the highest intensity and highest purity possible. After each 5 hours of measurement with $(\text{CH}_2)_n$ target, a short run of about 20 minutes with a ${}^{197}\text{Au}$ target was done to monitor the ${}^8\text{Li}$ beam production efficiency ϵ . The measured values of ϵ at each phase are shown at table 4. During the measurement with $E({}^8\text{Li}) = 18.7$ MeV, a slight drop on ϵ was observed, so the table shows both values measured.

Table 4: ${}^8\text{Li}$ production efficiency at each phase of the experiment.

$E({}^8\text{Li})_{\text{lab}}$	$\epsilon (\cdot 10^{-7})$
18.7 ⁽¹⁾	0.49(9)
18.7 ⁽²⁾	0.28(7)
15.9	0.28(7)

*Energies in MeV.

The $E - \Delta E$ telescope employed had 1000 μm for the E detector and 50 μm for the ΔE detector. In the measurement with $E({}^8\text{Li}) = 15.9$ MeV, another ΔE detector, of 20 μm , was also employed in an attempt to measure the lower energy part of the excitation function. The electronics were set up to be able to register events of both light and heavy particles with good resolution, with two different lines of amplification at each detector.

The experiment also used a MCP detector placed at central chamber that, together with the timing signal of the silicon detectors at main chamber, could perform time-of-flight measurements of the beams between central and main chambers. These measurements helped on the evaluation of purity of the ${}^8\text{Li}$ secondary beam.

At figure 50 is shown a detailed scheme of the experimental mounting of the whole RIBRAS System.

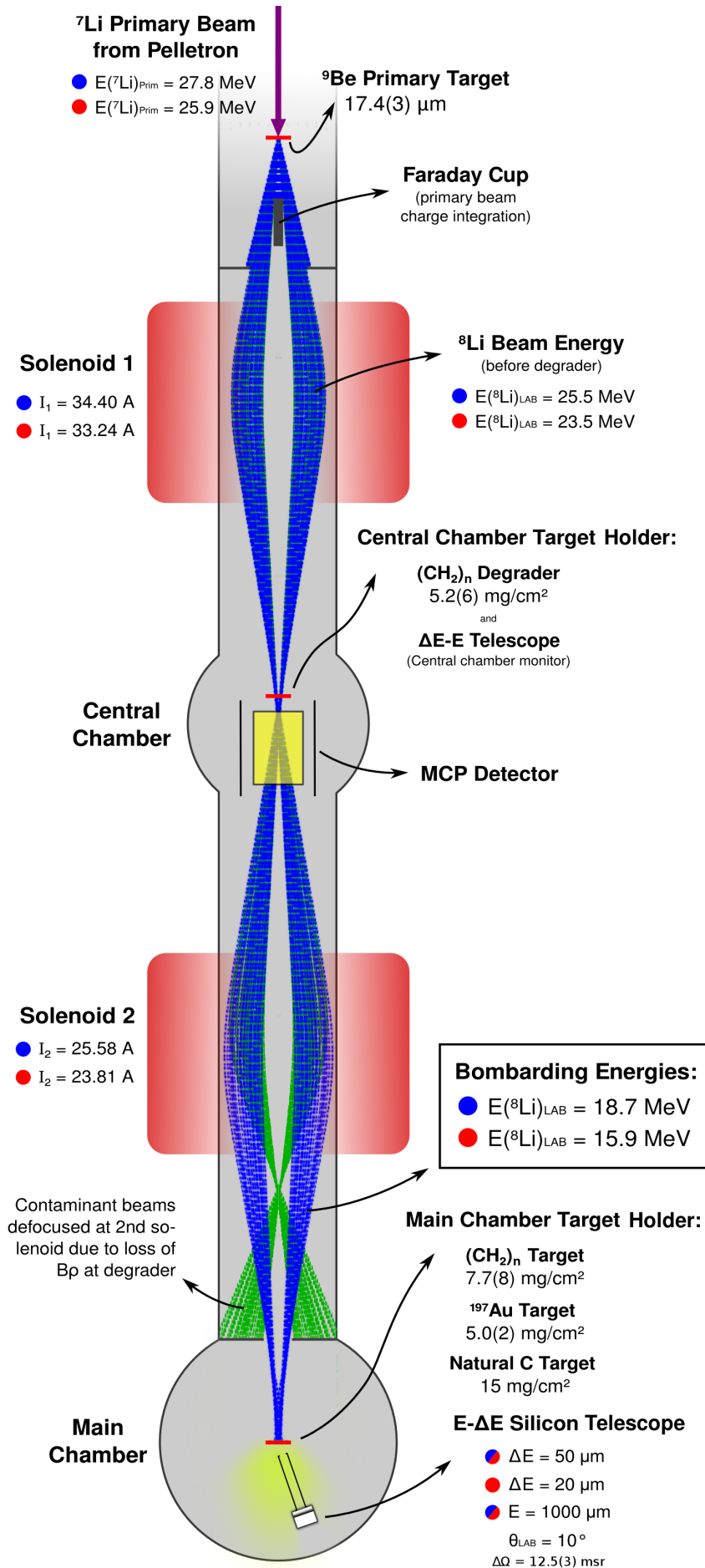


Figure 50: Scheme of the experimental mounting in the RIBRAS System for this experiment.

DATA REDUCTION AND ANALYSIS

The figures below contain the spectra obtained with the $E - \Delta E$ telescope at each detector configuration and at each bombarding energy impinging on the $(\text{CH}_2)_n$ target.

In figure 51 is shown the spectrum obtained at the highest bombarding energy ($E(^8\text{Li}) = 18.7 \text{ MeV}$). The hyperbolic strips containing the reaction products are easily identifiable. In the proton strip, a large yield can be noted, but it extends beyond the kinematical limit for the $^8\text{Li}(p,p)$ reaction at this bombarding energy, $E(p)_{\text{lab}} = 7.2 \text{ MeV}$, reaching up to $E(p)_{\text{lab}} = 12 \text{ MeV}$. This may indicate the presence of contaminant protons.

Both for deuteron and alpha strips the kinematical limits are respected and the high yield peaks observed are consistent with the predicted energies for contaminant beams selected at the second solenoid. Right above the deuteron strip, a triton strip is present but its kinematical behavior does not correspond to an $^8\text{Li}(p,t)$ reaction, and it may also be considered a contaminant. No other ion can be identified in this spectrum.

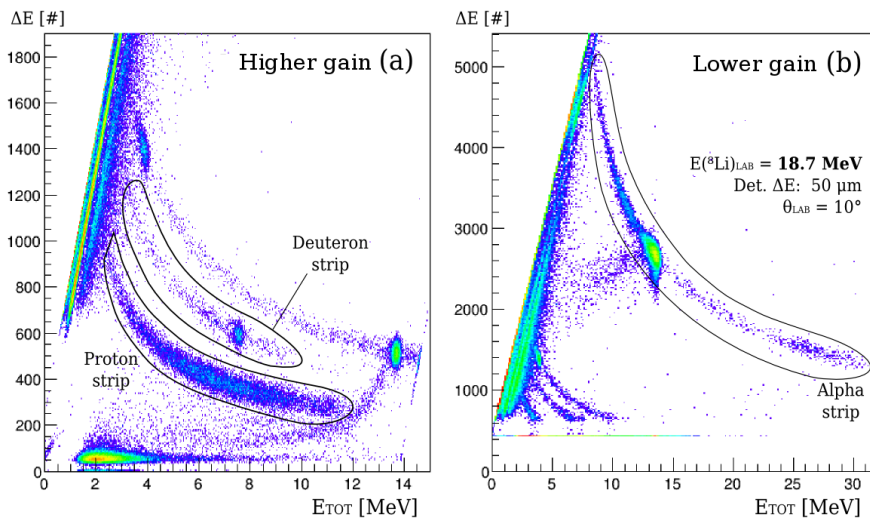


Figure 51: Spectra obtained with $(\text{CH}_2)_n$ target and ^8Li beam of $E(^8\text{Li}) = 18.7 \text{ MeV}$ for both amplification lines: (a) higher gain and (b) lower gain, showing the strips from which were extracted the reaction product yields.

In figure 52 is shown the spectrum obtained at the lowest bombarding energy ($E(^8\text{Li}) = 15.9 \text{ MeV}$) with the same ΔE detector as employed at the higher energy ($50 \mu\text{m}$). The same considerations about the reaction products' strips can be done about this spectrum. It is

important to note that the energies of the contaminant peaks (d, t and α) have decreased with the reduction of the ^8Li beam energy (and thus the magnetic rigidity), while the remaining of the spectra were kept almost unchanged, indicating that they were produced in a compound nucleus decay.

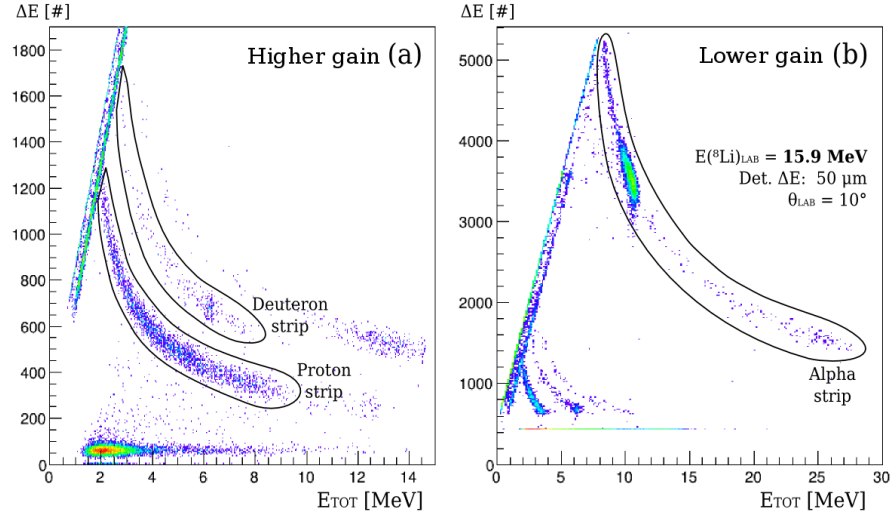


Figure 52: Spectra obtained with $(\text{CH}_2)_n$ target and ^8Li beam of $E(^8\text{Li}) = 15.9$ MeV for both amplification lines: (a) higher gain and (b) lower gain, showing the strips from which were extracted the reaction product yields.

In figure 53 is shown the spectrum obtained at the lowest bombarding energy ($E(^8\text{Li}) = 15.9$ MeV) but with a thinner ΔE detector of $20\ \mu\text{m}$. As expected, the resolution is much worse and the identification of the strips is severely impaired, but protons and deuterons with lower energies could be detected.

The proton strip can be relatively well defined from 1 to about 9 MeV. The identification of the deuteron strip is difficult due to its proximity with the proton strip. At the lower gain amplification line, an acquisition problem made every signal from the ΔE detector below 600# to be registered as 445#, but it did not impair the identification of the alphas in that region.

Despite the loss in resolution, the same structures and characteristics can be identified in the spectra obtained at the same bombarding energy but with different ΔE detectors.

The triton strip measured at the lower energy is proportionally less intense than the strip obtained at the higher bombarding energy, indicating that these tritons are probably contaminants.

The data processing is detailed in the following sections. First, it is important to introduce how to extract excitation functions from a measured spectrum through the concept of the TTIK method.

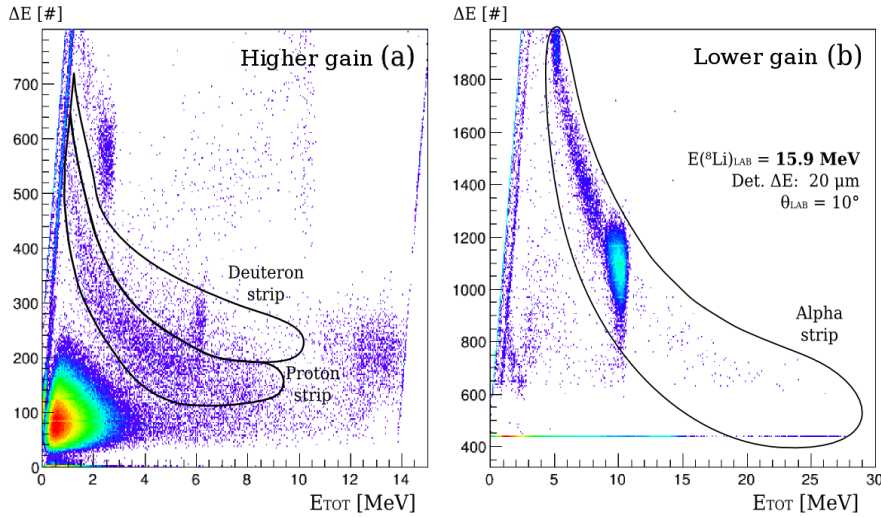


Figure 53: Spectra obtained with a thinner ΔE detector with $(\text{CH}_2)_n$ target and ${}^8\text{Li}$ beam of $E({}^8\text{Li}) = 15.9$ MeV for both amplification lines: (a) higher gain and (b) lower gain, showing the strips from which were extracted the reaction product yields.

4.1 EXCITATION FUNCTIONS FROM THE TTIK METHOD

In a detected spectrum, each energy *bin* δE will contain information about how many counts were detected of that specific particle inside a specific energy interval $[E, E + \delta E]$. To obtain the excitation function, the energy of the detected particle ($E(\alpha)$, $E(p)$ or $E(d)$ in the case) must be converted into energy of the ${}^8\text{Li}$ beam prior to the reaction ($E({}^8\text{Li})$) and into energy of the system at the center-of-mass reference (E_{cm}). These conversions correspond to the curves exhibited at figure 47 in section 3.9.

Also, each channel must be converted from counts (N_{det}) to differential cross section. The experimental differential cross section $d\sigma/d\Omega$ is given by [80]:

$$\left(\frac{d\sigma}{d\Omega}\right) = \frac{N_{\text{det}} J(E, \theta)}{N_{\text{inc}} N_{\text{targ}} \Delta\Omega} \quad (48)$$

in which:

N_{det} is the number of scattered particles detected in the considered energy interval $[E, E + \delta E]$, easily obtained from the detector spectrum;

N_{inc} is the total number of incident particles of the beam that hit the target (see the technique to obtain $N_{s_{\text{Li}}}$ described in sec.3.6.2);

N_{targ} is the number of scatterer nuclei inside the target per unit area (see eq.47 in sec.3.7);

The conversion from $E({}^8\text{Li})$ to E_{cm} is $E_{\text{cm}} = E({}^8\text{Li})/9$, see eq. 61.

$\Delta\Omega$ is the solid angle of the employed detector in relation to the target (see eq.42 in sec.3.5.1);

$J(E, \theta)$ is the Jacobian for the transformation from laboratory frame to center-of-mass frame, given the reaction energy E and the scattering angle θ in relation to the beam's direction (see appendix A).

Some adaptations are necessary on how the variables of equation 48 are calculated in order to consider the continuum nature of the TTIK method.

The main correction is at the number of scattering nuclei in the target, N_{targ} . It needs to be corrected to an equivalent N_{targ} that a ${}^8\text{Li}$ particle would face at each energy interval $[E, E + \delta E]$. This is done through the use of the stopping power of ${}^8\text{Li}$ on $(\text{CH}_2)_n$ (figure 54) to find the equivalent target thickness faced by the beam at a specific energy [41, 55]:

$$x_{\text{targ}} = \frac{\delta E}{\left(\frac{dE}{dx}\right)} \quad (49)$$

It should be emphasized that δE in this case is the equivalent energy step of the beam right before the reaction ($E({}^8\text{Li})$), as it must be in agreement to the stopping power units. If δE is in MeV and (dE/dx) is in $\text{MeV}/(\text{mg}/\text{cm}^2)$, the unit will be in mg/cm^2 for x_{targ} .

To convert it to N_{targ} , equation 47 can be used, but using the atomic mass of a $(\text{CH}_2)_n$ monomer ($A = 14.015$ a.m.u.) and considering that each monomer has 2 hydrogen atoms, so the N_{targ} obtained for $(\text{CH}_2)_n$ must be doubled in order to have the right amount of protons per unit area. The calculated (dE/dx) for ${}^8\text{Li}$ in $(\text{CH}_2)_n$ is displayed in figure 54.

The jacobian $J(E, \theta)$ for transformation from the laboratory frame to center-of-mass frame for each reaction is presented at figure 55. More details on how these curves are calculated are presented at appendix A.

Some other corrections may be needed to take into account the energy spread of the incident beam. As explained in section 3.8, an incident beam particle would be able to populate any point of the excitation function from its initial energy to zero. In a perfectly monochromatic ${}^8\text{Li}$ beam, every particle of the beam would be able to populate the same interval of the excitation function.

This is not valid if the incident beam has a large energy spread. Considering the energy of the inferior limit of the beam energy distribution (see fig. 37), all particles of the beam would be able to populate the excitation function up to that energy. But in the case of the superior limit of the energy distribution, just a diminute amount of particles would be able to populate the excitation function up to

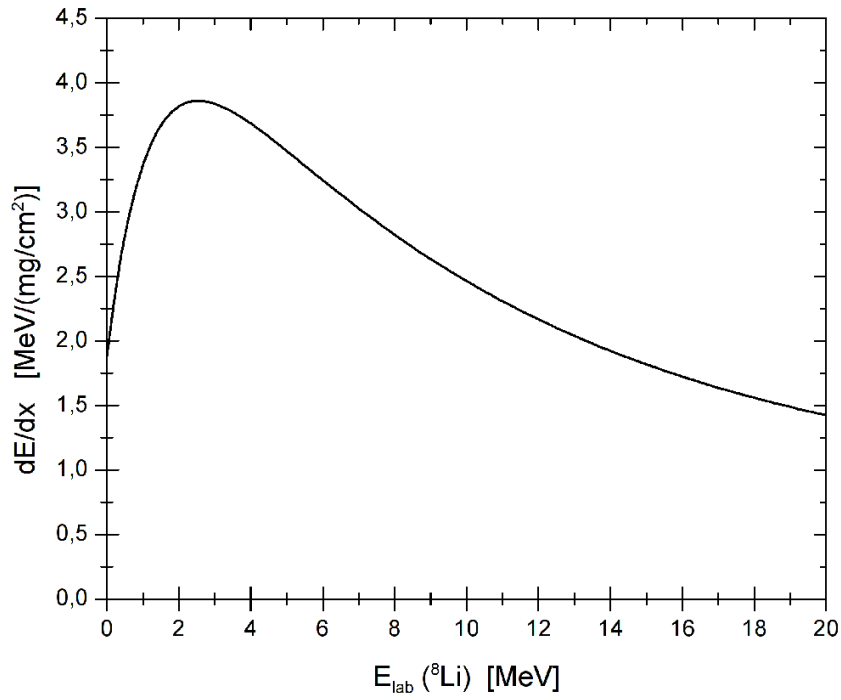


Figure 54: Stopping power of ${}^8\text{Li}$ in $(\text{CH}_2)_n$, calculated by the algorithm stopx (appendix B).

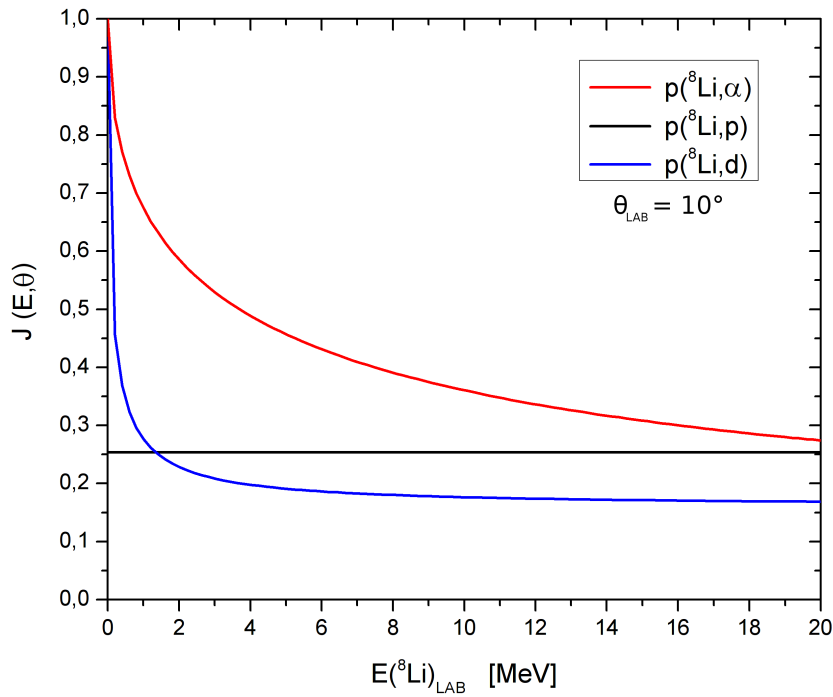


Figure 55: Jacobian for the transformation from laboratory frame to center-of-mass frame as a function of the energy $E({}^8\text{Li})$ for the relevant reactions.

that energy, as almost the whole beam does not have enough energy to populate that extreme energy.

This leads to a correction on the number of incident particles N_{inc} for this high energy region. For example, for a reaction energy that just half of the incident beam is able to populate, N_{inc} must also be corrected to half at that energy. At figure 56 are shown the corrections at N_{inc} for both bombarding energies.

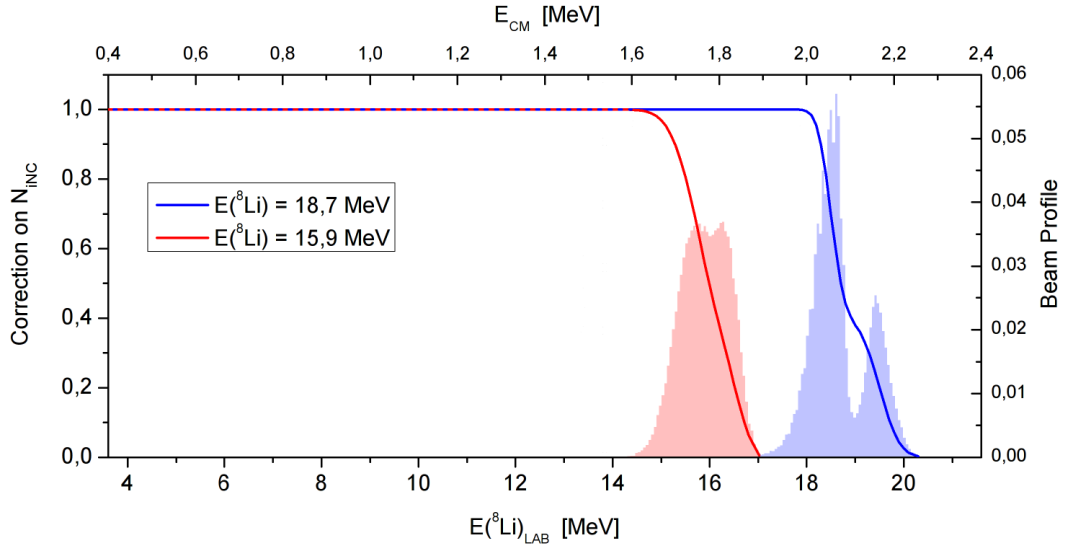


Figure 56: Correction of N_{inc} due to beam energy spread (fig.37) for both bombarding energies.

For the same reasons, if the incident beam has enough energy to cross the target without stopping inside it, an equivalent correction on N_{inc} is also needed in the low energy region of the spectrum. Another correction that may be needed is due to the target roughness; as part of the beam would cross more material than others, similar corrections on N_{targ} are needed at low energies.

In the case of this experiment, these corrections on the lower energy part of the excitation functions are negligible even at the most extreme case. But they may be important in other TTIK experiments, so the target roughness and beam the energy profile must be very well known in any case (see sec.3.7).

As the statistics of the measurement are low, it may be convenient to choose a larger energy bin size δE than the experimental resolution (see fig. 48) to avoid large statistical fluctuations. In this case, this procedure would result in an energy resolution loss and the uncertainty in energy will be given by $\delta E/\sqrt{12}$ [101].

4.2 ALPHA SPECTRA

The measured energy spectra, extracted from the alpha strips, are shown at figure 57.

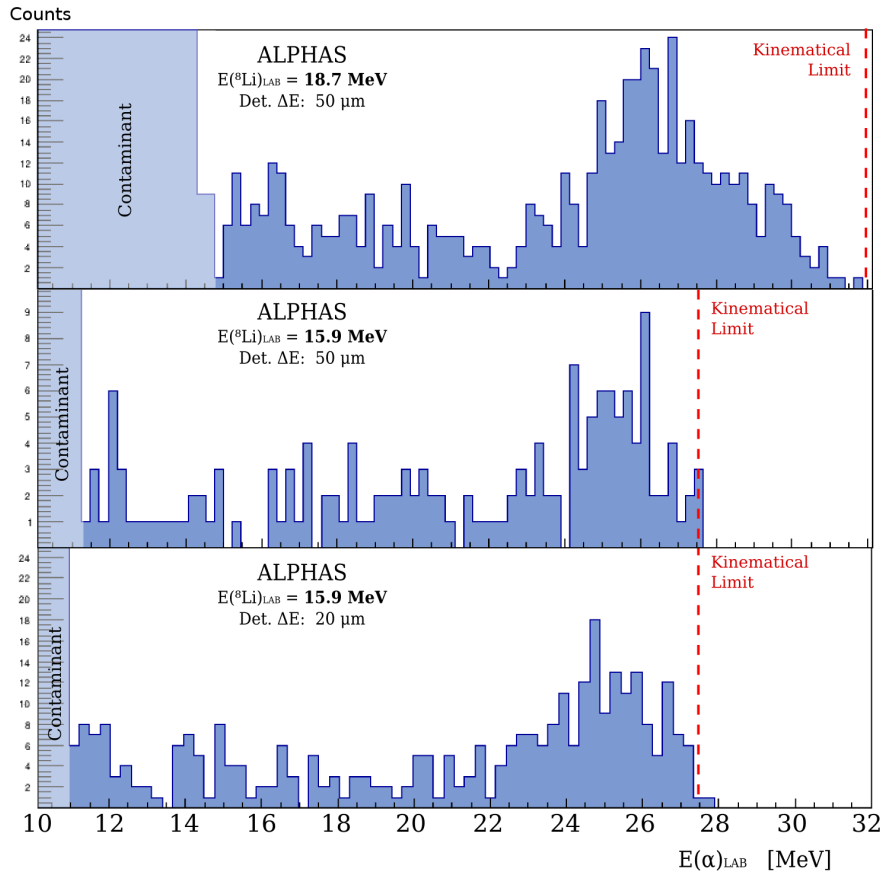


Figure 57: Energy spectra obtained with $(\text{CH}_2)_n$ target through the alpha strips at each bombarding energy and detector configuration at $\theta_{\text{lab}} = 10^\circ$. Energy bin: $\delta E = 0.275$ MeV.

These spectra have similar characteristics to the obtained in the previous work [41] (see figure 58): a broad peak around 26 MeV and an almost constant plateau between this broad peak and the contaminant alpha peak ($E(\alpha) \lesssim 14$ MeV). An important difference is that the peak due to the reaction $^{12}\text{C}(^7\text{Li}, \alpha)$ seems not to appear, probably due to the high purity of the ^8Li beam employed at this experiment. Unfortunately, the statistics obtained are not as good as in the previous experiment, pledging the precision of the final result.

The kinematical limits are respected, and part of the broad peak is not populated in the spectra with lower incident energy. As mentioned, the position of the contaminant alphas peak vary according to the incident energy, but not the remaining of the spectra, indicating they are originated in the decay of the compound nucleus.

However, three decay mechanisms can originate alpha particles from an excited ^9Be nucleus [41]: the direct $\alpha + \alpha + n$ three-body break-

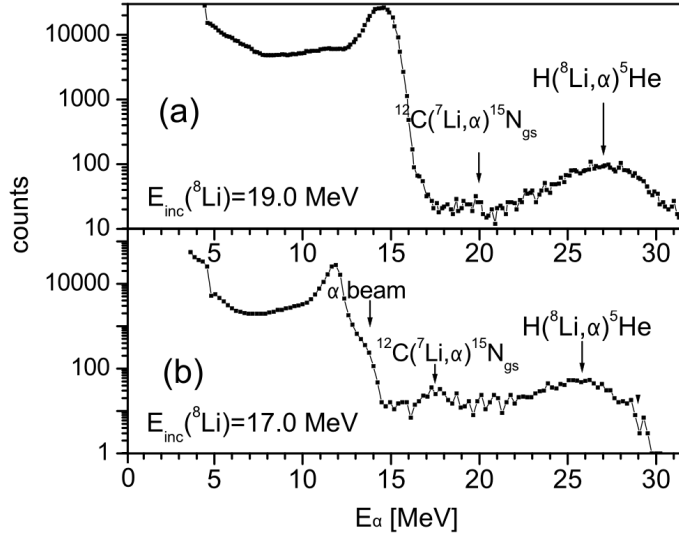


Figure 58: Alpha particle events per energy spectra obtained in the previous experiment at energies around those employed at this experiment and at $\theta_{\text{lab}} = 13.5^\circ$ (adapted from [41]).

up, the two-step decay into ${}^8\text{Be}+n$ channel and the subsequent break of the unbound ${}^8\text{Be}$ into two alpha particles, and finally the decay into $\alpha+{}^5\text{He}$, in which the recoiling ${}^5\text{He}$ is also unbound and disintegrates into $\alpha+n$. In any case, two alpha particles are generated in the decay and create a background in the excitation function.

4.2.1 Background

In the case of the ${}^8\text{Be}+n$ decay channel, the $p({}^8\text{Li}, {}^8\text{Be})n$ reaction also has a high Q value: 15.22 MeV, and the ${}^8\text{Be}$ would be produced up to 22.3 MeV and 25.1 MeV for the two ${}^8\text{Li}$ bombarding energies. Each alpha particle originated from the ${}^8\text{Be}$ decay typically take half of ${}^8\text{Be}$ energy [41]. Considering also the energy loss inside the target, the maximum energy expected for alpha particles originated from this decay channel would be around 9 MeV, which would appear below the contaminant alphas peak and, thus, out of the range of interest.

The ${}^5\text{He}$ decay and the ${}^9\text{Be}$ three-body break-up contribute to form a background in the excitation function. Their contributions should be subtracted in order to isolate the information about the relevant reaction: ${}^8\text{Li}(p, \alpha){}^5\text{He}$.

As they are all processes occurring in the compound nucleus, the subtractions should be done in the differential cross section (see sec. 4.1).

The background originated by the ${}^9\text{Be}$ three-body break-up can be described by Fermi's Phase Space Model [48, 41], which calculates the statistical probability of creation of alpha particles of energy E_α at a given incident energy E_{cm} :

$$P_\alpha(E_\alpha, E_{cm}) = \frac{4\sqrt{E_\alpha}}{\pi(E_\alpha^{\max})^2} \sqrt{E_\alpha^{\max} - E_\alpha} \quad (50)$$

The alpha energy distribution was obtained by integrating eq. 50 over the decreasing incident energy in the thick target. As this model gives no normalization for cross section, the distribution was normalized through the limitation that the sum of both background contributions should not be higher than the measured cross section.

In the case of the alphas produced at the ${}^5\text{He}$ decay, there is a direct compromise between them and the relevant alphas, as both are produced at different steps of the same decay, and consequently at the same amount. Monte-Carlo simulations were performed using the shape of the actual measured data and kinematical considerations of the $\alpha+n$ decay ($Q = 0.89$ MeV) to determine the contribution on the final spectra of alphas produced in the second step of ${}^9\text{Be}$ sequential decay [41].

The energy distribution of alphas from ${}^5\text{He}$ decay has a large broadening and do not form a well defined peak. They typically have lower energy than the alphas produced directly in the first step of the sequential decay.

An example of the background corrections employed are shown at figure 59.

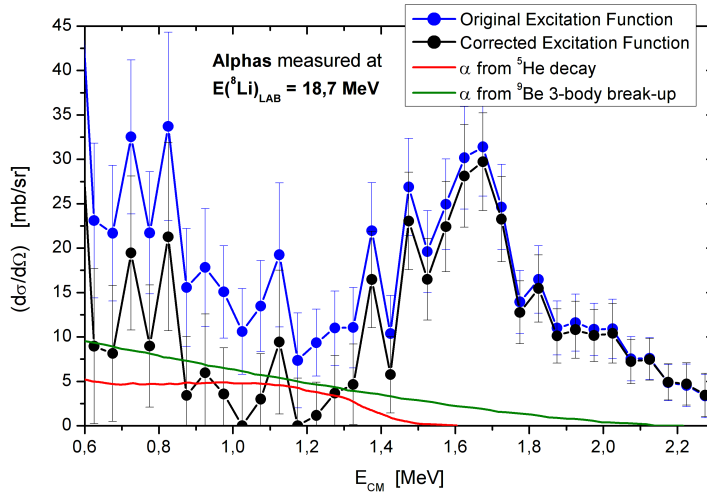


Figure 59: Measured and corrected excitation functions for alphas for bombarding energy of $E({}^8\text{Li}) = 18.7$ MeV, and the corrections due to ${}^5\text{He}$ decay and direct ${}^9\text{Be}$ 3-body break-up.

The measurements made with the natural carbon target revealed that no relevant correction is needed due to alphas generated in reactions between the beam and the carbon present in the $(\text{CH}_2)_n$ target,

E_α^{\max} is the maximum possible energy for the α particle created at energy E_{cm} (see reaction kinematics at appendix A).

as expected (see discussion at sec. 3.9.6). The measurements taken with ^{197}Au target also revealed that there was no presence of contaminant alphas in the relevant energy region of the spectra.

4.2.2 Final Spectra and Previous Results

As the statistics were low, an energy bin size δE of 50 keV in the center-of-mass frame was conveniently chosen, considering how much energy resolution loss this procedure would entail. In any case, the fine structures observed in the low energy part of the previous experiment (see fig. 7) would not be well described due to the low statistics.

The corrected excitation functions obtained at both energies and both detector configurations are all compatible with each other. The complete excitation function, shown in figure 60, is composed by the weighted average (by the statistical error) between the measurements, where the excitation functions overlap.

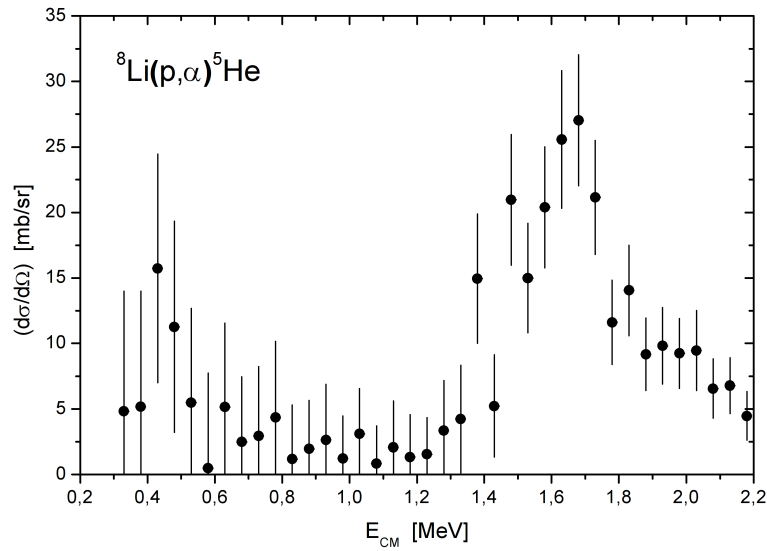


Figure 60: Complete excitation function for $^8\text{Li}(p,\alpha)^5\text{He}$ reaction measured at $\theta_{\text{lab}} = 10^\circ$.

In figure 61 the results of this experiment are compared with others that explored the $^8\text{Li}(p,\alpha)$ reaction.

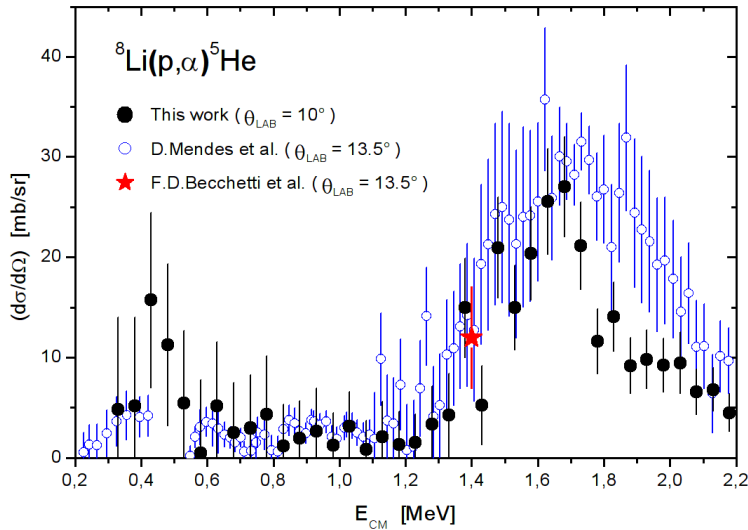


Figure 61: Excitation functions for ${}^8\text{Li}(p,\alpha)$ experiments measured at forward angles, comparing the results from this work and those from [41] and [102].

As can be seen, there is a good agreement between the results obtained at this experiments and the previous one (D.Mendes et al. [41]) at the whole excitation function¹, except for a small disagreement in the region around $E_{\text{cm}} = 1.8$ MeV that makes the peak looks broader in the previous experiment.

A possible explanation for that slight disagreement comes from the different experimental conditions between the two experiments. In the previous experiment, the ${}^8\text{Li}$ beam of 19.0 MeV was produced in the primary target with a primary ${}^7\text{Li}$ beam of 21.6 MeV. Neutrons of 37.2 MeV can also be generated at the primary target through the reaction ${}^9\text{Be}({}^7\text{Li},n)$. With this contaminant neutron beam, the reaction ${}^{12}\text{C}(n,\alpha)$ at the $(\text{CH}_2)_n$ target would produce an alpha particle around 28 MeV, consistent with the excess seen at $E_{\text{cm}} = 1.8$ MeV.

This experiment was performed at RIBRAS' main chamber, 2.25 times farther from the primary target than the central chamber, where the previous experiment was performed. Any contaminant neutron beam would have at least 5 times less intensity at main chamber than in the central chamber. Thus, the yield of alphas from the ${}^{12}\text{C}(n,\alpha)$ reaction would be considerably less in this experiment. This hypothesis would need further investigations as no study has been done for the behavior of contaminant neutron beams at RIBRAS System.

¹ There was a mistake in the data analysis of the previous experiment. In equation 1 of [41], the term $\frac{dE_{s_{\text{Li}}}}{dE_{\alpha}}$ is used to convert the yields after the transformation from $E(\alpha)$ to $E({}^8\text{Li})$, but this is already done by the term $\frac{dE}{dx}$. At figure 61 are shown the original data of [41] without the term $\frac{dE_{s_{\text{Li}}}}{dE_{\alpha}}$, thus different from figure 7.

A thin target experiment performed by Becchetti et al.[102] also measured this reaction for an energy² of $E_{cm} = 1.4$ MeV. Their result is also depicted at figure 61 and clearly agrees with those obtained at this experiment.

4.3 PROTON SPECTRA

The measured energy spectra extracted from the proton strips are shown at figure 62.

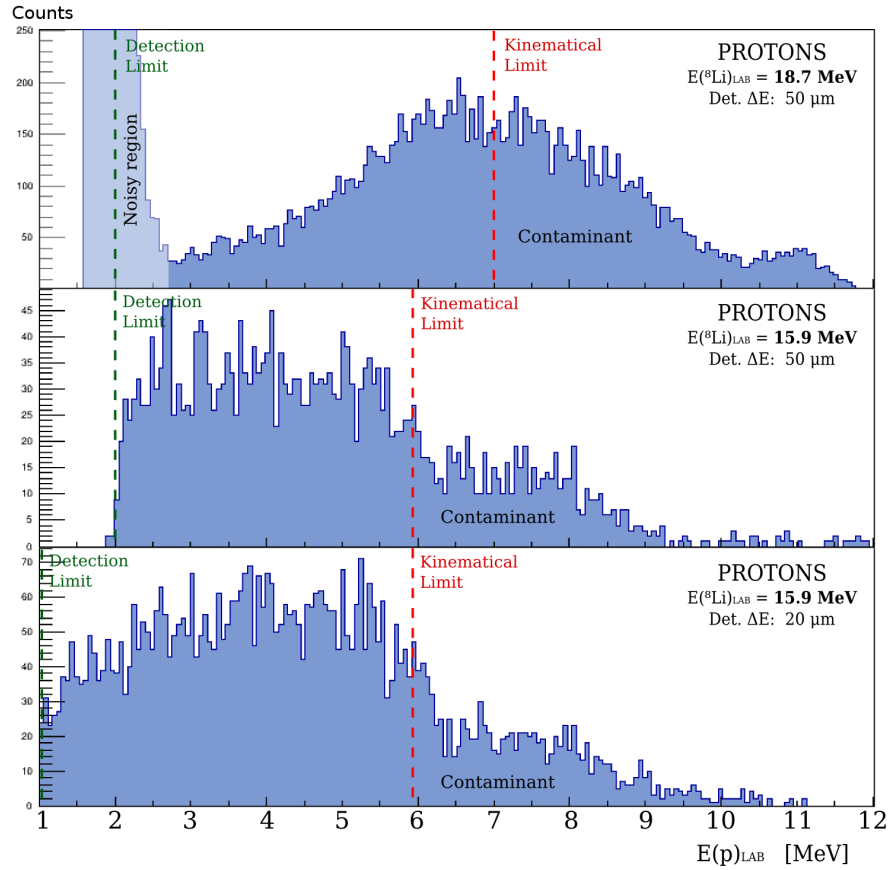


Figure 62: Energy spectra obtained with $(CH_2)_n$ target through the proton strips at each bombarding energy and detector configuration at $\theta_{lab} = 10^\circ$. Energy bin: $\delta E = 0.055$ MeV.

As mentioned, the proton spectra extend beyond the kinematical limits for the $^8Li(p,p)$ reaction. In the lower energy spectra, a sudden drop on the event count happens right in the kinematical limit for that energy. In the higher energy spectrum, a slight variation in the tendency also occurs in its kinematical limit. These are indications

² As [41] pointed out, there is a possible inconsistency of this energy. The authors argue that according to the beam energies and target thickness informed in the article, the measured energy should be $E_{cm} = 1.4$ MeV instead of 1.5 MeV [102]. This would not change the agreement between the results of [102] and those obtained through this experiment.

that relevant proton events are mixed with contaminant ones in the measured spectra.

4.3.1 Background

Contaminant protons that arrive in the $(\text{CH}_2)_n$ target also should appear in spectra taken with the ^{197}Au target. The spectra obtained with the ^{197}Au target are shown at figure 63, and a non-negligible background of protons can be observed at both incident energies.

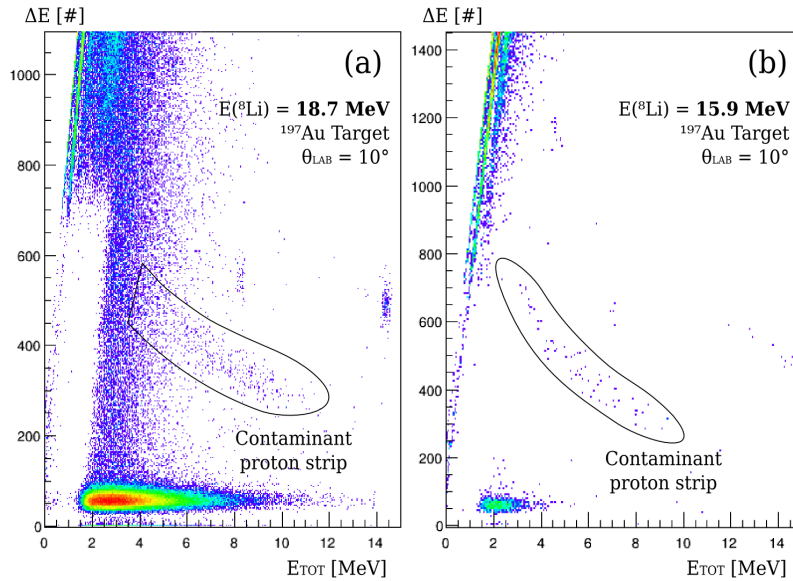


Figure 63: Spectra obtained with ^{197}Au target at both ^8Li beam energies of $E(^8\text{Li}) = 18.7 \text{ MeV}$ (a) and 15.9 MeV (b), putting into evidence the proton strips with the contaminants.

The origin of these contaminant protons may be from highly energetic protons produced at primary target that suffer multiple scattering at slits, collimators and blockers placed inside RIBRAS' beamline, or even from protons produced in the energy degrader placed at central chamber that manage to pass through second solenoid and reach the secondary target.

The spectra obtained with ^{197}Au target can be used to estimate the quantity of background protons to be subtracted from the measured spectra with $(\text{CH}_2)_n$ target. As the presence of contaminants is not a process occurring in the target, this correction must be done through a normalized subtraction in event count spectra.

Firstly, an energy conversion has to be performed between protons measured with ^{197}Au and $(\text{CH}_2)_n$ targets. Contaminant protons that arrive in the secondary target with the same energy will not appear with the same energy in the detected spectrum if they cross different targets. They would cross different amounts of material and lose different amounts of energy.

The energy of the protons measured with ^{197}Au target should be transformed to the energy they would have before the ^{197}Au target, and then transformed to the energy they would have after the $(\text{CH}_2)_n$ target. This is easily done with the code `stopx` (see appendix B).

Two normalizations due to difference in the yields are needed. The first one is to normalize the spectra by their expositions to the incident beam. It is reasonable to assume that the intensity of a contaminant beam is proportional to the intensity of the primary beam, which is directly measured through its integrated charge Q_{FC} in the Faraday Cup. So, the yields are divided by the integrated charge Q_{FC} during their respective acquisition runs.

As the exposure times of $(\text{CH}_2)_n$ targets were larger than those of the ^{197}Au target, the statistics obtained were quite different for the two targets. So it may be convenient to have different energy bin widths δE for the spectra obtained with each target. This gives rise to the second normalization: to compare both spectra they also should be normalized through their δE .

The normalized spectra for protons obtained with $(\text{CH}_2)_n$ and ^{197}Au targets are presented in figure 64 for the bombarding energy of $E(^8\text{Li}) = 15.9$ MeV. Also, the protons detected with the natural carbon target, analysed in the same way, are included in this figure.

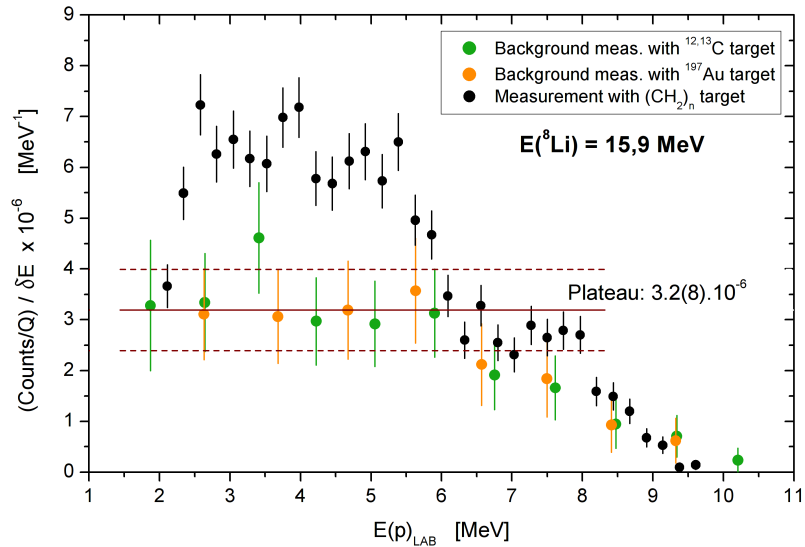


Figure 64: Spectra normalized by primary beam intensity and by energy bin width for protons detected with $(\text{CH}_2)_n$, natural carbon and ^{197}Au targets for the bombarding energy of $E(^8\text{Li}) = 15.9$ MeV.

The proton spectra detected with ^{197}Au and carbon targets are highly compatible, revealing that the protons that appear in the spectrum measured with carbon target are all contaminants present in the secondary beam and there is no sign of protons generated in reactions between the beam and the carbon nuclei present in the $(\text{CH}_2)_n$ target in the relevant energy region of the spectra.

The amount of contaminant protons with energies higher than the kinematical limit for ${}^8\text{Li}(p,p)$ is also compatible with the measured spectrum with $(\text{CH}_2)_n$ target, as expected. At energies lower than the kinematical limit, the contaminants seem to form a constant background, which can be subtracted from the spectrum taken with $(\text{CH}_2)_n$ target. After subtraction, the spectrum can be renormalized to the yield and the excitation function may be calculated.

In the case of the bidimensional spectrum obtained with ${}^{197}\text{Au}$ target at $E({}^8\text{Li}) = 18.7$ MeV, a large noisy region is present at $E(p)_{\text{lab}} \leq 5.0$ MeV, as can be seen at figure 63.a. This makes impossible the calculation of the ratio of protons of interest to contaminant protons in this low energy region. In this case, just a high energy part in which the contaminant protons are well defined can be obtained.

4.3.2 Final Spectra

The background subtraction generates a high systematic error in the final spectra, so a large energy bin size δE around 80 keV (in center-of-mass frame) was chosen.

The final excitation function is composed by the superposition of the spectra taken at both energies. Due to the contamination issues explained, the spectra taken at different energies do not overlap perfectly. The same weighted average procedure, done for the alpha excitation function, was done just for the two spectra measured at $E({}^8\text{Li}) = 15.9$ MeV.

The final excitation function for the proton decay channel is shown at figure 65. No previous measurement on the ${}^8\text{Li}(p,p)$ reaction in this energy range has been published so far.

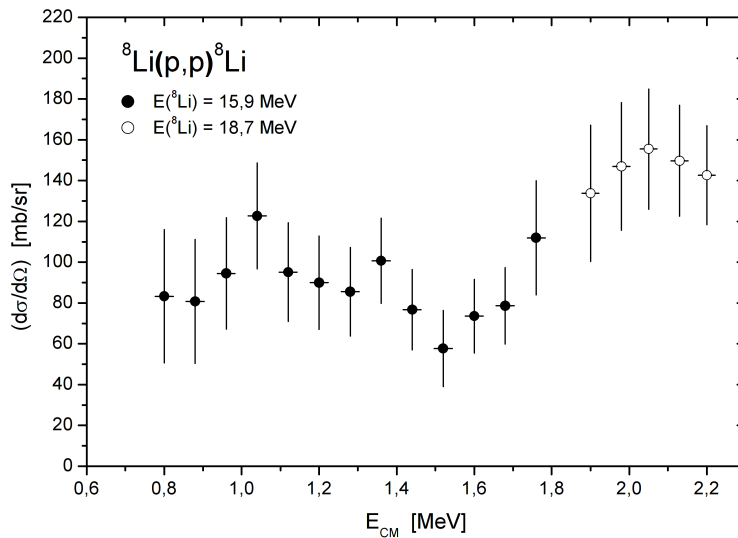


Figure 65: Complete excitation function for the ${}^8\text{Li}(p,p)$ reaction measured at $\theta_{\text{lab}} = 10^\circ$.

4.4 DEUTERON SPECTRA

The measured energy spectra with $(\text{CH}_2)_n$ target extracted from the deuteron strips are shown at figure 66.

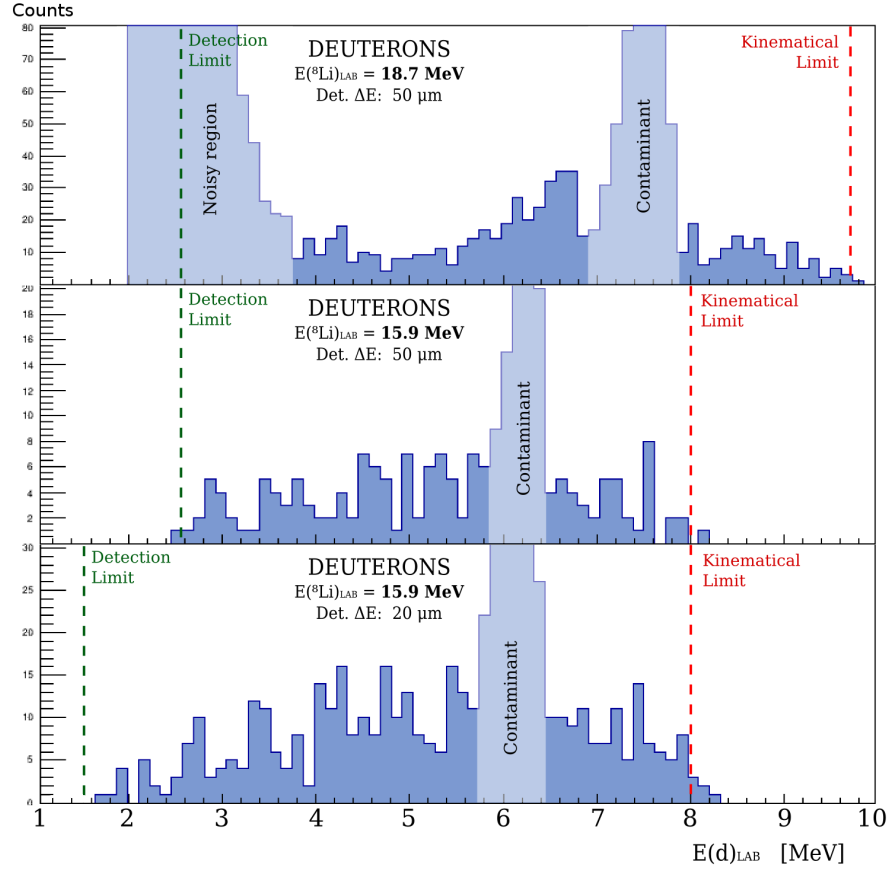


Figure 66: Energy spectra obtained with $(\text{CH}_2)_n$ target through the deuteron strips at each bombarding energy and detector configuration at $\theta_{\text{lab}} = 10^\circ$. Energy bin: $\delta E = 0.118 \text{ MeV}$.

The kinematical limits are respected, and just the position of the contaminant peak varies according to the incident energy. Besides the beam contamination, no deuteron was measured with natural carbon and ^{197}Au targets. Thus, no background correction is needed in the deuteron data.

A small peak can be identified at the spectrum obtained at $E(^8\text{Li}) = 18.7 \text{ MeV}$, but it is covered by the contaminant deuteron peak at the obtained at $E(^8\text{Li}) = 15.9 \text{ MeV}$.

4.4.1 Final Spectra and Previous Results

The chosen energy bin size δE was of 40 keV in center-of-mass frame. The excitation functions obtained at both energies and both detector configurations are all compatible with each other.

The complete excitation function is composed by a weighted average (by the statistical error) between the measurements where the excitation functions overlap and without the regions where the contaminant peak is present. The complete excitation function is shown at figure 67.

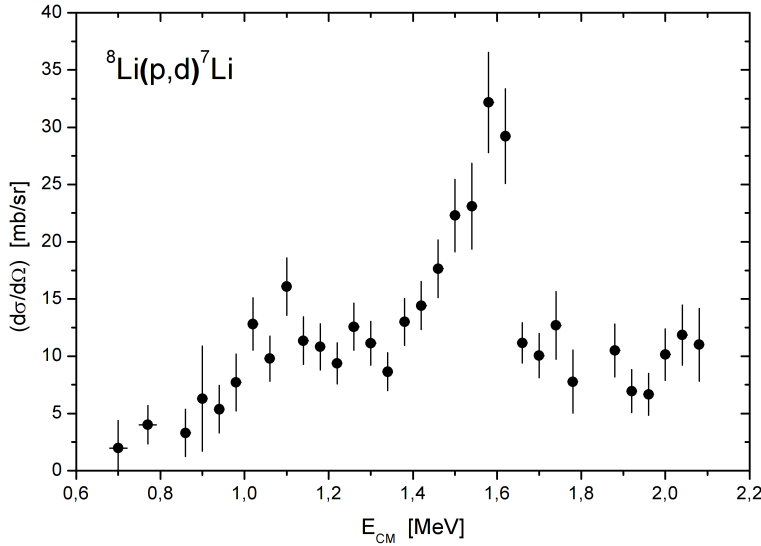


Figure 67: Complete excitation function for the ${}^8\text{Li}(p,d)$ reaction measured at $\theta_{\text{lab}} = 10^\circ$.

There is no previous measurement of the ${}^8\text{Li}(p,d)$ reaction in this energy range. A measurement was performed at $E_{\text{cm}} = 4.0$ MeV in inverse kinematics by a chinese group [103], the differential cross section measured at $\theta_{\text{cm}} = 160^\circ$ (about the same as this experiment) was 33(4) mb/sr

However, the inverse ${}^7\text{Li}(d,p){}^8\text{Li}$ reaction was measured by several groups [104, 105]. It is possible to deduce the integrated cross section for the inverse mechanism using the detailed balance theorem [43]:

$$\sigma_{{}^8\text{Li}(p,d)} = \left(\frac{k_{{}^7\text{Li}+d}}{k_{{}^8\text{Li}+p}} \right)^2 \frac{(2I_d + 1)(2I_{{}^7\text{Li}} + 1)}{(2I_p + 1)(2I_{{}^8\text{Li}} + 1)} \sigma_{{}^7\text{Li}(d,p)} \quad (51)$$

Upon the transformation to center-of-mass energy in the equivalent ${}^8\text{Li} + p$ system, and dividing the balanced integrated cross section to 4π in an approximation for differential cross sections, the ${}^7\text{Li}(d,p){}^8\text{Li}$ data can be compared to the ${}^8\text{Li}(p,d){}^7\text{Li}$ data, as shown in figure 68.

As can be seen, the ${}^8\text{Li}(p,d)$ data is comparable to the ${}^7\text{Li}(d,p)$ data. It should not be expected a perfect match due to the 4π approximation, but the orders of magnitude should be comparable. The structure at around $E_{\text{cm}} = 1.1$ MeV is reproduced by both sets of data,

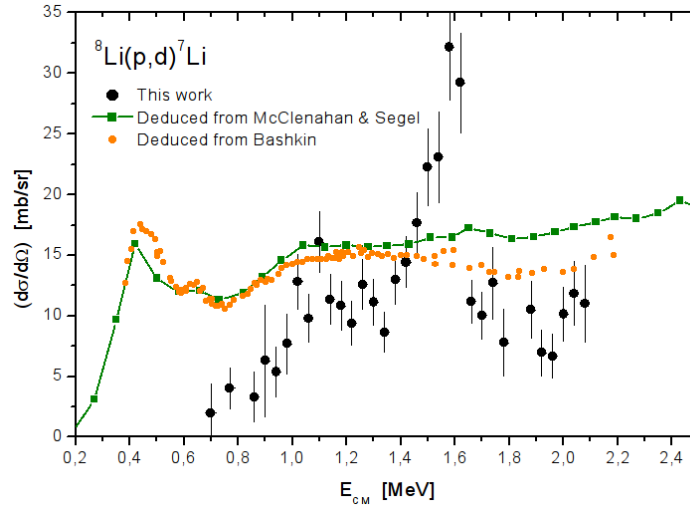


Figure 68: Excitation function for ${}^8\text{Li}(p,d){}^7\text{Li}$ reaction in comparison with the deduced from the inverse reaction measured by [104] and [105].

but not the peak at around $E_{\text{cm}} = 1.6$ MeV. In both data of [104] and [105] there is a slight rise from the baseline in the same position of the peak, but none of the authors reported it as a resonance.

One probable way this difference could happen is that in this resonance the population of the first excited state of ${}^7\text{Li}$ (0.477 MeV [106]) is dominant, thus it would not appear in the ${}^7\text{Li}(d,p){}^8\text{Li}$ data. Other considerations about this topic are made at section 4.6.

4.5 OTHER DECAY CHANNELS

The highly excited ${}^9\text{Be}$ nucleus has many open decay channels above the proton threshold (see figure 6). It is important to investigate also the other channels that could not be well explored through this experiment. Some data can still be extracted from the triton spectra and some information about the neutron and gamma decay channels is available in the literature.

4.5.1 Tritons

Besides alpha particles, protons and deuterons, it was also possible to observe a few tritons in the spectra.

In the spectrum measured at $E({}^8\text{Li}) = 18.7$ MeV (fig.51.a), the triton strip shows two contaminant peaks (at around $E(t) = 4$ and 13.5 MeV) and an almost constant yield between them. This constant yield does not show any reduction beyond the kinematical limit for the bombarding energy ($E(t) = 9.6$ MeV) unlike the deuteron and proton spectra, indicating that most of the detected tritons come from

contaminations. Tritons with energy between the two contaminant peaks were also detected in the spectrum measured with ^{197}Au target. Due to low statistics, a subtraction procedure like the one used for protons is not feasible.

However, in the spectra measured at incident energy $E(^8\text{Li}) = 15.9$ MeV (figs. 52 and 53), the triton yield is much lower than at the higher incident energy. The most energetic triton contaminant peak is broad and starts right after the kinematical limit ($E(t) = 8.0$ MeV). Also, there are no tritons in the ^{197}Au spectra between the two contaminant peaks. Even with very low statistics to testify it, it seems possible that there are very few contaminant tritons in the considered energy range.

Thereby, it is possible to analyse the triton spectrum at $E(^8\text{Li}) = 15.9$ MeV to determine a maximum value for the cross section, and to evaluate how relevant the $^8\text{Li}(p,t)^6\text{Li}$ reaction could be in comparison with other reactions. The excitation function obtained is shown at figure 69.

As can be seen, the maximum cross section of the triton excitation function 2.6(7) mb/sr, which is much lower than the measured for the other decay channels. Thus, the $t + ^6\text{Li}$ decay channel can be considered negligible if compared to the others.

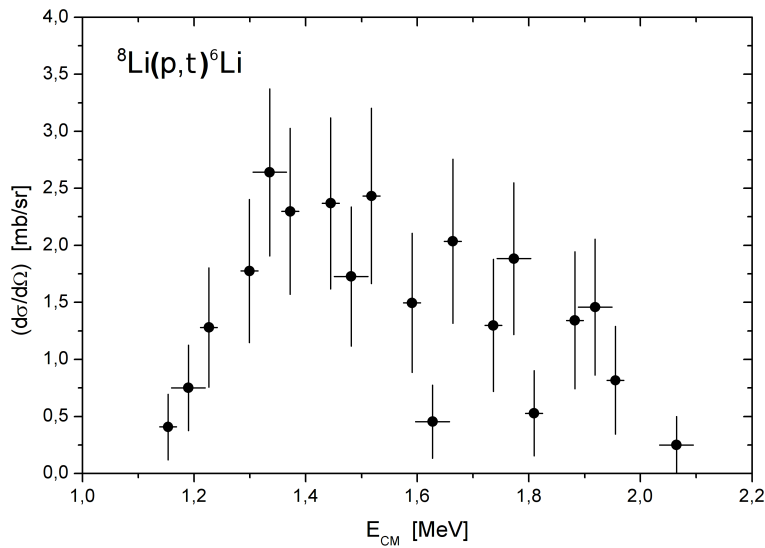


Figure 69: Excitation function for the $^8\text{Li}(p,t)^6\text{Li}$ reaction measured at $\theta_{\text{lab}} = 10^\circ$.

4.5.2 Neutrons and Gammas

One way of studying the $n + {}^8\text{Be}$ channel is to measure the α particles that are created in the decay of ${}^8\text{Be}$. However, as mentioned in section 4.2, these alphas are expected in an energy range covered by contaminants. Another way is to directly measure the neutrons, but this option was not available for this experiment.

An experiment with thin $(\text{CH}_2)_n$ target performed by D. Caussyn et al. [107] was able to measure an angular distribution for the ${}^8\text{Li}(p,n){}^8\text{Be}$ reaction at $E_{\text{c.m.}} = 1.5$ MeV. It is depicted at figure 70. As can be seen, at $\theta_{\text{c.m.}} \simeq 160^\circ$ a differential cross section of ~ 3 mb/sr should be expected.

This value is much lower than the differential cross section for the p , α and d channels at the same energy, and consequently the neutron decay channel is comparable to the triton channel, being both negligible.

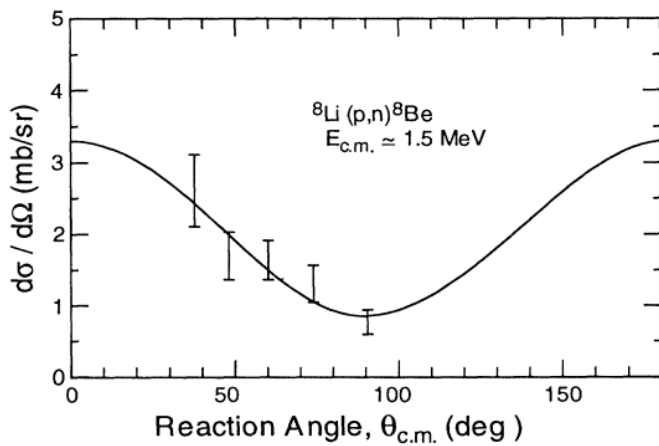


Figure 70: Differential cross section for the ${}^8\text{Li}(p,n)$ reaction at $E_{\text{c.m.}} = 1.5$ MeV measured by [107].

Gamma and beta channels usually have large lifetimes and low widths, thus they are probably negligible among the other decay channels at these high excitation energies. Information about the gamma decay channel could be obtained from the work of Su Jun et al. [26], in which the astrophysical S-factor for the ${}^8\text{Li}(p,\gamma){}^9\text{Be}$ (g.s.) reaction could be deduced from the analysis of the angular distribution of ${}^8\text{Li}(d,n){}^9\text{Be}$ (g.s.) reaction.

The calculated S-factor is shown at figure 71. The cross section between $E_{\text{c.m.}} = 1$ and 2 MeV would be around $7 \mu\text{b}$. This is a very indirect result and does not consider any resonance of the compound nucleus, also it does not consider the decay to other states of ${}^9\text{Be}$. This result is merely indicative on how much importance should be given to this channel.

As in the case of neutron and gamma channels there is no full excitation function available, it is not adequate to make strong assump-

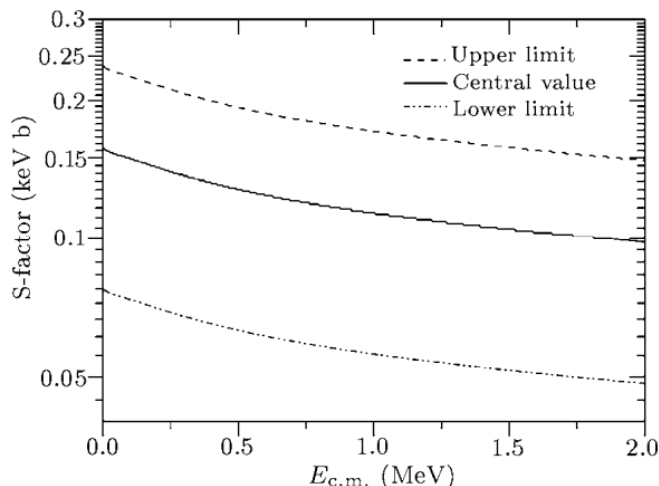


Figure 71: Calculated S-factor for the ${}^8\text{Li}(p,\gamma){}^9\text{Be}$ (g.s.) reaction done by [26].

tions about their behavior and their importance. The results from [107] and [26] were treated as evidences for the secondary role of these decay channels among those possible for ${}^9\text{Be}$ at the considered energy range. For simplicity, they were neglected in the subsequent analysis.

4.6 R-MATRIX ANALYSIS

The results of the measured excitation functions of all relevant decay channels is depicted at figure 72.

As can be seen, the positions of the broad peaks at deuteron and alpha excitation functions around $E_{\text{cm}} = 1.6$ MeV and of the resonance-like structure at the proton spectra are compatible with the position of ${}^9\text{Be}$ resonances at $E_r = 1.69(4)$ MeV and $E_r = 1.76(5)$ MeV ($E_x = 18.58(4)$ and $18.65(5)$ MeV, respectively).

Also, a peak in the deuteron excitation function at $E_{\text{cm}} \simeq 1.1$ MeV is compatible with the ${}^9\text{Be}$ resonance at $E_r = 1.13(5)$ MeV ($E_x = 18.02(5)$ MeV). The absence of any structure at this energy in the alpha excitation function suggests that this resonance does not decay by alpha emission.

As expected, the proton and deuteron measurements could not reach energies below $E_{\text{cm}} = 0.6$ MeV due to experimental limitations. At the alpha spectra, the statistics were not enough for a good description of the resonances at $E_r = 0.410(7)$ MeV and $0.605(7)$ MeV ($E_x = 17.298(7)$ and $17.493(7)$ MeV, respectively).

The great advantage of measuring several decay channels is to provide constraints on the analysis and reduce possible ambiguities from the previous work on ${}^8\text{Li}(p,\alpha)$ [41]. A R-matrix analysis was performed to obtain the spectroscopic parameters (widths, spins, pari-

E_r is the energy of the resonance in the excitation function, E_x is the excitation energy of the corresponding resonance among the ${}^9\text{Be}$ levels.

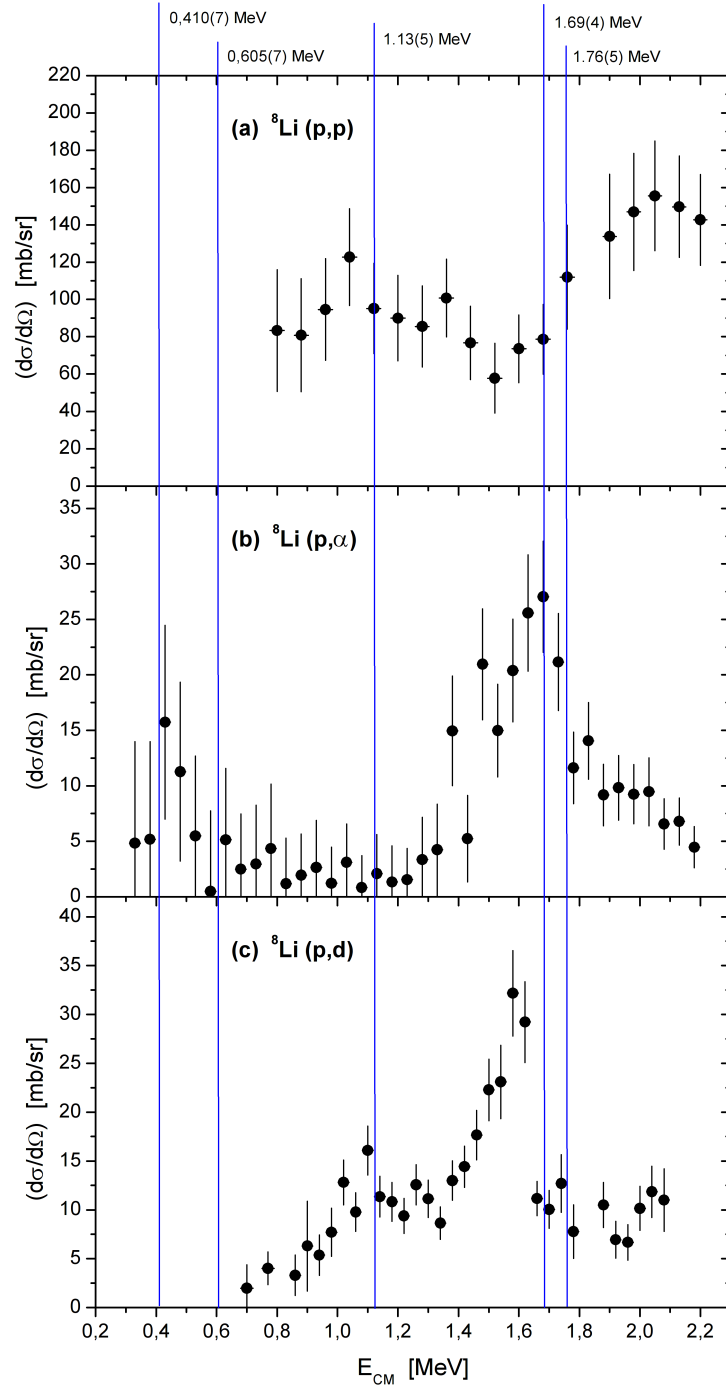


Figure 72: Measured excitation functions for the ${}^8\text{Li}(p,p)$ (a), the ${}^8\text{Li}(p,\alpha)$ (b) and the ${}^8\text{Li}(p,d)$ (c) reactions at $\theta_{\text{lab}} = 10^\circ$, with the energies of the ${}^9\text{Be}$ resonances found in the literature indicated (see table 1).

ties, etc.) of the ${}^9\text{Be}$ resonances measured, the software used was the code AZURE [108].

As there are evidences that the triton, neutron and gamma decay channels are not as important as the proton, alpha and deuteron channels, they were not considered in the calculations.

Depending on the channel and the resonance, several angular momenta ℓ may be consistent with spin couplings (see appendix C). For simplicity, a single set of (I, ℓ) was chosen for each resonance channel. The minimum possible ℓ was chosen as it should be the one with higher penetrability, and the channel spin I was chosen in order to optimize the R-matrix fit. The R-matrix channel radius used was $a = 5$ fm.

Initially, the parameters used in the R-matrix calculation were those found by [41] in the analysis of the ${}^8\text{Li}(p, \alpha)$ reaction. The resonances measured by [41] below $E_x = 17.5$ MeV ($E_r = -0.22, 0.38$ and 0.61 MeV) could not be well observed in this experiment, but were kept in the calculations for their possible background contributions, without any modification on their original parameters.

The table 1 summarizes the parameters in the literature; for convenience, it is reproduced here:

Table 5: (Copy of table 1) Available experimental data on ${}^9\text{Be}$ resonances near the ${}^8\text{Li} + p$ threshold (16.8882 MeV), including the compilation from [14] and the work of [41] on ${}^8\text{Li}(p, \alpha)$.

${}^9\text{Be}$ Res. E_x	Literature [14]				Previous Work - D. Mendes et al. [41]						
	E_r	$J^\pi; T$	Γ	Decay	E_r	J^π	$(I; \ell)$	Γ_p	Γ_α	Θ_p^2	Θ_α^2
15.97	-0.92(3)	$T = \frac{1}{2}$	~ 300	γ							
16.671	-0.217(8)	$(\frac{5}{2}^+); \frac{1}{2}$	41(4)	γ	-0.22	$\frac{5}{2}^+$	$(\frac{5}{2}; 0)$	550(100)	41(4)	19.7	0.3
16.9752	0.087(1)	$\frac{1}{2}^-; \frac{3}{2}^-$	0.389(10)	γ, n, p, d							
17.298	0.410(7)	$(\frac{5}{2}^-)$	200	γ, n, p, d, α	0.38(8)	$\frac{5}{2}^-$	$(\frac{5}{2}; 1)$	5(1)	180(50)	2.7	1.4
17.493	0.605(7)	$(\frac{7}{2}^+); \frac{1}{2}$	47	γ, n, p, d, α	0.61(3)	$\frac{7}{2}^+$	$(\frac{5}{2}; 2)$	1.4(4)	39(15)	3.5	0.3
18.02	1.13(5)			γ							
18.58	1.69(4)			γ, n, p, d, α	1.69(3)	$\frac{5}{2}^+$	$(\frac{5}{2}; 0)$	250(50)	430(80)	4.3	3.1
18.65	1.76(5)	$(\frac{5}{2}^-; \frac{3}{2}^-)$	300(100)	p	1.76(4)	$\frac{7}{2}^+$	$(\frac{3}{2}; 2)$	70(13)	420(80)	8.4	3.5
19.20	2.31(5)		310(80)	n, p, d, t							

Energies E in MeV, widths Γ in keV, dimensionless reduced widths Θ^2 in %. The relative uncertainties on the reduced widths are identical to those of the total widths.

R-matrix calculations with the parameters obtained by [41] for the proton and alpha channels are compared with the excitation functions measured in this experiment at figure 73. Even that the prediction for the ${}^8\text{Li}(p, p)$ reaction done in the previous experiment is good in order of magnitude and shape of the excitation function, it is evident that

some adjustments are necessary, and the deuteron channel must also be included.

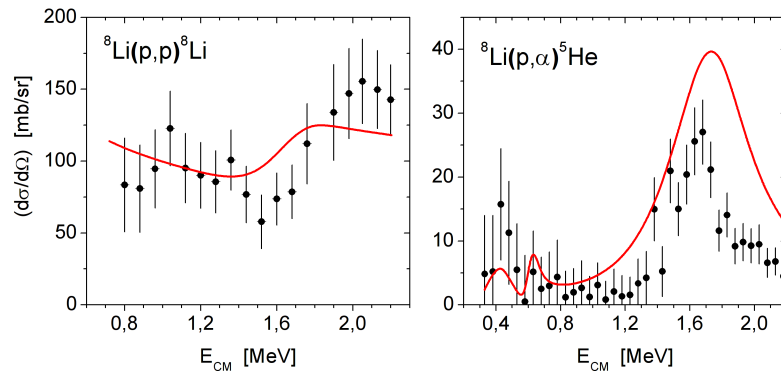


Figure 73: R-matrix calculations for proton and alpha channels using the parameters obtained by [41].

An immediate step is to assign deuteron partial widths to the broad resonances. In figure 74 are shown calculations in which both resonances at $E_{cm} = 1.69$ and 1.76 MeV decayed by deuteron emission with the same partial width Γ_d . The results of two calculations are shown in figure 74: with $\Gamma_d = 50$ keV (dashed line) and with $\Gamma_d = 200$ keV (solid line).

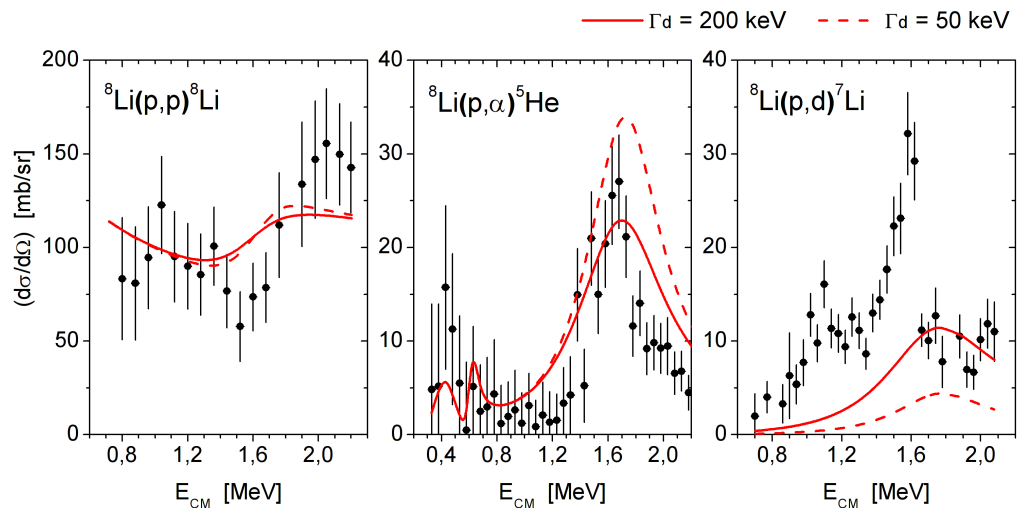


Figure 74: R-matrix calculations using the parameters obtained by [41] with the assignment of deuteron partial widths to the resonances at $E_{cm} = 1.69$ and 1.76 MeV. The same Γ_d was assigned to both resonances, and the results of two calculations are shown: $\Gamma_d = 200$ keV (solid) and $\Gamma_d = 50$ keV (dashed).

This approach clearly fails for the deuteron excitation function, in which the calculated peaks are shifted in energy, too small and too broad. This indicates that the parameters found in the work of [41] should be changed. However, the peak at $E_{cm} \simeq 1.1$ MeV, that was not observed in the alpha channel, should be investigated first, as it could provide new constraints for the calculation.

4.6.1 Resonance at $E_{cm} = 1.1$ MeV

The compilation of Tilley et al. [14] describes a poorly-known resonance at $E_x = 18.02(5)$ MeV among the energy levels of ${}^9\text{Be}$ that, following Tilley et al., decays only by gamma emission. However, an earlier compilation of Ajzenberg et al. [109] describes this resonance as decaying by gamma, neutron, proton and deuteron modes, and experiments measuring the reaction ${}^7\text{Li}(d,p)$ [104, 105] could also observe it. In this experiment, as well as in [41], no evidence of this resonance could be found in the ${}^8\text{Li}(p,\alpha)$ excitation function, which is also consistent with other works on the ${}^7\text{Li}(d,\alpha)$ reaction [110, 111].

In the excitation functions measured in this work, a prominent peak is present in the ${}^8\text{Li}(p,d)$ cross section at $E_{cm} \simeq 1.10$ MeV ($E_x = 17.99$ MeV, compatible with the reported 18.02(5) MeV from literature). In the proton excitation function, a slight rise around this energy can be noted, which is not a strong evidence due to large error bars.

The spin and parity J^π of this resonance is not known. A R-matrix analysis was performed with all possible J^π ; the most meaningful results are represented at figures 75 (for positive parities) and 76 (for negative parities). For visualization purposes, the calculations included an additional $5/2^+$ resonance³ at $E_{cm} = 1.76$ MeV to reproduce the proton excitation function, and the resonances below $E_{cm} = 0.8$ MeV for their background contributions (see table 1).

With $J^\pi = 1/2^\pm$, the calculation underestimates the height of the peak at $E_{cm} = 1.10$ MeV in the ${}^8\text{Li}(p,d)$ excitation function with any partial widths used in the calculation. With $J^\pi = 5/2^\pm$, on the contrary, the calculation was always too high with any partial widths used.

With $J^\pi = 3/2^\pm$, the peak at $E_{cm} = 1.10$ MeV in the ${}^8\text{Li}(p,d)$ excitation function could be well fit. However, the ${}^8\text{Li}(p,p)$ excitation function is not well reproduced with $J^\pi = 3/2^+$. Thus, $J^\pi = 3/2^-$ gives the best agreement with the ${}^8\text{Li}(p,d)$ and ${}^8\text{Li}(p,p)$ data. Considerations about the partial widths of this resonance are done at section 4.6.3.

³ The $J^\pi = 5/2^+$ for this resonance was assigned by reasons explained at section 4.6.2. The widths used were $\Gamma_p = 250$ keV, $\Gamma_\alpha = 50$ keV and $\Gamma_d = 0$.

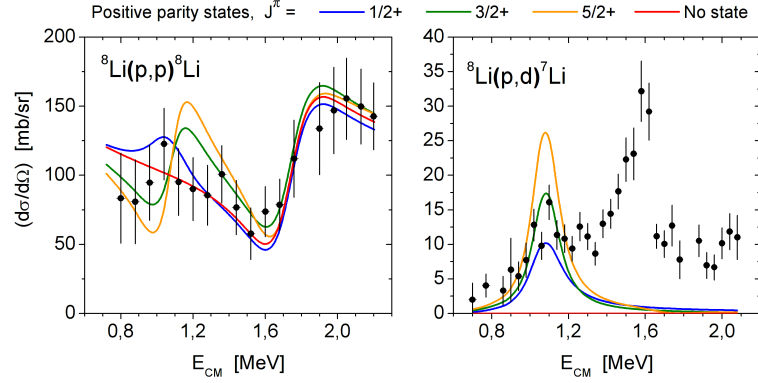


Figure 75: R-matrix analysis for a positive parity resonance at $E_{cm} = 1.10$ MeV with several total spins J^+ . Its partial widths were all set to $\Gamma_p = 100$ keV, $\Gamma_d = 50$ keV and $\Gamma_\alpha = 0$, except for the $J^\pi = 1/2^+$ resonance, in which $\Gamma_p = \Gamma_d = 100$ keV. A $5/2^+$ resonance at $E_{cm} = 1.76$ MeV in the ${}^8\text{Li}(p,p)$ excitation function was added for visualization purposes.

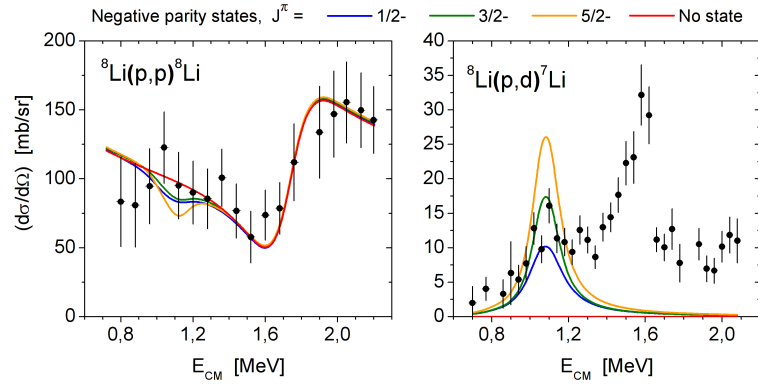


Figure 76: R-matrix analysis for a negative parity resonance at $E_{cm} = 1.10$ MeV with several total spins J^- . Its partial widths were all set to $\Gamma_p = 100$ keV, $\Gamma_d = 50$ keV and $\Gamma_\alpha = 0$, except for the $J^\pi = 1/2^-$ resonance, in which $\Gamma_p = \Gamma_d = 100$ keV. A $5/2^+$ resonance at $E_{cm} = 1.76$ MeV in the ${}^8\text{Li}(p,p)$ excitation function was added for visualization purposes.

4.6.2 Overlapping resonances at $E_{cm} \simeq 1.7$ MeV

In the previous work [41], the broad peak in the alpha spectrum was described by a $5/2^+$ resonance at $E_x = 18.58$ MeV overlapped with a $7/2^+$ resonance at $E_x = 18.65$ MeV. These overlapping resonances were necessary to describe the relatively high cross section and the large width of the peak. In this work, even if the alpha peak is com-

patible with a smaller width, it is still necessary to include both of these resonances to explain the three excitation functions.

$E_x = 18.65$ MeV resonance

In the work of [112] strong evidences are pointed that the 18.65 MeV resonance has the behavior of a $T = 3/2$ positive parity resonance, with total spin $1/2, 3/2, 5/2$ or $7/2$. A resonance with isospin $T = 3/2$ in ${}^9\text{Be}$ should decay only to ${}^8\text{Li} + p$, as the other decay modes ${}^5\text{He} + \alpha$ and ${}^7\text{Li} + d$ are not allowed by isospin conservation. So, it should be expected that the deuteron and alpha partial widths are zero or very small compared to the proton width.

In [14] a large total width of $\Gamma = 300(100)$ keV is assigned for this resonance.

A similar analysis with J^π variation was performed for this resonance comparing the calculations with the measured ${}^8\text{Li}(p,p){}^8\text{Li}$ data with the possible values pointed out in the analysis of [112]. The parameters from the literature were used: $T = 3/2$ ($\Gamma_\alpha = \Gamma_d = 0$) and $\Gamma_p = 300$ keV, and the overlapping resonance at $E_x = 18.58$ MeV was not included. The results are represented at figure 77.

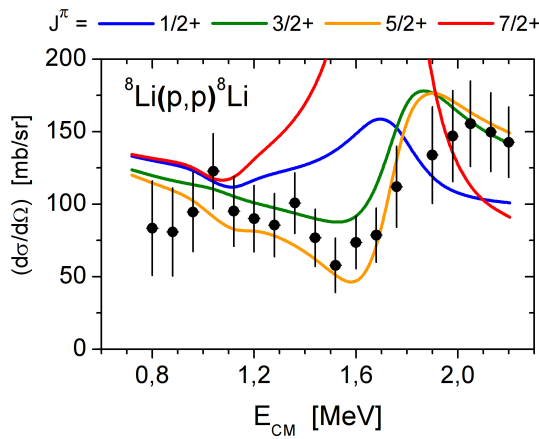


Figure 77: R-matrix analysis for a $T = 3/2$ positive parity resonance at $E_{cm} = 1.76$ MeV ($E_x = 18.65$ MeV) with several total spins J^+ . The widths were all set to $\Gamma_p = 300$ keV and $\Gamma_\alpha = \Gamma_d = 0$.

It is clear that $J^\pi = 1/2^+$ and $J^\pi = 7/2^+$ can be excluded due to the disagreement with the data. An ambiguity persists between $J^\pi = 3/2^+$ and $5/2^+$, but the inclusion of the other resonance at $E_x = 18.55$ MeV ($E_r = 1.66$ MeV) in the analysis may provide constraints to solve this issue.

$E_x = 18.55 \text{ MeV resonance}$

There is no other information in the literature about the $E_x = 18.58 \text{ MeV}$ resonance besides its energy. However, it should be expected that this resonance is responsible for the the peak around $E_{cm} \sim 1.6 - 1.7 \text{ MeV}$ in the deuteron and alpha excitation functions, which should be weakly populated from the broad $T = 3/2$ resonance at $E_x = 18.65 \text{ MeV}$.

As pointed out in section 4.4, this resonance could be barely observed in the data from experiments with the inverse mechanism ${}^7\text{Li}(d,p){}^8\text{Li}$ (see figure 68). The absence of a prominent peak like in the ${}^8\text{Li}(p,d)$ excitation function can only be explained by the preferential population of the first excited state of ${}^7\text{Li}$ (0.477 MeV , $J^\pi = 1/2^-$ [106]) from this resonance. Also, the peak in the deuteron spectrum is somewhat shifted, as its maximum is at $E_{cm} = 1.58 \text{ MeV}$ instead of 1.69 MeV , reinforcing this hypothesis.

This hypothesis was considered just for this resonance and just for the deuteron decay mode. In the case of ${}^8\text{Li}(p,p){}^8\text{Li}$ and ${}^8\text{Li}(p,\alpha){}^5\text{He}$ reactions, the population of the first excited state of ${}^8\text{Li}$ (0.98 MeV , $J^\pi = 1^+$ [14]) and ${}^5\text{He}$ (1.27 MeV , $J^\pi = 1/2^-$ [106]) is unlikely as they are at a quite higher excitation energy and the probability should drop exponentially due to the reduction in the penetrabilities. The work of [110] on the ${}^7\text{Li}(d,\alpha){}^5\text{He}$ reaction shows that the decay around the excitation energies of this resonance is much more likely to occur to the ground state of ${}^5\text{He}$.

Some important kinematical considerations must be done. One has to calculate the shift in the location of the observed peak in the deuteron energy spectrum and in the excitation function. Deuterons are produced with 0.95 MeV less energy (in the laboratory frame) in ${}^8\text{Li}(p,d){}^7\text{Li}^*$ than in ${}^8\text{Li}(p,d){}^7\text{Li}^{gs}$ at $\theta_{lab} = 10^\circ$. Taking into account the energy losses⁴, the same resonances populated in ${}^9\text{Be}$ decaying by ${}^7\text{Li}^* + d$ appear in the excitation function shifted to $E_{cm} - 0.225(2) \text{ MeV}$. See figure 78 for an example.

According to the comparison with the ${}^7\text{Li}(d,p){}^8\text{Li}$ data [104, 105] (see fig. 68 and related discussions), the ${}^7\text{Li}^* + d$ channel should be more important than the ${}^7\text{Li}^{gs} + d$ channel. To take it into account, an additional ${}^7\text{Li}^* + d$ channel was included in the calculations for the resonance at $E_x = 18.55 \text{ MeV}$.

A better agreement with the data was obtained with this resonance at $E_r = 1.66 \text{ MeV}$ ($E_x = 18.55 \text{ MeV}$), which is compatible with the value reported in the literature ($E_x = 18.58(4) \text{ MeV}$).

⁴ In this experiment, deuterons produced in the decay to ${}^7\text{Li}^{gs}$ and to ${}^7\text{Li}^*$ are indistinguishable. So, the whole deuteron spectra had to be converted from detected yield to experimental excitation function the same way. The conversion curve from detected $E(d)_{lab}$ to E_{cm} , which supposes the decay to the ground state of ${}^7\text{Li}$, was employed for the whole spectra (see figure 47). Also, the same jacobian was employed. The reaction $p({}^8\text{Li},d){}^7\text{Li}^*$ has a different $J(E,\theta)$ than $p({}^8\text{Li},d){}^7\text{Li}^{gs}$, but this difference is of $\sim 11\%$ in the energy of the resonance, thus still inside the error bar.

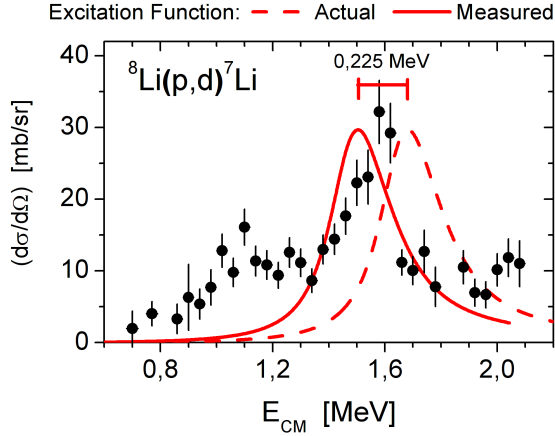


Figure 78: Observed shift in the excitation function of a ${}^9\text{Be}$ resonance which decays to ${}^7\text{Li}^* + \text{d}$.

A J^π analysis was done to this resonance. As there is an ambiguity between two possible J^π for the $E_x = 18.65$ MeV resonance, the analysis was done for both cases.

In all following calculations presented in figures 79, 80 and 81 the same partial widths were used, namely, $\Gamma_p = \Gamma_\alpha = \Gamma_{\text{d}+{}^7\text{Li}^*} = 70$ keV and $\Gamma_{\text{d}+{}^7\text{Li}^{9s}} = 10$ keV for the $E_x = 18.55$ MeV resonance, and $\Gamma_\alpha = \Gamma_d = 0$ and $\Gamma_p = 300$ keV for the $E_x = 18.65$ MeV resonance. The deuteron excitation function is presented as the sum of the calculations of the ${}^7\text{Li}^{9s} + \text{d}$ channel and ${}^7\text{Li}^* + \text{d}$ channel, with the proper energy shift for the last.

The R-matrix results for $J^\pi(18.65 \text{ MeV}) = 5/2^+$ are represented at figures 79 (for positive parities of $J^\pi(18.55 \text{ MeV})$) and 80 (for negative parities).

Among the results for positive parity resonance at $E_x = 18.55$ MeV and $J^\pi(18.65 \text{ MeV}) = 5/2^+$ (fig.79), all of the $J^+ \leq 7/2^+$ present cross sections too low for the alpha and deuteron channels. For the $J^\pi(18.55 \text{ MeV}) = 7/2^+$, any attempt in changing partial widths to increase the alpha peak impairs the proton excitation function. In this set, the $J^\pi(18.55 \text{ MeV}) = 9/2^+$ is at a fair agreement with the data; however other constraints will exclude this solution, as will be seen further.

In the negative parity group with $J^\pi(18.65 \text{ MeV}) = 5/2^+$ (fig.80), and with the partial widths used in the calculation no good results could be obtained. However, when changing the partial widths, good fits could be obtained with $J^\pi(18.55 \text{ MeV}) = 7/2^-$, as will be seen further.

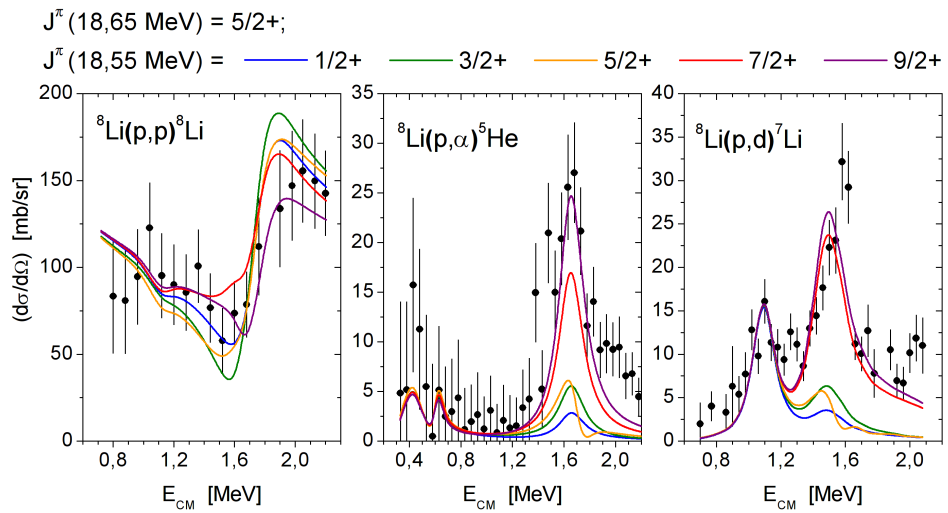


Figure 79: R-matrix calculations for a positive parity resonance at $E_{cm} = 1.66 \text{ MeV}$ ($E_x = 18.55 \text{ MeV}$) with several total spins J^+ and $J^\pi(18.65 \text{ MeV}) = 5/2^+$.

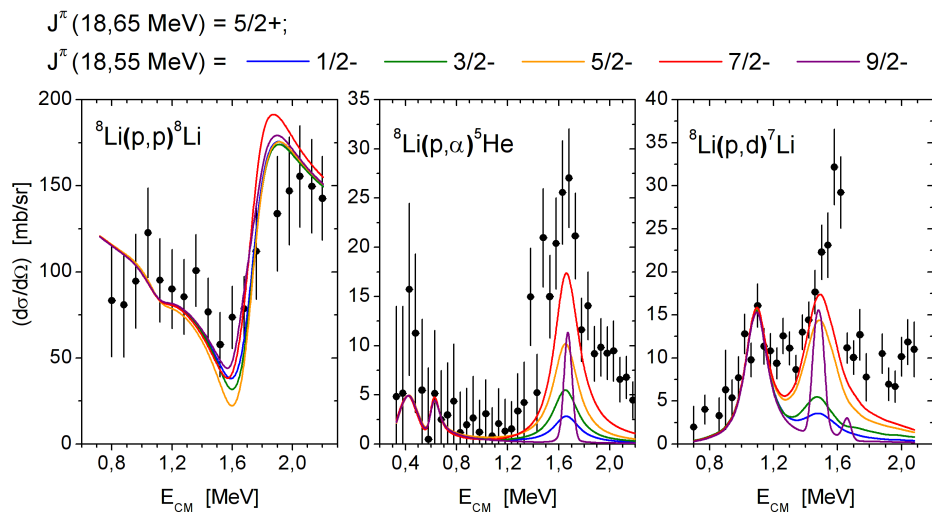


Figure 80: R-matrix calculations for a negative parity resonance at $E_{cm} = 1.66 \text{ MeV}$ ($E_x = 18.55 \text{ MeV}$) with several total spins J^- and $J^\pi(18.65 \text{ MeV}) = 5/2^+$.

The results for $J^\pi(18.65 \text{ MeV}) = 3/2^+$ are represented at figure 81. The results for $J \leq 5/2$ were omitted as they are similar to those for $J^\pi(18.65 \text{ MeV}) = 5/2^+$.

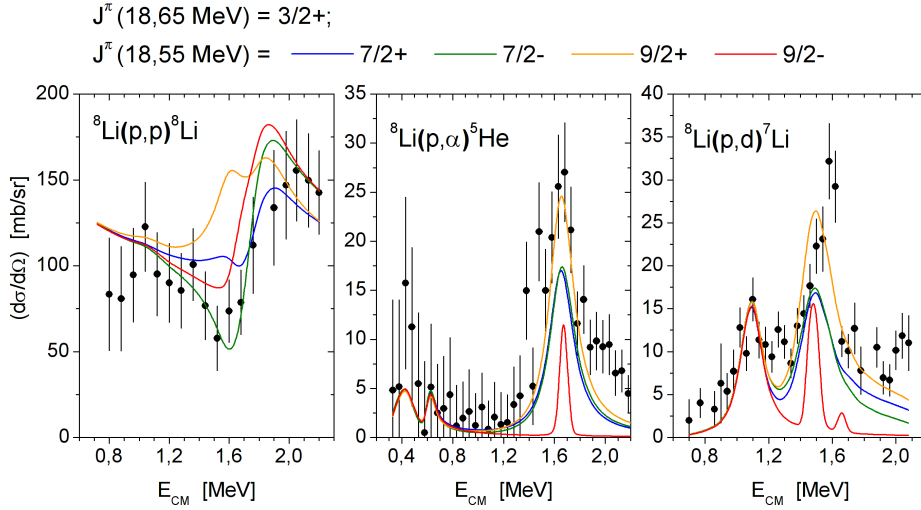


Figure 81: R-matrix calculations for a resonance at $E_{\text{cm}} = 1.66 \text{ MeV}$ ($E_x = 18.55 \text{ MeV}$) with several total spins J^π and $J^\pi(18.65 \text{ MeV}) = 3/2^+$.

Again, no good results could be obtained with the partial widths used. By changing the partial widths, the only good fit was obtained with $J^\pi(18.55 \text{ MeV}) = 7/2^-$, for $J^\pi(18.65 \text{ MeV}) = 3/2^+$.

For clarity, the pair (J_1^π, J_2^π) is defined as the J^π of $E_x = 18.55 \text{ MeV}$ resonance (J_1^π) together with the J^π of $E_x = 18.65 \text{ MeV}$ resonance (J_2^π).

Summing up, the analysis of (J_1^π, J_2^π) revealed that three J^π pairs may explain the measured data: $(7/2^-, 5/2^+)$, $(7/2^-, 3/2^+)$ and $(9/2^+, 5/2^+)$. The ambiguities among these three pairs are explored in the next section.

4.6.3 Widths, ambiguities and other considerations

The best fit for the resonance at $E_{\text{cm}} = 1.10 \text{ MeV}$ is shown at table 6. As mentioned, the value $J^\pi = 3/2^-$ is the one which gives the best agreement with the data and is preferred. Also, an alpha width of $\Gamma_\alpha = 5(5) \text{ keV}$ is still compatible with the measured data.

Table 6: Best R-matrix fit for the resonance at $E_{\text{cm}} = 1.10 \text{ MeV}$.

^9Be resonance			$^8\text{Li} + \text{p}$ channel			$^7\text{Li}^{9s} + \text{d}$ channel		
E_x	E_r	J^π	Γ_p	Θ_p^2	(L, ℓ)	Γ_d	Θ_d^2	(L, ℓ)
17.99(2)	1.10(2)	$3/2^-$	200	11.4	(3/2, 1)	50	1.5	(3/2, 0)

Energies E in MeV, widths Γ in keV, dimensionless reduced widths Θ^2 in %. The partial width for the $^5\text{He} + \alpha$ channel was set to zero.

For the overlapping resonances, $E_x = 18.55$ MeV and 18.65 MeV, three J^π pairs were identified as compatible with the data: $(7/2^-, 5/2^+)$, $(7/2^-, 3/2^+)$ and $(9/2^+, 5/2^+)$. As the width of the resonance at $E_x = 18.65$ MeV is larger than the distance between them, the arising of ambiguities in the analysis of the excitation functions is natural.

Many R-matrix calculations were performed to explore these ambiguities among all the J^π pairs. Some significant results are shown on figures 82, 83 and 84, while the parameters obtained in the fits are displayed in table 7.

χ_{red}^2 is the reduced chi-squared [101].

Table 7: R-matrix fits for the measured excitation functions, exploring the ambiguities between the two overlapping resonances.

Fit	${}^9\text{Be}$ resonance			${}^8\text{Li} + \text{p}$ channel			${}^5\text{He} + \alpha$ channel			${}^7\text{Li} + \text{d}$ channel [†]				χ_{red}^2
	E_x	E_r	J^π	Γ_p	Θ_p^2	(L, ℓ)	Γ_α	Θ_α^2	(L, ℓ)	Γ_d	Θ_d^2	(L, ℓ)	Mode	
(all)	17.99(2)	1.10(2)	$3/2^-$	200	11.4	$(3/2, 1)$	0	0	–	50	1.47	$(3/2, 0)$	${}^7\text{Li}^{9s}$	
1	18.55(5)	1.66(5)	$7/2^-$	200	6.2	$(5/2, 1)$	80	0.61	$(3/2, 2)$	80	12.3	$(3/2, 2)$	${}^7\text{Li}^*$	1.65
	18.65(4)	1.76(4)	$5/2^+$	300	5.0	$(5/2, 0)$	0	0	–	0	0	–		
2	18.55(5)	1.66(5)	$7/2^-$	100	3.1	$(5/2, 1)$	120	0.91	$(3/2, 2)$	120	18.4	$(3/2, 2)$	${}^7\text{Li}^*$	1.64
	18.65(4)	1.76(4)	$5/2^+$	300	5.0	$(5/2, 0)$	5	0.04	$(3/2, 1)$	5	0.20	$(3/2, 1)$	${}^7\text{Li}^*$	
3	18.55(5)	1.66(5)	$7/2^-$	60	1.9	$(5/2, 1)$	120	0.91	$(3/2, 2)$	150	23.0	$(3/2, 2)$	${}^7\text{Li}^*$	1.60
	18.65(4)	1.76(4)	$5/2^+$	300	5.0	$(5/2, 0)$	20	0.14	$(3/2, 1)$	20	0.80	$(3/2, 1)$	${}^7\text{Li}^*$	
4	18.55(5)	1.66(5)	$7/2^-$	200	6.2	$(5/2, 1)$	120	0.91	$(3/2, 2)$	120	18.4	$(3/2, 2)$	${}^7\text{Li}^*$	1.47
	18.65(4)	1.76(4)	$3/2^+$	350	5.8	$(3/2, 0)$	0	0	–	0	0	–		
5	18.55(5)	1.66(5)	$7/2^-$	100	3.1	$(5/2, 1)$	120	0.91	$(3/2, 2)$	120	18.4	$(3/2, 2)$	${}^7\text{Li}^*$	1.27
	18.65(4)	1.76(4)	$3/2^+$	350	5.8	$(3/2, 0)$	50	0.36	$(3/2, 1)$	50	2.0	$(1/2, 1)$	${}^7\text{Li}^*$	
6	18.55(5)	1.66(5)	$9/2^+$	75	10.4	$(5/2, 2)$	80	0.66	$(3/2, 3)$	70	93.9	$(3/2, 3)$	${}^7\text{Li}^*$	1.69
	18.65(4)	1.76(4)	$5/2^+$	330	5.5	$(5/2, 0)$	0	0	–	0	0	–		

Energies E in MeV, widths Γ in keV, dimensionless reduced widths Θ^2 in %. All of the fits also included the resonances below $E_{\text{cm}} = 0.8$ MeV for background (see table 1).

[†] - For simplicity, in the analysis performed, each channel was set to decay just by one mode of the deuteron channel, ${}^7\text{Li}^{9s}$ or ${}^7\text{Li}^*$.

For the spin-parity pair $(7/2^-, 3/2^+)$ (figure 83), a fair fit could be obtained considering the 18.65 MeV resonance a pure $T = 3/2$ resonance, with $\Gamma_d = \Gamma_\alpha = 0$ (fit 4).

In the case of the spin-parity pair $(7/2^-, 5/2^+)$ (figure 82), the fit 1, which considers $\Gamma_d = \Gamma_\alpha = 0$ for the 18.65 MeV ($T = 3/2$), has a too high peak at $E_{\text{cm}} \sim 1.8$ MeV in the ${}^8\text{Li}(p,p)$ excitation function. This disagreement could not be corrected by any change in the partial widths.

For both spin-parity pairs $(7/2^-, 5/2^+)$ and $(7/2^-, 3/2^+)$, allowing the $E_x = 18.65$ MeV resonance ($T = 3/2$) to have small Γ_d and Γ_α ,

but so that $\Gamma_d \ll \Gamma_p$ and $\Gamma_\alpha \ll \Gamma_p$, it is possible to obtain a better agreement with the data (see fits 2, 3 and 5).

However, a slight change in the Γ_d and Γ_α of the 18.65 MeV resonance causes some consequences in the Γ_p of the 18.55 MeV resonance in the Γ_p of the 18.55 MeV resonance (see the transition from fit 1 to fit 2 at table 7). This ambiguity between the proton width of the 18.55 MeV resonance and how strict the isospin conservation is taken for the 18.65 MeV resonance ($T = 3/2$) can be observed in both cases in which J^π of the 18.55 MeV resonance is $7/2^-$ (fits 1 to 5 in table 7).

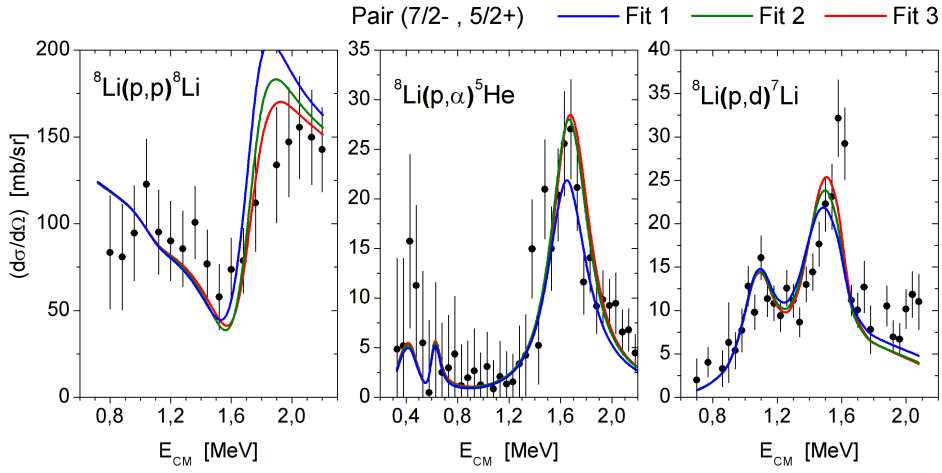


Figure 82: R-matrix fits considering the J^π pair ($7/2^-$, $5/2^+$) for the overlapping resonances (see table 7 for parameters).

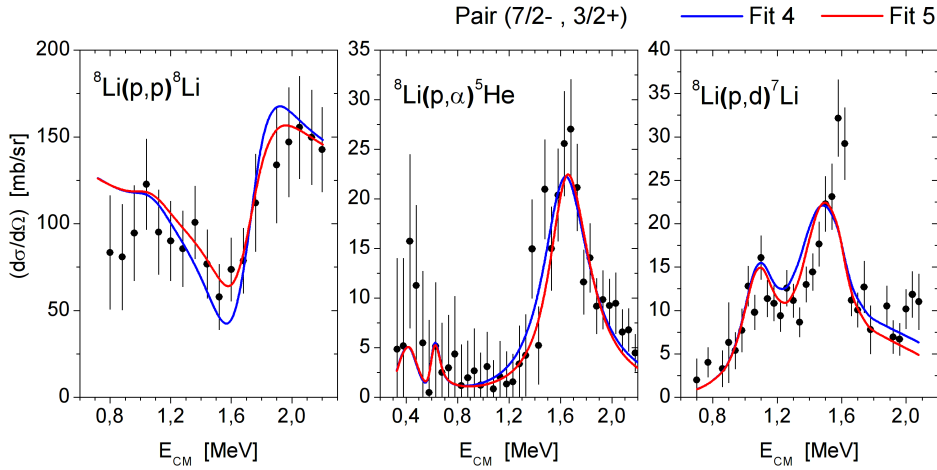


Figure 83: R-matrix fits considering the J^π pair ($7/2^-$, $3/2^+$) for the overlapping resonances (see table 7 for parameters).

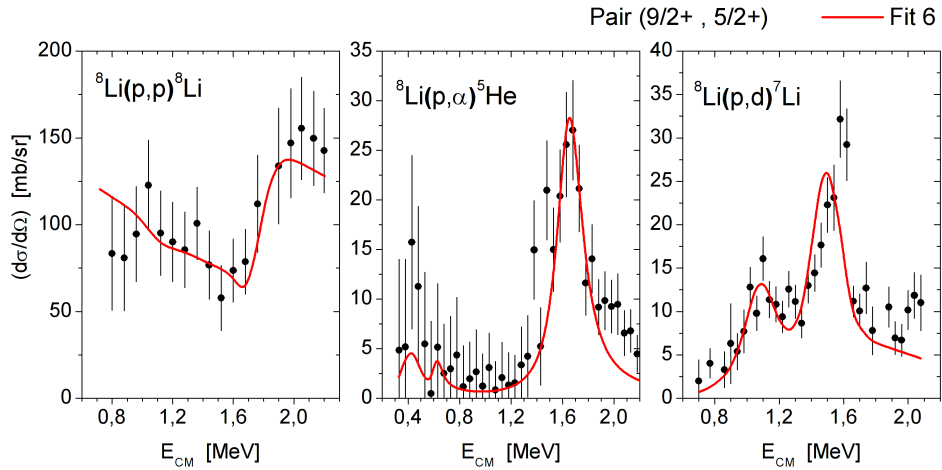


Figure 84: R-matrix fit considering the J^π pair ($9/2^+$, $5/2^+$) for the overlapping resonances (see table 7 for parameters).

If the J^π of the 18.55 MeV resonance is $9/2^+$ (pair ($9/2^+$, $5/2^+$), figure 84), the same ambiguity does not occur. The best fit found for this configuration (fit 6 at table 7) is very sensitive to small changes in the parameters. A very small Γ_d or Γ_α in the 18.65 MeV resonance impairs severely the agreement between the calculated cross section and the data for the three excitation functions.

However, for the 18.55 MeV resonance with $J^\pi = 9/2^+$, the lowest possible ℓ value is 3 in the deuteron channel, which results in a very low penetrability. The $\Gamma_d = 70$ keV, needed for the fit, results in a dimensionless reduced width of $\Theta_d^2 = 94\%$. This is too large and extremely unlikely. Therefore, $J^\pi = 9/2^+$ can be rejected for the 18.55 MeV resonance, which then should be a $7/2^-$ resonance.

It is also notable that, in all cases, the experimental cross section is higher than any R-matrix calculations for ${}^8\text{Li}(p,d)$ reaction in the region above $E_{\text{cm}} = 1.8$ MeV. This may be caused by the presence of a broad resonance reported at $E_r = 2.31$ MeV ($E_x = 19.2$ MeV, $\Gamma = 310(80)$ keV [14]) which was not included in the calculations.

Moreover, the drop in the cross section below $E_{\text{cm}} \leq 0.95$ MeV in the proton excitation function could not be described in the R-matrix analysis. It may correspond to the loss of protons at low energies due to non-uniformities in both target and in the ΔE silicon detector. As these energies are very close to the detection limit of protons, some may not be able to cross the ΔE detector, and the yields in this energy region may be underestimated. The deuteron excitation function is also subject to this problem at energies close to the detection limit.

The simultaneous measurement of the proton, alpha and deuteron decay channels and the four-channel R-matrix calculation with AZURE has allowed the determination of many unknown parameters of the ${}^9\text{Be}$ resonances in this energy region. The table 8 summarizes the final results that could be obtained from this analysis.

Table 8: Parameters of the measured ${}^9\text{Be}$ resonances obtained from the R-matrix analysis of this work.

E_x	E_r	J^π	Γ_p	Γ_α	Γ_d (${}^7\text{Li}^{gs}$)	Γ_d (${}^7\text{Li}^*$)
17.99(2)	1.10(2)	$3/2^-$	200(60)	5(5)	50(20)	–
18.55(5)	1.66(5)	$7/2^-$	120(70)	120(20)	–	130(30)
18.65(4)	1.76(4)	$5/2^+$ or $3/2^+$	320(30)	25(25)	–	25(25)

Energies E in MeV, widths Γ in keV. Uncertainties on widths roughly estimated through the variation of the parameters along several fits.

4.7 ASTROPHYSICAL REACTION RATE

The angle integrated cross section and the astrophysical S-factor can be obtained from the R-matrix calculations. Both were calculated for astrophysically relevant reactions ${}^8\text{Li}(p,\alpha)$ and ${}^8\text{Li}(p,d)$ using the best fit for each J^π pair, selected by the least χ^2_{red} . They are displayed at figure 85.

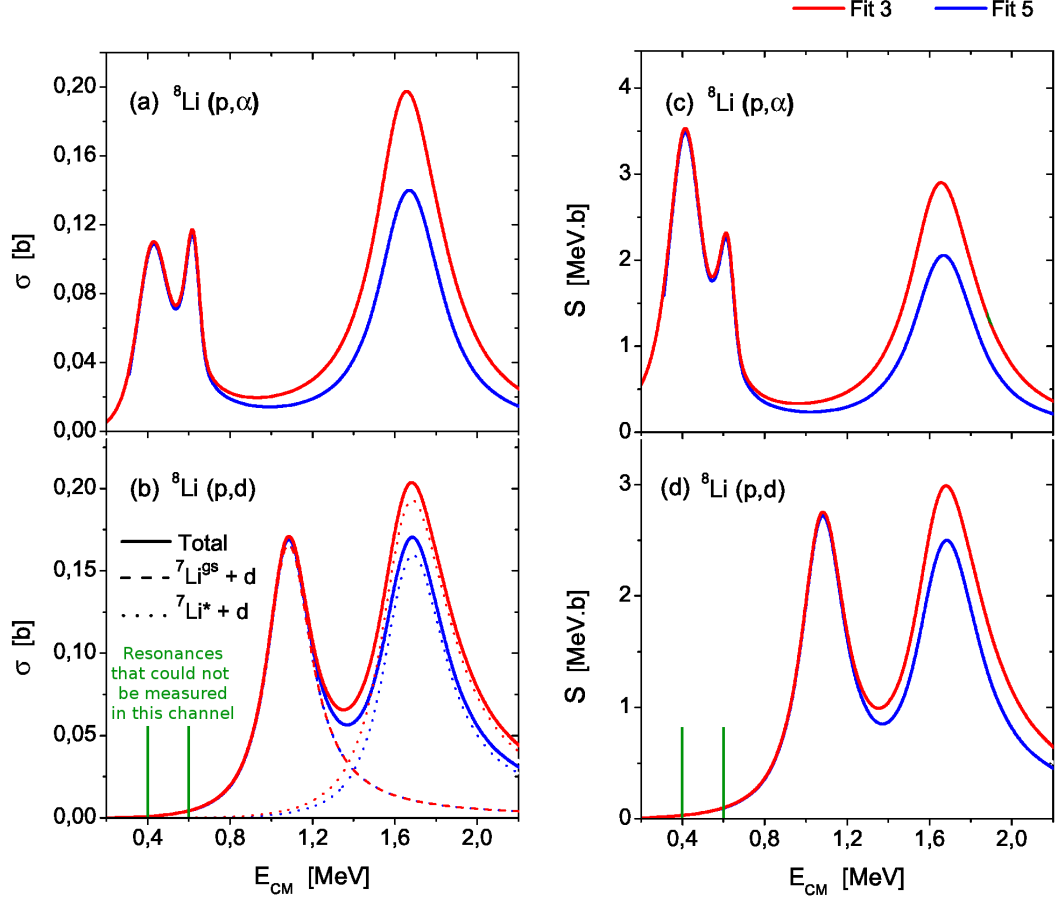


Figure 85: Integrated cross section (left column) and S-factor (right column) for the ${}^8\text{Li}(p,\alpha)$ and ${}^8\text{Li}(p,d)$ reactions obtained from the R-matrix fits.

The calculation of reaction rates was done by the code AZURE through numerical integration of equation 14 with the calculated cross section. The two ${}^8\text{Li}$ consuming reactions were studied, ${}^8\text{Li}(p,\alpha)$ and ${}^8\text{Li}(p,d)$, and the obtained results are shown at figure 86. The R-matrix fit used in this calculation was the number 3 (see table 7), but the others produce very close results.

The reaction rate for the ${}^8\text{Li}(p,d)$ reaction may be underestimated as the deuteron partial widths of the resonances at $E_{\text{cm}} = 0.38$ MeV and 0.61 MeV were not included in this analysis (see references [104, 105] and figure 68). The reaction rate for ${}^8\text{Li}(p,\alpha)$ is less than the

found in the previous work [41] (see fig. 8), mainly due to the narrower alpha peak measured at around $E_{cm} = 1.7$ MeV in the present work.

As can be seen, at BBN temperatures ($T \leq 1.1 \cdot 10^9$ K [113]) the ${}^8\text{Li}(p,\alpha)$ is probably more efficient than the ${}^8\text{Li}(p,d)$ reaction on destroying the available ${}^8\text{Li}$. At r-process temperatures (from $T = 2.5 \cdot 10^9$ K to $5 \cdot 10^9$ K [113]) the two reactions may have a comparable role. However, a better description could only be provided with the measurement of the resonances at $E_{cm} = 0.38$ MeV and 0.61 MeV in the deuteron channel.

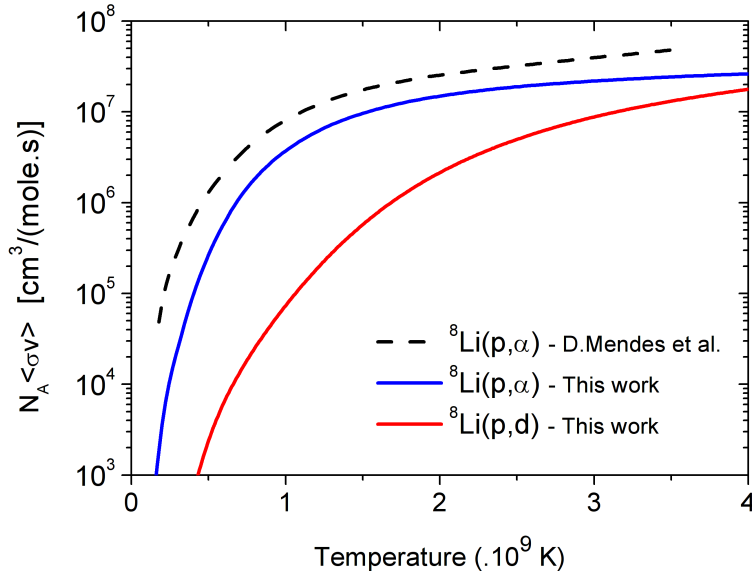


Figure 86: Calculated reaction rates for the reactions ${}^8\text{Li}(p,\alpha)$ and ${}^8\text{Li}(p,d)$. The rate for ${}^8\text{Li}(p,d)$ reaction is probably underestimated as the resonances at $E_{cm} = 0.38$ MeV and 0.61 MeV could not be measured in this work.

CONCLUSIONS AND OUTLOOK

In this work, the proton-induced reactions ${}^8\text{Li}(p,p)$, ${}^8\text{Li}(p,\alpha)$ and ${}^8\text{Li}(p,d)$ were measured in inverse kinematics between $E_{\text{cm}} = 0.7$ and 2.2 MeV.

A highly pure ${}^8\text{Li}$ beam selected by the RIBRAS System in the Pelletron Laboratory (IF-USP), São Paulo, was used impinging on a thick target made of polyethylene $((\text{CH}_2)_n)$, a hydrogen-rich plastic. The thick target inverse kinematics method was used, in which the beam slows down inside the target and performs reactions in a wide energy range, until it stops. The ejectiles were detected at $\theta_{\text{lab}} = 10^\circ$ by a $E - \Delta E$ telescope formed by silicon surface barrier detectors.

From the measured yields of protons, alphas and deuterons, the excitation functions for the three reactions could be obtained. Some corrections were needed to subtract the contribution of contaminant protons and to isolate the pure two-body $\alpha + {}^5\text{He}$ decay from the alpha spectra. The possible contribution of contaminant reactions between the ${}^8\text{Li}$ beam and the carbon present in the $(\text{CH}_2)_n$ target were considered negligible after measurements with a natural carbon target.

A maximum cross section of 2.6(7) mb/sr could be determined for the ${}^8\text{Li}(p,t){}^6\text{Li}$ reaction between $E_{\text{cm}} = 1.1$ and 2.1 MeV. This value is much lower than the values measured for the other reactions, so the triton decay channel was neglected in the calculations. Evidences were found in the literature that other decay channels like gamma and neutron are also less important.

The excitation functions obtained were consistent with previous measurements found in the literature. Three ${}^9\text{Be}$ resonances could be identified: at excitation energies of $E_x = 17.99(2)$, 18.55(5) and 18.65(4) MeV, all compatible with the values found in the literature (18.02(5), 18.58(4) and 18.65(5), respectively). The data were analysed through the R-matrix methodology using the program AZURE.

The resonance at $E_x = 17.99(2)$ MeV was observed in the ${}^8\text{Li}(p,d)$ excitation function; it is a $3/2^-$ resonance which decays mainly in the proton and deuteron channels. It has a proton partial width of 200(60) keV and a deuteron partial width of 50(20) keV. The absence of any structure at this energy in the alpha excitation function suggests that this resonance does not decay by alpha emission.

The other two, at $E_x = 18.55(5)$ and 18.65(4) MeV, are overlapping resonances, in which the width of the resonance at $E_x = 18.65(4)$ MeV is larger than the separation between them. They appear as a single broad peak in the measured spectra of each reaction. However, it is

impossible to explain the measured excitation functions by only one single resonance.

The J^π of the $E_x = 18.55(4)$ MeV resonance was determined as $7/2^-$, but a possible ambiguity persists between $5/2^+$ and $3/2^+$ for the resonance at $18.65(4)$ MeV.

The decay of the $E_x = 18.65(4)$ MeV resonance should be mostly through proton emission, whose partial width was evaluated as $320(30)$ keV. The isospin of this resonance is reported in the literature as $T = 3/2$, then the alpha and deuteron partial widths should be strictly zero for a pure $T = 3/2$ resonance. If the isospin conservation is strictly observed, the ambiguity between $J^\pi(18.65\text{MeV}) = 3/2^+$ and $5/2^+$ breaks down. Only $J^\pi = 3/2^+$ provides a good fit with $\Gamma_\alpha = \Gamma_d = 0$.

The alpha and deuteron partial widths of the $E_x = 18.55(5)$ MeV resonance were determined as $120(20)$ keV and $130(30)$ keV, respectively. Meanwhile, the proton width was found to be dependent on the J^π of the $18.65(4)$ MeV resonance and on how strict the isospin conservation is for the $E_x = 18.65(4)$ MeV resonance. Concerning the deuteron decay channel of the $E_x = 18.55(5)$ MeV resonance, evidences were found that it should decay mostly to the first excited state of ${}^7\text{Li}$, since it was not observed in the ${}^7\text{Li}(d,p){}^8\text{Li}$ reaction.

Possibly, the effect of a broad resonance at $E_x = 19.20(5)$ MeV, reported in the literature, was also observed as a tail in the high energy part ($E_{\text{cm}} \geq 1.8$ MeV) of the ${}^8\text{Li}(p,d)$ excitation function.

This simultaneous measurement of the proton, deuteron and alpha decay channels and the four-channel R-matrix calculations with AZURE have provided several parameters of ${}^9\text{Be}$ structure at high excitation energies that were previously unknown, such as spins, parities and partial widths of resonances around the proton threshold.

The relevant consequences on astrophysics of the ${}^8\text{Li}(p,\alpha)$ and ${}^8\text{Li}(p,d)$ reactions were also briefly studied. The reaction rates calculated for both reactions indicate that the ${}^8\text{Li}(p,\alpha)$ reaction should be much more efficient in the destruction of ${}^8\text{Li}$ during the Big Bang nucleosynthesis than the ${}^8\text{Li}(p,d)$ reaction, but the two may have a comparable role in a r-process scenario. However, the calculated reaction rate for ${}^8\text{Li}(p,d)$ reaction may be considerably underestimated since the resonances at $E_x = 17.298$ MeV and 17.493 MeV could not be measured in this experiment and, thus, were not included in the calculations.

This work could be improved and extended. Firstly, the measurement of the excitation functions with better statistics and at other scattering angles could help solving the ambiguity in J^π and reduce the error bars in partial widths.

A magnetic shielding in the central chamber could increase the efficiency of the MCP detector operating between the two solenoids. This

would allow the full implementation of the time-of-flight technique and then useful events could be easily discriminated from contaminant background, improving the accuracy of measurements.

The use of a thinner ΔE detector (such as gaseous detectors) could also eliminate the possible problem of yield loss of protons and deuterons for $E_{cm} \lesssim 0.95$ MeV and could even extend the measurable excitation functions to lower energies. Moreover, the resonances at $E_x = 17.298$ MeV and 17.493 MeV could be measured in the deuteron channel and a better description of the astrophysical role of the ${}^8\text{Li}(p,d)$ reaction could be provided.

The measurement of the inelastic ${}^8\text{Li}(p,p'){}^8\text{Li}^*$ reaction could provide further information about the ${}^9\text{Be}$ resonances around the proton threshold. There is also the possibility to measure the ${}^8\text{Li}(p,n)$ reaction if the large area neutron detector available in the Pelletron Laboratory becomes operational.

APPENDIX

REACTION KINEMATICS

In a fixed target experiment, a projectile nucleus (1) from the accelerated beam impinges on a fixed target nucleus (2). In a binary reaction $X_2(X_1, X_3)X_4$, the two interacting nuclei can form two other particles (3 and 4). It is usual to call the detected reaction product (3) as the ejectile or scattered nucleus and the other (4) as the recoiling nucleus. This two-body process is depicted at figure 87.

For more detailed discussions and deductions, see references [114], [43] and [5].

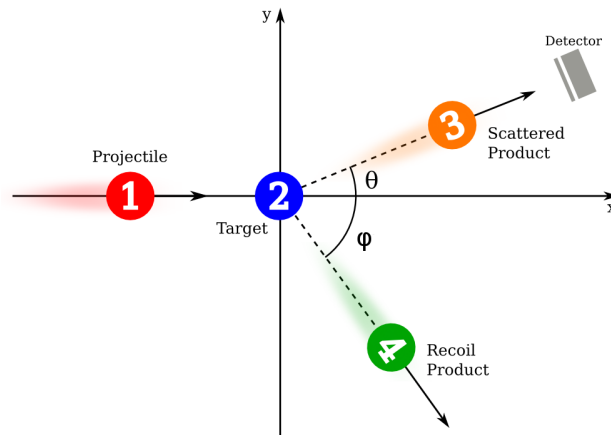


Figure 87: Scheme of collision geometry involved in a nuclear reaction in the laboratory frame.

Given the bombarding kinetic energy E_1 of the projectile, it is important to know what to expect from the scattered reaction product at a given detection angle θ from the beam's direction.

The total energy of the system must be conserved, as expressed in the equation below. Part of the initial energy E_{1+2} of the system may be used in the excitation of internal states E_{lev} of the reaction products, and this should be accounted in the final kinetic energy of the system E_{3+4} .

$$(m_1c^2 + E_1) + (m_2c^2 + E_2) = (m_3c^2 + E_3) + (m_4c^2 + E_4) + E_{lev}$$

$$((m_1 + m_2) - (m_3 + m_4)) \cdot c^2 - E_{lev} = (E_3 + E_4) - (E_1 + E_2) \quad (52)$$

Here comes the concept of the Q-value, which is the amount of energy released (if $Q > 0$) or retained ($Q < 0$) during the reaction. It is defined either as the difference of kinetic energy between the initial and final systems (right hand of equation 52):

$$Q = E_{3+4} - E_{1+2} \quad , \quad (53)$$

E_i , m_i and \vec{p}_i are the kinetic energy, the mass and the moment of the particle i . θ and ϕ are the scattering angles of the product nuclei 3 and 4, respectively.

or as the mass excess between the initial and final systems (left hand of equation 52), also considering how much of this mass excess was employed in the excitation of any reaction product:

$$Q = ((m_1 + m_2) - (m_3 + m_4)) \cdot c^2 - E_{lev} \quad . \quad (54)$$

When the reaction is an elastic scattering, the final products are the same as the initial particles, then $Q = 0$. When $Q \geq 0$ (exoergic reaction), the reaction can occur at any incident energy. Particularities when $Q < 0$ are not explored as no reaction relevant for this work fits this characteristic, but some considerations can be found in the references indicated in the beginning of this chapter.

There may be a reasonable probability that the ejectile nuclei are produced at excited states, then $E_{lev} \neq 0$, mainly for those whose first excited states are very close to the ground state. One good example is the secondary beam production reaction employed at this experiment: ${}^9\text{Be}({}^7\text{Li}, {}^8\text{Li})$. The ${}^8\text{Li}$ may be produced at its ground state or in its first excited state ($E_{lev} = 0.9808$ MeV [14]).

In the laboratory frame, the kinetic energy E_2 of the fixed target nucleus is zero, and its momentum \vec{p}_2 as well. In this case, the equations for conservation of energy and momentum can be written as:

$$E_1 + Q = E_3 + E_4 \quad , \quad (55)$$

$$\vec{p}_1 = \vec{p}_3 + \vec{p}_4 \quad . \quad (56)$$

As particle 3 is the relevant ejectile, it is convenient to isolate the terms dependent on particle 4. Even more convenient is to work with the magnitudes p_i of the momentum vectors by taking their scalar product with themselves:

$$\vec{p}_4 \cdot \vec{p}_4 = (\vec{p}_1 - \vec{p}_3) \cdot (\vec{p}_1 - \vec{p}_3) \quad ,$$

and by applying the cossines law, the dependence on the detection angle θ becomes clear:

$$p_4^2 = p_1^2 + p_3^2 - 2p_1 p_3 \cos\theta \quad . \quad (57)$$

At the energies employed at this experiment, relativistic effects are negligible. By applying the classical approximation $p^2 = 2mE$ and equation 55 to equation 57, it is possible to establish a kinematic relation between E_3 and E_1 that, after some manipulations, is given by:

$$\left(\frac{m_3}{m_4} + 1\right) E_3 - \left(2 \frac{\sqrt{m_1 m_3 E_1}}{m_4} \cos\theta\right) \sqrt{E_3} + \left(\frac{m_1}{m_4} E_1 - (E_1 + Q)\right) = 0 \quad . \quad (58)$$

This is a quadratic equation in $\sqrt{E_3}$, which admits two solutions:

$$\begin{aligned}
E_3 &= \left(\sqrt{E_3}\right)^2 \\
&= \left(\frac{\sqrt{m_1 m_3 E_1}}{m_3 + m_4} \cos\theta \pm \frac{\sqrt{m_1 m_3 E_1 \cos^2\theta + (m_3 + m_4) [m_4 Q + (m_4 - m_1) E_1]}}{m_3 + m_4}\right)^2
\end{aligned} \tag{59}$$

At figure 88 are presented the solutions of equation 59 for each of the relevant reaction products of this work.

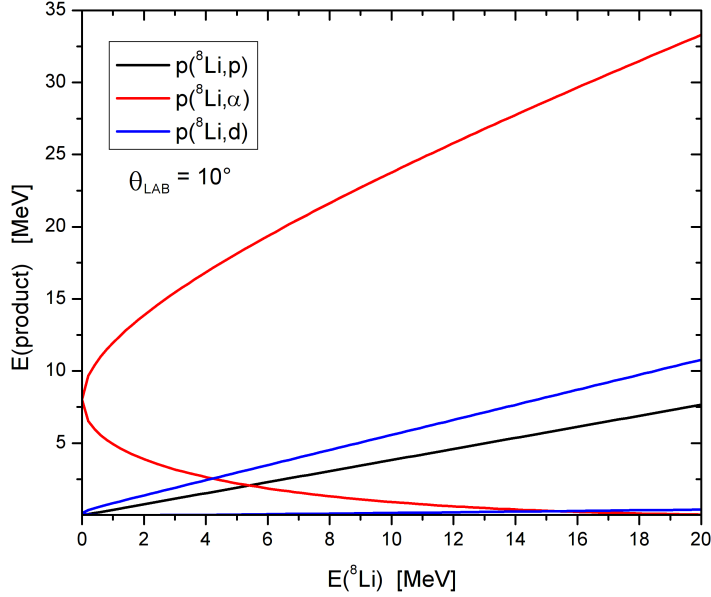


Figure 88: Kinematics for the relevant reactions in this experiment.

From the conservation of momentum (eq. 56), it is possible to obtain the relation between the angles θ and ϕ :

$$\text{sen}\phi = \sqrt{\frac{m_3 E_3}{m_4 E_4}} \text{sen}\theta \quad . \tag{60}$$

A.1 CENTER-OF-MASS FRAME

It is conventional to present data not in the laboratory coordinate system but in a reference invariant to the change of target and projectile. This reference system is the one in which the total momentum is zero, and both particles are traveling towards each other with equal linear momenta. It is the center-of-mass system, whose scheme is depicted in figure 89.

It is important to know how to perform conversions from laboratory frame to the center-of-mass frame for experimental data like energy, angle and cross section.

From this point, the indexes $_{\text{lab}}$ and $_{\text{cm}}$ will be employed to designate the reference system of the displayed quantity. When no index is specified, assume it to be in the laboratory frame.

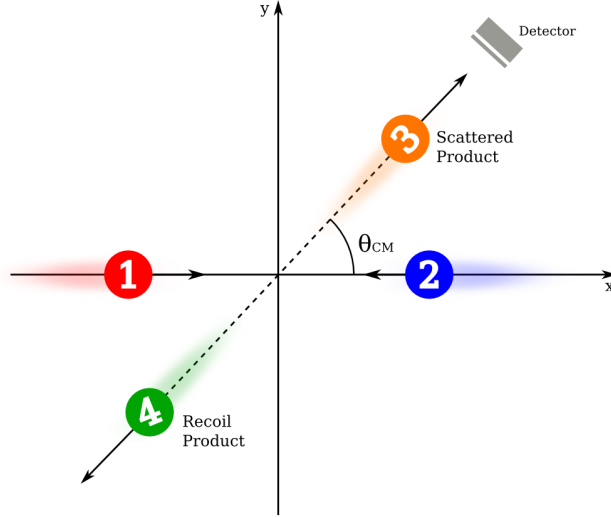


Figure 89: Scheme of collision geometry involved in a nuclear reaction at the center-of-mass frame.

Being $E_{lab} = E_1$, the conversion from laboratory total energy to center-of-mass total energy is immediately:

$$E_{cm} = \frac{A_{targ}}{A_{targ} + A_{proj}} \cdot E_{lab} = \frac{m_2}{m_2 + m_1} \cdot E_1 \quad . \quad (61)$$

For angle conversions, the following factor χ is needed¹:

$$\chi = \sqrt{\frac{m_1 m_3}{m_2 m_4} \frac{E_{cm}}{E_{cm} + Q}} \quad . \quad (62)$$

The relation between the detected particle's angle in both laboratory and center-of-mass frames is given by

$$\tan(\theta_{lab}) = \frac{\sin(\theta_{cm})}{\chi + \cos(\theta_{cm})} \quad . \quad (63)$$

As the total momentum must be conserved and it is zero in the center-of-mass system, the angle of the recoil particle must be $\phi_{cm} = \pi - \theta_{cm}$, as depicted in figure 89.

In the transformation of cross sections, the elements of solid angles in both reference systems must detect the same number of particles. So, the differential cross sections are related by:

$$\sigma_{cm} = \frac{d\Omega_{lab}}{d\Omega_{cm}} \sigma_{lab} \quad . \quad (64)$$

The factor $(d\Omega_{lab}/d\Omega_{cm})$ is called Jacobian and is given by

$$J = \frac{\sqrt{1 - \chi^2 \sin^2(\theta_{lab})}}{[\chi \cos(\theta_{lab}) + \sqrt{1 - \chi^2 \sin^2(\theta_{lab})}]^2} \quad . \quad (65)$$

¹ The χ -factor is the ratio of the speed of the system's center-of-mass in the laboratory frame and the speed of the outgoing particle (3) in the center-of-mass frame. For a detailed deduction, see [43].

The jacobians for the reactions employed at this experiment are depicted at figure 55 in section 4.1. Note that in the case of an elastic scattering, χ and the jacobian are constant with energy.

A.2 INVERSE KINEMATICS

In this experiment, the mass of the projectile (${}^8\text{Li}$) is larger than the mass of the fixed target (${}^1\text{H}$). This is called inverse kinematics, and some special considerations must be done about this kind of reaction.

In inverse kinematics, the center-of-mass energy of the system is much lower than the laboratory energies, as can be easily verified as a corollary of equation 61. For example, the center-of-mass energy of a ${}^8\text{Li} + \text{p}$ system of $E({}^8\text{Li})_{\text{lab}} = 18.7\text{MeV}$ is $E_{\text{cm}} = 2.08\text{MeV}$. This improves the energy resolution in the center-of-mass frame and therefore the measurement of excitation functions.

It is also intuitive that the scattering of both projectile and target particles at laboratory angles should be limited to forward angles, as a heavy projectile hitting a lightweight particle will not scatter backwards. Center-of-mass angles will be compressed inside a limited laboratory angles range, and the precision measurement of angular distributions would require excellent angular resolutions. At figure 90 is shown the energy-angle dependence of a beam of mass $m_1 = 8$ elastically scattered at several targets.

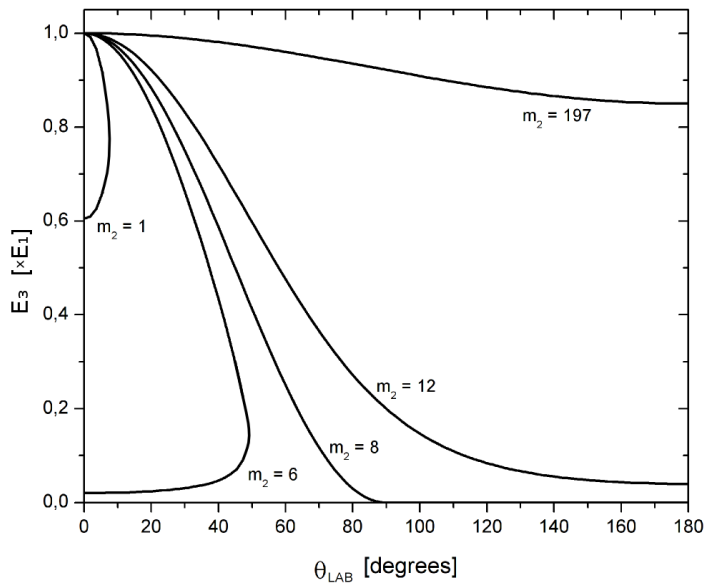


Figure 90: Relation between elastic scattering energy and scattering angle of a beam of mass $m_1 = 8$ for several targets.

It is clear that a maximum laboratory angle θ_{\max} rises when the system becomes an inverse kinematics situation. From equation 59 an expression for θ_{\max} can be derived:

$$\theta_{\max} = \arccos \left(\sqrt{\frac{(m_3 + m_4)[(m_1 - m_4) E_1 - m_4 Q]}{m_1 m_3 E_1}} \right) . \quad (66)$$

It is also evident, by both figures 90 and 88, that at inverse kinematics there are two solutions for the same laboratory angle. In fact, one of the solutions, actually the one with higher laboratory energy and more easily measured, corresponds to the backward $(\pi - \theta_{\text{cm}})$ center-of-mass angle.

In the past few years members of the RIBRAS collaboration have developed a useful set of codes to subserve RIBRAS' users [84, 115, 116]. The most recent contribution is SIM-RIBRAS [93], a ROOT-based [117] set of Monte-Carlo routines specially designed to provide support for experience planning and experimental setup enhancing. It is divided into two main programs: CineRIBRAS and SolFocus.

The programs included in the SIM-RIBRAS can save much time for RIBRAS' users, as it replaces methods and other programs that require much more manual labor, providing more complete and accurate results. They are very easy to use and execute, as they run under ROOT's framework and each step is carefully explained and documented. Both codes are designed to cover the complexity of any RIBRAS' experiment done in the last years, but allow the user to make changes for specific requirements of an experiment.

The programs in this package also make use of algorithms provided by the UPAK programs [118] Stopx and Kineq. The Kineq program provides quick calculations for reaction kinematics, as described in appendix A. Stopx performs stopping power and energy loss calculations based on experimental data and on extrapolations from them, mainly for exotic beams for which stopping power data is not available. The Stopx algorithm has been thoroughly tested for the beams, energies and materials usually employed at RIBRAS for many years and is considered accurate enough for the requirements of this experiment.

B.1 CINE RIBRAS

CineRIBRAS provides beam kinematics simulations for the whole RIBRAS System. It can be used to calculate beam energy losses, calibrate detectors and to calculate contaminant beam energies for each step from the incoming primary beam to the last detector signal.

The user has to define the characteristics of the beams (primary, secondary, secondary reaction products and contaminants, if desired) and the characteristics of every energy absorber present, like targets, degraders and detectors.

The algorithm starts by simulating a primary beam particle interacting with the primary target at the specified energy. Following the Monte-Carlo simulation concept, a position for the primary reaction is randomly chosen, then it calculates the energy loss the particle will

suffer to arrive at that point. The energy of the reaction product is calculated at the reaction point and after traversing the target.

This concept follows the simulated particle along the whole beamline, passing through degraders, interacting with targets, performing reactions and arriving at detectors. The program takes into account any processes occurring at each element that influences the beam, like energy loss, nuclear reactions, straggling, etc. The random choices on reaction position in targets and scattering angles have a uniform probability distribution set as default, but may be modified if desired. The process is repeated for hundreds or thousands of particles for beams of interest and contaminants, and several secondary reactions may be simulated in a single run.

Beam configurations are registered before and after any change (energy loss, reaction, etc.) and are stored at an Root TTree object, making easy to visualize the simulated beam behavior at any point of the beamline. An example concerning this experiment is shown in figures 91 and 92.

A highly accurate calculation would require some thousands of iterations, while a quick simulation using just a few hundred iterations would be enough to evaluate beam or product energies, resolution and general characteristics of the expected $E - \Delta E$ spectrum.

The easiness of calculating the final result upon changes at any parameter of the experimental setup, like beam energy, target or degrader thickness and detector configurations makes CineRIBRAS a very powerful tool for planning experiments.

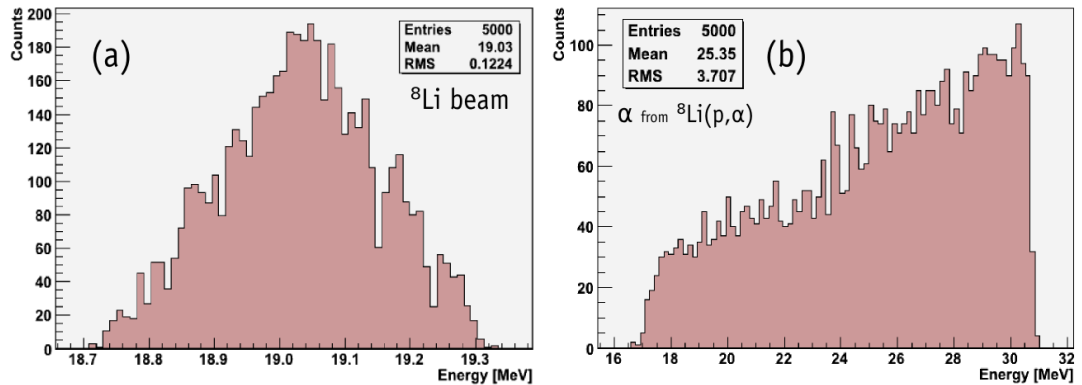


Figure 91: Energy profiles for $^8\text{Li} + p$ experiment simulated using CineRIBRAS: (a) of ^8Li beam after passing through the degrader and (b) of α particles from $^8\text{Li}(p, \alpha)$ reaction detected at 10° after a $(\text{CH}_2)_n$ target [93].

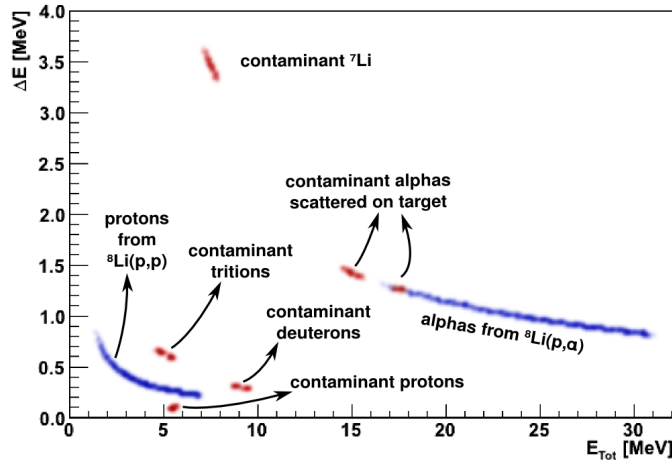


Figure 92: Simulated biparametric spectrum of an $E - \Delta E$ telescope positioned at 10° , with thickness of $20\mu\text{m}$ for ΔE detector and $1000\mu\text{m}$ for E detector. In blue are the expected protons (from ${}^8\text{Li}(p,p)$) and alphas (from ${}^8\text{Li}(p,\alpha)$). In red are possible contaminants [93].

B.2 SOLFOCUS

SolFocus is written to calculate geometrical effects at RIBRAS' beam selection and focalization. With a full description of RIBRAS' geometry and magnetic field, it can search for the optimal electric current in the solenoids for the selection of a specific secondary beam, providing beam tracks and beam spots at the focal planes. It also considers possible contaminant beams and allows the user to include any control element like collimators, blockers and energy degraders.

SolFocus uses the Boris' Method [119, 120], a fast and accurate method for solving charged particles equations of motion in non-uniform magnetic fields. Unlike CineRIBRAS, it deals only with the secondary beam and starts the particle simulation from the point right after the primary target and ends it before interacting with the secondary target. So, it must be provided just secondary beam energy distribution and emittance. The same calculations may be done for contaminant beams, that may be set at an specific energy or automatically the one that matches the magnetic rigidity of the secondary beam (eq. 39).

RIBRAS' geometry configurations are already built-in, but the user may change them if needed (e.g to reposition the focalization point in a chamber to adequate it to any unusual experimental configuration) or include new control element like collimators and degraders, which is also very useful for experiment planning.

One of the main features of SolFocus is the optimal current search. The algorithm fixes beam energy and varies the solenoid currents to find which one best focuses the secondary beam at that energy. The criteria employed takes into account the ratio of focused beam particles that successfully reach the target and the spatial distribution

of the beam spot in the target. The curves presented at figure 25 (section 3.4.2) were created using this algorithm. The results are in perfect agreement with the observed in experiments, turning SolFocus by far the best tool to determine optimal focalization currents.

The main outputs of SolFocus are particle tracks like those shown in figure 34, which were directly extracted from SolFocus results, and in the composition done at figure 50. They are very important in a beam purity study and in the dimensioning of degraders, blockers and collimators, as it clearly shows the behavior of contaminants inside the beamline in relation to the relevant ion.

Other auxiliary outputs are the ratio of focused particles as a function of solenoid current if the search tool is used, and the spatial distribution of the beam spot in the target. Examples of these are shown in figure 93. With some simple modifications, time-of-flights can also be extracted from SolFocus' simulations.

The beam spot shown in figure 93.b also certifies the good accuracy of SolFocus on beam tracking when compared to the measurements done with a PSD shown in figure 40, which revealed a beam spot about 7mm of diameter.

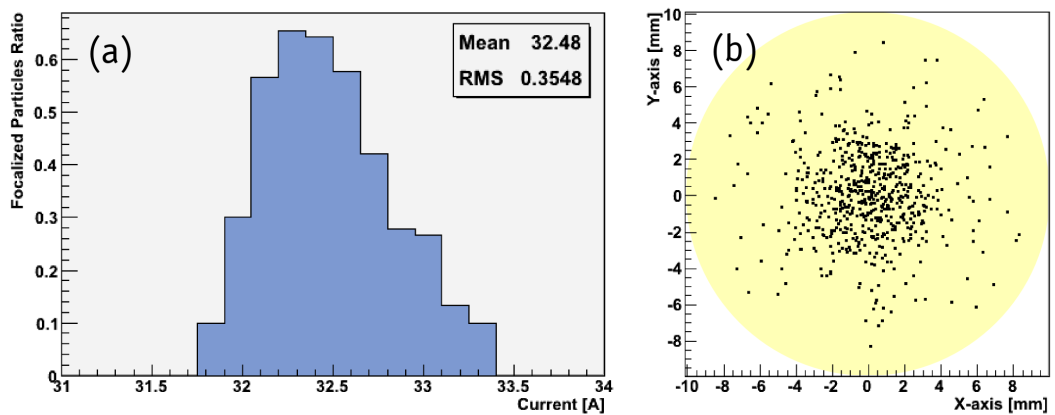


Figure 93: A few results on the ^8Li beam simulation using SolFocus. (a) Ratio of focalized ^8Li particles (22.8 MeV) in the target position of central chamber as a function of the current in the first solenoid simulated by SolFocus. (b) ^8Li beam spot profile in the secondary target (in light yellow) at main chamber [93].

SELECTION RULES

In the process of formation and decay of a compound nucleus the multiplicity of relative angular momentum and spins of both entrance and decay channels may lead to a huge amount of possible combinations. Thus, it is important to establish very clear selection rules for the population of allowed states.

By the concept of the independence hypothesis (eq.1), this appendix is divided into sections for formation selection rules and decay selection rules. For auxiliary purposes, at table 9 are exhibited the spins and parities of each particle that can be associated with a channel of formation and decay of ${}^9\text{Be}$.

Table 9: Spins and parities of pairs of nuclei (in the ground state) that may be channels of the ${}^9\text{Be}$ compound nucleus.

Particle	${}^8\text{Li}$	p	${}^5\text{He}$	α	${}^7\text{Li}$	d	${}^8\text{Be}$	n	${}^9\text{Be}$
J^π	2^+	$1/2^+$	$3/2^-$	0^+	$3/2^-$	1^+	0^+	$1/2^+$	$3/2^-$

FORMATION

In the formation of a compound nucleus, two particles of spins I_1 and I_2 and parities π_1 and π_2 fuse together to create a nucleus in a state of total spin and parity J^π . The relative angular momentum ℓ between the two initial particles could in principle assume any discretized value ($0, 1, 2, \dots$), but the fusion would occur preferentially for low ℓ values due to the dependence of the penetrability on ℓ .

The total angular momentum and the parity of the system are conserved quantities in the reaction. The total parity of the compound system is related to the parity of the two subsystems by the following relation [54]:

$$\pi = \pi_1 \pi_2 (-1)^\ell \quad . \quad (67)$$

Thus, in the case of this experiment in which the entrance channel is always the ${}^8\text{Li} + \text{p}$ system ($\pi_1 = \pi_2 = +1$), even ℓ values could populate positive parity states, while odd ℓ values could populate negative parity states.

The selection on angular momentum is done by the rules of sum of angular momentum. Firstly, the coupling of spins of the two particles should range from $I_{\min} = |I_1 - I_2|$ to $I_{\max} = |I_1 + I_2|$, assuming any integer-spaced value between them two. For the ${}^8\text{Li} + \text{p}$ system,

$I_{\min} = 3/2$ and $I_{\max} = 5/2$, thus they are the only two possible values.

Coupling the spin with the relative angular momentum should give $J = I \pm \ell$. As ℓ can assume any integer value, a wide range of states could be populated. At table 10 are displayed the possible couplings between ℓ and the two possible spin values, the resultant J^π already includes the parity rule.

Table 10: J^π of ${}^9\text{Be}$ states that can be populated by the ${}^8\text{Li} + p$ system.

$\pm\ell$	-2	-1	0	+1	+2	+3	...
$J^\pi = \frac{3}{2} + \ell$		$\frac{1}{2}^-$	$\frac{3}{2}^+$	$\frac{5}{2}^-$	$\frac{7}{2}^+$	$\frac{9}{2}^-$...
$J^\pi = \frac{5}{2} + \ell$	$\frac{1}{2}^+$	$\frac{3}{2}^-$	$\frac{5}{2}^+$	$\frac{7}{2}^-$	$\frac{9}{2}^+$	$\frac{11}{2}^-$...

As can be seen, the ${}^8\text{Li} + p$ system could populate any resonance of ${}^9\text{Be}$ above the threshold, as its internal odd structure admits only half integer states. Thus, it is a good choice as an entrance channel for spectroscopy studies. If the entrance channel could be, for example, ${}^5\text{He} + \alpha$, many of the J^π combinations would not be allowed¹.

DECAY

In terms of selection rules, the decay is the inverse process of the formation. An excited nucleus at a J^π state decays into two subsystems of spins I_3 and I_4 and parities π_3 and π_4 with an relative angular momentum of ℓ .

The sum I of spins of the two formed particles should also follow the rule of sum, ranging from $I_{\min} = |I_3 - I_4|$ to $I_{\max} = |I_3 + I_4|$. The decay in allowed ℓ s should also follow the rule, being inside the range $J = |I \pm \ell|$ for each I and respect the conservation of parity.

To illustrate this with a very simple example, a $J^\pi = 5/2^+$ state of ${}^9\text{Be}$ decays into ${}^5\text{He} + \alpha$. In this case, the only allowed I is $3/2$, as the alpha particle has spin 0. The compound state has positive parity, while $\pi_3 \pi_4 = -1$. To conserve parity, the relative angular momentum of the resultant pair should be odd (eq.67).

Then, all the possible odd ℓ s should be investigated to see which of them matches the required conservation of total angular momentum. In the case of $\ell = 1$, there is one case inside the range $|3/2 \pm \ell| = 5/2$ that satisfies the conservation of angular momentum, so $\ell = 1$ is allowed. It is the same for $\ell = 3$, but from $\ell = 5$ the minimum the term $|3/2 \pm \ell|$ can assume is $7/2$, not satisfying the conservation anymore.

¹ This is not a realistic entrance channel, as ${}^5\text{He}$ is not bound.

BIBLIOGRAPHY

- [1] E. Margaret Burbidge, G. R. Burbidge, William A. Fowler, and F. Hoyle. Synthesis of the Elements in Stars. *Rev. Mod. Phys.*, 29:547–650, Oct 1957. doi: 10.1103/RevModPhys.29.547. URL <http://link.aps.org/doi/10.1103/RevModPhys.29.547>.
- [2] Hans E. Suess and Harold C. Urey. Abundances of the Elements. *Rev. Mod. Phys.*, 28:53–74, Jan 1956. doi: 10.1103/RevModPhys.28.53. URL <http://link.aps.org/doi/10.1103/RevModPhys.28.53>.
- [3] A. G. W. Cameron. Elemental and nuclidic abundances in the solar system. In Charles A. Barnes, D. N. Schramm, and Donald D. Clayton, editors, *Essays in Nuclear Astrophysics*. Cambridge Univ. Press, September 1982. ISBN 9780521288767.
- [4] Jordi José and Christian Iliadis. Nuclear astrophysics: the unfinished quest for the origin of the elements. *Reports on Progress in Physics*, 74(9):096901, 2011. URL <http://stacks.iop.org/0034-4885/74/i=9/a=096901>.
- [5] Carlos A. Bertulani and Hélio Schechter. *Introdução à Física Nuclear*. UFRJ, 2007. ISBN 9788571082885.
- [6] Elisabeth Vangioni-Flam and Michel Cassé. Cosmic Lithium-Beryllium-Boron Story. *Astrophysics and Space Science*, 265(1-4): 77–86, 1999. ISSN 0004-640X. doi: 10.1023/A:1002197712862. URL <http://dx.doi.org/10.1023/A:1002197712862>.
- [7] John W. Hill. Energy and Problems of a Technical Society (Kraushaar, Jack J.; Ristinen, Robert A.). *Journal of Chemical Education*, 62(12):A327, 1985.
- [8] Eduardo Bravo and Gabriel Martínez-Pinedo. Sensitivity study of explosive nucleosynthesis in type ia supernovae: Modification of individual thermonuclear reaction rates. *Phys. Rev. C*, 85:055805, May 2012. doi: 10.1103/PhysRevC.85.055805. URL <http://link.aps.org/doi/10.1103/PhysRevC.85.055805>.
- [9] Michael S. Smith and K. Ernst Rehm. Nuclear astrophysics measurements with radioactive beams¹. *Annual Review of Nuclear and Particle Science*, 51(1):91–130, 2001. doi: 10.1146/annurev.nucl.51.101701.132430. URL <http://www.annualreviews.org/doi/abs/10.1146/annurev.nucl.51.101701.132430>.

- [10] Y. Blumenfeld, T. Nilsson, and P. Van Duppen. Facilities and methods for radioactive ion beam production. *Physica Scripta*, 2013(T152):014023, 2013. URL <http://stacks.iop.org/1402-4896/2013/i=T152/a=014023>.
- [11] K. Hagino, I. Tanihata, and H. Sagawa. *Exotic Nuclei Far from the Stability Line*, chapter 9, pages 231–272. doi: 10.1142/9789814425810_0009. URL http://www.worldscientific.com/doi/abs/10.1142/9789814425810_0009.
- [12] R. Lichtenthaler, A. Lepine-Szily, V. Guimaraes, C. Perego, V. Placco, O. Camargo jr., R. Denke, P.N. de Faria, E.A. Benjamim, N. Added, G.F. Lima, M.S. Hussein, J. Kolata, and A. Arazi. Radioactive ion beams in brazil (ribbras). *The European Physical Journal A - Hadrons and Nuclei*, 25(1):733–736, 2005. ISSN 1434-6001. doi: 10.1140/epjad/i2005-06-043-y. URL <http://dx.doi.org/10.1140/epjad/i2005-06-043-y>.
- [13] A. Lepine-Szily, R. Lichtenthaler, and V. Guimaraes. The radioactive ion beams in brazil (ribbras) facility. *Nuclear Physics News*, 23(3):5–11, 2013. doi: 10.1080/10619127.2013.821911. URL <http://www.tandfonline.com/doi/abs/10.1080/10619127.2013.821911>.
- [14] D.R. Tilley, J.H. Kelley, J.L. Godwin, D.J. Millener, J.E. Purcell, C.G. Sheu, and H.R. Weller. Energy levels of light nuclei $a=8,9,10$. *Nuclear Physics A*, 745(3–4):155 – 362, 2004. ISSN 0375-9474. doi: <http://dx.doi.org/10.1016/j.nuclphysa.2004.09.059>. URL <http://www.sciencedirect.com/science/article/pii/S0375947404010267>.
- [15] J. C. Blackmon, A. E. Champagne, J. K. Dickens, J. A. Harvey, M. A. Hofstee, S. Kopecky, D. C. Larson, D. C. Powell, S. Raman, and M. S. Smith. Measurement of ${}^7\text{Li}(n,\gamma){}^8\text{Li}$ cross sections at $e>=1.5\text{--}1340$ ev. *Phys. Rev. C*, 54:383–388, Jul 1996. doi: 10.1103/PhysRevC.54.383. URL <http://link.aps.org/doi/10.1103/PhysRevC.54.383>.
- [16] J. Gorres, H. Herndl, I. J. Thompson, and M. Wiescher. Two-neutron capture reactions in supernovae neutrino bubbles. *Phys. Rev. C*, 52:2231–2235, Oct 1995. doi: 10.1103/PhysRevC.52.2231. URL <http://link.aps.org/doi/10.1103/PhysRevC.52.2231>.
- [17] V Guimaraes, O Camargo, R Lichtenthaler, V Scarduelli, J.J. Kolata, H Amro, F.D. Becchetti, Hao Jiang, E.F. Aguilera, D Lizcano, E Martinez-Quiroz, and H Garcia. Transfer reactions in the investigation of light-nuclei nucleosynthesis.

- Revista mexicana de fisica*, 54:63 – 68, 12 2008. ISSN 0035-001X. URL http://www.scielo.org.mx/scielo.php?script=sci_arttext&pid=S0035-001X2008000900011&nrm=iso.
- [18] L. Weissman, C. Broude, G. Goldring, R. Hadar, M. Hass, F. Schwamm, and M. Shaanan. A new measurement of the ${}^7\text{Li}(d,p){}^8\text{Li}$ cross section and consequences for ${}^7\text{Be}(p,\gamma){}^8\text{B}$. *Nuclear Physics A*, 630(3–4):678 – 688, 1998. ISSN 0375-9474. doi: [http://dx.doi.org/10.1016/S0375-9474\(98\)00811-2](http://dx.doi.org/10.1016/S0375-9474(98)00811-2). URL <http://www.sciencedirect.com/science/article/pii/S0375947498008112>.
- [19] Hironobu Ishiyama, Takashi Hashimoto, Kanako Yamaguchi, Yutaka Watanabe, Nobuaki Imai, Yoshikazu Hirayama, Hiroari Miyatake, MasaHiko Tanaka, Nobuharu Yoshikawa, Sunchan Jeong, Yoshihide Fuchi, Ichiro Katayama, Toru Nomura, Tomoko Ishikawa, Suranjan K. Das, Yutaka Mizoi, Tomokazu Fukuda, Katsuhisa Nishio, Shinichi Mitsuoka, Hiroshi Ikezoe, Makoto Matsuda, Shinichi Ichikawa, Tadashi Shimoda, Kori Otsuki, and Toshiki Kajino. A systematic study of astrophysical reaction rates through ${}^8\text{Li}$. *AIP Conference Proceedings*, 1120(1):177–182, 2009. doi: <http://dx.doi.org/10.1063/1.3141643>. URL <http://scitation.aip.org/content/aip/proceeding/aipcp/10.1063/1.3141643>.
- [20] M La Cognata, A Del Zoppo, R Alba, S Cherubini, N Colonna, A Di Pietro, P Figuera, M Gulino, L Lamia, A Musumarra, M G Pellegriti, R G Pizzone, C Rolfs, S Romano, C Spitaleri, and A Tumino. Toward correction-free ${}^8\text{Li}(\alpha,n){}^{11}\text{B}$ data at the gamow energy of explosive nucleosynthesis. *Journal of Physics G: Nuclear and Particle Physics*, 37(10):105105, 2010. URL <http://stacks.iop.org/0954-3899/37/i=10/a=105105>.
- [21] M La Cognata and A Del Zoppo. Role of exotic cluster structures in astrophysics: the case of ${}^8\text{Li}(\alpha,n){}^{11}\text{B}$. *Physica Scripta*, 2012(T150):014019, 2012. URL <http://stacks.iop.org/1402-4896/2012/i=T150/a=014019>.
- [22] M. La Cognata, A. Del Zoppo, R. Alba, S. Cherubini, N. Colonna, A. Di Pietro, P. Figuera, M. Gulino, L. Lamia, A. Musumarra, M. G. Pellegriti, R. G. Pizzone, C. Rolfs, S. Romano, C. Spitaleri, and A. Tumino. Solving the large discrepancy between inclusive and exclusive measurements of the ${}^8\text{Li} + {}^4\text{He} \rightarrow {}^{11}\text{B} + n$ reaction cross section at astrophysical energies. *The Astrophysical Journal Letters*, 706(2):L251, 2009. URL <http://stacks.iop.org/1538-4357/706/i=2/a=L251>.
- [23] Carlos A Bertulani. The astrophysical reaction ${}^8\text{Li}(n,\gamma){}^9\text{Li}$ from measurements by reverse kinematics. *Journal of Physics*

- G: Nuclear and Particle Physics*, 25(9):1959, 1999. URL <http://stacks.iop.org/0954-3899/25/i=9/a=313>.
- [24] P. D. Zecher, A. Galonsky, S. J. Gaff, J. J. Kruse, G. Kunde, E. Tryggestad, J. Wang, R. E. Warner, D. J. Morrissey, K. Ieki, Y. Iwata, F. Deak, A. Horvath, A. Kiss, Z. Seres, J. J. Kolata, J. von Schwarzenberg, and H. Schelin. Measurement of the $^8\text{Li}(n,\gamma)^9\text{Li}$ cross section at astrophysical energies by reverse kinematics. *Phys. Rev. C*, 57:959–966, Feb 1998. doi: 10.1103/PhysRevC.57.959. URL <http://link.aps.org/doi/10.1103/PhysRevC.57.959>.
- [25] O. Camargo, V. Guimarães, R. Lichtenthäler, V. Scarduelli, J. J. Kolata, C. A. Bertulani, H. Amro, F. D. Becchetti, Hao Jiang, E. F. Aguilera, D. Lizcano, E. Martinez-Quiroz, and H. Garcia. The $^9\text{Be}(^8\text{Li},^9\text{Be})^8\text{Li}$ elastic-transfer reaction. *Phys. Rev. C*, 78:034605, Sep 2008. doi: 10.1103/PhysRevC.78.034605. URL <http://link.aps.org/doi/10.1103/PhysRevC.78.034605>.
- [26] Su Jun, Li Zhi-Hong, Guo Bing, Liu Wei-Ping, Bai Xi-Xiang, Zeng Sheng, Lian Gang, Yan Sheng-Quan, Wang Bao-Xiang, and Wang You-Bao. Astrophysical reaction rates of the $^8\text{Li}(p,\gamma)^9\text{Be}$ (g.s.) direct capture reaction. *Chinese Physics Letters*, 23(1):55, 2006. URL <http://stacks.iop.org/0256-307X/23/i=1/a=017>.
- [27] Zeng Sheng, Liu Wei-Ping, Li Zhi-Hong, Bai Xi-Xiang, Yan Sheng-Quan, Wang Bao-Xiang, Lian Gang, and Su Jun. Measurement of $^2\text{H}(^8\text{Li},^9\text{Be})\text{n}$ reaction relevant to primordial nucleosynthesis. *Chinese Physics Letters*, 22(9):2219, 2005. URL <http://stacks.iop.org/0256-307X/22/i=9/a=022>.
- [28] Fabio Iocco, Gianpiero Mangano, Gennaro Miele, Ofelia Pisanti, and Pasquale D. Serpico. Primordial nucleosynthesis: From precision cosmology to fundamental physics. *Physics Reports*, 472(1–6):1 – 76, 2009. ISSN 0370-1573. doi: <http://dx.doi.org/10.1016/j.physrep.2009.02.002>. URL <http://www.sciencedirect.com/science/article/pii/S0370157309000374>.
- [29] David N Schramm. Big bang nucleosynthesis: the standard model and alternatives. *Physica Scripta*, 1991(T36):22, 1991. URL <http://stacks.iop.org/1402-4896/1991/i=T36/a=003>.
- [30] Michael J. Fromerth and Johann Rafelski. Hadronization of the quark Universe. 2002. URL <http://arxiv.org/abs/astro-ph/0211346>.
- [31] Brian D. Fields. The primordial lithium problem. *Annual Review of Nuclear and Particle Science*, 61(1):47–68, 2011. doi: 10.1146/

- annurev-nucl-102010-130445. URL <http://www.annualreviews.org/doi/abs/10.1146/annurev-nucl-102010-130445>.
- [32] R. Cayrel. The first generations of stars. *Astronomy and Astrophysics Review*, 7:217–242, 1996. doi: 10.1007/s001590050005. URL <http://adsabs.harvard.edu/abs/1996A%26ARv...7..217C>.
- [33] J. Christopher Howk, Nicolas Lehner, Brian D. Fields, and Grant J. Mathews. Observation of interstellar lithium in the low-metallicity small magellanic cloud. *Nature*, 489:121–123, Sep 2012. doi: 10.1038/nature11407. URL <http://www.nature.com/nature/journal/v489/n7414/full/nature11407.html>.
- [34] Kimmo Kainulainen, Hannu Kurki-Suonio, and Elina Sihvola. Inhomogeneous big-bang nucleosynthesis in light of recent observations. *Phys. Rev. D*, 59:083505, Mar 1999. doi: 10.1103/PhysRevD.59.083505. URL <http://link.aps.org/doi/10.1103/PhysRevD.59.083505>.
- [35] M. Orito, T. Kajino, R. N. Boyd, and G. J. Mathews. Geometrical effects of baryon density inhomogeneities on primordial nucleosynthesis. *The Astrophysical Journal*, 488(2):515, 1997. URL <http://stacks.iop.org/0004-637X/488/i=2/a=515>.
- [36] X. Gu, R.N. Boyd, M.M. Farrell, J.D. Kalen, C.A. Mitchell, J.J. Kolata, M. Belbot, K. Lamkin, K. Ashktorab, F.D. Becchetti, J. Brown, D. Roberts, K. Kimura, I. Tanihata, K. Yoshida, and M.S. Islam. The $8\text{Li}(\alpha, n)_{11}\text{B}$ reaction and primordial nucleosynthesis. *Physics Letters B*, 343(1–4):31 – 35, 1995. ISSN 0370-2693. doi: [http://dx.doi.org/10.1016/0370-2693\(94\)01480-Z](http://dx.doi.org/10.1016/0370-2693(94)01480-Z). URL <http://www.sciencedirect.com/science/article/pii/037026939401480Z>.
- [37]
- [38] Hou Su-Qing, Wu Kai-Su, Chen Yong-Shou, Shu Neng-Chuan, and Li Zhi-Hong. The main path to c, n, o elements in big bang nucleosynthesis. *Chinese Physics Letters*, 27(8):082601, 2010. URL <http://stacks.iop.org/0256-307X/27/i=8/a=082601>.
- [39] Ian J. Thompson and Filomena M. Nunes. *Nuclear Reactions for Astrophysics*. Cambridge University Press, 2009. ISBN 978-0-521-85635-5.
- [40] T. Sasaqui, K. Otsuki, T. Kajino, and G. J. Mathews. Light-element reaction flow and the conditions for r-process nucleosynthesis. *The Astrophysical Journal*, 645(2):1345, 2006. URL <http://stacks.iop.org/0004-637X/645/i=2/a=1345>.

- [41] D. R. Mendes, A. Lépine-Szily, P. Descouvemont, R. Lichtenhaler, V. Guimaraes, P. N. de Faria, A. Barioni, K. C. C. Pires, V. Morcelle, R. Pampa Condori, M. C. Morais, E. Leistenschneider, C. E. F. Lima, J. C. Zamora, J. A. Alcantara, V. Zagatto, M. Assuncao, and J. M. B. Shorto. The $8\text{Li}(p,\alpha)5\text{He}$ reaction at low energies, and 9Be spectroscopy around the proton threshold. *Phys. Rev. C*, 86:064321, Dec 2012. doi: 10.1103/PhysRevC.86.064321. URL <http://link.aps.org/doi/10.1103/PhysRevC.86.064321>.
- [42] A. M. Lane and R. G. Thomas. R-matrix theory of nuclear reactions. *Rev. Mod. Phys.*, 30:257–353, Apr 1958. doi: 10.1103/RevModPhys.30.257. URL <http://link.aps.org/doi/10.1103/RevModPhys.30.257>.
- [43] G.R. Satchler. *Introduction to Nuclear Reactions*. MacMillan Education, London, 2nd edition, 1990. ISBN 0-333-52379-2.
- [44] S. N. Ghoshal. An experimental verification of the theory of compound nucleus. *Phys. Rev.*, 80:939–942, Dec 1950. doi: 10.1103/PhysRev.80.939. URL <http://link.aps.org/doi/10.1103/PhysRev.80.939>.
- [45] Ernst W. Hamburger. *Reaço Direta e Ncleo Composto*. Universidade de So Paulo, February 1968.
- [46] W. Heisenberg. Uber den anschaulichen inhalt der quantentheoretischen kinematik und mechanik. *Zeitschrift fur Physik*, 43 (3-4):172–198, 1927. ISSN 0044-3328. doi: 10.1007/BF01397280. URL <http://dx.doi.org/10.1007/BF01397280>.
- [47] A. Tveter. Resonance levels in 28Si from $27\text{Al}+p$ reactions. *Nuclear Physics A*, 185(2):433 – 458, 1972. ISSN 0375-9474. doi: [http://dx.doi.org/10.1016/0375-9474\(72\)90023-1](http://dx.doi.org/10.1016/0375-9474(72)90023-1). URL <http://www.sciencedirect.com/science/article/pii/0375947472900231>.
- [48] Kyung Yuk Chae. *Interference effects among $J^{\pi}=3/2^{+}$ resonances in 19Ne system and seaching for resonances in the unbound 6Be nucleus*. PhD thesis, University of Tennessee, Knoxville, December 2006. URL http://trace.tennessee.edu/utk_graddiss/1920.
- [49] Milton Abramowitz and Irene A. Stegun. *Handbook of Mathematical Functions with Formulas, Graphs, and Mathematical Tables*. Dover Publications, 1972. ISBN 978-0-486-61272-0.
- [50] A.R. Barnett. High-precision evaluation of the regular and irregular coulomb wavefunctions. *Journal of Computational and Applied Mathematics*, 8(1):29 – 33, 1982. ISSN 0377-0427. doi: [http://dx.doi.org/10.1016/0771-050X\(82\)90004-3](http://dx.doi.org/10.1016/0771-050X(82)90004-3). URL <http://www.sciencedirect.com/science/article/pii/0771050X82900043>.

- [51] K. Hagino and A. B. Balantekin. Wkb approximation for multi-channel barrier penetrability. *Phys. Rev. A*, 70:032106, Sep 2004. doi: 10.1103/PhysRevA.70.032106. URL <http://link.aps.org/doi/10.1103/PhysRevA.70.032106>.
- [52] Normand M. Laurendeau. *Statistical thermodynamics: fundamentals and applications*. Cambridge University Press, 2005. ISBN 0-521-84635-8.
- [53] F. Hoyle, D. N. F. Dunbar, W. A. Wenzel, and W. Whaling. A state in ^{12}C predicted from astrophysical evidence. *Physical Review*, 92(1095), 1953.
- [54] P. Descouvemont and D. Baye. The r-matrix theory. *Reports on Progress in Physics*, 73(3):036301, 2010. URL <http://stacks.iop.org/0034-4885/73/i=3/a=036301>.
- [55] Djalma Rosa Mendes Jr. *Estudo da Reação $^8\text{Li}(p,\alpha)^5\text{He}$ com Feixe Radioativo de ^8Li* . PhD thesis, Universidade de São Paulo, September 2009. URL <http://www.teses.usp.br/teses/disponiveis/43/43134/tde-26042010-132233>.
- [56] C. R. Brune. Alternative parametrization of r-matrix theory. *Phys. Rev. C*, 66:044611, Oct 2002. doi: 10.1103/PhysRevC.66.044611. URL <http://link.aps.org/doi/10.1103/PhysRevC.66.044611>.
- [57] Oscar Sala and George Spalek. The nuclear structure facility at the university of são paulo. *Nuclear Instruments and Methods*, 122:213 – 225, 1974. ISSN 0029-554X. doi: [http://dx.doi.org/10.1016/0029-554X\(74\)90484-4](http://dx.doi.org/10.1016/0029-554X(74)90484-4). URL <http://www.sciencedirect.com/science/article/pii/0029554X74904844>.
- [58] R.G. Herb. Pelletron accelerators for very high voltage. *Nuclear Instruments and Methods*, 122(0):267 – 276, 1974. ISSN 0029-554X. doi: [http://dx.doi.org/10.1016/0029-554X\(74\)90487-X](http://dx.doi.org/10.1016/0029-554X(74)90487-X). URL <http://www.sciencedirect.com/science/article/pii/0029554X7490487X>.
- [59] R. Middleton and Charles T. Adams. A close to universal negative ion source. *Nuclear Instruments and Methods*, 118(2):329 – 336, 1974. ISSN 0029-554X. doi: [http://dx.doi.org/10.1016/0029-554X\(74\)90634-X](http://dx.doi.org/10.1016/0029-554X(74)90634-X). URL <http://www.sciencedirect.com/science/article/pii/0029554X7490634X>.
- [60] Ragnar Hellborg, editor. *Electrostatic Accelerators - Fundamentals and Applications*. Springer, 2005. ISBN 978-3-540-23983-3.
- [61] Jerry B. Marion and Frank C. Young. *Nuclear Reaction Analysis: Graphs and Tables*. North-Holland, 1968.

- [62] I. I. Rabi, J. R. Zacharias, S. Millman, and P. Kusch. A new method of measuring nuclear magnetic moment. *Phys. Rev.*, 53: 318–318, Feb 1938. doi: 10.1103/PhysRev.53.318. URL <http://link.aps.org/doi/10.1103/PhysRev.53.318>.
- [63] V. Rotberg, D. Pereira, M.N. Rao, N. Ueta, and O. Sala. Calibration of the TANDEM Pelletron Accelerator. *Revista Brasileira de Física*, 6(3):413–427, 1976. URL <http://www.sbfisica.org.br/bjp/download/v06/v06a26.pdf>.
- [64] M. J. Dresser. The saha-langmuir equation and its application. *Journal of Applied Physics*, 39(1):338–339, 1968. doi: <http://dx.doi.org/10.1063/1.1655755>. URL <http://scitation.aip.org/content/aip/journal/jap/39/1/10.1063/1.1655755>.
- [65] F. Touchard, J. Biderman, M. de Saint Simon, C. Thibault, G. Huber, M. Epherre, and R. Klapisch. Production of ionic and atomic beams of alkaline elements. *Nuclear Instruments and Methods in Physics Research*, 186(1–2):329 – 334, 1981. ISSN 0167-5087. doi: [http://dx.doi.org/10.1016/0029-554X\(81\)90922-8](http://dx.doi.org/10.1016/0029-554X(81)90922-8). URL <http://www.sciencedirect.com/science/article/pii/0029554X81909228>.
- [66] David R. Lide, editor. *CRC Handbook of Chemistry and Physics*. CRC Press, 84th edition, 2003. ISBN 0-8493-0484-9.
- [67] R. G. Wilson. Vacuum thermionic work functions of polycrystalline nb, mo, ta, w, re, os, and ir. *Journal of Applied Physics*, 37(8):3170–3172, 1966. doi: <http://dx.doi.org/10.1063/1.1703180>. URL <http://scitation.aip.org/content/aip/journal/jap/37/8/10.1063/1.1703180>.
- [68] National Electrostatics Corp. Negative ion beam sources, January 2014. URL <http://www.pelletron.com/negion.htm>.
- [69] National Electrostatics Corp. Pelletron accelerators - tutorials, January 2014. URL <http://www.pelletron.com/tutor.htm>.
- [70] National Electrostatics Corp. Charging system, January 2014. URL <http://www.pelletron.com/charging.htm>.
- [71] Pedro Neto de Faria. *Estudo do Espalhamento Elástico e Reações de Feixes Secundários de Núcleos Exóticos*. PhD thesis, Universidade de São Paulo, November 2008. URL www.teses.usp.br/teses/disponiveis/43/43134/tde-26032009-103941.
- [72] R. Flukiger, S. Y. Hariharan, R. Kuntzler, H. L. Luo, F. Weiss, T. Wolf, and J. Q. Xu. *Landolt-Bornstein - Group III Condensed Matter - Numerical Data and Functional Relationships in Science*

- and Technology*, volume 21b2: Nb-H - Nb-Zr, Nd - Np. Springer-Verlag, 1994. ISBN 978-3-540-57541-2. doi: 10.1007/10423690_53. URL <http://www.springermaterials.com>.
- [73] K. C. C. Pires, R. Lichtenthäler, A. Lépine-Szily, V. Guimarães, P. N. de Faria, A. Barioni, D. R. Mendes Junior, V. Morcelle, R. Pampa Condori, M. C. Morais, J. C. Zamora, E. Crema, A. M. Moro, M. Rodriguez-Gallardo, M. Assunção, J. M. B. Shorto, and S. Mukherjee. Experimental study of $6\text{He}+9\text{Be}$ elastic scattering at low energies. *Phys. Rev. C*, 83:064603, Jun 2011. doi: 10.1103/PhysRevC.83.064603. URL <http://link.aps.org/doi/10.1103/PhysRevC.83.064603>.
- [74] J. C. Zamora, V. Guimarães, A. Barioni, A. Lépine-Szily, R. Lichtenthäler, P. N. de Faria, D. R. Mendes, L. R. Gasques, J. M. B. Shorto, V. Scarduelli, K. C. C. Pires, V. Morcelle, E. Leisten-schneider, R. P. Condori, V. A. Zagatto, M. C. Morais, and E. Crema. $7,9,10\text{Be}$ elastic scattering and total reaction cross sections on a 12C target. *Phys. Rev. C*, 84:034611, Sep 2011. doi: 10.1103/PhysRevC.84.034611. URL <http://link.aps.org/doi/10.1103/PhysRevC.84.034611>.
- [75] P. N. de Faria, R. Lichtenthäler, K. C. C. Pires, A. M. Moro, A. Lépine-Szily, V. Guimarães, D. R. Mendes, A. Arazi, M. Rodriguez-Gallardo, A. Barioni, V. Morcelle, M. C. Morais, O. Camargo, J. Alcantara Nunez, and M. Assunção. Elastic scattering and total reaction cross section of $6\text{He}+120\text{Sn}$. *Phys. Rev. C*, 81:044605, Apr 2010. doi: 10.1103/PhysRevC.81.044605. URL <http://link.aps.org/doi/10.1103/PhysRevC.81.044605>.
- [76] A. Barioni, V. Guimarães, A. Lépine-Szily, R. Lichtenthäler, D. R. Mendes, E. Crema, K. C. C. Pires, M. C. Morais, V. Morcelle, P. N. de Faria, R. P. Condori, A. M. Moro, D. S. Monteiro, J. M. B. Shorto, J. Lubian, and M. Assunção. Elastic scattering and total reaction cross sections for the $8\text{Li}+12\text{C}$ system. *Phys. Rev. C*, 80:034617, Sep 2009. doi: 10.1103/PhysRevC.80.034617. URL <http://link.aps.org/doi/10.1103/PhysRevC.80.034617>.
- [77] E.A. Benjamim, A. Lépine-Szily, D.R. Mendes Junior, R. Lichtenthäler, V. Guimarães, P.R.S. Gomes, L.C. Chamon, M.S. Hussein, A.M. Moro, A. Arazi, I. Padron, J. Alcantara Nuñez, M. Assunção, A. Barioni, O. Camargo Jr., R.Z. Denke, P.N. de Faria, and K.C.C. Pires. Elastic scattering and total reaction cross section for the $6\text{He} + 27\text{Al}$ system. *Physics Letters B*, 647(1):30 – 35, 2007. ISSN 0370-2693. doi: <http://dx.doi.org/10.1016/j.physletb.2007.01.048>. URL <http://www.sciencedirect.com/science/article/pii/S0370269307000949>.

- [78] Glenn F. Knoll. *Radiation Detection and Measurement*. John Wiley and Sons, 4th edition, 2011. ISBN 978-0-470-13148-0.
- [79] *Application Note 40 - Heavy-Ion Spectroscopy with Silicon Surface-Barrier Detectors*. ORTEC, . URL <http://www.ortec-online.com/Library/index.aspx>.
- [80] William R. Leo. *Techniques for Nuclear and Particle Physics Experiments*. Springer, 1994. ISBN 978-3-540-57280-0.
- [81] F S Goulding and B G Harvey. Identification of nuclear particles. *Annual Review of Nuclear Science*, 25(1):167–240, 1975. doi: 10.1146/annurev.ns.25.120175.001123. URL <http://www.annualreviews.org/doi/abs/10.1146/annurev.ns.25.120175.001123>.
- [82] *Am-1 - Ultra-thin Windows Alpha Source*. ORTEC, . URL <http://www.ortec-online.com/Solutions/alpha-spectroscopy.aspx>.
- [83] Juan Pablo Urrego-Blanco. *Studies on a Polarized Proton Target for Reactions with Radioactive Ion Beams*. PhD thesis, University of Tennessee, Knoxville, August 2009. URL http://trace.tennessee.edu/utk_graddiss/70.
- [84] R. Lichtenthäler. Code ribras (fortran). Universidade de São Paulo, 2005.
- [85] R.R. Betts. Time of flight detectors for heavy ions. *Nuclear Instruments and Methods*, 162(1–3):531 – 538, 1979. ISSN 0029-554X. doi: [http://dx.doi.org/10.1016/0029-554X\(79\)90731-6](http://dx.doi.org/10.1016/0029-554X(79)90731-6). URL <http://www.sciencedirect.com/science/article/pii/S0029554X79907316>.
- [86] Jean-Pierre Coffin and Pierre Engelstein. Time-of-flight systems for heavy ions. In D.Allan Bromley, editor, *Treatise on Heavy-Ion Science*, pages 273–330. Springer US, 1985. ISBN 978-1-4615-8108-6. doi: 10.1007/978-1-4615-8106-2_7. URL http://dx.doi.org/10.1007/978-1-4615-8106-2_7.
- [87] P. Boccaccio, L. Vannucci, R.A. Ricci, I. Massa, G. Vannini, and A. Sarti. Time-of-flight telescope for mass identification of heavy ions. *Il Nuovo Cimento A*, 71(3):420–428, 1982. ISSN 0369-3546. doi: 10.1007/BF02898936. URL <http://dx.doi.org/10.1007/BF02898936>.
- [88] Joseph Ladislav Wiza. Microchannel plate detectors. *Nuclear Instruments and Methods*, 162(1–3):587 – 601, 1979. ISSN 0029-554X. doi: [http://dx.doi.org/10.1016/0029-554X\(79\)90734-1](http://dx.doi.org/10.1016/0029-554X(79)90734-1). URL <http://www.sciencedirect.com/science/article/pii/S0029554X79907341>.

- [89] K. L. Brown and G. W. Tautfest. Faraday-cup monitors for high-energy electron beams. *Review of Scientific Instruments*, 27(9):696–702, 1956. doi: <http://dx.doi.org/10.1063/1.1715674>. URL <http://scitation.aip.org/content/aip/journal/rsi/27/9/10.1063/1.1715674>.
- [90] R.V. Ribas. Controlling camac instrumentation through the usb port. *AIP Conference Proceedings*, 1423(1):437–440, 2012. doi: <http://dx.doi.org/10.1063/1.3688842>. URL <http://scitation.aip.org/content/aip/proceeding/aipcp/10.1063/1.3688842>.
- [91] A.A.P. Suaide. Pelroot software package. Universidade de São Paulo, 2004–2013. URL <http://www.dfn.if.usp.br/~suaide/pelletron/>.
- [92] *Extracting Position Information from Single Dimension Position Sensitive Detectors*. ORTEC, . URL <http://www.ortec-online.com/>.
- [93] E. Leistenschneider, A. Lépine-Szily, and R. Lichtenthäler. Sim-ribras: A monte-carlo simulation package for riabras system. *AIP Conference Proceedings*, 1529(1):206–208, 2013. doi: <http://dx.doi.org/10.1063/1.4804118>. URL <http://scitation.aip.org/content/aip/proceeding/aipcp/10.1063/1.4804118>.
- [94] N. Ueta, W.G.P. Engel, and J.J.G. Leandro. Confecção de alvos nucleares. Universidade de São Paulo, 2007.
- [95] Cleuza Maria Wasilkoski. Caracterização de polietileno de baixa densidade através da técnica de análise dinâmico-mecânica e comparação com a análise por impedância dielétrica. Master’s thesis, Universidade Federal do Paraná, January 2002. URL <http://www.pipe.ufpr.br/portal/defesas/dissertacao/027.pdf>.
- [96] K.-M. Källman, V.Z. Goldberg, T. Lönnroth, P. Manngård, A.E. Pakhomov, and V.V. Pankratov. Thick-target backscattering technique to measure alpha-particle elastic scattering cross sections. *Nuclear Instruments and Methods in Physics Research Section A: Accelerators, Spectrometers, Detectors and Associated Equipment*, 338(2–3):413 – 418, 1994. ISSN 0168-9002. doi: [http://dx.doi.org/10.1016/0168-9002\(94\)91324-2](http://dx.doi.org/10.1016/0168-9002(94)91324-2). URL <http://www.sciencedirect.com/science/article/pii/0168900294913242>.
- [97] M. Benjelloun, Th. Delbar, W. Galster, P. Leleux, E. Liénard, P. Lipnik, P. Duhamel, J. Vanhorenbeeck, C. Rolfs, G. Roters, H.P. Trautvetter, and W. Rodney. Precise measurement of the j_{π^1} = 1- resonance in ^{14}N by $^{13}\text{C}+\text{p}$ elastic scattering on a thick target. *Nuclear Instruments and Methods in Physics Research Section A: Accelerators, Spectrometers, Detectors and Associated Equipment*, 321(3):521 – 528, 1992. ISSN 0168-9002. doi: [http://dx.doi.org/10.1016/0168-9002\(92\)90000-2](http://dx.doi.org/10.1016/0168-9002(92)90000-2).

- [//dx.doi.org/10.1016/0168-9002\(92\)90062-9](http://dx.doi.org/10.1016/0168-9002(92)90062-9). URL <http://www.sciencedirect.com/science/article/pii/0168900292900629>.
- [98] A. Galindo-Uribarri, J. Gomez del Campo, J.R. Beene, C.J. Gross, J.F. Liang, S.D. Paul, D. Shapira, D.W. Stracener, R.L. Varner, E. Chavez, A. Huerta, M.E. Ortiz, E. Padilla, and S. Pascual. Study of resonant reactions with radioactive ion beams. *Nuclear Instruments and Methods in Physics Research Section B: Beam Interactions with Materials and Atoms*, 172(1-4):647 – 654, 2000. ISSN 0168-583X. doi: [http://dx.doi.org/10.1016/S0168-583X\(00\)00220-2](http://dx.doi.org/10.1016/S0168-583X(00)00220-2). URL <http://www.sciencedirect.com/science/article/pii/S0168583X00002202>. 8th International Conference on Accelerator Mass Spectrometry.
- [99] V. Z. Goldberg, G. V. Rogachev, W. H. Trzaska, J. J. Kolata, A. Andreyev, C. Angulo, M. J. G. Borge, S. Cherubini, G. Chubarian, G. Crowley, P. Van Duppen, M. Gorska, M. Gulino, M. Huyse, P. Jesinger, K.-M. Kallman, M. Lattuada, T. Lonnroth, M. Mutterer, R. Raabe, S. Romano, M. V. Rozhkov, B. B. Skorodumov, C. Spitaleri, O. Tengblad, and A. Tumino. Investigation of the alpha-cluster structure of ^{22}Ne and ^{22}Mg . *Phys. Rev. C*, 69:024602, Feb 2004. doi: [10.1103/PhysRevC.69.024602](https://doi.org/10.1103/PhysRevC.69.024602). URL <http://link.aps.org/doi/10.1103/PhysRevC.69.024602>.
- [100] Chris Ruiz. *Aspects of Nuclear Phenomena Under Explosive Astrophysical Conditions*. PhD thesis, University of Edinburgh, 2003.
- [101] P. R. Bevington and D. K. Robinson. *Data Reduction and Error Analysis for the Physical Sciences*. McGraw Hill, 2002. ISBN 978-0-072-47227-1.
- [102] F.D. Becchetti, J.A. Brown, W.Z. Liu, J.W. Jänecke, D.A. Roberts, J.J. Kolata, R.J. Smith, K. Lamkin, A. Morsad, R.E. Warner, R.N. Boyd, and J.D. Kalen. Reaction rates for $^8\text{Li}(p,a)$ and $^8\text{Li}(p,n,a)$ and their effect on primordial nucleosynthesis. *Nuclear Physics A*, 550(3):507 – 516, 1992. ISSN 0375-9474. doi: [http://dx.doi.org/10.1016/0375-9474\(92\)90020-K](http://dx.doi.org/10.1016/0375-9474(92)90020-K). URL <http://www.sciencedirect.com/science/article/pii/037594749290020K>.
- [103] Li Yun-Ju, Li Zhi-Hong, Guo Bing, Wang You-Bao, Bai Xi-Xiang, Su Jun, Lian Gang, Zeng Sheng, Wang Bao-Xiang, Qin Xing, Jiang Chao, Liu Wei-Ping, and Zhao Wei-Juan. Measurement of angular distribution for the $^8\text{Li}(p,d)^7\text{Li}$ reaction. *Chinese Physics Letters*, 25(2):455, 2008. URL <http://stacks.iop.org/0256-307X/25/i=2/a=028>.
- [104] Charles R. McClenahan and Ralph E. Segel. Cross sections for the $^7\text{Li}(d,p)^8\text{Li}$, $^6\text{Li}(^3\text{He},n)^8\text{B}$, $^6\text{Li}(d,a)^4\text{He}$, $^6\text{Li}(d,p)^7\text{Li}$ and

- 6li(d,n)7be reactions. *Phys. Rev. C*, 11:370–382, Feb 1975. doi: 10.1103/PhysRevC.11.370. URL <http://link.aps.org/doi/10.1103/PhysRevC.11.370>.
- [105] Stanley Bashkin. 7li(d,p)8li yield curve. *Phys. Rev.*, 95:1012–1015, Aug 1954. doi: 10.1103/PhysRev.95.1012. URL <http://link.aps.org/doi/10.1103/PhysRev.95.1012>.
- [106] D.R. Tilley, C.M. Cheves, J.L. Godwin, G.M. Hale, H.M. Hofmann, J.H. Kelley, C.G. Sheu, and H.R. Weller. Energy levels of light nuclei a=5, 6, 7. *Nuclear Physics A*, 708(1–2):3 – 163, 2002. ISSN 0375-9474. doi: [http://dx.doi.org/10.1016/S0375-9474\(02\)00597-3](http://dx.doi.org/10.1016/S0375-9474(02)00597-3). URL <http://www.sciencedirect.com/science/article/pii/S0375947402005973>.
- [107] D. D. Caussyn, N. R. Fletcher, K. W. Kemper, E. E. Towers, J. J. Kolata, K. Lamkin, R. J. Smith, F. D. Becchetti, J. A. Brown, J. W. Janecke, D. A. Roberts, and D. L. Gay. Cross section for the primordial reaction 8li(p,n)9be(g.s.) at ecm=1.5 mev. *Phys. Rev. C*, 47:387–391, Jan 1993. doi: 10.1103/PhysRevC.47.387. URL <http://link.aps.org/doi/10.1103/PhysRevC.47.387>.
- [108] R. E. Azuma, E. Uberseder, E. C. Simpson, C. R. Brune, H. Costantini, R. J. de Boer, J. Gorres, M. Heil, P. J. LeBlanc, C. Ugalde, and M. Wiescher. Azure: An r-matrix code for nuclear astrophysics. *Phys. Rev. C*, 81:045805, Apr 2010. doi: 10.1103/PhysRevC.81.045805. URL <http://link.aps.org/doi/10.1103/PhysRevC.81.045805>.
- [109] F. Ajzenberg-Selove and T. Lauritsen. Energy levels of light nuclei a = 5-10. *Nuclear Physics A*, 227(1):1 – 243, 1974. ISSN 0375-9474. doi: [http://dx.doi.org/10.1016/0375-9474\(74\)90780-5](http://dx.doi.org/10.1016/0375-9474(74)90780-5). URL <http://www.sciencedirect.com/science/article/pii/0375947474907805>.
- [110] P. Paul and D. Kohler. Alpha-particle spectra produced in the reactions of deuterons on 7li. *Phys. Rev.*, 129:2698–2704, Mar 1963. doi: 10.1103/PhysRev.129.2698. URL <http://link.aps.org/doi/10.1103/PhysRev.129.2698>.
- [111] E. Friedland and I. Venter. Die reaktion 7li(d,alpha)5he im energiegebiet von 0.6 bis 2.0 mev. *Zeitschrift für Physik*, 243(2): 126–131, 1971. ISSN 0044-3328. doi: 10.1007/BF01397857. URL <http://dx.doi.org/10.1007/BF01397857>.
- [112] S. Dixit, W. Bertozzi, T. N. Buti, J. M. Finn, F. W. Hersman, C. E. Hyde-Wright, M. V. Hynes, M. A. Kovash, B. E. Norum, J. J. Kelly, A. D. Bacher, G. T. Emery, C. C. Foster, W. P. Jones, D. W. Miller, B. L. Berman, and D. J. Millener. Structure of 9be from proton scattering at 180 mev. *Phys. Rev. C*, 43:1758–1776, Apr

1991. doi: 10.1103/PhysRevC.43.1758. URL <http://link.aps.org/doi/10.1103/PhysRevC.43.1758>.
- [113] Marco La Cognata and Antonio Del Zoppo. The $8\text{Li}(a,n)_{11}\text{B}$ reaction rate at astrophysical temperatures. *The Astrophysical Journal*, 736(2):148, 2011. URL <http://stacks.iop.org/0004-637X/736/i=2/a=148>.
- [114] Kenneth S. Krane. *Introductory Nuclear Physics*. John Wiley and Sons, 1987. ISBN 978-0-471-80553-3.
- [115] P. Lauridsen Ribeiro. Code t2. Universidade de São Paulo, 2001.
- [116] E. Leistenschneider. Sam-ribbras - user's guide. Universidade de São Paulo, 2011.
- [117] I. Antcheva, M. Ballintijn, B. Bellenot, M. Biskup, R. Brun, N. Buncic, Ph. Canal, D. Casadei, O. Couet, V. Fine, L. Franco, G. Ganis, A. Gheata, D. Gonzalez Maline, M. Goto, J. Iwaszkiewicz, A. Kreshuk, D. Marcos Segura, R. Maunder, L. Moneta, A. Naumann, E. Offermann, V. Onuchin, S. Panacek, F. Rademakers, P. Russo, and M. Tadel. {ROOT} — a c++ framework for petabyte data storage, statistical analysis and visualization. *Computer Physics Communications*, 180(12):2499 – 2512, 2009. ISSN 0010-4655. doi: <http://dx.doi.org/10.1016/j.cpc.2009.08.005>. URL <http://www.sciencedirect.com/science/article/pii/S0010465509002550>. 40 YEARS OF CPC: A celebratory issue focused on quality software for high performance, grid and novel computing architectures.
- [118] W.T.Milner. Upak software package. Oak Ridge National Laboratory, 1987. URL <http://www.phy.ornl.gov/computing/daqsupport.html>.
- [119] J.P. Boris. Relativistic plasma simulation-optimization of a hybrid code. *Proceedings of the Fourth Conference on Numerical Simulation of Plasma*, 1970.
- [120] Hann-Shin Mao and Richard Wirz. Comparison of charged particle tracking methods for non-uniform magnetic fields. *Proceedings of the Fourth Conference on Numerical Simulation of Plasma*, 2011. doi: 10.2514/6.2011-3739. URL <http://arc.aiaa.org/doi/abs/10.2514/6.2011-3739>.

LIST OF FIGURES

Figure 1	Local galactic abundances of isobars, adapted from [3].	1
Figure 2	Average binding energy per nucleon as a function of the atomic mass number A . Adapted from [7].	2
Figure 3	Cross section measurements of the ${}^8\text{Li}(\alpha, n){}^{11}\text{B}$ reaction at astrophysical energies [22].	4
Figure 4	Possible astrophysical reaction chains with low mass nuclides, emphasizing the role of ${}^8\text{Li}$. Sequential decays are not depicted.	5
Figure 5	Predicted paths of r-process, showing the waiting-points (red region) and their paths upon β^- decay (red arrows). Magic numbers are represented by dashed lines. Paths of other processes are also depicted (adapted from [39]).	6
Figure 6	Energy levels for ${}^9\text{Be}$, the ${}^8\text{Li} + p$ threshold is emphasized [14].	7
Figure 7	${}^8\text{Li}(p, \alpha)$ differential cross sections at $\theta_{\text{lab}} = 13.5^\circ$, with the R-matrix fit (solid line): (a) full measured spectrum and (b) zoom at lower energies. Taken from [41].	8
Figure 8	${}^8\text{Li}(p, \alpha){}^5\text{He}$ and ${}^8\text{Li}(\alpha, n){}^{11}\text{B}$ reaction rates multiplied by proton and alpha mass fractions for adequate comparison [41].	9
Figure 9	Scheme of an excitation function for a reaction obtained through the entrance system $a + A$. The peaks are related to states of the compound nucleus C . Picture taken from [43].	13
Figure 10	Measurements of differential cross section for the ${}^{27}\text{Al}(p, p)$ reaction at several angles around 1579 keV resonance [47], showing the several shapes a resonance can assume. A typical Breit-Wigner shape can be seen at the measurements at $\theta_{\text{cm}} = 92.1^\circ$	14
Figure 11	Scheme of the Coulomb barrier for two interacting nuclei in function of their distance.	15
Figure 12	Typical dependence of the cross section and S-factor with energy observed in the ${}^3\text{He}(\alpha, \gamma){}^7\text{Be}$ data. Picture taken from [39].	16
Figure 13	Schematic example of a Gamow window at some nucleosynthesis environments.	17

Figure 14	Scheme of the Oscar Sala building, showing the main parts of the accelerator facility (Author: J.C. Terassi).	23
Figure 15	Probability ϕ_i of emerging from the carbon stripper foil for each charge state i of a ${}^7\text{Li}$ beam as a function of particle's energy [61].	24
Figure 16	Scheme of the Pelletron Laboratory's Experimental Hall, showing the experimental beamlines available (Author: J.C. Terassi).	25
Figure 17	Detailed scheme of the Pelletron Laboratory beamline (Author: J.C. Terassi).	26
Figure 18	Scheme of the operation of the MC-SNICS ion source [68].	27
Figure 19	Scheme of the Pelletron accelerator, including its charging system and the acceleration tube. Picture adapted from [70].	29
Figure 20	Scheme of the Pelletron accelerator's energy control system (adapted from [60]).	30
Figure 21	RIBRAS System at Pelletron Laboratory's 45-B Beamline. Panoramic picture (above) and schematic drawing (below), showing its main components (adapted from [71]).	32
Figure 22	Scheme of the Production Target Setup at RIBRAS System (adapted from [71]).	33
Figure 23	Schematic cross section of the solenoids employed at RIBRAS (adapted from [55]).	34
Figure 24	Example of simulated ion trajectories inside RIBRAS, leaving the production target and being focused in the center of the central scattering chamber (red line) by the first solenoid [71].	35
Figure 25	Simulated focalization curves for ${}^8\text{Li}$, showing the electrical current that must be applied in the solenoids in order to focus ${}^8\text{Li}$ at various energies in the scattering chambers. These curves were generated by the code <code>sol-focus</code> (appendix B).	35
Figure 26	Example of a typical biparametric $E - \Delta E$ spectrum (not calibrated), showing the energy loss in the thin ΔE detector (ordinate axis) as a function of the remaining energy of the detected particle left on the thick E detector. This clearly evidence the identification in mass and charge.	39

Figure 27	Energy spectrum of a radioactive ^{241}Am alpha source [82]. A spectrum like this can be used to calibrate the detector relating the position (in channels) of the measured peaks to their known energies.	40
Figure 28	Example of a typical biparametric $E - \Delta E$ spectrum, showing the characteristic channeling tail that follows an intense peak, before (a) and after (b) a proper calibration. The calibrated spectrum is in function of the particle's total energy E_{tot}	41
Figure 29	Scheme of the MCP timing detector setup. The permanent magnets are not shown.	44
Figure 30	MCP timing detector setup, showing its main parts. The permanent magnets are not shown.	44
Figure 31	MCP's performance dependance over polarization bias: detection efficiency (a) and timing resolution (b). Tests performed with alpha particles (details in the text).	45
Figure 32	$E - \Delta E$ spectra acquired simultaneously from the same detectors, but passed through different amplification lines: (a) high gain to favor light particles and (b) low gain to favor heavier particles.	48
Figure 33	Scheme of the electronics employed in the experiment.	50
Figure 34	Particle tracks along RIBRAS' beamline simulated by the code <code>sol-focus</code> (appendix B). (a) ^8Li secondary beam, properly focused on secondary target (green block at main chamber). (b) Deuteron contaminant beam, focused with ^8Li in the central chamber but hitting a collimator instead of the secondary target, exemplifying the effect of an energy degrader (red block at central chamber) on changing the contaminant's $B\rho$. (c) ^7Li from primary beam hitting a blocker.	54
Figure 35	Spectra taken at main chamber with the secondary beam scattered in a gold target, (a) without the use of a degrader in central chamber and (b) with the degrader, pointing to its purifying properties.	54
Figure 36	ToF \times energy spectrum, showing ^8Li beam purity in a non-optimized situation.	55

Figure 37	^8Li beam energy profile at main chamber at two situations during the experiment. Average energies:(a) 15.9 MeV and (b) 18.7 MeV.	56
Figure 38	Typical angular distribution of the elastic scattering of ^8Li on ^{197}Au at $E(^8\text{Li})_{\text{lab}} = 19$ MeV [55].	57
Figure 39	Focusing quality analysis for ^8Li beam at central chamber. (a) PSD spectra, emphasizing the ^8Li . (b) Spatial distribution spectra of ^8Li , extracted from the PSD spectra. The grey strips correspond to the masks put in front of the PSD, each strip is 2 mm wide.	59
Figure 40	Focusing quality analysis for ^8Li beam at the main chamber. (a) PSD spectra, emphasizing the ^8Li . (b) Spatial distribution spectra of ^8Li , extracted from the PSD spectra. The grey strips correspond to the masks put in front of the PSD, each strip is 2 mm wide.	59
Figure 41	Microscopic photo of the surface of the $(\text{CH}_2)_n$ target employed in the experiment, showing its roughness.	61
Figure 42	Thickness measurements of the $(\text{CH}_2)_n$ secondary target. (a) Microscopic photo of a transversal cut of the target. (b) Thickness profile extracted from multiple photos of one cut, red dashed line marks the average.	62
Figure 43	Distribution of thickness measurements of the $(\text{CH}_2)_n$ secondary target, with gaussian fit.	63
Figure 44	Illustrative scheme of the thick target method applied to the experiment.	64
Figure 45	R-matrix prediction of $^8\text{Li}(p,p)$ differential cross section at $\theta_{\text{lab}} = 10^\circ$ based on data of the previous work on $^8\text{Li}(p,\alpha)$ [41], shown at table 1.	66
Figure 46	Simulations for ^8Li energy (and equivalent center-of-mass reaction energy for $^8\text{Li} + p$) in function of $(\text{CH}_2)_n$ target depth for both ^8Li bombarding energies employed.	67
Figure 47	Conversion curves for the energy of reaction products – proton (a), deuteron (b) and alpha (c) – right after emerging from the $(\text{CH}_2)_n$ target in function of the correspondent ^8Li energy (and equivalent center-of-mass energy for $^8\text{Li} + p$) for both ^8Li bombarding energies employed.	68

Figure 48	Simulated dispersion (in standard deviation) of the energy of ^8Li beam at the reaction point in function of the detectable energy of the products: (a) alphas, (b) protons and (c) deuterons, for bombarding energy of $E(^8\text{Li}) = 18.7$ MeV.	71
Figure 49	Photo of the experimental mount at main chamber.	73
Figure 50	Scheme of the experimental mounting in the RIBRAS System for this experiment.	75
Figure 51	Spectra obtained with $(\text{CH}_2)_n$ target and ^8Li beam of $E(^8\text{Li}) = 18.7$ MeV for both amplification lines: (a) higher gain and (b) lower gain, showing the strips from which were extracted the reaction product yields.	77
Figure 52	Spectra obtained with $(\text{CH}_2)_n$ target and ^8Li beam of $E(^8\text{Li}) = 15.9$ MeV for both amplification lines: (a) higher gain and (b) lower gain, showing the strips from which were extracted the reaction product yields.	78
Figure 53	Spectra obtained with a thinner ΔE detector with $(\text{CH}_2)_n$ target and ^8Li beam of $E(^8\text{Li}) = 15.9$ MeV for both amplification lines: (a) higher gain and (b) lower gain, showing the strips from which were extracted the reaction product yields.	79
Figure 54	Stopping power of ^8Li in $(\text{CH}_2)_n$, calculated by the algorithm stopx (appendix B).	81
Figure 55	Jacobian for the transformation from laboratory frame to center-of-mass frame as a function of the energy $E(^8\text{Li})$ for the relevant reactions.	81
Figure 56	Correction of N_{inc} due to beam energy spread (fig.37) for both bombarding energies.	82
Figure 57	Energy spectra obtained with $(\text{CH}_2)_n$ target through the alpha strips at each bombarding energy and detector configuration at $\theta_{lab} = 10^\circ$. Energy bin: $\delta E = 0.275$ MeV.	83
Figure 58	Alpha particle events per energy spectra obtained in the previous experiment at energies around those employed at this experiment and at $\theta_{lab} = 13.5^\circ$ (adapted from [41]).	84
Figure 59	Measured and corrected excitation functions for alphas for bombarding energy of $E(^8\text{Li}) = 18.7$ MeV, and the corrections due to ^5He decay and direct ^9Be 3-body break-up.	85

Figure 60	Complete excitation function for ${}^8\text{Li}(p,\alpha){}^5\text{He}$ reaction measured at $\theta_{\text{lab}} = 10^\circ$	86
Figure 61	Excitation functions for ${}^8\text{Li}(p,\alpha)$ experiments measured at forward angles, comparing the results from this work and those from [41] and [102].	87
Figure 62	Energy spectra obtained with $(\text{CH}_2)_n$ target through the proton strips at each bombarding energy and detector configuration at $\theta_{\text{lab}} = 10^\circ$. Energy <i>bin</i> : $\delta E = 0.055$ MeV.	88
Figure 63	Spectra obtained with ${}^{197}\text{Au}$ target at both ${}^8\text{Li}$ beam energies of $E({}^8\text{Li}) = 18.7$ MeV (a) and 15.9 MeV (b), putting into evidence the proton strips with the contaminants.	89
Figure 64	Spectra normalized by primary beam intensity and by energy bin width for protons detected with $(\text{CH}_2)_n$, natural carbon and ${}^{197}\text{Au}$ targets for the bombarding energy of $E({}^8\text{Li}) = 15.9$ MeV.	90
Figure 65	Complete excitation function for the ${}^8\text{Li}(p,p)$ reaction measured at $\theta_{\text{lab}} = 10^\circ$	91
Figure 66	Energy spectra obtained with $(\text{CH}_2)_n$ target through the deuteron strips at each bombarding energy and detector configuration at $\theta_{\text{lab}} = 10^\circ$. Energy <i>bin</i> : $\delta E = 0.118$ MeV.	92
Figure 67	Complete excitation function for the ${}^8\text{Li}(p,d)$ reaction measured at $\theta_{\text{lab}} = 10^\circ$	93
Figure 68	Excitation function for ${}^8\text{Li}(p,d){}^7\text{Li}$ reaction in comparison with the deduced from the inverse reaction measured by [104] and [105].	94
Figure 69	Excitation function for the ${}^8\text{Li}(p,t)$ reaction measured at $\theta_{\text{lab}} = 10^\circ$	95
Figure 70	Differential cross section for the ${}^8\text{Li}(p,n)$ reaction at $E_{\text{cm}} = 1.5$ MeV measured by [107].	96
Figure 71	Calculated S-factor for the ${}^8\text{Li}(p,\gamma){}^9\text{Be}$ (g.s.) reaction done by [26].	97
Figure 72	Measured excitation functions for the ${}^8\text{Li}(p,p)$ (a), the ${}^8\text{Li}(p,\alpha)$ (b) and the ${}^8\text{Li}(p,d)$ (c) reactions at $\theta_{\text{lab}} = 10^\circ$, with the energies of the ${}^9\text{Be}$ resonances found in the literature indicated (see table 1).	98
Figure 73	R-matrix calculations for proton and alpha channels using the parameters obtained by [41].	100

- Figure 74 R-matrix calculations using the parameters obtained by [41] with the assignment of deuteron partial widths to the resonances at $E_{cm} = 1.69$ and 1.76 MeV. The same Γ_d was assigned to both resonances, and the results of two calculations are shown: $\Gamma_d = 200$ keV (solid) and $\Gamma_d = 50$ keV (dashed). 100
- Figure 75 R-matrix analysis for a positive parity resonance at $E_{cm} = 1.10$ MeV with several total spins J^+ . Its partial widths were all set to $\Gamma_p = 100$ keV, $\Gamma_d = 50$ keV and $\Gamma_\alpha = 0$, except for the $J^\pi = 1/2^+$ resonance, in which $\Gamma_p = \Gamma_d = 100$ keV. A $5/2^+$ resonance at $E_{cm} = 1.76$ MeV in the ${}^8\text{Li}(p,p)$ excitation function was added for visualization purposes. 102
- Figure 76 R-matrix analysis for a negative parity resonance at $E_{cm} = 1.10$ MeV with several total spins J^- . Its partial widths were all set to $\Gamma_p = 100$ keV, $\Gamma_d = 50$ keV and $\Gamma_\alpha = 0$, except for the $J^\pi = 1/2^-$ resonance, in which $\Gamma_p = \Gamma_d = 100$ keV. A $5/2^+$ resonance at $E_{cm} = 1.76$ MeV in the ${}^8\text{Li}(p,p)$ excitation function was added for visualization purposes. 102
- Figure 77 R-matrix analysis for a $T = 3/2$ positive parity resonance at $E_{cm} = 1.76$ MeV ($E_x = 18.65$ MeV) with several total spins J^+ . The widths were all set to $\Gamma_p = 300$ keV and $\Gamma_\alpha = \Gamma_d = 0$ 103
- Figure 78 Observed shift in the excitation function of a ${}^9\text{Be}$ resonance which decays to ${}^7\text{Li}^* + d$ 105
- Figure 79 R-matrix calculations for a positive parity resonance at $E_{cm} = 1.66$ MeV ($E_x = 18.55$ MeV) with several total spins J^+ and $J^\pi(18.65 \text{ MeV}) = 5/2^+$ 106
- Figure 80 R-matrix calculations for a negative parity resonance at $E_{cm} = 1.66$ MeV ($E_x = 18.55$ MeV) with several total spins J^- and $J^\pi(18.65 \text{ MeV}) = 5/2^+$ 106
- Figure 81 R-matrix calculations for a resonance at $E_{cm} = 1.66$ MeV ($E_x = 18.55$ MeV) with several total spins J^π and $J^\pi(18.65 \text{ MeV}) = 3/2^+$ 107
- Figure 82 R-matrix fits considering the J^π pair ($7/2^-, 5/2^+$) for the overlapping resonances (see table 7 for parameters). 109
- Figure 83 R-matrix fits considering the J^π pair ($7/2^-, 3/2^+$) for the overlapping resonances (see table 7 for parameters). 109

Figure 84	R-matrix fit considering the J^π pair ($9/2^+$, $5/2^+$) for the overlapping resonances (see table 7 for parameters).	110
Figure 85	Integrated cross section (left column) and S-factor (right column) for the ${}^8\text{Li}(p,\alpha)$ and ${}^8\text{Li}(p,d)$ reactions obtained from the R-matrix fits.	112
Figure 86	Calculated reaction rates for the reactions ${}^8\text{Li}(p,\alpha)$ and ${}^8\text{Li}(p,d)$. The rate for ${}^8\text{Li}(p,d)$ reaction is probably underestimated as the resonances at $E_{\text{cm}} = 0.38$ MeV and 0.61 MeV could not be measured in this work.	113
Figure 87	Scheme of collision geometry involved in a nuclear reaction in the laboratory frame.	121
Figure 88	Kinematics for the relevant reactions in this experiment.	123
Figure 89	Scheme of collision geometry involved in a nuclear reaction at the center-of-mass frame.	124
Figure 90	Relation between elastic scattering energy and scattering angle of a beam of mass $m_1 = 8$ for several targets.	125
Figure 91	Energy profiles for ${}^8\text{Li} + p$ experiment simulated using CineRIBRAS: (a) of ${}^8\text{Li}$ beam after passing through the degrader and (b) of α particles from ${}^8\text{Li}(p,\alpha)$ reaction detected at 10° after a $(\text{CH}_2)_n$ target [93].	128
Figure 92	Simulated biparametric spectrum of an $E - \Delta E$ telescope positioned at 10° , with thickness of $20\mu\text{m}$ for ΔE detector and $1000\mu\text{m}$ for E detector. In blue are the expected protons (from ${}^8\text{Li}(p,p)$) and alphas (from ${}^8\text{Li}(p,\alpha)$). In red are possible contaminants [93].	129
Figure 93	A few results on the ${}^8\text{Li}$ beam simulation using SolFocus. (a) Ratio of focalized ${}^8\text{Li}$ particles (22.8 MeV) in the target position of central chamber as a function of the current in the first solenoid simulated by SolFocus. (b) ${}^8\text{Li}$ beam spot profile in the secondary target (in light yellow) at main chamber [93].	130

LIST OF TABLES

Table 1	Available experimental data on ${}^9\text{Be}$ resonances near the ${}^8\text{Li} + \text{p}$ threshold (16.8882 MeV), including the compilation from [14] and the work of [41] on ${}^8\text{Li}(\text{p},\alpha)$	9
Table 2	Examples of radioactive beams that can be produced at RIBRAS [13].	32
Table 3	Common contaminants present with ${}^8\text{Li}$ beam and their expected energies relative to ${}^8\text{Li}$'s energy (in MeV).	52
Table 4	${}^8\text{Li}$ production efficiency at each phase of the experiment.	74
Table 5	(Copy of table 1) Available experimental data on ${}^9\text{Be}$ resonances near the ${}^8\text{Li} + \text{p}$ threshold (16.8882 MeV), including the compilation from [14] and the work of [41] on ${}^8\text{Li}(\text{p},\alpha)$	99
Table 6	Best R-matrix fit for the resonance at $E_{\text{cm}} = 1.10\text{MeV}$	107
Table 7	R-matrix fits for the measured excitation functions, exploring the ambiguities between the two overlapping resonances.	108
Table 8	Parameters of the measured ${}^9\text{Be}$ resonances obtained from the R-matrix analysis of this work.	111
Table 9	Spins and parities of pairs of nuclei (in the ground state) that may be channels of the ${}^9\text{Be}$ compound nucleus.	131
Table 10	J^π of ${}^9\text{Be}$ states that can be populated by the ${}^8\text{Li} + \text{p}$ system.	132